Microwave-optic interconnects for superconducting circuits

by

Georg Arnold

October, 2024

A thesis submitted to the
Graduate School
of the
Institute of Science and Technology Austria
in partial fulfillment of the requirements
for the degree of
Doctor of Philosophy

Committee in charge:

Christopher Wojtan, Chair
Johannes Fink
Onur Hosten
Mohammad Mirhosseini

Institute of
Science and
Technology
Austria

The thesis of Georg Arnold, titled *Microwave-optic interconnects for superconducting circuits*, is approved by:

Supervisor: Johannes Fink, ISTA, Klosterneuburg, Austria

Signature: ______________________________

Committee Member: Onur Hosten, ISTA, Klosterneuburg, Austria

Signature: ______________________________

Committee Member: Mohammad Mirhosseini, Caltech, Pasadena, USA

Signature: ______________________________

Defense Chair: Christopher Wojtan, ISTA, Klosterneuburg, Austria

Signature: ______________________________

Signed page is on file

ISTA Thesis, ISSN: 2663-337X

I hereby declare that this thesis is my own work and that it does not contain other people's work without this being so stated; this thesis does not contain my previous work without this being stated, and the bibliography contains all the literature that I used in writing the dissertation.

I accept full responsibility for the content and factual accuracy of this work, including the data and their analysis and presentation, and the text and citation of other work. I declare that this

is a true copy of my thesis, including any final revisions, as approved by my thesis committee, and that this thesis has not been submitted for a higher degree to any other university or institution.

I certify that any republication of materials presented in this thesis has been approved by the relevant publishers and co-authors.

Signature: ____________________

Georg Arnold
October, 2024

Signed page is on file

Abstract

"Can we do this with a new type of computer - a quantum computer?". This famous quotation of the brilliant Richard Feynman within a conference talk on "Simulating physics with computers." is often reverently praised as the origin of the field of quantum computing. The idea was to use quantum mechanical systems itself to simulate "Nature", which is inherently quantum mechanical. Now, 43 years later, the theoretical framework of how such a computer can operate has been developed. Two main important concepts for a potential quantum supremacy, superposition and entanglement, have been exploited to design quantum algorithms to significantly speed up certain tasks. Yet, the specific hardware implementation is still far from being certain, in fact the race between the most promising platforms such as superconducting qubits, bosonic codes, cold atoms, trapped ions, optical computing as well as spin qubits has recently intensified. If one also includes the most mature applications of quantum communication technologies, secure quantum key distribution and quantum random number generators, as part of a quantum information technology ecosystem, we are confronted with a plethora of different materials, concepts, and also operation frequencies. While superconducting qubits, bosonic codes and spin qubits work in the regime of approximately 5 GHz and are controlled by electrical fields, trapped ions, cold atoms, and optical quantum computing operate with light in the infrared or visible range.

Consequently, a quantum frequency converter or microwave-optic transducer is required to interface the different frequency domains or establish a long-range network connection with suitable telecom fibers. In fact, the combination of different frequency regimes is also an essential part in our classical modern communication network, where computations are performed in electrical circuits and the information exchange over longer distances happens via optical fibers. However, the specific challenges specific to building a quantum computer, also apply to the development of such a quantum frequency transducer: 1) As we deal with single excitations as the carrier of information, i.e. the smallest possible quantity, the signal can easily be corrupted by other noise sources which needs to be avoided by all means. This is also the reason why microwave quantum computers operate at temperature environments close to zero temperature (< 0.1 Kelvin) to avoid corruption by thermal noise. 2) The frequency interface generally needs to preserve the phase of the signal as an essential part of the quantum state. And 3) Quantum signals cannot be copied which would be a typical strategy to account for errors in classical computers. And finally, there is a challenge specific to microwave-optic transducers: While quantum computers are operating in one specific frequency domain, microwave-optic transducers combine microwave and optical fields in one device. This results in the particular challenge that high-energy optical radiation, which is usually well-shielded from superconducting microwave quantum processors, are now an essential part of the device. The concomitant optical radiation in the operating transducer will inevitably have a detrimental effect on the superconducting microwave components. Together with the requirement of minimal background noise for quantum-limited operation as described above, heating from the absorption of optical photons within the same device where single microwave excitations are processed forms a formidable challenge.

This thesis aims to address this challenge by developing microwave-optic transducers where the impact of optical absorption on superconducting circuits in general and superconducting qubits specifically can be mitigated. In our first approach, we developed a compact device with optimized interaction strengths between the different frequency domains. This minimizes the optical powers used for transducer operation and thus the optical absorption heating. This work was - to the best of our knowledge - the first comprehensive noise study, in an integrated microwave-optic transducer. Unfortunately, we saw that the optical absorption heating added noise way above a single excitation. Consequently, a potential quantum signal would have been buried in the noise, added by the transduction.

Building on this insight, we utilized a three-dimensional microwave-optic transducer instead of an integrated device. The larger heat capacity of the macroscopic device with a size of a few millimeters can absorb a larger fraction of the optical heating before it increases the temperature of the device. This allowed us to interface the transducer directly with a superconducting qubit to readout the qubit state in a novel all-optical manner. We showed that the microwave-optic transducer can be operated in a regime in which optical fields don't harm the sensitive qubit. This is an important prerequisite for the operation of microwave-optic transducers in conjunction with microwave quantum processors and brings the integration and seamless orchestration of different frequency components in a quantum network a step closer.

Acknowledgements

It has been a fulfilling journey at ISTA, joining Johannes' group only one year after he started. I will always remember the almost empty optical tables when I arrived, and I thought to myself "Wow, so many things we can build here" (Yes, so many things we HAD TO build before we could get started). The clean room opened only a few months later and the machines were not running yet. The dilution refrigerators dedicated to our experiments were not even ordered. It took a huge collaborative effort from all of us, Matthias, Shabir, Alfredo, Matilda, and Nikolai as the starting team, and then Martin, Lena, Farid, William, Rishabh, Riya, Yuan to get the whole pipeline running: Simulations and design, clean room fabrication, measurements and analysis. As everyone of us was driven by this ultimate quest for discovery, combined with a good sense of humor in the periods where things just didn't work out, I enjoyed every single minute. It was rewarding to see that our first results raised attention in the community and attracted skilled applicants, leading to get Liu, Lucky, and Thomas on board, who all contributed esssentially to the work presented here, and later then Erfan, Andrei and Samarth. I also acknowledge the hard work and refreshing spirit from the summer interns I had to pleasure to supervise: Donald and Moritz significantly expanded the simulation library with diligence and gumption. As I had the pleasure to work on most main topics in our group from superconducting qubits over mechanics to telecom optics, I eventually worked with all of you and benefited from each of you, master student or senior postdoc alike, in one way or the other. Thank you for the productive and proactive environment. Naturally, big credits for that have to be given to my supervisor Johannes who makes sure everyone stays on track and did a lot of great hirings.

However, the exciting aspect in my opinion arises from the fact, that the situation doesn't feel like leaning back and patting ourselves on the back. Things just got started. Together with our "friendly competitors" at Jila, Caltech, Harvard, and TU Delft to just name a few, we managed to push the performance and scalability of microwave-optic transducer that the field developed from an important concept without realistic implementation to an emerging technology with a substantial traction that attracts first interest of important players in the field of superconducting quantum computing. In this regard, I would also like to thank the students, postdocs and PIs of the aforementioned research groups. Despite the competition, they were always open to discussion and the exchange of tips and tricks.

I am also very grateful for the incredible support of the A2P (assistants to Professors), especially Sandra, who always had a helping hand for any kind of administrative issues. Todor and his machine shop turned our vague ideas into technical drawings and actual components in no time. Salvo and his clean room team, who always had to find solutions in the tension between our desire for best device performance and sticking to developed recipes on the one side, and health and safety requirements on the other (buzzword: NMP liftoff). In general, the whole administrative support as well as the service units have always provided fast and direct help, so we could just focus on the thing we love: science.

This work was supported by the European Research Council under grant agreement no. 758053 (ERC StG QUNNECT) and the European Union's Horizon 2020 research, innovation program under grant agreement no. 899354 (FETopen SuperQuLAN) and the Austrian Science Fund (FWF) through BeyondC (F7105). I want to acknowledge generous support from the Austrian Academy of Sciences from a DOC [Doctoral program of the Austrian Academy of Sciences] fellowship (no. 25129).

About the Author

I completed my bachelor and master studies in engineering physics at the Graz University of Technology in the field of electron and ion beam fabrication methods. For my master thesis, I could develop a prize winning nano-mechanical gas sensor prototype. After joining the group of Johannes Fink at ISTA as a PhD student in 2018, I worked on microwave-optic transducers to be used for quantum applications. My research interests comprise all aspects of prototype and product development starting from simulation and modelling over fabrication to testing and analysis. The main research fields include quantum optics and quantum communication. Besides that, I am dedicated to impart knowledge which manifests itself in a second BSc and MSc degree from a teacher training program in Physics and Sports.

List of Collaborators and Publications

G. Arnold*, M. Wulf*, S. Barzanjeh, E. S. Redchenko, A. Rueda, W. J. Hease, F. Hassani, and J. M. Fink. Converting microwave and telecom photons with a silicon photonic nanomechanical interface. *Nature Communications*, 11(1):4460, 2020. URL: `https://doi.org/10.1038/s41467-020-18269-z`

G. Arnold*, T. Werner*, R. Sahu, L. N. Kapoor, L. Qiu, and J. M. Fink. All-optical single-shot readout of a superconducting qubit. *arXiv preprint arXiv:2310.16817*, 2023. URL: `https://arxiv.org/abs/2310.16817` (accepted for publication in *Nature Physics* under `https://doi.org/10.1038/s41567-024-02741-4`)

S. Barzanjeh, E. S. Redchenko, M. Peruzzo, M. Wulf, D. P. Lewis, G. Arnold, and J. M. Fink. Stationary entangled radiation from micromechanical motion. *Nature*, 570(7762):480–483, 2019. doi: `https://www.doi.org/10.1038/s41586-019-1320-2`

W. Hease*, A. Rueda*, R. Sahu, M. Wulf, G. Arnold, H. G. Schwefel, and J. M. Fink. Bidirectional Electro-Optic Wavelength Conversion in the Quantum Ground State. *PRX Quantum*, 1(2): 020315, 2020. URL: `https://www.doi.org/10.1103/PRXQuantum.1.020315`

R. Sahu, W. Hease, A. Rueda, G. Arnold, L. Qiu, and J. M. Fink. Quantum-enabled operation of a microwave-optical interface. *Nature Communications*, 13(1):1276, 2022. URL: `https://www.doi.org/10.1038/s41467-022-28924-2`

R. Sahu*, L. Qiu*, W. Hease, G. Arnold, Y. Minoguchi, P. Rabl, and J. M. Fink. Entangling microwaves with light. *Science*, 380(6646):718–721, 2023. ISSN 0036-8075. URL: `https://www.doi.org/10.1126/science.adg3812`

L. Qiu, R. Sahu, W. Hease, G. Arnold, and J. M. Fink. Coherent optical control of a superconducting microwave cavity via electro-optical dynamical back-action. *Nature Communications*, 14(1):3784, 2023. URL: `https://www.doi.org/10.1038/s41467-023-39493-3`

---

* These authors contributed equally.

Table of Contents

List of Figures

List of Tables

List of Abbreviations

$BaTiO_3$ barium titanate. 4

$LiNbO_3$ lithium niobate. 4, 6, 13, 16, 17, 24, 26, 27, 29, 42, 84

$LiTaO_3$ lithium tantalate. 4

EM electro-mechanical. xiv, 25, 33–35, 38–43, 46, 48, 53, 54, 60–62, 67, 70–72, 74–77

EO electro-optical. xiv, 2, 4, 6, 24, 33–35, 42, 43, 45, 46, 48, 54, 70–74, 78, 90, 93, 94, 109

EOM electro-opto-mechanical. xiv, 3, 27, 29, 53, 55, 61–64, 70–76

FEM finite element method. 19, 21–25, 27, 31

GHZ Greenberger–Horne–Zeilinger. 106

HEMT high-electron-mobility transistor. 64, 65, 90, 95–99, 103, 115

HF hydrofluoric acid. 20, 27, 63

JJ Josephson tunnel junction. 46–48, 90

LO local oscillator. 99–101

OM opto-mechanical. xiv, 2, 4, 6, 17, 19, 25, 33–35, 38–44, 46, 48, 53, 54, 58–62, 65–68, 70–76, 78, 115

QLE Quantum Langevin equation. 10, 12, 32, 34, 36, 38

QND quantum non-demolition. 50, 51

SEM scanning electron microscopy. 18, 25, 53, 77

SNR signal-to-noise ratio. 50, 97, 99–101, 103, 106

SOI silicon-on-insulator. 77

TLS two-level systems. 28, 30, 31

TMS two-mode squeezing. 76, 77

Transmon transmission line shunted plasma oscillation qubit. 47, 84

WGM whispering gallery mode. 16, 17, 19, 24, 26–29, 42, 43

CHAPTER 1

Introduction

Over the past few decades, the convergence of quantum mechanics with information science has led to the demonstration of some revolutionary advances that are pushing the boundaries of what is possible with classical technology. This fusion has not only expanded our understanding of the quantum world but also paved the way for groundbreaking innovations such as quantum computing and the concept of a "Quantum Internet" [Kimble, 2008; Wehner et al., 2018]. This new paradigm promises to revolutionize how we process, store, and communicate information on a global scale for specific tasks and applications. Quantum information science itself relies on the principles of quantum mechanics, particularly superposition and entanglement, which enable quantum systems to perform tasks that are impossible for classical systems. While superposition can be seen as the interference of two basis states which form together a new valid state of the quantum system, entanglement may be interpreted as a maximal, quantum mechanical correlation beyond classical limits between non-local quantum systems [Einstein et al., 1935; Bell, 1964]. In this context, quantum networks emerged as crucial structures for both the formal analysis, e.g. for the demonstration of fundamental quantum mechanical properties such as entanglement, and practical implementation of quantum technologies such as protocols like quantum teleportation which allows for the instantaneous transfer of quantum states across vast distances [Bouwmeester et al., 1997]. These networks consist of quantum nodes that generate, process, and store quantum information, connected by quantum channels that distribute entanglement and transfer information in form of quantum states between distant network nodes. It was exactly the extension of this idea which lead to the concept of such a "Quantum Internet," a concept that bases on the analogy to our current internet and necessitates quantum processors, quantum memories, and quantum repeaters to allow the signals to travel over long distances. A quantum network could perform tasks that are unattainable in the classical world, even if the processing capabilities, e.g. the bandwidth, are only moderate, such as distributed quantum computing algorithms.

An unprecedented property of such a network without classical counterpart is the establishment of entanglement between the quantum bits (qubits) of distant processors. These bits are then "maximally correlated", a feature that does not exist in our classical world. Naturally, this characteristic is a useful benefit for any task that requires coordinated processing. Quantum entanglement can provide this feature over arbitrary long distances. Although it is impossible to conceive all future applications of this novel technology, it will provably allow for capabilities beyond any classical information processing systems. Applications that have already been detected comprise secure access to the resources of a distant quantum computer, also known as blind quantum computing [Broadbent et al., 2009], clock synchronization, secure communication or cryptography, and, in principle, arbitrary long baseline interferometry [Gottesman et al., 2012].

One of the main challenges in realizing quantum networks is the need for quantum interconnects —interfaces that allow for the reversible transfer of quantum states between different physical systems, such as between light (photons) and matter (atoms) [Covey et al., 2023; Awschalom et al., 2021; Ang et al., 2022; Bravyi et al., 2022; Han et al., 2021; Lambert et al., 2020; Lauk et al., 2020]. Achieving high-fidelity quantum state transfer is critical for the functioning of a quantum network, as it ensures that the delicate quantum information is preserved during transmission.

This is where *Microwave-Optic Transducers* could play a crucial role. These devices convert quantum information coherently between microwave and optical frequencies. This capability is essential for interfacing different quantum systems and bridging the gap between various platforms, such as superconducting qubits [Wallraff et al., 2004] and optical photons. Superconducting qubits are highly promising for quantum computing due to their long coherence times compared to their gate processing time and scalability. However, they operate at microwave frequencies, which are not suitable for long-range communication due to their susceptibility to thermal noise and significant loss in transmission. On the other hand, optical photons, which operate at higher frequencies in the terahertz range can travel over long distances through fiber optic cables with minimal loss and noise corruption even at room temperature, making them ideal for quantum communication. Microwave-optic transducers facilitate the seamless conversion between these two domains, allowing quantum information to be processed by superconducting qubits and then transmitted over optical channels to distant nodes in the network.

These quantum transducers are typically based on nonlinear optical processes, such as electro-optical (EO) modulation [Tsang, 2010] or opto-mechanical (OM) interaction [Aspelmeyer et al., 2014], where a mechanical resonator is coupled to both a microwave cavity and an optical cavity. The precise control of these interactions allows for efficient and low-noise conversion of quantum states between microwave and optical photons, making it possible to integrate diverse quantum systems into a cohesive network and preserve the coherence of a quantum state.

While significant progress has been made in the development of quantum networks, there are still many challenges to overcome before they can be realized on a large scale. One of the main obstacles is the need for reliable quantum memories, which can store quantum information for long periods without significant loss of coherence. Quantum memories are essential for the operation of quantum repeaters and for the synchronization of quantum operations across the network.

Another challenge is the implementation of quantum error correction protocols, which are necessary to protect quantum information from the inevitable errors that occur during transmission and processing. These protocols require the ability to detect and correct errors without disturbing the quantum state, which is a non-trivial task given the fragility of quantum information. These quantum error correction schemes may depend on the physical realization and, thus, have to be developed for all components individually, such as processors [Xu et al., 2024; Bravyi et al., 2024], quantum memories [Terhal, 2015] and quantum repeaters [Azuma et al., 2023] and remote operations [Beukers et al., 2024].

Furthermore, as quantum networks become more complex, the task of verifying and characterizing entanglement across the entire network becomes increasingly difficult [Kimble, 2008; Wehner et al., 2018]. Traditional methods of state verification, such as quantum tomography, are impractical for large-scale networks due to the exponential growth in the size of the state space. New approaches, potentially inspired by techniques from quantum many-body physics, will be needed to assess the functionality and performance of quantum networks.

Despite the challenges, the pursuit of a large-scale quantum network remains one of the most exciting frontiers in modern quantum information science. The development of quantum networks will likely involve a combination of different technologies, including cavity QED, atomic ensembles, and other platforms such as quantum dots and superconducting circuits. Thus, these heterogeneous networks will require significant improvements in the device hardware, novel protocols for interfacing different quantum systems, but they may also offer unprecedented capabilities, especially when the researchers have developed the building blocks of quantum networks, such as quantum repeaters, single-photon sources, quantum memories, and microwave-optic transducers. Then, the focus will shift towards integrating these components [Hermans et al., 2022] into larger and more complex networks, ultimately leading to the realization of a heterogenous quantum network.

1.1 Microwave-optic transducers

The main topic of this thesis are microwave-optic transducers and its integration with superconducting quantum processors. Superconducting qubits, which are among the most promising candidates for building quantum processors [Arute et al., 2019; Wu et al., 2021]. As mentioned above, a microwave-optic transducer is a pressing need to transfer quantum information from microwave frequencies of superconducting qubits around typically $5\,\mathrm{GHz}$ in cold environments below $100\,\mathrm{mK}$ to optical frequencies around $200\,\mathrm{THz}$. The quantum state of photons with such high energy is resilient to thermal noise, even at room temperature, and can be transmitted over long-distances due to the low loss of telecom optical fibers. This allows different parts of a quantum network to communicate effectively. The usage of telecom communication channels also allows to re-use some essential parts of modern optical fiber communication which has been optimized for decades and it nowadays the backbone of our current information technoloy ecosystem. Even though there exist microwave waveguides with similarly low loss [Niu et al., 2023], the used materials need to be in the superconducting state for such a performance, which requires a cold environment also for the transmission channel in addition to the superconducting processing node. This makes microwave transmission channels unfeasible for long-distance communication.

The development of microwave-optic transducers has seen significant progress in recent years, driven by advances in various quantum technologies and materials science. Several approaches have been explored, each with its own set of advantages and challenges.

Electro-opto-mechanical (EOM) systems are one of the leading approaches to microwave-optic transduction [Andrews et al., 2014; Higginbotham et al., 2018; Arnold et al., 2020; Brubaker et al., 2022]. In these systems, a mechanical resonator is coupled to both a microwave circuit and an optical system. The mechanical resonator acts as a mediator, converting microwave photons into vibrations (phonons), which are then converted into optical photons through interactions with the optical cavity via optomechanics [Aspelmeyer et al., 2014]. Such as device is described and characterized in chapter 3. In order to enhance the interaction strength these systems use three resonators, a microwave, a mechanical and an optical resonator. All frequencies need to be aligned to form a triply resonant system with optimized transduction efficiency. The system of [Higginbotham et al., 2018] still holds the record efficiency for microwave-optic conversion. However, the bandwidth is currently limited to a few kHz and the low mechanical frequency of $\approx 1\,\mathrm{MHz}$ poses an ultimate limit on the achievable bandwidth.

In the last years, research groups and companies have shown increasing interest for piezo-OM platforms. The mechanical strain or displacement in a piezoelectric material is proportional to the electric field of the microwave mode (linear electromechanical effect or, in the language of nonlinear optics, $\chi^{(1)}$). Subsequently an OM resonator converts the mechanical excitation to an optical field [Vainsencher et al., 2016; Jiang et al., 2020; Han et al., 2020; Forsch et al., 2020; Mirhosseini et al., 2020; Weaver et al., 2024]. The process is in principle bidirectional. Such devices offer strong coupling between microwave photons and phonons. However, in order to combine strong piezo-electrical interaction with large OM conversion, a heterogeneous approach is often pursued comprising different material platforms. This typically increases the complexity of the device fabrication and reduces the quality of the individual components. The higher linewidth, especially of the mechanical mode, increases the bandwidth to $\sim\mathrm{MHz}$, but comes with a concomitant reduction in conversion efficiency. Recently, the necessity of a piezo-electric material as a requirement for strong microwave-phonon coupling at GHz frequencies could be lifted while maintaining a comparable transduction using a DC bias across a parallel plate capacitor with one mechanically compliant electrode [Zhao et al., 2023; Bozkurt et al., 2023; Zhao et al., 2024]. The otherwise only moderate interaction between the electric field of the microwave mode in the capacitor gap and mechanical thermal and quantum fluctuations of the order of only a few fm is strongly enhanced by the electrostatic field from the DC bias.

Besides the piezoelectric-effect for electromechanical coupling between microwave photons and acoustic waves or phonons, another useful material effect is the Pockels effect or linear electro-optical (EO) effect. An electric field, e.g. from a microwave circuit, can change the refractive index of an EO material which in turn affects the optical properties of the material. By that, a direct coupling between microwave and optical photons can be created without the need of a mechanical mediator. This effect is an active field of research for microwave-optic transduction for different materials such as lithium niobate ($\mathrm{LiNbO_3}$), lithium tantalate ($\mathrm{LiTaO_3}$), and barium titanate ($\mathrm{BaTiO_3}$). While the first has been used for many promising realizations [Rueda et al., 2016; Wang et al., 2018; Jiang et al., 2020] and is also the main material for commercial non-integrated electro-optic modulators, it poses challenges on industrial fabrication of integrated optical circuits at low cost. In contrast, $\mathrm{LiTaO_3}$ is commercially used and has a lower birefringence which is advantageous for the package density because mode mixing is avoided also at stronger waveguide bends. However, only recently electro-optic integrated circuits have been shown on this material [Wang et al., 2024]. $\mathrm{BaTiO_3}$ has presumably the largest electro-optic coupling of the aformentioned materials [Abel et al., 2019] but poses additional challenges on the fabrication. [1] Additionally, the strong electro-optic coefficient seems to decrease at lower temperatures, which is highly disadvantageous considering the environments of microwave quantum circuits below $100\,\mathrm{mK}$. The application of such a direct electro-optic converter for the readout of the state of a superconducting qubit is described in chapter 4.

Microwave-optic transduction has also been shown in Rydberg atoms [Gard et al., 2017; Han et al., 2018], as well as crystals doped with rare-earth-ions [Fernandez-Gonzalvo et al.,

---

[1] A particular problem arises for poling of domains. First, $\mathrm{BaTiO_3}$ can exhibit multidirectional poling while $\mathrm{LiNbO_3}$ naturally polarizes along one specific axis. Secondly, the Curie temperature of $\mathrm{BaTiO_3}$ is low which restricts the temperature of subsequent fabrication steps.

2019; Bartholomew et al., 2020; Rochman et al., 2023] and magnetomechanical mediators [Hisatomi et al., 2016; Zhu et al., 2020]. A recent proposal combines aspects of the platforms described above with an atomic defect to convert the microwave quantum state to the spin of a silicon-vacancy center [Anand et al., 2024]. One advantage of the integration of atomic species is the potential use as other quantum network components such as a quantum memory [Lago-Rivera et al., 2021b] besides the optical communication.

However, despite the variety of available platforms, all current realizations do not meet all stringent requirements needed to widely implement microwave-optic transducers in a quantum network.

Efficiency: One of the primary challenges is the efficiency of the transduction process. For microwave-optic transducers to be practical for quantum communication, they must achieve near-unity conversion efficiency. A deterministic process that works on demand requires efficiencies $>50\,\%$. However, most current systems operate with transduction efficiencies $\eta \sim 10\,\%$, which is insufficient for many quantum applications where loss must be minimized.

Bandwidth: The transduction bandwidth limits the minimal pulse duration of the input signal, or more general, determines the temporal shape of a signal the can be transduced without distortion. The current transducers with the highest efficiency exhibit bandwidths between $\sim 1\,\mathrm{kHz}$ and $\sim 10\,\mathrm{MHz}$. As the coherence of a quantum state is limited and the number of operations during this lifetime shall be maximized, the duration of each operation shall be kept as short as possible without compromising its fidelity. For superconducting qubit quantum processors, typical state-of-the-art timescales are $\leq 10\,\mathrm{ns}$ for qubit gates and $\leq 50\,\mathrm{ns}$ for qubit readout which is slightly below the threshold determined roughly by the inverse of the transduction bandwidth. Thus, a further increase of the transduction bandwidth to $\geq 100\,\mathrm{MHz}$ or even GHz would be advantageous for seamless integration with microwave signals of superconducting qubit quantum processors.
In practice, efficiency and bandwidth are competing metrics for electro-optic modulators or microwave-optic transducers in general with $\Delta f \propto V_\pi^2 \propto \eta^{-1}$ [Zhang et al., 2021]. Only recently, the use of superconducting electrodes without ohmic lossess lifted this constraint for traveling-wave electro-optic transducers [Shen et al., 2024]. However, microwave-optic transducer with the currently highest efficiencies leverage resonators to increase the efficiency thereby imposing bandwidth constraints. The product of efficiency and bandwidth is therefore a suitable metric to quantify the achievable throughput of the microwave-optic transducer as $R = \eta \cdot BW$.

Noise and Decoherence: Another significant challenge is the introduction of noise and decoherence during the transduction process. Quantum information is highly sensitive to noise, and any disturbance can degrade the fidelity of the converted quantum state. Current transducers often struggle with maintaining coherence, i.e. the phase information of the input state, particularly when converting from microwave to optical frequencies, where thermal noise can be problematic.

The above metrics can be combined to the *input-referred added noise*. It can be determined by dividing the measured output noise by the conversion efficiency. This simple method allows to be ignorant about the actual noise source, i.e. at which stage the noise was added during the conversion process. Individually, noise and efficiency are not sufficient to evaluate the performance of a microwave-optical transducer for quantum applications [Zeuthen et al., 2020]. If a microwave quantum state is efficiently converted to optical frequencies, but the conversion process itself adds thermal noise to the output signal, the signal-to-noise ratio decreases. The same applies to a transduction process with minimal thermal noise, but low efficiency that also decreases the output signal. There are several operation regimes for quantum transducers. First, the *quantum enabled regime* is often characterized by an input-referred added noise < 1 [Sahu et al., 2022; Kumar et al., 2023; Zhao et al., 2024], even though the exact requirements are protocol-dependent [Zeuthen et al., 2020]. Exploiting heralding, the selection of successful trials without interfering with the state of interest, can increase the fidelity of the transduction. The requirement of low noise for quantum application has led to the development that many microwave-optic transducers are operated in pulsed mode to avoid heating. Consequently, the aforementioned throughput of the transduction signal has to be expanded by the duty cycle, comprising now the product of efficiency, bandwidth and duty cycle in decimal units, i.e. $R = \eta \cdot BW \cdot DT$. In addition to the requirement on the added noise, a conversion efficiency above $50\,\%$ is needed to enter the deterministic regime of quantum transduction. This has not been reached so far, but would represent a significant step towards a hybrid quantum network of vastly different frequencies.

Scalability and Integration: To be viable for a large-scale quantum internet, microwave-optic transducers must be scalable and integrable with existing quantum technologies. This means that transducers need to be compact, compatible with cryogenic environments (at least for superconducting qubits), and capable of being mass-produced using standard fabrication techniques. Achieving this level of integration is a major engineering challenge, which has for example still prevented a widely-used adoption of $\mathrm{LiNbO_3}$ for integrated circuits despite its superior performance for EO modulation [Wang et al., 2024].

Bidirectionality: True bidirectional transduction is necessary for many quantum networking protocols with microwave-optic transducers to operate in the deterministic regime with success probabilities exceeding $50\,\%$, such as the deterministic creation of remote entanglement creation (e.g. achieved for microwave frequencies by [Kurpiers et al., 2018; Campagne-Ibarcq et al., 2018] among others). While the physical principles of the majority of currently investigated transducer platforms are bidirectional, practical limitations such as spurious modes and different limitations for individual steps in multi-step conversion techniques have so far led to direction-dependent performance, e.g. for piezo-OM transducers. Developing transducers that can efficiently and coherently convert quantum states in both directions will be increasingly important when transducers enter the deterministic regime. The implicit requirement of the transduction efficiency itself exceeding $\sqrt{0.5}$ because of consecutive microwave-optic and optic-microwave transduction in the example above (neglecting all other loss mechanisms) is, however, far beyond capabilities of current platforms. Hence, many protocols to date rely on techniques in the optical regime to account for transducer performance deficits, such as optical heralding and measurement-based entanglement using optical single-photon detection. This lifts the requirement for bidirectionality and a higher focus lies on microwave-to-optic transduction nowadays. A discussion of some relevant protocols can be found in chapter 5.

Overall, the future of microwave-optic transducers is closely linked to the broader development of the quantum internet. As demand for robust quantum communication networks increases, so will the need for efficient and reliable transduction technologies. Future research is likely to focus on improving the materials and designs used in microwave-optic transducers. This could involve the development of new materials with better coupling properties, the optimization of mechanical resonators for lower loss, and the refinement of superconducting-photonic integration techniques. Advances in nanofabrication and quantum materials science will play a crucial role in these developments. Current transducer will not be able to connect remote modules reliably within the time scales required to prevent decoherence of quantum states in the individual module. Thus, multiple improvements need to be combined, namely, 1) enhance the rate for heralded schemes to create more remote connections per unit time, 2) combine transduction and remote communication processes with quantum memories to extend the lifetime and coherence time of the involved elements, and 3) exploit processes that improve the fidelity of the operation such as entanglement distillation. In the long term, incorporating quantum error correction directly into the transduction process would be a gigantic step forward. By designing transducers that can detect and correct errors in real-time, it may be possible to mitigate the effects of noise and decoherence, leading to more reliable quantum communication. Fault-tolerant transduction, where the process can continue even in the presence of errors, would be essential for the practical deployment of these technologies.

However, with various platforms still competing for key components of quantum technology, such as processing nodes, quantum memories, and repeaters, it is difficult to predict the ultimate role of microwave-optic transducers. That said, high-performance transducers have the potential to accelerate the establishment of a quantum network, positioning themselves as a vital element in quantum communication.

1.2 Outline

The current chapter 1 'Introduction' has introduced the basic concept of a quantum network, the remaining chapters will describe the experimental realizations of some specific aspects of it. As they span from the basic elements of processing nodes, superconducting microwave qubits, over microwave-optic transducers to optical components and also partly cover various physical implementations, the individual topics are grouped on an abstract level by the theoretical description. This intuitively also allows to extract the fundamental mechanisms and physics of the basic components despite the otherwise rather specific technical realization. Thus, in chapter 2 'Theoretical description and basic experimental characterization', we first describe how we developed optical, microwave, and mechanical resonators for various aspects of our experiments. As we needed strong pump tones in addition to the weak signals of interest and both were short pulses of the order of $100\,\mathrm{ns}$, we had to develop custom filters to remove unwanted spectral components of short pulses 2.1.1.1. Secondly, we used resonators to improve the interaction time 2.1.1.2 - 2.1.3 in order to increase a moderate coupling between two systems (2.2 or 2.4). In chapter 3 'An integrated electrooptomechanical converter', we build on individual components from the previous chapter and combine them to the first integrated electro-opto-mechanical converter based on photon-phonon interaction mediated by the radiation-pressure force. In chapter 4 'All-optical state readout of a superconducting qubit with an electrooptic interface', we exploit a direct electro-optic transducer to probe the state of the basic element of a quantum processing node, a qubit in form of a superconducting circuit, via optical control. We send and detect telecom optical tones with a more than 10^4 times higher frequency to the qubit operating at around $9\,\mathrm{GHz}$. Finally, we provide an in-depth discussion in chapter 5 'Future directions and conclusions' about the - presumably - most important near-term goal of microwave-optic quantum transducer: the entanglement of distant superconducting qubits established via an optical link. We describe different protocols and explain the advantages and challenges of each protocol when using the micrwoave-optic transducer of the previous chapter, substantiated by numerical simulations.

CHAPTER 2

Theoretical description and basic experimental characterization

The development of microwave-optic quantum transducers [Lauk et al., 2020; Han et al., 2021] that are efficient enough to convert ultra-low input signal powers down to single photons and that operate in conjunction with fragile superconducting qubits require careful engineering. In this chapter, we first review the basic building blocks needed to build devices that can be used for these sensitive measurements of weak classical or quantum signals and their efficient signal transfer. Additionally, we lay out the choice of material and design to reach the desired properties. This is complemented by theoretical models to give a comprehensive overview of all aspects required for the development of the final devices: Theory, Design, Fabrication, Measurements. These basic elements are then combined with increasing complexity, i.e. from a single resonator in chapter 2.1 to the devices used for the experiments described in this thesis comprising two coupled resonator (chapter 2.2), a resonator strongly coupled to a qubit as slightly anharmonic resonators (chapter 2.4), or even three coupled resonators (chapter 3). Thus, instead of a general introduction, I aim for enabling readers to rebuild specialized parts of our experiments that may be useful for them supported by a basic theoretical description. As minimizing signal loss is an absolute crucial requirement for detecting signals from quantum systems, a special focus is put on this topic for various platforms.

Acknowledgements I would like to especially thank three brilliant colleagues with an intuitive but complementary understanding of theoretical models for introducing me to many of the herein used concepts: Yuri Minoguchi, Shabir Barzanjeh, and Alfredo Rueda.

2.1 Resonators

Resonators and cavities (more precise cavity resonators) allow waves to circulate within a closed path. The supported resonator modes reproduce themselves after each round trip. If the loss of the cavity κ[1] is low, i.e. the quality factor as the ratio between frequency and linewidth $Q = \omega/\kappa$ is high, it leads to a significant number of round trips which enhances the interaction time of the resonator field compared to the travelling input signal alone. The increase of power inside the resonator compared to the input signal is often called resonant enhancement.

---

[1] In general, frequency components are defined in angular frequency throughout the thesis. In this specific case $\kappa = 2\pi\Delta\nu_{\mathrm{FWHM}}$ is the power decay in radiants.

Thereby, resonators can highly increase the sensitivity of measurements or detection of features with otherwise small interaction with the measured field. The increase in sensitivity or coupling is directly related to the quality factor of the resonator. Thus, resonators are widely used in quantum mechanics, where signals are often of the order of a single excitation. Focusing only on examples related to the scope of this thesis, resonators have for example enabled the detection of minimal mechanical displacements and the emergence of the field cavity of optomechanics enhancing the otherwise weak radiation pressure force [Aspelmeyer et al., 2014] (cf. chapter 2.2.1). In a similar manner, it also led to the establishment of cavity electrooptics based on the Pockels effect [Tsang, 2010; Sahu, 2023] (chapter 2.2.3 between electrical and optical waves, or cavity electromechanics between electrical and mechanical modes using again the radiation pressure force [Teufel et al., 2011b; Bozkurt et al., 2023] or the piezoelectric effect [Mirhosseini et al., 2020] (chapter 2.2.2). Additionally, resonators allow for an off-resonant and non-destructive readout of the state of a superconducting qubit [Wallraff et al., 2005] (chapter 2.4).
Many of the applications mentioned above use - in addition to the cavity enhancement - a strong coherent drive for a parametric enhancement of the interaction. As the power of these parametric pumps is usually orders of magnitudes higher than the power of the signal of interest, they have to be filtered out prior to measuring the signal. As resonators support certain frequency bands and suppress others, they can also be used for filters to select certain frequency ranges. We used such filter cavities to suppress a pump tone of 100s of mW (chapter 2.1.1.1) to measure comparably weak signals from superconducting circuits in chapter 4. The enumeration of multiple resonator applications above highlights their importance for this work.

Proceeding with a short theoretical description of a resonator, it is important to mention that a resonator can never be fully isolated. This would lead to an infinite quality factor and it would prevent coupling a signal into the resonator. There always exists at least a weakly coupling to the environment, which is often denoted as 'bath'. From an experimental point of view, it is desired to also intentionally couple signals effectively to the resonator e.g. via a waveguide. In the theoretical description, one therefore often distinguishes between an intrinsic loss port, i.e. unintentional loss to the bath, and an external loss (coupling) port, i.e. intentional signal transfer to a measurement line. Such open (quantum) systems are often modelled by either a Quantum Langevin equation (QLE) or a master equation. While the latter describes the effective evolution of the density operator in the Schrödinger picture, the QLE provides equations for the Heisenberg operators of the system. Specifically for coherent states, linear systems or systems in equilibrium, QLE offer a convenient way to model an open system with one or more dissipation channels. Additionally, together with the input-output relations from [Gardiner and Collett, 1985] it can directly connect the state of the system to measurable quantities and is therefore a powerful tool to analyse the measured signal. Assuming that all excited modes are centered at the cavity resonance, travel in the same direction and have - if this can be altered - the same polarization, the QLE for a resonator mode c with total power decay rate $\kappa = \kappa_e + \kappa_i$ [2] and resonance frequency ω_c is given by

$$\dot{c}(t) = -\left(i\omega_c(t) + \frac{\kappa}{2}\right) c(t) - \sqrt{\kappa_e} c_{in} \tag{2.1}$$

where κ_e is the external coupling rate to the waveguide and κ_i is the intrinsic coupling rate to the bath. We assume here that the bath and the waveguide modes are not thermally populated and therefore do not contribute to the total cavity input field. The input signal mode c_{in} is

---

[2] If one uses the amplitude decay rate $\kappa \rightarrow 2\kappa$

guided to the resonator via the waveguide. [3] While the resonator mode decays with the total loss rate κ, the measurable output field exits the resonator again through the waveguide port leading to the input-output relation.

$$c_{out} = c_{in} + \sqrt{\kappa_e} c \tag{2.2}$$

This describes the reflected output field of a single resonator mode.

In steady-state, i.e. for continuous driving or rectangular drive pulses being switched on for times $\tau\kappa \gg 1$, it is convenient to derive the resonator characteristics from the frequency spectrum because eq. 2.2 can be solved analytically in Fourier space [4] and the reflective scattering parameter becomes

$$S_{11}(\omega) = \frac{c_{out}(\omega)}{c_{in}(\omega)} = 1 - \frac{k_e}{\frac{\kappa}{2} - i\Delta_c} \tag{2.3}$$

with $\Delta_c = \omega - \omega_c$ and setting the baseline to 1, i.e. neglecting losses in the waveguide.

We can utilize this model to analyze a measurement of resonator, more specific a cylindrical microwave cavity (cf. chapter 2.1.2.2), where the signal couples via a single port from a coaxial cable to the resonator and vice versa. When a rectangular signal pulse is sent on resonance with the cavity ($\Delta_\mathrm{c} = 0$), the reflected power can be used to extract relevant parameters such as the coupling rates. Fits of $|c_\mathrm{out}|^2$ in eq. 2.2 after numerical integration of eq. 2.1 yield a coupling rate to the coaxial cable (the waveguide) of $\kappa_\mathrm{e} = 3.42\,\mathrm{MHz}$ and an intrinsic loss rate to the remaining environment or bath of $\kappa_\mathrm{e} = 6.27\,\mathrm{MHz}$ (fig. 2.1a). The initial and final peaks in the temporal response are related to the finite bandwidth and loading time respectively. The latter is inversely proportional to the coupling rate κ_e. The exact shape depends on the ratio between extrinsic and intrinsic coupling. In the steady state region, the normalized reflected power level is given by $1 - 2\kappa_\mathrm{e}/\kappa$. Considering the complex scattering parameter containing information about both phase and amplitude of the reflected signal, i.e. $S_{11}(t) = c_\mathrm{out}(t)/c_\mathrm{in}(t)$, the real and imaginary part follow the measured in-phase and quadrature components (fig. 2.1b). When the signal consists of a long coherent tone with duration $\tau \gg \kappa$, e.g. from a vector network analyzer, and the signal frequency is varied to probe the frequency response, the measurement is modelled by eq. 2.3. In a real-life experiment, this equation may be expanded to

$$S_{11,exp}(\omega) = \frac{c_{out}(\omega)}{c_{in}(\omega)} = e^{-i(\theta\omega+\phi_0)}\left(1 - \frac{k_e - i\delta\nu}{\frac{\kappa}{2} - i\Delta_c}\right) \tag{2.4}$$

θ accounts for the group delay of the measurement path, i.e. in the coaxial cables, and ϕ_0 an arbitrary phase offset. Especially because this measurement is carried out in a mK environment with a relatively long signal path between measurement instrument with multiple connectors that can cause unintended reflections, the resonator response can also become asymmetric in frequency which is taken into account by a Fano-factor $\delta\nu$. Again, the power spectrum (fig. 2.1c) and the real and imaginary part of the complex scattering parameter (fig. 2.1d) are

---

[3] The input field is defined as $c_{in}(t) = \frac{1}{\sqrt{2\pi}} \int d\omega\ e^{-i\omega(t-t_0)} c_{in,0}$. Some textbooks, e.g. [Walls and Milburn, 2008] define input and output fields to propagate in different directions and use a negative sign for one of them to account for the phase difference. This consequently changes the sign of the input-output relation to $c_{out} = -c_{in} + \sqrt{\kappa_e} c_{out}(t)$.

[4] With a phasor rotating clockwise in Fourier space $c(t) = \frac{1}{\sqrt{2\pi}} \int d\omega\ e^{-i\omega t} c(\omega)$ and $\dot{c}(\omega) = -i\omega\ c(\omega)$.

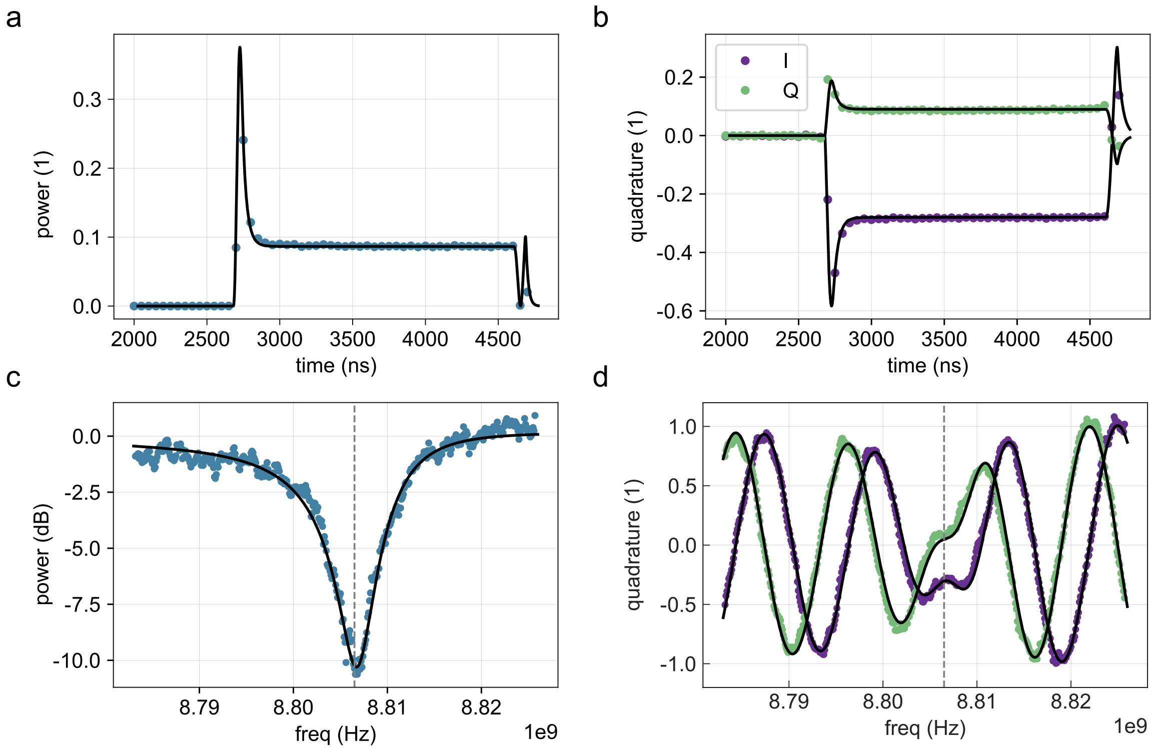

Figure 2.1: **Reflection from a resonator** with a external single port (waveguide-cavity coupling $\kappa_e/(2\pi) = 3.42$ MHz) and intrinsic loss rate $\kappa_i/(2\pi) = 6.27$ MHz (device used in section 4). **a**, Normalized power of the reflected signal from a rectangular pulse on resonance (gray dashed line in bottom panels) and fit to $|c_{\text{out}}|^2$ in eq. 2.2 and the numerical integration of eq. 2.1. **b**, corresponding real (in-phase component) and imaginary part (quadrature component) of the complex response. **c**, Normalized power of the reflected signal from a frequency sweep around the resonator resonance and fits to eq. 2.3, expanded by the group delay of the measurement path, an arbitrary phase offset, and a Fano-parameter accounting for the slightly asymmetric shape. **d**, Corresponding in-phase and quadrature component.

well described by $|S_{11,\text{exp}}|^2$ as well as $Re(S_{11,\text{exp}})$ and $Im(S_{11,\text{exp}})$ respectively using the same coupling rates as for the temporal response in the top panels.

If a resonator is measured in transmission via directly coupled ports, i.e. there are two separate waveguides both coupled to the resonator in addition to the bath [5], the output fields in frequency domain for reflection and transmission is given by

$$S_{11}(\omega) = \frac{c_{out}(\omega)}{c_{in}(\omega)} = 1 - \frac{k_{e1}}{\frac{\kappa_{e1}+\kappa_{e2}+\kappa_i}{2} - i\Delta_c} \tag{2.5a}$$

$$S_{21}(\omega) = \frac{c_{out}(\omega)}{c_{in}(\omega)} = \frac{\sqrt{k_{e1}k_{e2}}}{\frac{\kappa_{e1}+\kappa_{e2}+\kappa_i}{2} - i\Delta_c} \tag{2.5b}$$

The transmitted power on resonance is $4\kappa_{e,1}\kappa_{e,2}/(\kappa_{e,1}+\kappa_{e,2}+\kappa_i)^2$ and, hence, approaches unity for $\kappa_i \to 0$ and $\kappa_{e,1} \approx \kappa_{e,2}$.

---

[5] the QLEs for side-coupling where a resonator is coupled to a single waveguide slightly differ

The theoretical model above is generally applicable to resonators and important to characterize their properties. In the following, we investigate the actual implementation of various resonators operating in highly different frequency domains.

2.1.1 Optical resonators

We utilized three different types of optical resonators throughout the thesis:

a) A free-space cavity between two mirrors of finite reflectivity (Fabry-Perot cavity)

b) A whispering gallery mode resonator made of $\mathrm{LiNbO_3}$

(c) A photonic crystal cavity patterned in silicon

While the phenomenological description of these resonators is identical (see chapter 2.1), the geometry, material, and physical mechanism vastly differ. Nevertheless, the fundamental description of light propagating through these various resonators naturally originates in Maxwell's equations. We assume in the following 1) negligible frequency dependence of the dielectric constant $\epsilon(\omega, \mathbf{r}) \approx \epsilon(\mathbf{r})$, 2) an isotropic material where the dielectric tensor ϵ_{ij} reduces to a scalar, 3) the material is largely transparent and $\epsilon(\mathbf{r})$ is real, and 4) small field strengths, hence, a linear material with $\mathbf{D} \approx \epsilon(\mathbf{r})\mathbf{E}$. Then, Maxwell's equations for harmonic modes [6] of the electric field $\mathbf{E}(\mathbf{r}, t) = \mathbf{E}(\mathbf{r})e^{-i\omega t}$ can be cast in

$$\nabla \times \frac{1}{\mu_{\mathrm{r}}(\mathbf{r})} \nabla \times \mathbf{E}(\mathbf{r}) = \left(\frac{\omega}{c}\right)^2 \epsilon(\mathbf{r})\mathbf{E}(\mathbf{r}) \tag{2.6}$$

under the condition that the modes are transverse electromagnetic waves, i.e. there are neither sources nor sinks and $\nabla \cdot \mathbf{H}(\mathbf{r}) = \nabla \cdot [\epsilon(\mathbf{r})E(\mathbf{r})] = 0$. In the following, I will describe the different optical resonators and the application we developed them for. Besides, I will also briefly lay out how the origin of the description of the electromagentic waves propagating through various materials and geometries can be found in Maxwell's equation.

2.1.1.1 Fabry-Perot cavity filter

As mentioned in the introduction, our experiments use a parametric pump in addition to the applied measurement signal, to enhance the desired interaction between microwave and optical fields in $\mathrm{LiNbO_3}$. Thus, we had to isolate our optical measurement signals from the strong drive but also from broadband noise caused by optical amplifiers. While multiple vendors provide various cavity filters for this purpose, our specific requirements - large bandwidth for short pulses on the order of 100 ns, high total optical power of up to 1 Watt, and low measurement signal strength on the order of only a few photons requiring large suppression of more than $100\,\mathrm{dB}$ in total - led to a custom solution we developed in-house. A critical parameter is also the insertion loss of the filter to transmit the weak signals efficiently. The insertion loss could be minimized to 1 dB in our filters. In the following, I will quickly lay out the design considerations which allow specifications tailored to the respective experimental needs.

---

[6] any other solution can be obtained by a combination of harmonic modes

Acknowledgements Based on valuable input from the Onur Hosten lab at ISTA Austria, my colleague William Hease developed the original design with a thermal frequency stabilisation using a Peltier element and a thermistor. I expanded the existing scheme by a piezoelectric frequency tuning and feedback and adjusted the mechanical and electrical design accordingly.

Cavity length Firstly, the frequency difference between the signal tone from our device and the unwanted tones we want to filter out ($\nu_{\mathrm{FSR,D}} \approx$ 8.9 GHz) determines the free spectral range $\nu_{\mathrm{FSR,F}}$ of the Fabry-Perot filter. Generally, ν_{FSR} is the frequency spacing between neighbouring resonances of the same spatial mode T_{qmn} and T_{q+1mn}. We chose a mirror spacing $L =$ 9.5 mm equivalent to $\nu_{\mathrm{FSR,F}} \approx$ 15.8 GHz for the fundamental mode: [7]

$$\nu_{\mathrm{FSR,F}} = \frac{c}{2L} \tag{2.7}$$

The selected $\nu_{\mathrm{FSR,F}}$ ensures the desired high suppression around $\nu_{\mathrm{FSR,D}}$ with the maximum rejection ratio at $\approx \nu_{FSR,F}/2$, but avoids an overlap between other resonances of the cavity filter and the sample resonator, i.e. $\nu_{\mathrm{FSR,F}} \neq 2\nu_{\mathrm{FSR,D}}$.

Bandwidth A crucial parameter of a filter is its bandwidth Γ_{F}. On the one hand, it naturally determines the rejection ratio; on the other hand, the inverse $1/\Gamma_{\mathrm{F}}$ limits the time resolution of the pulses that can be transmitted through the filter without significant distortion. We balanced these two competing effects by aiming for a bandwidth of $\approx$ 50 MHz. For a high finesse Fabry-Perot cavity, bandwidth and finesse F are related by $\nu_{\mathrm{FSR,F}}$

$$\Gamma_F = \nu_{\mathrm{FSR,F}}/F \tag{2.8}$$

with a finesse F depending on the reflectivity of the cavity mirrors. If both mirrors are assumed to have identical reflectivity coefficients r the finesse becomes

$$F = \frac{\pi\sqrt{r}}{1-r} \tag{2.9}$$

Thus, a linear cavity with the used mirrors from Layertec GmbH ($r = 0.99$), spaced by 9.5 mm as described above provides the desired bandwidth of of $\approx$ 50 MHz. The sputtered antireflection coatings ensure low loss so that $r+t \approx 1$ with t being the transmission coefficient. In this limit, the normalized transmitted intensity is simplified to [8]

$$I_{out}(\omega) = \frac{1}{1 + \frac{4r}{(1-r)^2}\sin^2\left(\frac{\pi\omega}{\nu_{\mathrm{FSR}}}\right)} \tag{2.10}$$

Efficient coupling The considerations above assume that the incoming light field is monochromatic. In vacuum ($\mu_r = \epsilon_r = 1$) such as in the herein described Fabry-Perot cavity, every component u of the magnetic or electric field vector fulfills the scalar wave

---

[7] The exact cavity characteristics slightly depend on the spatial mode number

[8] In general, the intensity spectrum of a resonator with two mirrors along a single axis can be described by the Airy formula [Gagliardi and Loock, 2014] $I_{out}(\omega) = \frac{t_1 t_2}{(1-\sqrt{r_1 r_2})^2} \frac{1}{1+(\frac{2\sqrt{r_1 r_2}}{1-r_1 r_2})^2 \sin^2(\frac{\pi\omega}{\nu_{\mathrm{FSR}}})}$

equation derived from the source-free equation 2.6 [9] without sources or sinks in the following form

$$\nabla^2 u + k^2 u = 0 \tag{2.11}$$

with the wave-vector magnitude $k = \omega / c$. If the beam differs not more than slightly from a plane wave (paraxial assumption), the spatial dependence of the beam follows a Gaussian profile. If that radial distribution matches the cavity's fundamental TEM mode TEM_{00} in spot size and position, mode matching is achieved. In turn, this means that the beam wave fronts match the mirror surface curvature and the incoming beam is aligned with the optical axis. In practice, this requires careful alignment in all three spatial axes and a suitable focus length of the coupling lens. We used molded aspheric lenses (Thorlabs C230TMD-C) with a focal length f of $4.51\,\mathrm{mm}$ at a wavelength around $1300\,\mathrm{nm}$ and $4.6\,\mathrm{mm}$ at the wavelength of interest around $1550\,\mathrm{nm}$. The light was coupled from a SMF-28 single mode fiber. The beam spot size at the fiber facet and the radius of the mirror surface $R = 100\,\mathrm{mm}$ defines for Gaussian beams together with f the ideal position of the lens to achieve efficient coupling between fiber and Fabry-Perot cavity and the desired mode matching, i.e. suppressing higher order cavity modes.

Practically speaking, the goal is to focus the light diverging from the fiber facet with a mode radius of $w_{0,\mathrm{fib}} \approx 5.2\,\mathrm{\mu m}$ to match the beam spot size of the fundamental mode inside the cavity. The beam waist of the cavity, i.e. the minimal spot radius, is given by

$$w_0 = \sqrt{\frac{\lambda}{n\pi}\sqrt{\frac{LR}{2} - \frac{L^2}{4}}} \tag{2.12}$$

A wavelength of $\lambda = 1550\,\mathrm{nm}$ and the parameters from above yield a cavity waist of $w_{0,\mathrm{cav}} \approx 102\,\mathrm{\mu m}$. We used the complex beam parameter q of Gaussian beams to conveniently determine the expected distances between the fiber facet and the coupling lens as well as the distance between the lens and the Fabry-Perot cavity center. A comprehensive introduction to this approach can be found in [Nagourney, 2010]. The complex beam parameter at the cavity waist and the optical fiber facet, where the wavefronts are flat, is given by

$$q = i\frac{\pi}{\lambda}\omega_0^2 \tag{2.13}$$

In this notation, the complex beam parameter after free space propagation from the fiber facet with q_{fib} to the lens over a distance z_1 is simply

$$q_1(z_1) = q_{\mathrm{fib}} + z_1 \tag{2.14}$$

After passing the lens, the complex beam parameter with respect to the distance z_2 from the lens is given by

$$q_2(q_1, z_2) = \frac{q_1}{1 - \frac{q_1}{f}} + z_2 \tag{2.15}$$

---

[9] Using $\nabla \times \nabla \mathbf{f} = \nabla(\nabla \cdot \mathbf{f}) - \nabla^2 \mathbf{f} = -\nabla^2 \mathbf{f}$

Converting the complex beam parameter after the lens again to a beam waist via eq. 2.13 and matching it to the cavity waist $w_{0,\mathrm{cav}}$, one can find the estimated distances $z_1 \approx 4.8\,\mathrm{mm}$ between the fiber end-face and the lens as well as $z_2 \approx 93\,\mathrm{mm}$ between the lens and the cavity center. Despite several simplifications e.g. neglecting the finite thickness of the lens and omitting the input mirror, these calculation were in good agreement with the actual length scales after optimizing the coupling between fiber and cavity. Hence, these equations give a reasonable estimate to select the appropriate components to build the Fabry-Perot filter cavity. As a comparison, the calculation above for our confocal cavities with mirrors of $R = L = 10\,\mathrm{mm}$ yields $z_1 \approx 5.1\,\mathrm{mm}$ and $z_2 \approx 47\,\mathrm{mm}$. These results indicated that certain components in the optical assembly had to be adapted compared to the larger radii mirror described above, highlighting the utility of this approximate prediction of the distance between different optical components.

The lens was mounted inside a lens adapter (Thorlabs S05TM09) and a rotation mount (Thorlabs RSP05/M). By this, the position of the lens relative to the optical fiber facet and the cavity center can be fine-tuned to reach the desired spatial mode matching. Additionally, the lens was mounted on translation stages (Thorlabs RSP05/M) to align the beam with the linear cavity axis.

Frequency tuning and feedback Our cavity design offers two mechanisms to stabilize the cavity frequency. First, we utilized the temperature dependence of the cavity length, i.e. the cavity resonance frequency by a *Peltier element* (European Thermodynamics GM200-127-10-15) underneath the Aluminum cavity housing. The feedback signal can originate from 1) a fraction of the transmitted light or 2) a temperature sensor nearby or in form of a thermistor (TE Connectivity G10K3976) inside the cavity housing. In the first case, the Fabry-Perot cavity filter will adapt for drifts of the incoming laser light. However, the time-scale of thermal elements is relatively large. This is sufficient for slow, e.g. thermal, drifts of the cavity frequency but prohibits the compensation of faster fluctuations. Hence, we additionally used a piezo-electric actuator mounted inside the cavity to allow changes of the cavity length (and frequency) with high rates. While we originally planed to compensate for slow drifts with thermal control offering and only fast changes with the piezoelectric element, we eventually only used a piezo-ceramic actuator (PiCeramic PD150.3) with a tuning strength of 0.4 MHz/mV for this cavity design. The frequency changes transduced from fluctuations of the voltage applied to the actuator were $15\,\mathrm{dB}$ below the cavity linewidth Γ_{F}.

We used one of the cavity filters described above in [Hease et al., 2020; Sahu et al., 2022, 2023; Arnold et al., 2023] and for the experiment presented in chapter 4 in the device input path to suppress broad-band noise from our erbium-doped fiber amplifier. It is needed to create the strong optical pump that enhances the electro-optic interaction in $\mathrm{LiNbO_3}$ (chapter 2.2.3). In currently ongoing efforts, we use multiple cascaded cavity filters of this kind in the sample output path to sufficiently suppress the strong optical pump after its interaction with the sample, and simultaneously minimizing the signal loss transmitted on resonance with the cavity filters.

2.1.1.2 Whispering gallery mode resonator

While the Fabry-Perot cavity described above is a linear cavity with standing waves reflected between two mirrors, a whispering gallery mode (WGM) resonator uses a curved object to guide waves along its surface. Even though such resonators were firstly discovered for acoustic waves, they also exist for electromagnetic waves. We used a $\mathrm{LiNbO_3}$ disc of $5\,\mathrm{mm}$ diameter and $150\,\mu\mathrm{m}$ thickness and a rim curvature of below $1\,\mathrm{mm}$. Total internal reflection guides the electromagnetic field along the surface leading to a circular path. The modes of light propagating through the material obey the Helmholtz equation similar to eq. 2.11, which can therefore be directly derived from Maxwell's equations for harmonic modes without sources and sinks:

$$\Delta\mathbf{E}(\mathbf{r}) + k^2\epsilon_r(\mathbf{r})\mathbf{E}(\mathbf{r}) = 0 \tag{2.16}$$

Analytical solutions of such an WGM can be found in [Demchenko and Gorodetsky, 2013; Breunig et al., 2013]. Additionally, [Rueda Sanchez, 2018; Sahu, 2023] provide a detailed description of the used device geometry. Such an optical resonator made of $\mathrm{LiNbO_3}$ has been used to create a direct conversion between microwave and optical frequencies (cf. chapter 4).

2.1.1.3 Photonic crystal resonator

Acknowledgements I want to thank Amir Safavi-Naeini for sharing his original design [Safavi-Naeini et al., 2013] which built the basis for our modifications. The optical fiber-pulling setup was designed and tested by Farid Hassani. Design, fabrication, and measurements of photonic crystal resonators were performed together with Matthias Wulf and Yuan Chen. Donald Swen and Moritz Laber contributed with valuable and extensive optical and OM simulations.

Photonic crystals are periodic optical structures of materials with different refractive index [Joannopoulos et al., 2008]. The periodicity in the dielectric function $\epsilon(\mathbf{r})$ is used to control the characteristic properties of light propagating through the structure. If the difference in refractive index between the different regions is high, one can analogously reproduce many properties that atomic crystals provide for electrons. In this spirit, a suitable ansatz for the electric or magnetic field is a Bloch state or Floquet state of the form

$$\mathbf{H_k}(\mathbf{r}) = e^{i\mathbf{k}\cdot\mathbf{r}}\mathbf{u_k}(\mathbf{r}) \tag{2.17}$$

with $\mathbf{R}$ imposing $\mathbf{u_k}(\mathbf{r}) = \mathbf{u_k}(\mathbf{r}+\mathbf{R})$ and $\mathbf{R}$ as a composition of primitive lattice vectors. This ansatz accounts for both the periodic structure of the crystal and a plane wave. Inserting the solution in the magnetic field counterpart of eq. 2.6 yields [Joannopoulos et al., 2008].

$$\hat{\Phi}_\mathbf{k}\mathbf{u_k}(\mathbf{r}) = (i\mathbf{k}+\nabla)\times\frac{1}{\epsilon(\mathbf{r})}(i\mathbf{k}+\nabla)\times\mathbf{u_k}(\mathbf{r}) = \left(\frac{\omega(\mathbf{k})}{c}\right)^2\mathbf{u_k}(\mathbf{r}) \tag{2.18}$$

Consequently, we could derive the governing equations for all optical resonators, that is a Fabry-Perot cavity (eq. 2.11), a WGM (eq. 2.16) and a photonic crystal cavity (eq. 2.18), from Maxwell's equation for harmonic modes (eq. 2.6). Interestingly and as a bridge to quantum mechanics, the master-equation-type eq. 2.18 as the specific case of Maxwell's equation for an harmonic mode in a periodically mixed dielectric medium has the form of an eigenvalue problem. Additionally, the periodic localization of the fields results in an infinite set of discrete eigenmodes ω_n instead of a continuous distribution, analog to atomic crystals. The periodicity allows to fully characterize the photonic crystal by considering a single unit cell. In reciprocal space, described by the wave vector $\mathbf{k}(\mathbf{r})$ as in eq. 2.18 and a result of the Fourier transform of the lattice in real space, this restricts the analysis to the first irreducible Brillouin zone, as discussed in the following.

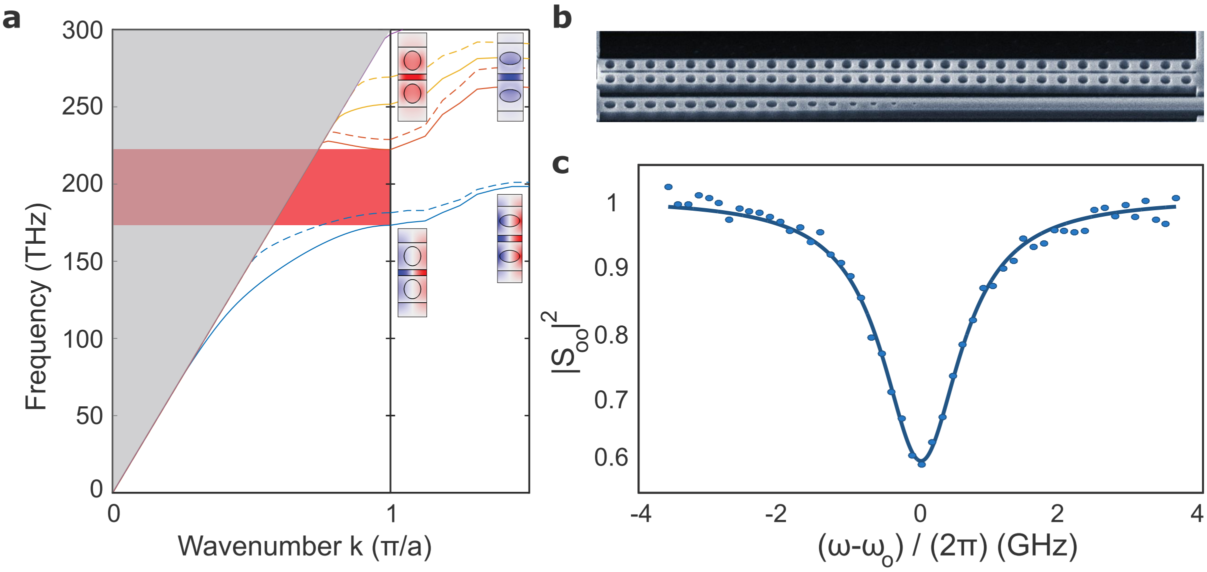

Figure 2.2: **Photonic crystal resonator a**, Band diagram of the photonic crystal along the reciprocal lattice vector $k_\mathrm{x} \in [0, \pi/a]$ for the resonator mirror. The diagram is further extended by the tapered defect cells that pushes the lowest band into the bandgap of the mirror cells enabling a resonator with high quality factor. Solid lines show modes with high field intensity in the gap between the beams (symmetric modes in the y-direction), while dashed lines show modes anti-symmetric in y. **b**, Scanning electron microscopy (SEM) image of the used "zipper" resonator comprising two photonic crystal cavities and the coupling waveguide **c**, Normalized reflected optical power and fit to the absolute square of 2.3. The individual panels are published in different Figures in [Arnold et al., 2020].

Photonic band diagrams We reduce the considerations now to a merely one-dimensional photonic crystal, which has been used throughout this thesis. The periodicity - or discrete translational symmetry - in one dimension with the characteristic length or lattice constant of the unit cell a sets the periodicity in reciprocal space to $k_\mathrm{x} = 2\pi/a$ and limits the first Brillouin zone to $-\pi/a < k_\mathrm{x} \leq \pi/a$. Employing other symmetries of the lattice group leads to the first irreducible Brillouin zone with limits $0 \leq k_\mathrm{x} \leq \pi/a$. Solutions for eigenfrequencies $\omega_\mathrm{n}(\mathbf{k})$ to eq. 2.18 for varying wavevectors $(\mathbf{k})$ form the bands of the photonic crystal. The periodically changing dielectric constant ϵ_x imposes a photonic bandgap between the first and the second band. The mode at the lower edge of the bandgap experiences a higher effective refractive index $n_\mathrm{x} = \sqrt{\epsilon_\mathrm{x}}$, i.e. is more confined to the region of the unit cell with higher refractive index. It is therefore often referred to as the dielectric band, the upper band as the air band. The size of the bandgap depends on the difference of ϵ_x between the two materials.

Of particular interest are photonic crystals, where a defect in the periodic crystal structure locally creates a solution of eq. 2.18 within the band gap of the photonic crystal. The mode will be strongly confined because it cannot propagate in the photonic crystal and, hence, forms a cavity. Due to the flexibility in design, small footprint, good confinement and large quality factors of several millions [Sekoguchi et al., 2014], they have been coupled to various quantum systems such as quantum dots[Yoshle et al., 2004], nitrogen-vacancy centers [Faraon et al., 2012], and trapped atoms [Thompson et al., 2013].

In our experiment, we used two one-dimensional photonic crystal nanobeams separated only by a small gap of $<100\,\mathrm{nm}$. A scanning electron microscopy (SEM) image of this structure can be seen in fig. 2.2b. The geometry is inspired by [Safavi-Naeini et al., 2013] and slightly adapted. The photonic crystal comprises periodic holes in a silicon beam of thickness $220\,\mathrm{nm}$

and width $450\,\mathrm{nm}$. The high refractive index of silicon ($n = 3.42$ at $\lambda = 1550\,\mathrm{nm}$) provides good confinement and a large difference to the refractive index of the perforated air holes, i.e. a large photonic bandgap. The band diagram of the photonic crystal unit cell used at both ends of the nanobeam is shown in fig. 2.2a and exhibits a considerable bandgap around $1550\,\mathrm{nm}$. In general, the bandgap is likely to occur at frequencies with wavelengths comparable to the lattice constant. In turn, the fact that the physical extent of the photonic devices is now on the order of the wavelength makes it difficult to find analytical solutions such as in the case of the optical WGM above. As a consequence, we use a finite element method (FEM) approach (Comsol Multiphysics)to numerically solve the source-free Maxwell equations (eq. 2.18) for the desired geometry and materials. Insets in fig. 2.2a show the electric field distribution of the in-plane component perpendicular to the beam axis, E_{y}, of the air band mode and dielectric band mode obtained from such FEM simulations. As we are mainly interested in "TE-like" modes with even symmetry in the z-plane and thus, strongest fields at the symmetry point $z = 0$, we restrict ourselves to this subset of modes. In simulations, these symmetries can be obtained by applying certain boundary conditions to the symmetry planes of the device. [10]

The photonic crystal forms the resonator mirrors. In the center, the hole dimensions as well as the distance between neighboring holes is gradually changed and the lowest mode frequency is pushed inside the bandgap of the mirror region, forming the photonic crystal defect (cf. extended band diagram). Due to the invariance of Maxwell's equation to scaling, the modes in the band structure remain qualitatively unchanged and only the frequency of the corresponding mode is shifted. The gray area in fig. 2.2a marks the light cone with a boundary set by $\omega = c\kappa_{\mathrm{x}}$. This region hosts a continuum of *radiation modes* that are not confined to the photonic crystal, while the relevant bands in the diagram are *guided modes*, where the electromagnetic fields are localized inside the structure through internal reflection or a small region around. A nearby waveguide is used to couple light to the resonator. The presence of this waveguide leads to additional modes that lie in the light cone but are localized close to the waveguide. Generally, the bandgap in such photonic crystal nanobeams can never exhibit a full bandgap but only a partial bandgap valid for guided modes. A fit of a laser frequency sweep around the resonance according to eq. 2.3 yields an internal quality factor of 1.4 $\cdot 10^5$ at a resonance frequency of 198.08 THz. This devices also features a strong opto-mechanical (OM) interaction (chapter 2.3).

Efficient coupling between fiber and waveguide As we usually measure signals in the range of a few photons, minimizing the losses between the device and the detection system is of essential importance. Hence, we optimized the coupling between the silicon waveguide of the device and the commercial SMF28 single mode fiber used to transmit the signal through the remaining setup. We followed two different strategies for an increased mode matching and efficient transfer between chip and fiber: Tapered fibers from OZ Optics Ltd. and in-house tapered fibers.

The former are sharply tapered and form a focal spot with a Gaussian beam waist of $2.5\,\mu\mathrm{m}$ at a distance of $14\,\mu\mathrm{m}$ from the tip. Additionally, the tapered region is covered by an anti-reflection coating. We use them for edge- or butt-coupling, where the tip of the tapered fiber points towards the waveguide front face and the fiber axis is aligned with the waveguide propagation direction. Fig. 2.3a shows an optical microscope image of a tapered fiber coupled to a photonic crystal structure. An optimization of this coupling is achieved by nanopositioners for all three

---

[10] A useful resource to find the correct boundary conditions in my early simulation days was a blog on 'PMC/PEC Boundary Conditions and Plane Wave Simulation'from Optiwave Design Software.

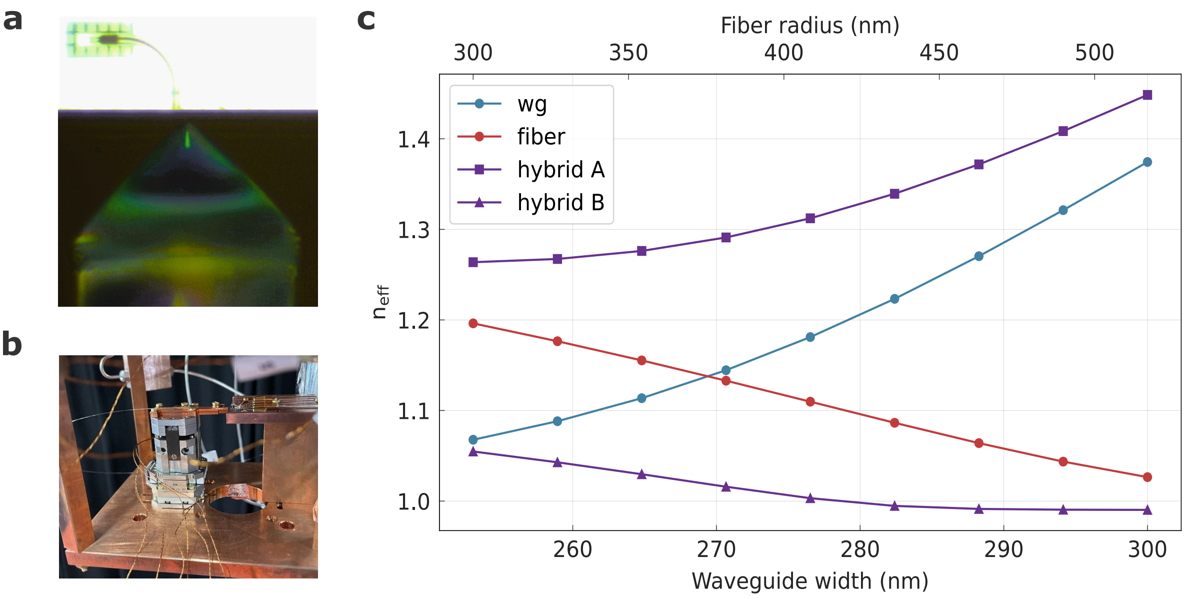

Figure 2.3: **Fiber-chip-coupling a**, Optical microscope image of a tapered fiber from OZ Optics used to couple to a silicon waveguide. **b**, Cryo-compatible Attocube piezo stack to control the position of the fiber in all three dimensions in order to optimize the coupling to the on-chip waveguide **c**, Coupling simulation of an in-house tapered fiber to a silicon waveguide. The effective refractive index is plotted over the relevant part of the contact region of a tapered fiber with an opening angle of 3 degrees and the tapered waveguide width.

spatial axes (Attocube ANPz101 and two ANPx101, fig. 2.3b). When the fiber's tip position is aligned to the center of the waveguide in the transverse directions, a one-way coupling efficiency of $50\text{-}60\,\%$ is achieved at a distance of $\approx 6\,\mu\text{m}$ between fiber tip and waveguide. The Si waveguide thickness is $220\,\text{nm}$ and its width is tapered from $275\,\text{nm}$ to $495\,\text{nm}$ over a length of $14\,\mu\text{m}$.

The in-house tapered fiber has been produced from an SMF28 fiber via wet etching with 48 % hydrofluoric acid (HF) covered with O-Xylene to prevent etching of the fiber above the liquid surface. A high precision actuator (Standa 8CMA16DC-25/15) with a resolution of 0.0281 µm slowly pulls out the fiber with a speed of $2\,\mu\text{m/s}$, creating a conical profile. In conjunction with the experimentally predicted etch rate of $2\,\mu\text{m/min}$ for an optical fiber in $48\,\%$ hydrofluoric acid (HF), the predicted full opening angle is $1.9°$. In practice, we realized an opening angle of $2.1°$ over a tapering length of $\approx 4\,\text{mm}$. In the front section close to the tip the tapering angle increases to $6°$. The tip diameter is $400\,\text{nm}$.

In order to have an efficient transfer between the fiber and the waveguide, one employs adiabatic coupling. The concept foresees a slow change of the relevant system parameter, so that the system remains in the desired eigenstate [Zener, 1932]. Translated to wave optics, the beating between two neighbouring eigenmodes with effective refractive indices $n_{\text{eff,i}}$ defines a length $l = \lambda / |n_{\text{eff},1} - n_{\text{eff},2}|$, that has to be small compared to the tapering length [Tiecke et al., 2015]. Practically speaking, this entails a slow change of the waveguide width and fiber diameter over the tapering length. At the beginning of the taper, the two relevant modes are the fundamental and the first higher-order fiber mode. Their difference in refractive index sets a limit on the tapering angle. In the contact region between waveguide and fiber, the effective index $n_{\text{eff,i}}$ stems from hybrid waveguide-fiber modes. The adiabatic criterion can relate the separation between the supermodes and the change of the uncoupled modes, i.e. the bare tapered waveguide and tapered fiber [Gröblacher et al., 2013]

$$\frac{\delta n_{\mathrm{bare,i}}(y)}{\delta y} \ll \frac{2\pi}{\lambda}|n_{\mathrm{eff},1}(y) - n_{\mathrm{eff},2}(y)|^2. \tag{2.19}$$

Fig. 2.3c shows simulations of $n_{\mathrm{eff,i}}$ ($n_{\mathrm{bare,i}}$) in purple (red and blue) lines for the contact region. Designs fulfilling the criterion for adiabatic coupling (eq. 2.19) are validated with FEM simulations. This procedure led to a change of the waveguide design used for the tapered fiber from OZ optics. The tapering length was increased to $18.5\,\mu\mathrm{m}$ and the waveguide tip width decreased to $250\,\mathrm{nm}$. These changes increased the coupling efficiency for the same tapered fiber with an aforementioned opening angle of 2°-6° from 40% to >80%. Imperfections include the non-point-like tip with a minimal diameter of $400\,\mathrm{nm}$ and the relatively large tapering angle of 6° in the relevant section of the first $20\,\mu\mathrm{m}$ from the tip. A further optimization towards record values reported in literature >90% [Gröblacher et al., 2013; Tiecke et al., 2015; Burek et al., 2017] has not been pursued. From an application point of view, the tapered fiber from OZ Optics is used for end-fire coupling at the edge of a chip. The in-house tapered fiber can access devices on the whole chip, but imaging is needed to place the fiber at the correct position.

Efficient transmission through the waveguide The waveguide consists of a released $220\,\mathrm{nm}$ thick silicon membrane. In order to mechanically stabilize it, it needs to be anchored at the surrounding plane by thin connections we refer to as 'tethers'. Simulations indicate that anti-nodes close to the tethers cause significant loss in waveguide transmission. While a general increase of the waveguide width, which counteracts the single-mode nature of the waveguide, and a decrease in tether width, which needs to be balanced with mechanical stability, did not lead to satisfactory results, we adapted the way tethers are connected to the waveguide. We temporarily increased the waveguide width at the tethers from 495 to $895\,\mathrm{nm}$ over a distance of $3\,\mu\mathrm{m}$ to reach an adiabatic mode transfer. This reduced the simulated losses per tether from up to $40\,\%$, when an anti-node of the standing wave between waveguide tip and photonic crystal mirror coincides with the tether, to $\approx 5\,\%$. In experiment, the losses per tether were not that pronounced. The average improvement on the losses per tether due to the tapered design was on the order of $<5\,\%$ and could only be separated from fabrication-related variations for large statistics.

In the last part of this chapter about optical resonators we derived the basic description of photonic crystal resonators, where a defect in the periodic structure of a photonic crystal forms a resonator within the bandgap of the photonic crystal. As these devices can be made highly compact, are compatible with industrial silicon fabrication techniques, and can feature a strong interaction between GHz mechanical modes and optical telecom frequencies, they represent a widely used component in microwave-optic transducers [Vainsencher et al., 2016; Arnold et al., 2020; Forsch et al., 2020; Mirhosseini et al., 2020]. Additionally, we introduced simulations to minimize the transmission losses between the optical fiber and the on-chip waveguide, as well as the losses within the silicon waveguide.

2.1.2 Microwave resonators

Besides the optical components above discussed, we also engineered and fabricated devices with similar purposes in the microwave domain within the frequency range of 4-$12\,\mathrm{GHz}$. Only the usage of resonators in all domains involved in the respective microwave-optic transducer, i.e. optical resonator (chapter 2.1.1), microwave resonators as described in this chapter and optionally mechanical resonators (chapter 2.1.3), provides the maximum cavity enhancement of the otherwise moderate interaction between these different frequency regimes. The underlying mathematical principles of microwave resonators, i.e. Maxwell's equation, are equivalent to the optical domain. However, microwaves propagate within a metallic enclosure or - in case of an integrated circuit - along leads where the transverse dimensions is much smaller than the wavelength, e.g. a coplanar waveguide. In contrast to optical devices, the electrical wavelength $\sim \mathcal{O}(\mathrm{cm})$ is typically on the order of the physical device dimensions for non-integrated microwave components. Additionally, metallic surfaces are excellent reflectors for microwave fields essentially imposing a "hard" boundary condition which makes the radiation loss through the surface negligible. Analogue to the case of photonic crystal resonators described above, we employed FEM simulations to design our devices. For integrated microwave circuits that can be approximated as a planar structure, we use the software Sonnet that exploits the method of moments [Harrington and Harrington, 1996].

2.1.2.1 Tunable rectangular cavity

Acknowledgements I am grateful for initial assistance with microwave cavity simulations and fabrication by my colleagues Farid Hassani and Martin Zemlicka. I also want to thank our rotation student Phan Duc and my colleague Riya Sett, who developed the tunable coupling in our lab [Sett et al., 2024].

Besides the resonant enhancement for microwave-optic transduction, we also used a resonator to be able to detect the state of a superconducting qubit with weak coherent tones (chapter 2.4.2). For that, we used a rectangular cavity (light gray in fig. 2.4a)) that hosts the chip with the superconducting qubit (dark gray). A rectangular cavity is a rectangular waveguide that is closed (terminated with metallic shorts) on both ends. The rectangular cross-section (30 x $18\,\mathrm{mm}$) determines the shape and frequency of the fundamental mode (fig. 2.4b). As the third dimension ($9\,\mathrm{mm}$) is the shortest and a perfect electric conductor imposes the boundary condition $n \times E = 0$ resulting in a vanishing tangential electric field, the lowest frequency mode is TM_{110}. The strong electric field at the position of the superconducting qubit chip ensures a large capacitive coupling between the resonator field and the dipole of the qubit (chapter 2.4.2). In fabrication, 6061 aluminum alloy was milled to the desired dimensions. As it simplifies the milling, we rounded the sidewalls of the cavity. Coupling between a coaxial cable and the cavity is achieved by two metal pins in the lower half of the cavity that are connected to the inner conductor of the coaxial cable.
As the output field of this cavity serves as an input to our microwave-optic transducer in the experiment described in chapter 4, the cavity has to meet specific requirements: 1) the cavity bandwidth or power decay rate needs to be equal or smaller than the transduction bandwidth and the incoupling rate of the transducer microwave resonator. And, 2) the resonance frequency has to match the microwave resonance of the microwave-optic transducer. This demands the tunability of both parameters, the frequency and the waveguide-resonator coupling rate. We mounted two nanopositioners (attocube ANPz101/LT) on the cavity housing (dark red in cf. fig. 2.4a) to tune 1) the coupling to the coaxial cable by changing how much the coupling pin is inserted into the cavity and chip 2) the frequency by a metallic plate parallel to the superconducting qubit chip. In order to certainly meet the bandwidth and frequency matching to the converter it is required to offer both a large enough tuning range and precision. The tuning range of the position of the nanopositioners is $4.5\,\mathrm{mm}$. This translates into a wide tuning range of the resonator frequency between approximately $7\,\mathrm{GHz}$ and $9\,\mathrm{GHz}$ with some

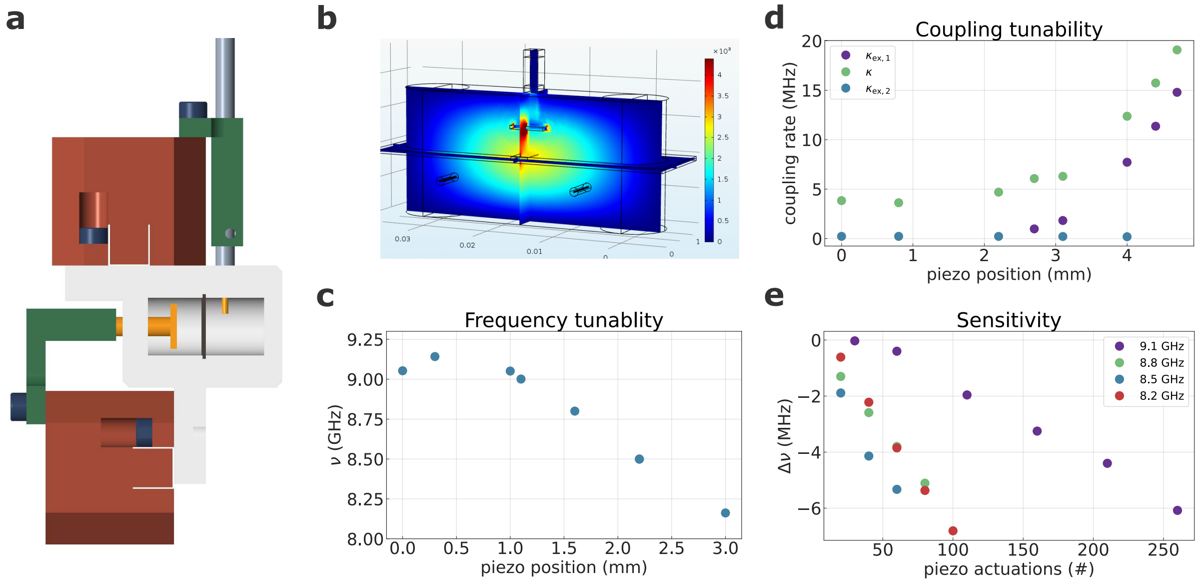

Figure 2.4: **Tunable microwave cavity a**, Technical drawing of the designed microwave cavity including a sample holder and the piezoelectrical nanopositioners to tune the frequency and coupling to the coaxial cable. **b**, Norm of the electric field for the fundamental mode in the resonator from a FEM simulation. The two coupling pins are shown as well **c**, Measured change of the external coupling by changing the position of the coupling pin with the translational stage. **d**, Measured frequency tuning with respect to the position of the metallic plate controlled again by a translational stage. **e**, Sensitivity of the frequency tuning for an actuation voltage of $30\,\mathrm{V}$ at room temperature and various positions of the tuner.

selected points being shown in fig. 2.4c. The initial increase in resonance frequency is caused by a slight compression of the intracavity mode field by the metallic plate moving towards the cavity center. Once the tuning plate dives into the region of strong electric field, the field is being pushed to the sides which reduces the frequency.

The second nanopositioner controls the position of the coupling pin. The total tuning range of the nanopositioner translates into a range of 0.1 to $20\,\mathrm{MHz}$ for the coupling between cavity and waveguide, i.e. κ_{e1} in eq. 2.5. The second port had a fixed coupling of $\kappa_{\mathrm{e2}}/(2\pi) = 0.1\,\mathrm{MHz}$. When matching the resonance frequencies of two devices, an important parameter is also the sensitivity of the tuning, i.e. the frequency shift corresponding to the smallest possible translation by the nanopositioner. Tests at different positions and an actuation voltage of $30V$ at room temperature yielded a minimal frequency shift of only $20\,\mathrm{kHz}$ per step of the nanopositioner when the tuning plate is at its outermost position, i.e. the highest frequency. This frequency shift per nanopositioner step increased to up to $80\,\mathrm{kHz}$ when the tuner was already further inside the cavity (fig. 2.4e). However, both values are more than an order of magnitude below the desired bandwidth of $\kappa/2\pi = 1.5\,\mathrm{MHz}$ and, hence, sufficient to ensure a reasonable frequency matching. Additionally, a further enhancement of the sensitivity can be achieved by reducing the actuation voltage. However, especially at cryogenic environments these piezo nanopositioners often fail to move at all below a certain actuation voltage. The herein used $30\,\mathrm{V}$ is usually above this threshold.[11].

---

[11] In principle, the nanopositioners allow a continuous change of position between two steps, when constantly applying a DC voltage, which is, however, not ideal at an environment of only a few mK because it may heat up the cavity.

2.1.2.2 3D whispering gallery mode resonator

Acknowledgements This cavity was originally designed by Alfredo Rueda and has been modified and improved by several generations of researcher in our electro-optic team. The herein used design was developed by William Hease and Alfredo Rueda.

The microwave-optic transducer based on EO material effects (chapter 4 and 2.2.3) used two WGM resonators to enhance the EO interaction. Similar to the optical whispering gallery mode (WGM) in 2.1.1.2, the concept of repeating reflections along a circular boundary between regions with different refractive indices also applies to electrical fields and metallic walls. A cylindrical cavity surrounded by bulk aluminium that turns superconducting below $1.2\,\mathrm{K}$ [Cochran and Mapother, 1958] and which can be modelled as a perfect electric conductor leads to a circular shaped microwave mode. A rod in the center of the cavity whose position is controlled by nanopositioners is used to adjust the resonance frequency. Additionally, this specific geometry features a small gap capacitor, where the electric field strength is maximal. This gap is also used to house an optical WGM as described in 2.1.1.2. The dielectric $\mathrm{LiNbO_3}$ does not only further increase the capacitance but also leads to a maximum overlap between the optical field inside the optical WGM and the microwave field which is strongest across the capacitor. Thus, this configuration ensures optimized coupling between microwave and optical fields in a non-linear process (cf. section 2.2). A detailed description of such a device can be found in [Rueda Sanchez, 2018; Hease et al., 2020; Sahu, 2023].

2.1.2.3 Planar resonator

Acknowledgements After initially developed by Johannes Fink at Caltech, I want to thank Elena Redchenko and Andrea Trioni for adapting the fabrication recipes of the densely packed coils for our clean room.

Besides the three-dimensional, millimeter-sized microwave-optic transducer based on the EO interaction in $\mathrm{LiNbO_3}$ and exploiting three dimensional WGM resonators (chapter 2.1.1.2 and 2.1.2.2), we also developed integrated microwave-optic transducers based on optomechanical photonic crystals (chapter 2.1.1.3) and an integrated microwave resonator with a footprint of only tens of $\mu\mathrm{m}$. This is realized by an LC-circuit (fig. 2.5a). We used $60\,\mathrm{nm}$ thick aluminum to pattern the circuit. The inductor is a square coil which consists of 48 turns with a pitch of $0.5\,\mu\mathrm{m}$. Its inductance has an analytically calculated value of $L = 59.8\,\mathrm{nH}$ [Mohan et al., 1999]. The capacitance comprises two parallel plate capacitors with aluminum electrodes on top of a silicon beams separated by a $\sim 70\,\mathrm{nm}$ gap etched into the silicon (fig. 2.5b). The capacitance of each capacitor from FEM simulations is $C_\mathrm{s} = 0.43\,\mathrm{fF}$ (fig. 2.5c). The compact coil with high turn density and therefore a favorable inductance over capacitance scaling and minimized wiring length was chosen to reduce the stray capacitance of the circuit. It can be approximated from the measured resonance frequency $f_0 = 10.5\,\mathrm{GHz}$ via

$$C_{\sum} = C_\mathrm{c} + C_\mathrm{s} = \frac{1}{(2\pi f_0)^2 L} \tag{2.20}$$

and yields a value of $C_\mathrm{s} \approx 3\,\mathrm{fF}$. A simulation with Sonnet (fig. 2.5d) of the circuit yields a resonance frequency that is very close to the measured value $10.4\,\mathrm{GHz}$. The resonator couples inductively via the magnetic field of the coil inductor and a microwave feed-line shunting the coplanar waveguide and thereby creating a large current and magnetic field. The coupling rate κ_e can be controlled by the distance between inductor and feedline. The simulated value

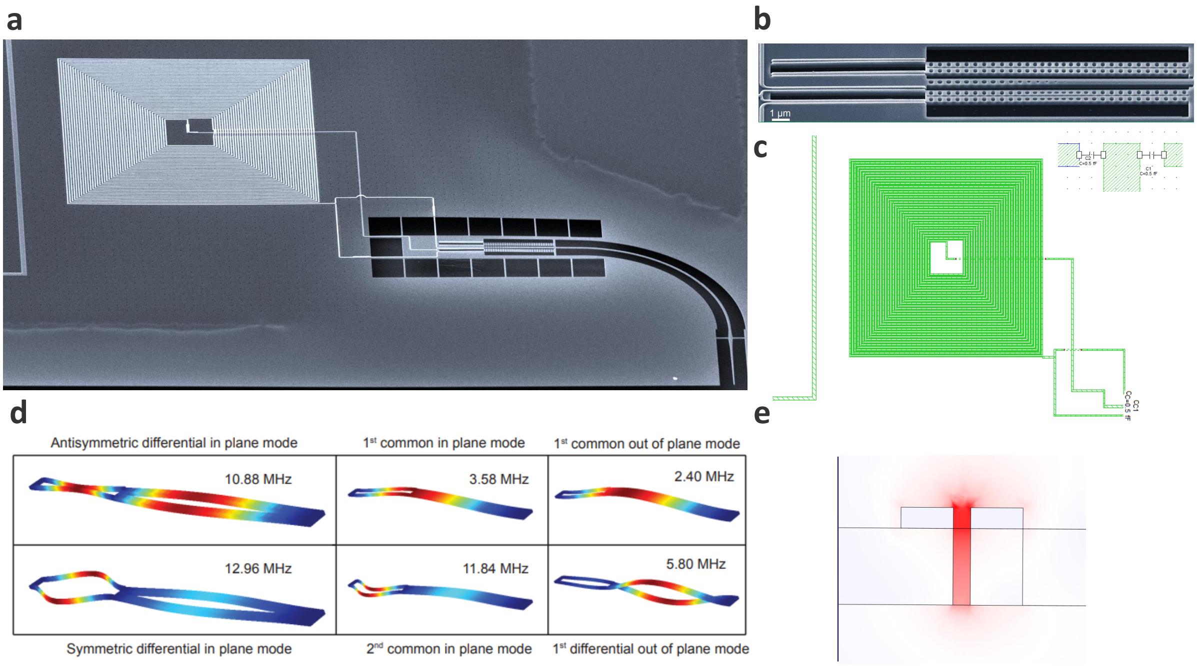

Figure 2.5: **Integrated mechanical resonator coupled to a microwave resonator circuit and optical photonic crystal resonator a**, SEM image of the central device **b**, Zoom-in on the mechanical resonator comprising an electrode of a parallel plate capacitor and one beam of a photonic crystal 'zipper' cavity. **c**, electrical cirucit simulation model in Sonnet of the inductor and the two parallel plate capacitors. **d** FEM simulations for various mechanical eigenmodes. The modes of interest were the two differential in-plane modes. **e**, Electric field distribution of the parallel plate capacitor between two $60\,\mathrm{nm}$ aluminum electrodes. The field significantly extends to the $220\,\mathrm{nm}$ thick silicon membrane which enhances the coupling between the mechanical displacement and the electric field.

of $0.9\,\mathrm{MHz}$ for the designed distance of $9.5\,\mathrm{\mu m}$ was in reasonable agreement with the actually measured value of $\kappa_\mathrm{e}/(2\pi) \approx 1.1\,\mathrm{MHz}$.

2.1.3 Mechanical resonators

The last type of resonators we discuss comprises mechanical modes. It consists of a pair of doubly clamped beams with an additional thin and elastic connection of around $50\,\mathrm{nm}$ width in the center. This node separates two regions: 1) the EM part: two oscillating beams with a width of only $150\,\mathrm{nm}$ each and aluminum electrodes on top form together with two additional aluminum electrodes on the substrate the two parallel-plate capacitors of the integrated LC resonator with a gap of only $70\,\mathrm{nm}$ (cf. section 2.1.2.3). 2) the OM part. Two photonic crystal resonator nanobeams are separated by only $80\,\mathrm{nm}$ and represent again a pair of doubly clamped beams (fig. 2.5b). If the central connection between the two regions, that is the moving capacitor electrodes and the moving photonic crystal nanobeams, would be rigid, both regions would feature independent mechanical oscillations. This was observed for central connections with a width $>500\,\mathrm{nm}$ at a thickness of $220\,\mathrm{nm}$. Owing to the elasticity of this herein realized connection ($50\,\mathrm{nm}$ width) the mechanical modes of the two regions are not independent but hybridize. Thus, the lowest lying out-of-phase, i.e. differential, in-plane mode comprises *two* eigenmodes at simulated frequencies of 11 and $13\,\mathrm{MHz}$ (fig. 2.5e, left). As expected for hybridization, the frequency separation of these modes scales inversely with the width of the central connection, i.e. is proportional to the coupling of the modes in the two regions. The advantage of such a tuning fork geometry for an out-of-phase oscillation of two symmetric parts is that the elastic waves at the clamps interfere destructively. In other words, the total force on the clamps at the domain diminishes which greatly reduces the clamping losses. As the deformation is more localized for such a tuning fork geometry, this also reduces the dissipation due to strain-induced heating and material defect and, overall, leads to an improved quality factor Q_m of the mechanical resonator [Zhang et al., 2015]. Additionally, it pushes the mechanical resonance frequency ω_m of these tuning fork modes and thereby further increases the product $\omega_\mathrm{m} \cdot Q_\mathrm{m}$. The effective mass, i.e. the mass weighted by the displacement of the respective eigenmode, is $1.3\,\mathrm{pg}$ for the geometry shown in fig. 2.5b. In addition to the discussed differential in-plane modes, there naturally occur other mechanical modes that are not used for the experiment (fig. 2.5e, center and right). Importantly, these modes are separated by $\geq 1\,\mathrm{MHz}$ from the differential modes we are interested in. This avoids undesired cross-coupling.

2.1.4 Loss mechanisms and quality factors

The motivation for leveraging resonators originates from an increase in sensitivity or coupling as a consequence of the number of round trips related to the quality factor Q. The quality factor, however, cannot be made arbitrarily high. In practice, the main limitations of the achievable Q are often categorized into losseses from radiation ($\propto Q_\mathrm{rad}^{-1}$), surface scattering due to imperfections ($\propto Q_\mathrm{surf}^{-1}$) or absorption in the material or at the surface ($\propto Q_\mathrm{abs}^{-1}$). Following the notation in eq. 2.1 where we distinguish between an external, i.e. desired, coupling to a waveguide for further signal routing (κ_e) and internal loss inside the resonator (κ_i), we focus the further discussion on quality factors on maximizing the quality factor by minimizing the internal loss $\kappa_\mathrm{i} = \frac{\nu_\mathrm{c}}{Q_\mathrm{i}}$.

2.1.4.1 Optical resonators

Starting with the macroscopic optical WGM in section 2.1.1.2, the intrinsic loss comprises three potential sources: radiation loss from imperfect internal reflection at the curved surface, material loss due to absorption e.g. from impurities in the $\mathrm{LiNbO_3}$ crystal, and surface scattering. As the radius and the radius of curvature of the resonator disc is on the order of mm and is thereby much larger than the optical wavelength, the theoretical quality factor due to radiation loss is tens of orders of magnitude above the experimentally observed values. Hence, even though radiation loss is the only fundamental loss mechanism in optical WGM, it is practically irrelevant [Sahu, 2023]. Secondly, molecule-sized features on the resonator surface, where the field is strongly confined, lead to scattering. In an attempt to relate the quality factor to the surface roughness, [Gorodetsky et al., 2000] state for Raleigh scattering for spheres

$$Q_\mathrm{surf} = \frac{3\lambda^3 R}{8\pi^2 n B^2 \sigma^2} \tag{2.21}$$

with the radius R, σ as the rms size of the surface inhomogeneity and B as the roughness correlation length along the WGM resonator surface. The surface loss is also the reason for multiple surface polishing steps with diamond slurry of decreasing grain sizes between $1\,\mathrm{\mu m}$ and $9\,\mathrm{\mu m}$ in the fabrication of our resonators [Sahu, 2023] and a final chemical-mechanical polishing mixture. The intrinsic quality factor increases during these polishing steps from

$\sim 10^6$ to $> 10^8$ with the $\leq 8 \cdot 10^8$ as our highest ever measured quality factor in $\mathrm{LiNbO_3}$ without magnesium doping. As these values are similar to the reported material loss for bulk $\mathrm{LiNbO_3}$ [Leidinger et al., 2015], we assume that we are mainly limited by absorption and bulk Rayleigh scattering in the material for the mm-sized WGM resonators rather than surface scattering.

Similarly, in photonic crystal resonators, the experimentally measured quality factor is typically also limited rather by material imperfections than the radiation loss of the corresponding design. In case of photonic crystal resonators in silicon as in section 2.1.1.3, it has been shown that the surface chemistry plays a crucial role for the optical quality factor. Removal of the $\mathrm{SiO_x}$ with hydrofluoric acid (HF), either diluted [Sekoguchi et al., 2014; Meenehan et al., 2015] or as a vapor HF etch [MacCabe et al., 2020] leads to a significant decrease in the surface-state absorption loss [Sekoguchi et al., 2014]. The oxide removal and hydrogen passivation by HF is often preceded by an oxidation in piranha solution $(\mathrm{H_2SO_4/H_2O_2})$ to remove organic residuals [Borselli et al., 2006]. The formation of a native oxide on silicon under oxygen atmosphere can again reduce the optical quality factor. Thus, exposure to atmosphere should be minimized and an immediate transfer to a $\mathrm{N_2}$ environment is favorable. Scattering loss can originate from surface scattering - even though the surface from inductively-coupled reactive ion etching is rather smooth and the oxidation and oxide stripping cycles with piranha and HF have an additional smoothing effect [Sparacin et al., 2005]. Additionally, random design variations on the order of nm, e.g. in size and position of air holes in the silicon beam, degrade the quasi-bandgap in the photonic crystal resonator and lead to increased loss. This loss can be modelled via FEM simulations by introducing Gaussian noise on the design parameters. In general, the relative contribution of the different loss mechanisms also depends on the photonic crystal design. We measured the highest average internal quality factors Q_i for single 1D nanobeams with a breathing-mode design [Chan et al., 2012], where the highest optical field intensity lies inside the silicon nanobeam. In the "zipper" geometry [Safavi-Naeini et al., 2013] with two parallel nanobeams as presented in section 2.1.1.3 and chapter 3, the highest intensity of the optical field is in the narrow gap between the beams, which makes the design more susceptible to surface imperfections. Our measured quality factors of these devices were typically around $Q_\mathrm{i} \sim 10^5$. Following this trend, we measured the lowest internal quality factor on average with $Q_\mathrm{i} \sim 10^4$ in sliced nanobeam designs [Leijssen and Verhagen, 2015] which exhibit the smallest mode-volume with the strongest field confinement in short, narrow gaps between two silicon surfaces. This design also exhibits the largest variation in quality factor, emphasizing the susceptibility to local variations in design and surface condition. Besides that, the fact that we could not achieve state-of-the-art internal quality factors exceeding $\simeq 10^6$ can be a consequence of the heterogeneous platform including the microwave resonator, omission of piranha oxidation, and the relatively long air exposure while setting up the optical alignment and microwave connections to the EOM transducer before starting the evaporation and cooldown.

2.1.4.2 Microwave resonators

The loss mechanisms in microwave resonators 3D cavities with electrical fields naturally differ from the optical domain, as microwave fields are excellently confined by metals due to the density of free electrons and consequently high plasma frequency. Hence, the skin depth, i.e. the penetration depth after which the current density has dropped to $1/e$, is much smaller than the microwave wavelength of $\sim 10\,\mathrm{mm}$ in free space. In 3D cavities such as rectangular (section 2.1.2.1) and WGM cavities (section 2.1.2.2) the loss can be separated in three categories: dielectric loss, conductive loss and seam loss. As we use superconducting aluminum alloy 6061 for all used resonators, we will focus the discussion on this example.

Aluminum forms a thin oxide layer on the surface. Thus, the *dielectric loss* will limit the achievable quality factor to [Reagor et al., 2013]

$$Q_{\mathrm{diel}} = \frac{1}{p_{\mathrm{diel}} \tan \delta} \tag{2.22}$$

with the loss tangent $\tan \delta$ of the thin oxide layer. p_{diel} is surface dielectric participation ratio being composed of the the surface-to-volume ratio weighted by the electric field intensity, i.e. $\epsilon_{\mathrm{r}}\epsilon_0 t \int_{\mathrm{S}} |\vec{E}|^2 dA / \int_{\mathrm{V}} \epsilon_0 |\vec{E}|^2 dV$ with the oxide layer thickness t and relative permittivity ϵ_{r}. The rectangular TE101 mode shown in fig. 2.4b has a comparably strong electric field on parts of the surface and will thereby be subject to dielectric loss. Nevertheless, this limitation is orders of magnitudes less than in planar resonators placed on a dielectric substrate. Additionally, the lack of a power dependency in the linewidth for the herein measured 3D microwave cavities even for microwave drive tones leading to high intracavity photon numbers of $n_{\mathrm{c}} > 10^9$ suggests that dielectric effects are not dominating. Otherwise, the saturation of dielectric two-level systems (TLS) typically leads to power-dependent lifetimes [Crowley et al., 2023]. In the planar resonator from section 2.1.2.3, however, we observed a significant increase of linewidth and decrease in resonance frequency with high microwave driver power, both in agreement with a temperature increase in a superconductor. This has been modelled by resonant and dispersive TLS-coupling complemented with a self-heating effect [Mittal et al., 2024]. While resonant TLS coupling describes a direct energy exchange and can therefore saturate for large driver power or temperatures, the dispersive coupling only shifts the energy levels of off-resonant TLS out of equilibrium followed by a subsequent relaxation. The additionally introduced self-heating effect assumes simply a temperature increase due to the dissipated heat via the internal resonator loss and becomes only noticeable at very high drive powers.

Secondly, even a superconductor exhibits a finite surface resistance and therefore *conductive loss* from e.g. quasiparticles [Lei et al., 2023]. Its participation is defined by the magnetic field weighted participation ratio $\lambda \int_{\mathrm{S}} |\vec{H}|^2 dA / \int_{\mathrm{V}} |\vec{H}|^2 dV$ and the quality factor limit due to conductive loss is given by [Reagor et al., 2013]

$$Q_{\mathrm{cond}} = \frac{\omega \mu \lambda}{R_s p_{\mathrm{diel}}} \tag{2.23}$$

with the surface resistance R_s. It grows monotonically with frequency ω. Typical quasiparticle densities as origins of the surface resistance have been found to be between $10^{-5} - 10^{-7}$ per Cooper pair [Paik et al., 2011; Catelani et al., 2012]. This refers to quasiparticles that are not in thermal equilibrium and can limit both quality factors of resonators and the coherence of qubits. The measured qubit coherence decrease with increasing temperature giving rise to additional equilibrium quasiparticles showed also agreement with these out-of-equilibrium quasiparticle densities (section 4.3). Due to the smaller participation, the influence of the surface conductance on a 3D resonator was again found to be orders of magnitudes smaller than for planar resonator [Reagor et al., 2013].

A third loss mechanism occurs only for 3D cavities. As these devices cannot be fabricated from a single piece, there will be microscopic gaps between the adjacent surfaces of the two pieces forming the cavity. This results in the so-called *seam loss*. The seam admittance per unit length is described as [Brecht et al., 2015]

$$y_{\text{seam}} = \frac{\int_{\text{seam}} |\vec{J}_{\text{s}} \times \vec{l}|^2 dl}{\omega \mu_0 \int_{\text{vol}} |\vec{H}|^2 dv} \tag{2.24}$$

We tried to mitigate this effect by sealing these gaps with indium which turns superconducting below $3.4\,\mathrm{K}$. Unfortunately, the requirement of having frequency tunable rectangular and WGM microwave frequencies with associated coupling pins through the cavity wall introduces further gaps in the cavity surface leading to further seam losses due to an effective resistance and thereby Ohmic losses. As they scale quadratically with current, it would be important to place them at positions with low current density. However, due to space constraints the cavity frequency tuner in the rectangular tunable cavity was placed at the top where the current is maximum (fig. 2.4b). This may have played a pivotal role because it is the position with the highest current density.
It should be noted that the microwave resonator losses in the final packaging of the devices used for the experiments in chapter 3 and 4 were limited by other external factors. The planar resonator leveraged for the integrated EOM transducer suffered from optical heating due to the nearby optical pump (fig. 3.5); the rectangular 3D microwave cavity coupled to the qubit suffered from dielectric losses from the qubit chip placed at the electric field maximum for large qubit-cavity coupling (fig. 2.4), and the WGM microwave resonator had the $\mathrm{LiNbO_3}$ optical resonator (fig. 2.1.1.2 and [Sahu, 2023]) placed in its center which causes significant microwave losses due to the piezoelectricity of lithium niobate ($\mathrm{LiNbO_3}$) and the concomitant coupling of microwaves to bulk mechanical modes. These losses could be decreased by a factor of three by softly clamping the $\mathrm{LiNbO_3}$ disc with Indium in the disc center instead of being tightly clamped to the aluminum cavity [Sahu, 2023].

2.1.4.3 Mechanical resonators

A fundamental difference of elastic loss mechanisms compared to electromagnetic waves arises from the fact that phonons cannot propagate in vacuum and that an oscillation is related to the physical displacement of the host material. Thus, *gas molecules* can damp the mechanical displacement during oscillation. This damping can be minimized by vacuum environments. Other extrinsic dissipation mechanism are associated with *clamping loss* (often also denoted as radiation loss) or electric and magnetic fields [Schmid et al., 2016]. Additionally, there are intrinsic processes related to the material itself associated with internal friction. This is well-described by a Zener model as a lagged response between the oscillations of stress σ_0 and strain field ϵ_0 acquiring a phase shift [Zener, 1937, 1938]. Young's modulus relating the two quantities $\epsilon_0 = E\epsilon_0$ exhibits then a complex component [Tsaturyan et al., 2017]. There exist also other intrinsic loss mechanisms related to more fundamental effects:

1. *phonon-phonon scattering*
   Coherent phonons from specific modes can scatter with thermal phonons due to the anharmonic potential of the crystal lattice allowing for frequency mixing. The phonon

relaxation time and its relation to the period of one mechanical oscillation divides here two different regimes. In the Akhiezer regime [Akhiezer, 1939] the relaxation times are much shorter than the mechanical period ($\omega_\mathrm{m}\tau_\mathrm{ph} \ll 1$). The strain wave of a mechanical mode modulates the phonon frequencies and thereby distorts the thermal equilibrium distribution in the presence of the anharmonic lattice potential. As the relaxation time is much shorter than the acoustic oscillation period, the phonons relax into the modulated equilibrium distribution and this equilibrium distribution becomes time-dependent. However, as the relaxation is not instantaneous because of the finite relaxation rate, there will be a lagged response of the phonon population to the new equilibrium distribution which leads to dissipation of elastic energy from the strain wave [Iyer and Candler, 2016]. The quality factor is inversely proportional to the head capacity, temperature and frequency of the mode ($Q^{-1} \propto C_\mathrm{v}T\omega_\mathrm{m}$). The product $f \cdot Q$ from Akhiezer damping lies on the order of 10^{13} for silicon [Rodriguez et al., 2019].
A second regime is characterized by relaxation rates that are much slower than the mechanical period, i.e. $\omega_\mathrm{m}\tau_\mathrm{ph} \gg 1$. Thus, the time-dependent equilibrium distribution changes too fast for the phonons to relax to them. This is referred to as Lanau-Rumer regime [Landau and Rumer, 1937] and can be described by phonon scattering from the distorted mode of interest to individual thermal modes in equilibrium [MacCabe et al., 2020] (single mode approximation). Thus, the dissipation is independent of the mechanical mode frequency but shows a heavy dependency on the temperature ($Q \propto T^{-4}$) [Rodriguez et al., 2019].

2. *thermoelastic damping*
   If the temperature can locally vary on the order of a mechanical wavelength, i.e. if the mean free path is much smaller than the wavelength, the temperature gradient and the strain gradient can couple proportionally to the thermal expansion coefficient and elastic energy can be dissipated as heat flow [Lifshitz and Roukes, 2000; Rodriguez et al., 2019].

3. *two-level systems (TLS)*
   Defects that occur typically in amorphous materials or close to surfaces or material boundaries can act as TLS, when there exist two configurations of an atomic position with similar energy levels. They can exhibit an electrical and mechanical dipole and therefore react to both strain fields and electrical fields or even act as a mediator between electrical and mechanical modes [Chen et al., 2024]. Similar to the situation in microwave circuits (see above), TLS can couple resonantly to the coherent mode or dispersively and dissipate energy by cascaded relaxation mechanisms to other defects. Additionally, they can act as a mediating coupler between two acoustic modes. Their role has been studied in both MHz membranes [Faust et al., 2014] and GHz acoustic modes [MacCabe et al., 2020].

Thus, the achievable Q-factor limited by several loss mechanisms for mechanical modes can be composed of the following components

$$Q^{-1} = Q^{-1}_\mathrm{gas} + Q^{-1}_\mathrm{rad} + Q^{-1}_\mathrm{ph-ph} + Q^{-1}_\mathrm{TED} + Q^{-1}_\mathrm{tls} + Q^{-1}_\mathrm{other} \tag{2.25}$$

In the following, we will briefly discuss the influence of each effect on nano- and micromechanical resonators in a cryogenic vacuum environment.

Our experiments are typically conducted in vacuum with pressures around $10^{-6}\mathrm{mbar}$. Thus, the dissipation from gas molecules can be neglected.

Clamping or radiation loss, however are an essential loss mechanism. Fortunately, there exist several excellent mitigation strategies. Generally, a high impedance mismatch between the supporting substrate and the microresonator is favorable and leads to internal reflection of the mechanical wave at the support. The radiation follows approximately a simple scaling with the geometric dimensions of e.g. a nanobeam's width and length $Q_{\mathrm{rad}} \propto L/w$ [Sementilli et al., 2022]. They can be simulated with FEM. Secondly, phononic bandgaps have been exploited successfully to create ultrahigh mechanical life times in MHz [Yu et al., 2014; Tsaturyan et al., 2017] and GHz resonators [MacCabe et al., 2020]. The phononic bandgap area around the central resonator suppresses the propagation of acoustic waves exponentially with the number of unit cells and therefore prevents the acoustic mode from radiating into the substrate. As a last point, nested structures with low-pass filter devices around the central acoustic resonator also turns out to effectively reduce radiation loss [Weaver et al., 2016]. In the experiment of chapter 3, we followed a different approach and chose a tuning fork geometry that reduces the net force on the clamp ideally to zero for the in-plane differential mode of interest [Zhang et al., 2015].
Moving towards the intrinsic loss mechanisms, the phonon-phonon scattering regime for our experimental settings with temperatures below $100\,\mathrm{mK}$ depends on the used mechanical resonance frequency. The phonon relaxation time for silicon is on the order of $\sim 10\,\mathrm{ps}$ at room temperature but approaches ns for cryogenic environments [Sahasrabudhe and Lambade, 1999]. Thus, acoustic modes in the GHz regime at low temperatures, e.g. e.g. [Mirhosseini et al., 2020; Meesala et al., 2024; Weaver et al., 2024; Zhao et al., 2024], are in the limit of $\omega_{\mathrm{m}}\tau_{\mathrm{ph}} \gg 1$. In case of membranes and clamped strings with MHz frequencies, e.g. [Yu et al., 2014; Norte et al., 2016; Tsaturyan et al., 2017; Ghadimi et al., 2018], the relaxation times are much faster than the acoustic oscillation period for. These devices are therefore in the Akhiezer regime $\omega_{\mathrm{m}}\tau_{\mathrm{ph}} \ll 1$. For both frequency regimes, phonon-phonon scattering was not identified as the dominant loss-mechanism [Tsaturyan et al., 2017; MacCabe et al., 2020].
As the photoelastic dissipation in a cryogenic environment is also negligilbe because the thermal expansion coefficient of silicon approaches zero for temperatures $<10\,\mathrm{K}$ [Rodriguez et al., 2019], the discrepancy was attributed to the coupling to TLS [Tsaturyan et al., 2017; MacCabe et al., 2020].

Next, the role of stress in our double clamped string resonator (fig. 2.5) should be discussed. We found that the measured mechanical resonance frequency deviates significantly from FEM after aluminum evaporation. After including a tensile stress of $600\,\mathrm{MPa}$ (cf. also [Barzanjeh et al., 2019]), the good matching between FEM simulations and measured resonance frequency could be reestablished for all measured mechanical modes (fig. 2.5d). In general, the introduction of tensile stress is a very effective method do increase the quality factor for MHz frequency resonators without decreasing the intrinsic dissipation called *dissipation dilution*. It essentially changes the ratio of lost energy per mechanical period to the total energy stored in the mechanical oscillator (this is probably also the most fundamental definition of the quality factor). The resonator's strain wave due to elongation and bending are the source of the aforementioned intrinsic loss mechanisms. Tensile stress however can increase the stored energy without introducing additional loss and thereby enhances the quality factor

$$\frac{2\pi}{Q} = \frac{\Delta W_{\mathrm{Elongation}} + \Delta W_{\mathrm{Bending}}}{W_{\mathrm{Elongation}} + W_{\mathrm{Bending}} + W_{\mathrm{Tensile}}} \tag{2.26}$$

The tensile energy mostly depends on the tensile stress, in contrast to the elongation and bending energy [Tsaturyan et al., 2017; Sementilli et al., 2022], which remain widely unaffected. The dissipation dilution factor, the enhancement due to tensile stress σ, scales roughly $\propto \sqrt{\sigma}$ and a geometric factor $\propto L/w$. Thus, mechanical resonators from materials, which were prestressed during material growth, such as silicon nitride, have shown remarkable quality factors [Yu et al., 2014; Norte et al., 2016; Tsaturyan et al., 2017; Ghadimi et al., 2018]. Nevertheless, the dissipation dilution efficacy is often decreased by large bending energies at the clamps. In order to suffice the boundary condition of a fixed anchor at the support, especially fundamental modes exhibit a large curvature close to the clamping region giving rise to an increased $\Delta W_{\text{Bending}}$. Thus, minimizing clamping loss and dissipation dilution would require competing strategies. A small impedance mismatch between bulk and resonator mode would reduce the bending energy and therefore increase the dissipation dilution, but decrease total internal reflection at the interface and therefore increase the radiation loss. One way to overcome this discrepancy is *soft clamping* which often accompanies the strategy of dissipation dilution. The idea behind it is a localization of the mode around the center to avoid large bending at the clamp region with fixed anchor points. This has been achieved by phononic bandgaps in membranes [Tsaturyan et al., 2017] and beams [Ghadimi et al., 2018]. In the latter, the authors additionally exploited *strain engineering* besides dissipation dilution and soft clamping, to further enhance the quality factor. This comprises the technique to increase the tensile stress in the area of interest by geometric changes. It exploits the redistribution of stress after releasing the mechanical resonator from the bottom material. In general, the total stress of a uniform released string can never be higher than for an unreleased beam. In fact, stress relaxation always occurs during release to some extend. However, as the tension force being the product of the cross section and stress $F_{\text{T}} = \sigma A$ has to be constant along the beam, a change in the cross-section results in a change of force upon release [Sementilli et al., 2022]. As the net force needs to be zero, a smaller cross-section will be compensated by a strain on the smaller region increasing the stress and thereby compensating the reduction in cross-section. In order to increase the stress in a region by a given factor, the cross-section and length of the neighboring region should be larger by the same factor. The ultimate limit for tensile stress enhancement is given by the material yield strength. If the stress is above this value, the stress will lead to plastic instead of elastic deformation.

Besides the tensile stress at the aluminum-silicon-interface, we did not further investigate the effect of dissipation dilution which could be the reason for the relatively large dissipation rate of $150\,\mathrm{Hz}$ without optical heating.

It is worth mentioning that the strategies to create dissipation dilution in prestressed films for increased quality factors are only applicable for moderate mechanical frequencies. As ω_{m} approaches the GHz regime and the oscillation wavelengths become shorter, the local strain energy is larger than the tensile stress and one has to reduce the intrinsic absorption mechanisms to improve the quality factors. A comprehensive investigation can be found in [MacCabe et al., 2020].

2.1.5 Conclusions

In summary, we introduced the universal theoretical description of harmonic oscillators by means of QLE together with input-output theory [Gardiner and Collett, 1985] and discussed various implementations in different frequency regimes and materials as well as the diversity of applications of these widely used components. All these components are needed for improved measurement capabilities, e.g. dispersive state readout of a superconducting qubit (chapter 2.1.2.1) or filtering of undesired tones (chapter 2.1.1.1), or to enhance the microwave-optic transducer device performance by resonant enhancement of interaction strengths. In the next chapter, we will look in a similar manner at exactly this interaction or coupling between different frequency domains, enhanced by resonators on each end. We realized such a coupling in three different implementations: an electro-optical (EO) modulator to couple electric fields directly to optical modes, an electro-mechanical (EM) device, where mechanical vibrations couple to the electric field and an opto-mechanical (OM) resonator, where the mechanical oscillations couple to the optical field inside the resonator. While the basic loss principles are similar and include radiation loss, material absorption and surface loss, the exact loss mechanism and individual contribution naturally differs for optical, electrical and acoustic fields.

2.2 Weak coupling between two harmonic oscillators - electrooptics and optomechanics

In this chapter, we will expand the description of harmonic oscillators introduced in 2.1 to two resonators that are additionally coupled to each other. The coupling will be in the weak-coupling-regime and therefore smaller than or comparable to (some of) the individual resonators loss rates. Hence, the information couples faster from the resonators to the environment than it is exchanged between the two resonators [12]. Based on these models, we will demonstrate how we experimentally characterized the strength of these couplings and thereby the performance of our devices. Again, we will start with the mathematical model and continue with the introduction of different implementations of such a device:

1. We couple electrical resonator modes directly to optical fields (cavity electro-optics [Tsang, 2010; Rueda et al., 2016; Javerzac-Galy et al., 2016; Fan et al., 2018; Jiang et al., 2020; Hease et al., 2020])
2. an EM device [Palomaki et al., 2013; Lecocq et al., 2016; Fink et al., 2016], where mechanical vibrations couple to the electric field and
3. an OM resonator [Hill et al., 2012; Verhagen et al., 2012] a coupling between mechanical oscillations and the optical field of a resonator.

Two uncoupled harmonic oscillators with modes $\hat{a}$ and $\hat{b}$ are described as

$$H_0 = \hbar\omega_a \hat{a}^\dagger \hat{a} + \hbar\omega_b \hat{b}^\dagger \hat{b} \tag{2.27}$$

Fundamentally, if one introduces the interaction between the two resonators for the examples mentioned above it is described by a three-wave mixing process represented by three operators. Consequently, it is a nonlinear process. In the herein discussed weak coupling regime, where the single-photon interaction between both resonators g_0 is small compared to their decay rates $\kappa_{\mathrm{a,b}}$, one typically uses a coherent drive to enhance the coupling rate by the amplitude of the driving field. In the following, we

- separate the mode fields into a classical part and a fluctuating term e.g. quantum fluctuations or thermal noise: $\hat{a} \rightarrow \bar{\alpha} + \hat{a}$ and $\hat{b} \rightarrow \bar{\beta} + \hat{b}$

---

[12] In fact, we will see that, in case of the electro-optic transducer, the coupling is smaller than the loss rates of microwave and optical resonator, i.e. $G \ll \kappa_{\mathrm{e}}, \kappa_{\mathrm{o}}$. For the EM and OM device, however, the regime is characterized by $\kappa_{\mathrm{m}} \ll G \ll \kappa_{\mathrm{e}}, \kappa_{\mathrm{o}}$

- switch to a frame rotating with the frequency of a strong pump in mode a [13], i.e. $\omega_\mathrm{a} \rightarrow \tilde{\Delta}_\mathrm{a} = \omega_\mathrm{drive} - \omega_\mathrm{a}$. The classical mean amplitude renormalizes this detuning to $\Delta_\mathrm{a} = \tilde{\Delta}_\mathrm{a} - g_0(\beta^* + \beta)$
- are only considering interactions that are enhanced by the strong coherent field $\bar{\alpha}\sqrt{\bar{n}_\mathrm{a}}$ with $\bar{n}_\mathrm{a}$ as the real-valued number of photons in resonator a. Thus, we neglect cubic interactions in the fluctuation operators.

This transforms the Hamiltonian for weakly coupled resonators with parametric drives into its linearized [14] form with only quadratic operator interactions [Aspelmeyer et al., 2014]

$$H \simeq \underbrace{-\hbar\Delta_\mathrm{a}\hat{a}^\dagger\hat{a}}_{\text{free evolution A}} + \underbrace{\hbar\omega_b\hat{b}^\dagger\hat{b}}_{\text{free evolution B}} \underbrace{+\hbar g_0\sqrt{\bar{n}_\mathrm{a}}(\hat{a}^\dagger + \hat{a})(\hat{b}^\dagger + \hat{b})}_{\text{interaction}} \tag{2.28}$$

Rearranging the interaction part leads to

$$H_\mathrm{int} \simeq +\hbar g_0\sqrt{\bar{n}_\mathrm{a}}(\underbrace{\hat{a}^\dagger\hat{b}^\dagger + \hat{a}\hat{b}}_{\text{amplification}} + \underbrace{\hat{a}^\dagger\hat{b} + \hat{a}\hat{b}^\dagger}_{\text{beamsplitter}}) \tag{2.29}$$

The *amplification* term describes the downconversion of a pump photon to correlated pairs of photons from mode $\hat{a}$ and $\hat{b}$. The drive frequency needs to fulfill $\omega_\mathrm{drive} = \omega_\mathrm{b} + \omega_\mathrm{a}$ or $\Delta_\mathrm{a} = +\omega_\mathrm{b}$. This allows for the parametric amplification of a signal of mode $\hat{a}$ or $\hat{b}$ and the entanglement between those two. The result is a two-mode squeezed state with beyond-classical correlations between the two individually Gaussian fields with rate $2\sqrt{\bar{n}_\mathrm{a}}g_0$. We exploited this interaction in our work on entangled microwave radiation [Barzanjeh et al., 2019] and electro-optic entanglement [Sahu et al., 2023] among a variety of other entanglement demonstrations from other research groups on various platforms. This process also amplifies vacuum noise and can thus be attributed to heating.

The *beamsplitter* interaction describes the coherent conversion between the states of the modes $\hat{a}$ and $\hat{b}$. A pump photon at detuning $\Delta_\mathrm{a} = -\omega_\mathrm{b}$ can be upconverted to a photon at frequency ω_a by the annihilation of a photon at frequency ω_b and vice versa. This exchange of states between the two resonators enables state conversion between both resonators but also cooling of resonator $\hat{b}$ as long as $\hat{a}$ has a low occupancy.

In a similar fashion as for the single resonator in section 2.1, the time dynamics of the system as well as the steady-state frequency spectrum is well-described by the QLE. It is derived for a system operator $\hat{o}_\mathrm{s}$ by inserting the Hamiltonian of eq. 2.28 into $\dot{o}_\mathrm{s} = -i/\hbar[\hat{o}_\mathrm{s}, H]$ and adding the interaction with the system's input field. As a difference to section 2.1, we also include now the quantum fluctuations in our description:

---

[13] The choice of applying the strong pump to mode a and not b is of course arbitrary. In EO systems we approached strong coupling for both microwave and optical drive fields. (see Supplementary Information of [Hease et al., 2020] and [Sahu et al., 2022] respectively). For OM and EM systems without the possibility of a mechanical drive the parametric enhancement of the single-photon coupling constant naturally stems from optical or electrical pump fields (cf. section 2.3)

[14] The term 'linearized' refers to the fact that the quantum Langevin equations are linear for up to quadratic interactions between operators

$$\dot{a}(t) = \left(i\Delta_\text{a} - \frac{\kappa_\text{a}}{2}\right)\hat{a}(t) - ig_0\sqrt{\bar{n}_\text{a}}\left(\hat{b}+\hat{b}^\dagger\right) + \sqrt{\kappa_\text{ex,a}}\hat{a}_{ex} + \sqrt{\kappa_\text{in,a}}\hat{a}_{in} \tag{2.30a}$$

$$\dot{b}(t) = \left(i\Delta_\text{b} - \frac{\kappa_\text{b}}{2}\right)\hat{b}(t) - ig_0\sqrt{\bar{n}_\text{a}}\left(\hat{a}+\hat{a}^\dagger\right) + \sqrt{\kappa_\text{ex,b}}\hat{b}_{ex} + \sqrt{\kappa_\text{in,b}}\hat{b}_{in} \tag{2.30b}$$

The parametrically enhanced coupling is here a real number with $g_0\sqrt{\bar{n}_\text{a}} = (g_0\sqrt{\bar{n}_\text{a}})^*$. In experimental practice it is convenient to distinguish between waveguide ports that guide a control signal with an external coupling rate $\kappa_{\text{ex},j}$ to the device and thermal baths coupled to the device by an intrinsic coupling rate $\kappa_{\text{in},j}$. The corresponding input fields $\hat{a}_{in}, \hat{b}_{in}$ represent quantum fluctuations or thermal noise from the environment the mode field is coupled to. In practice, this is mostly determined by the physical temperature of the device, resulting in a given occupation according to the Bose-Einstein distribution $\bar{n}_\text{in} = 1/(e^{\hbar\omega/(k_\text{B}T_\text{in})} - 1)$. $\hat{a}_{ex}, \hat{b}_{ex}$ correspond to fluctuations in the waveguide with a thermal contribution of $\bar{n}_\text{ex}$ but can also represent a weak coherent probe field sent to the device. The total linewidth of the resonator in absence of the coupling to another resonator ($g_0 = 0$ in the example above) is given as $\kappa = \kappa_\text{ex} + \kappa_\text{in}$. The steady-state mode occupation is then simply the mean of the thermal occupations of the coupled ports j weighted by the coupling ratio, that is [Rigetti et al., 2012]

$$\bar{n} = \sum_j \frac{k_\text{j}}{\kappa}\bar{n}_j = \frac{\kappa_\text{ex}\bar{n}_\text{ex} + \kappa_\text{in}\bar{n}_\text{in}}{\kappa_\text{ex} + \kappa_\text{in}} \tag{2.31}$$

The noise terms have the correlation functions

$$\langle\hat{a}_{\text{ext},j}(t)\hat{a}^\dagger_{\text{ext},j}(t')\rangle = \langle\hat{a}^\dagger_{\text{ext},j}(t)\hat{a}_{\text{ext},j}(t')\rangle + \delta(t-t') = (\bar{n}_{\text{ext},j}+1)\delta(t-t'), \tag{2.32a}$$

$$\langle\hat{a}_{\text{in},j}(t)\hat{a}^\dagger_{\text{in},j}(t')\rangle = \langle\hat{a}^\dagger_{\text{in},j}(t)\hat{a}_{\text{in},j}(t')\rangle + \delta(t-t') = (\bar{n}_{\text{in},j}+1)\delta(t-t') \tag{2.32b}$$

Together with the input-output relation $\hat{c}_\text{out} = \sqrt{\kappa_\text{ex,c}}\hat{c} - \hat{c}_{ex}$ with $\hat{c} = \hat{a}, \hat{b}$, it is possible to describe the system's coherent and noise response to a given input.

In the following table 2.1 we put some experimental constraints on the general relations introduced above depending on the type of coupled oscillators. Please note, that this is a high level comparison of the different interaction schemes exploited for devices within the scope of this thesis. It mainly underlines the fact that phonons are controlled and generated indirectly by optical and microwave fields [15], whereas an EO realization allows to excite directly both resonator modes by applying microwave and optical photon pump and probe fields.

The actual implementation, e.g. if one uses more than one mode of a single resonator such as in section 2.2.3, will additionally change the system equations from eq. 2.30. This will be discussed in detail for an OM and EM device (section 2.2.2.1) and for an EO interface (section 2.2.3).

Experimentally, we measure the coherent output fields $\hat{a}_\text{out}(t)$ and $\hat{b}_\text{out}(t)$ by extracting the quadrature voltages $I(t)$ and $Q(t)$ from the complex amplitude of the measured signal

---

[15] Nevertheless, precise control down to the quantum level has been shown for phonons using optomechanics for bulk modes and interdigitated transducers for surface acoustic waves including entanglement of mechanical oscillators [Palomaki et al., 2013; Riedinger et al., 2018; Wollack et al., 2022], deterministic generation and detection of single photons with qubits [Bienfait et al., 2019], and phononic beam splitters [Qiao et al., 2023] among others.

Table 2.1: **Various platforms for two coupled resonators.** Different experimental realizations are related to the general system equations 2.30 for two coupled harmonic oscillators.

	optomechanics	electromechanics	electrooptics
fields	optical & displacement	electrical & displacement	optical & electrical
pump α	optical	microwave	opt / mw
probe field $\hat{a}_{\text{ex}}$	optical	microwave	opt / mw
probe field $\hat{b}_{\text{ex}}$	/	/	mw / opt

$s = I(t)\cos\omega_{\text{IF}}t + Q(t)\sin\omega_{\text{IF}}t$ after analog downconversion to an intermediate frequency ω_{IF} of a few MHz [Eichler et al., 2012a].

The noise fluctuations of the modes $\hat{a}^\dagger_{\text{out}}(t)\hat{a}_{\text{out}}(t')$ and $\hat{b}^\dagger_{\text{out}}(t)\hat{b}_{\text{out}}(t')$ are related to the power spectral density according to the Wiener-Khinchin theorem. For a mode a, this reads as

$$\mathbf{S}_{\text{aa,out}}(\omega) = \int_{-\infty}^{\infty} \langle \hat{a}_{\text{out}}(t)\hat{a}_{\text{out}}(t')\rangle e^{-i\omega t}\, dt \tag{2.33}$$

as long as the process is stationary which in practice requires a constant drive power $\bar{n}_{\text{a}}$ and a constant temperature.

2.2.1 Characterization in Fourier space (steady-state)

In order to characterize a system we are often interested in the steady-state properties of the device. Relation 2.33 additionally motivates a characterization of the device in Fourier space for stationary processes. Lastly, the spectral view makes it easier to distinguish separate modes with different eigenfrequencies. Exploiting $\dot{c}(\omega) = -i\omega\, c(\omega)$ (cf. section 2.1) and writing the system in compact matrix form, one can solve the QLE (eq. 2.30) in Fourier space simply by matrix operations. A few useful quantities that can be calculated are

1. The mode operators, that is $\langle\hat{a}(\omega)\rangle$ and $\langle\hat{b}(\omega)\rangle$, and consequently the mean field amplitudes as a response to a certain input probe field $\mathbf{S}_{\text{in}}(\omega)$

$$\mathbf{S}(\omega) = \chi(\omega)\ \mathbf{B}\ \mathbf{S}_{\text{in}}(\omega) = \boldsymbol{\Upsilon}_0(\omega)\mathbf{S}_{\text{in}}(\omega) \tag{2.34}$$

2. the experimentally measurable output fields $\langle\hat{a}_{\text{out}}(\omega)\rangle, \langle\hat{b}_{\text{out}}(\omega)\rangle$ via the scattering matrix $\boldsymbol{\Upsilon}(\omega)$ relating system outputs to its inputs

$$\mathbf{S}_{\text{out}}(\omega) = \Big(\mathbf{C}\ \chi(\omega)\ \mathbf{B} - \mathbf{D}\Big)\mathbf{S}_{\text{in}}(\omega) = \boldsymbol{\Upsilon}(\omega)\mathbf{S}_{\text{in}}(\omega) \tag{2.35}$$

   In this description we assume that each resonator is reflectively coupled to a waveguide.

3. The noise occupation of various system modes $2\pi\,\mathbf{S}_{\text{SD}}(\omega)\delta(\omega-\omega') = \langle\mathbf{S}(\omega')^\dagger\mathbf{S}(\omega)\rangle$, i.e. $\langle\hat{a}^\dagger(\omega')\hat{a}(\omega)\rangle$ and $\langle\hat{b}^\dagger(\omega')\hat{b}(\omega)\rangle$

$$\mathbf{S}_{\text{SD}}(\omega) = \boldsymbol{\Upsilon}_0\boldsymbol{\Sigma}\boldsymbol{\Upsilon}_0^T. \tag{2.36}$$

4. the measurable output noise or output photon flux, e.g. $\langle \hat{a}^\dagger_{\mathrm{out}}(\omega')\hat{a}_{\mathrm{out}}(\omega)\rangle$ and $\langle \hat{b}^\dagger_{\mathrm{out}}(\omega')\hat{b}_{\mathrm{out}}(\omega)\rangle$

$$\mathbf{S}_{\mathsf{SD,out}}(\omega) = \mathbf{\Upsilon}\mathbf{\Sigma}\mathbf{\Upsilon}^T. \tag{2.37}$$

The equations are fully solved by the susceptibility $\chi = [-i\omega\mathbf{I} - \mathbf{A}]^{-1}$ together with the noise correlations in eq. 2.32. The mode operators are combined into $\mathbf{S} = [\hat{a}, \hat{b}, \hat{a}^\dagger, \hat{b}^\dagger]^T$, the applied input fields or input fluctuations are $\mathbf{S}_{\mathsf{in}} = [\hat{a}_{\mathsf{ex}}, \hat{a}_{\mathsf{in}}, \hat{b}_{\mathsf{ex}}, \hat{b}_{\mathsf{in}}, \hat{a}^\dagger_{\mathsf{ex}}, \hat{a}^\dagger_{\mathsf{in}}, \hat{b}^\dagger_{\mathsf{ex}}, \hat{b}^\dagger_{\mathsf{in}}]^T$, and the measurable output fields are $\mathbf{S}_{\mathsf{out}} = [\hat{a}_{\mathsf{out}}, \hat{b}_{\mathsf{out}}, \hat{a}^\dagger_{\mathsf{out}}, \hat{b}^\dagger_{\mathsf{out}}]^T$. The matrix $\mathbf{A}$ defines the coefficients of the mode operators from the coupled quantum Langevin equations 2.30, $\mathbf{B}$ defines the coupling rates of the input fields, $\mathbf{C}$ defines the coupling to the corresponding output fields and $\mathbf{D}$ accounts for the reflective coupling. The respective definitions using the enhanced coupling strength $G = G^* = g_0\sqrt{\bar{n}_{\mathrm{a}}}$ and colored coefficients for the beam-splitter and amplification interaction as defined in eq. 2.29 are

$$\mathbf{A} = \begin{bmatrix} -(\frac{\kappa_{\mathsf{a}}}{2} + i\Delta_{\mathsf{a}}) & -iG & 0 & -iG \\ -iG & -(\frac{\kappa_{\mathsf{b}}}{2} + i\omega_{\mathsf{b}}) & -iG & 0 \\ 0 & iG & -(\frac{\kappa_{\mathsf{a}}}{2} - i\Delta_{\mathsf{a}}) & iG \\ iG & 0 & iG & -(\frac{\kappa_{\mathsf{b}}}{2} - i\omega_{\mathsf{b}}) \end{bmatrix} \tag{2.38}$$

$$\mathbf{B} = \begin{bmatrix} \sqrt{\kappa_{\mathsf{ex,a}}} & \sqrt{\kappa_{\mathsf{in,a}}} & 0 & 0 & 0 & 0 & 0 & 0 \\ 0 & 0 & \sqrt{\kappa_{\mathsf{ex,b}}} & \sqrt{\kappa_{\mathsf{in,b}}} & 0 & 0 & 0 & 0 \\ 0 & 0 & 0 & 0 & \sqrt{\kappa_{\mathsf{ex,a}}} & \sqrt{\kappa_{\mathsf{in,a}}} & 0 & 0 \\ 0 & 0 & 0 & 0 & 0 & 0 & \sqrt{\kappa_{\mathsf{ex,b}}} & \sqrt{\kappa_{\mathsf{in,b}}} \end{bmatrix}, \tag{2.39}$$

$$\mathbf{C} = \begin{bmatrix} \sqrt{\kappa_{\mathsf{ex,a}}} & 0 & 0 & 0 \\ 0 & \sqrt{\kappa_{\mathsf{ex,b}}} & 0 & 0 \\ 0 & 0 & \sqrt{\kappa_{\mathsf{ex,a}}} & 0 \\ 0 & 0 & 0 & \sqrt{\kappa_{\mathsf{ex,b}}} \end{bmatrix}, \tag{2.40}$$

$$\mathbf{D} = \begin{bmatrix} 1 & 0 & 0 & 0 & 0 & 0 & 0 & 0 \\ 0 & 0 & 1 & 0 & 0 & 0 & 0 & 0 \\ 0 & 0 & 0 & 0 & 1 & 0 & 0 & 0 \\ 0 & 0 & 0 & 0 & 0 & 0 & 1 & 0 \end{bmatrix}, \tag{2.41}$$

The noise inputs for the different modes, i.e. the occupations of the internal baths as well as the external waveguides, are given in matrix form

$$\mathbf{\Sigma} = \begin{bmatrix} \mathbf{N} & 0 \\ 0 & \mathbf{N}+1 \end{bmatrix}. \tag{2.42}$$

with thermal occupation $\mathbf{N} = \mathrm{diag}[\bar{n}_{\mathsf{ex,a}}, \bar{n}_{\mathsf{in,a}}, \bar{n}_{\mathsf{ex,b}}, \bar{n}_{\mathsf{in,b}}]$.

2.2.2 Stationary response of an optomechanical and electromechanical device

In this section we investigate how the general case of two coupled oscillators eq. 2.30 is applied to a system that couples a mechanical mode to an electric and optical field respectively.

The aforementioned constraint of the herein used mechanical resonators is that they are not directly excited, i.e. $\kappa_{\mathrm{ex,b}} = 0$. The coupling of the mechanical oscillator to the internal bath is then typically represented by $\kappa_{\mathrm{in,b}} = \gamma_{\mathrm{m}}$ The mechanical oscillations impose frequency sidebands on the impinging microwave or optical pump. The magnitude of the sidebands allows to detect the state of a mechanical oscillator. That reduces the field inputs to $\mathbf{S}_{\text{in,om}} = [\hat{a}_{\text{ex}}, \hat{a}_{\text{in}}, \hat{b}_{\text{in}}, \hat{a}_{\text{ex}}^{\dagger}, \hat{a}_{\text{in}}^{\dagger}, \hat{b}_{\text{in}}^{\dagger}]^T$, the occupations to $\mathbf{N} = \text{diag}[\bar{n}_{\text{ex,a}}, \bar{n}_{\text{in,a}}, \bar{n}_{\text{in,b}}]$, and the matrices to

$$\mathbf{B} = \begin{bmatrix} \sqrt{\kappa_{\text{ex,a}}} & \sqrt{\kappa_{\text{in,a}}} & 0 & 0 & 0 & 0 & \\ 0 & 0 & \sqrt{\kappa_{\text{in,b}}} & 0 & 0 & 0 & \\ 0 & 0 & 0 & \sqrt{\kappa_{\text{ex,a}}} & \sqrt{\kappa_{\text{in,a}}} & 0 & \\ 0 & 0 & 0 & 0 & 0 & 0 & \sqrt{\kappa_{\text{in,b}}} \end{bmatrix}, \tag{2.43}$$

$$\mathbf{C} = \begin{bmatrix} \sqrt{\kappa_{\text{ex,a}}} & 0 & 0 & 0 \\ 0 & 0 & \sqrt{\kappa_{\text{ex,a}}} & 0 \end{bmatrix}, \tag{2.44}$$

$$\mathbf{D} = \begin{bmatrix} 1 & 0 & 0 & 0 & 0 & 0 \\ 0 & 0 & 0 & 1 & 0 & 0 \end{bmatrix}, \tag{2.45}$$

These equations apply to both our EM (cf. fig. 2.5) and OM (fig. 2.2) device. In the EM sample, however, the mechanical frequency is larger than the resonator linewidth ($\omega_{\mathrm{b}} > \kappa_{\mathrm{a}}$) and is therefore in the so-called *sideband-resolved regime*. This allows us to select the specific interaction type between the mechanical and microwave mode (2.29). Placing the microwave pump tone above $\Delta_{\mathrm{a}} \approx \omega_{\mathrm{b}}$ favors the amplification interaction that can create two-mode squeezed states between photons and phonons or amplify the signal from the mechanical oscillator (fig. 2.6a). A microwave pump detuned by the mechanical frequency below the microwave resonance $\Delta_{\mathrm{a}} \approx -\omega_{\mathrm{b}}$ enhances the beam-splitter interaction used for cooling of the microwave mode or coherent conversion between photons and phonons (fig. 2.6b). The off-resonant sideband with absolute detuning from the cavity by $2\omega_{\mathrm{b}}$ is suppressed by $(\frac{\kappa_{\mathrm{a}}}{4\omega_{\mathrm{b}}})^2$ [Andrews et al., 2014; Arnold et al., 2020] which results in a suppression of >99% in our EM device with $\kappa_{\mathrm{a,e}}/(2\pi)$ =2.7 MHz and $\omega_{\mathrm{b}}/(2\pi)$ =11.84 MHz. Consequently the respective coefficients in eq. 2.38 may be neglected which significantly simplifies the analytical solution of the QLE. In our OM device with $\frac{\kappa_{\mathrm{a}}}{4\omega_{\mathrm{b}}} \approx 34$ due to the broader optical linewidth of $\kappa_{\mathrm{a,o}}/(2\pi)$ =1.6 GHz both scattering processes need to be taken into account, as illustrated in fig. 2.6c.

2.2.2.1 Characterization of the optomechanical and electromechanical coupling strength

The interaction between phonons and photons allows to detect the mechanical occupation in a mechanical resonator if the scattering rates of the system are known. In turn, it is possible to calculate the coupling strength between both harmonic oscillators if the mechanical occupation is well-defined, e.g. by the precise knowledge of the sample temperature T_{s}. This results in a thermal occupation of mode b (the mechanical oscillator) of $\bar{n}_{\mathrm{in,b}} = 1/(e^{\hbar\omega_{\mathrm{b}}/(k_{\mathrm{B}}T_{\mathrm{s}})} - 1)$. Experimentally, we measure the output noise in the reflected microwave or optical signal

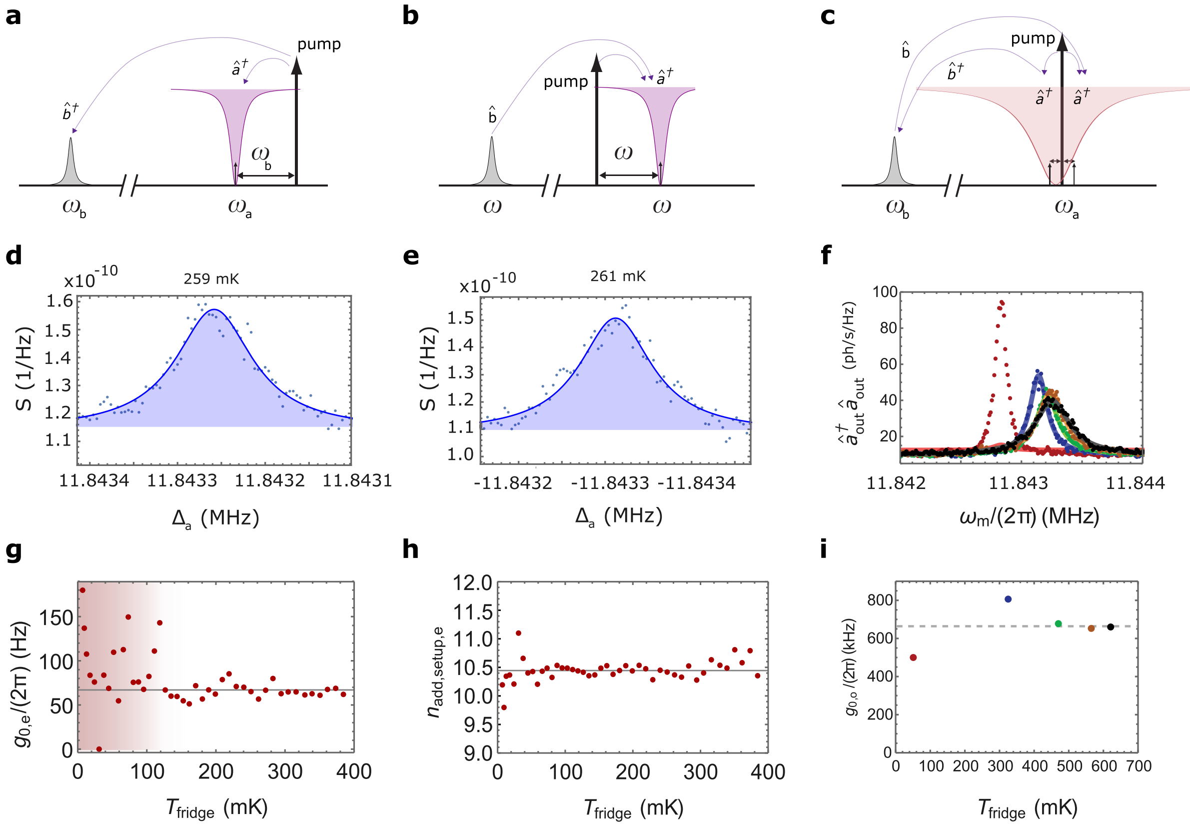

Figure 2.6: **EM and OM characterization** **a**, Amplification for a pump with detuning $\Delta_\mathrm{a} = \omega_\mathrm{pump} - \omega_\mathrm{a} = \omega_\mathrm{b}$ **b**, Beam splitter or 'cooling' interaction with $\Delta_\mathrm{a} = -\omega_\mathrm{b}$ **c**, Interaction scheme of our OM system with the pump on resonance. Both scattering processes occur for a non-sideband-resolved system, that is $\omega_\mathrm{b} \ll \kappa_\mathrm{a}$ **d,e** The sideband strengths relative to the pump for the two pump configurations in a) and b) are equal for a microwave pump with low photon number and, thus, low cooperativity $g_{0,\mathrm{e}}^2 \bar{n}_\mathrm{a} \ll \kappa_\mathrm{a}\kappa_\mathrm{b}$. This is the appropriate regime for our characterization of the coupling strength via a temperature sweep. Fits are to eq. 2.46 **f** Optical output noise for various temperatures. Fits are from numerical simulations of the quantum Langevin equations. **g** Extracted single photon EM coupling rate $g_{0,\mathrm{e}}$ for various fridge temperatures. When the sample is not thermalized to the environment, the method breaks down (red shaded area). **h** System noise added by the microwave measurement chain determined from the background offset for various temperatures. **i** Extracted single photon OM coupling rate $g_{0,\mathrm{o}}$ for various fridge temperatures. Again, the method relies on a well-defined mechanical mode occupation and therefore good thermalization of the sample to the environment. Panels f-i adapted from [Arnold et al., 2020]

$a^\dagger_\mathrm{out}(\omega)a_\mathrm{out}(\omega')$ after the detection chain, sweep the temperature of the sample stage in our dilution refridgerator and assume that the sample is thermalized to it, i.e. $T_\mathrm{s} = T_\mathrm{fridge}$.[16]

Electromechanical device If the scattering rate and the cooperativity defined as $C := 4g_0^2\bar{n}_\mathrm{a}/(\kappa_\mathrm{a}\kappa_\mathrm{b})$ is low, that is $C \ll 1$, the noise peaks have a similar magnitude for both sideband processes at pump detunings $\Delta_\mathrm{a} = \pm\omega_\mathrm{b}$. The normalized noise power spectrum

---

[16] Experimentally, it is therefore crucial to wait until refrigerator and sample have reached a stable temperature after a new setpoint in the temperature sweep. Empirically, this is accomplished after 30-60 minutes, whereas lower temperatures need more waiting time.

$S_{0,\mathrm{a}}(\omega)$ reduces to

$$S_{0,\mathrm{a}}(\omega) = \frac{S_\mathrm{a}}{P_\mathrm{r}} = \mathcal{A} + \frac{64 n_\mathrm{m} \kappa_{\mathrm{ex,a}}^2 \gamma_\mathrm{m} g_{0,\mathrm{a}}^2}{(4\Delta_\mathrm{a}^2 + (\kappa_\mathrm{a} - 2\kappa_{\mathrm{ex,a}})^2)(\kappa_\mathrm{a}^2 + 4(\Delta_\mathrm{a} - \omega)^2)(\gamma_\mathrm{m}^2 + 4(\omega_\mathrm{m} - \omega)^2)}. \tag{2.46}$$

A detailed derivation can be found in [Fink et al., 2016]. The measured spectrum $S_\mathrm{e}(\omega)$ is normalized to the reflected microwave pump power P_r. This removes the measurement chain dependence because the sideband spectrum and the reflected pump both are amplified by the same output gain assuming that the gain is constant over the frequency range $2\omega_b$. If we are now able to quantify the mechanical occupation n_m, we can extract the EM single-photon coupling strength g_0 from eq. (2.46) since all other parameters can be measured and derived independently.

Fig. 2.6d (e) shows the normalized noise spectrum at the Stokes (Anti-stokes) sideband for a pump detuning of $\Delta_\mathrm{a} = \omega_\mathrm{b}$ ($\Delta_\mathrm{a} = -\omega_\mathrm{b}$). As expected for the low cooperativity regime, the sideband noise peaks show a similar height. The slightly higher amplitude for $\Delta_\mathrm{a} = -\omega_\mathrm{b}$ can be attributed to a small amount of parametric gain that is observable also at low cooperativities. Calculating the single photon coupling strength from eq. 2.46 yields an average of $\bar{g}_{0,\mathrm{e}}/(2\pi) = 67\,\mathrm{Hz}$ for environmental temperatures above $120\,\mathrm{mK}$ with a further reduced scattering of the derived values at high thermal occupations above $300\,\mathrm{mK}$ (fig. 2.6g). At low temperatures the extracted values vary because the assumption $T_\mathrm{s} = T_\mathrm{fridge}$ is not fulfilled. Additionally, a strong variance in the noise response for low cooperativities and low temperatures has been reported before [Wollman et al., 2015]. We observe that this vanishes for stronger pump powers (higher cooperativities) or higher temperatures.

The background $\mathcal{A}$ allows to calculate the equivalent added noise or measurement efficiency of the detection chain by [Fink et al., 2016; Arnold et al., 2020]

$$\mathcal{A} = (1/2 + n_{\mathrm{add,setup}}) \frac{4\kappa_{\mathrm{ex,a}}}{\bar{n}_\mathrm{a}(4\Delta_\mathrm{a}^2 + (\kappa_\mathrm{a} - 2\kappa_{\mathrm{ex,a}})^2)}. \tag{2.47}$$

Fig. 2.6h yields 10.4 added noise photons for temperatures above $120\,\mathrm{mK}$ and a measurement efficiency of $\eta = 1/n_{\mathrm{add,setup}} = 0.096$. [17] As a last comment, one needs to state that eq. 2.47 requires the precise knowledge of the intra-cavity photon number of the pump $\bar{n}_\mathrm{a}$. With the knowledge of $g_{0,\mathrm{e}}$, a coherent probe measurement for a detuning $\Delta_\mathrm{a} = -\omega_\mathrm{b}$ and a fit of the arising electromagnetically-induced transparency window [Safavi-Naeini et al., 2011] is an excellent method to determine the intrinsic mechanical linewidth κ_b at low drive powers and the attenuation at higher drive power (cooperativities).

Optomechanical device In case of the OM device we again measure the power spectral density for several fridge temperatures and make the assumptions that the sample and specifically the mechanical resonator is thermalized to the fridge temperature. The independently calibrated optical measurement gain allows to convert the measured power spectral density to the number of output photons $\hat{a}_{out}^\dagger \hat{a}_{out}(\omega)$ which can be directly fitted to the quantum Langevin equations of motion (fig. 2.6f). Since the OM devices is not in the sideband resolved regime because the optical linewidth is much larger than the mechanical frequency, eq. 2.46 is not valid and we use the full interaction described by the matrices 2.38 and 2.39-2.41 for these fits. Independent knowledge of the optical and mechanical resonator parameters

---

[17] If one includes the heterodyne detection that necessarily adds noise becuase of the measurement of both conjugate quadratures the measurement efficiency reduces to $\eta = 1/(1/2 + n_{\mathrm{add,setup}})$ [Delaney et al., 2022]

allows to extract the OM single-photon couping rate for various temperatures (fig. 2.6i) and yields $g_{0,\mathrm{o}}/(2\pi) = 660\,\mathrm{kHz}$. Similar to the EM coupling rate (cf. fig. 2.6g) the extracted OM coupling strength is not reliable at lower temperatures. Even though optical and electrical resonator are coupled to the same mechanical resonator, $g_{0,\mathrm{o}}$ converges only above $400\,\mathrm{mK}$ and thereby at even higher temperatures than the EM coupling rate ($>120\,\mathrm{mK}$). We attribute this to additional heating introduced by the optical pump, a behavior that is described in detail in section 3.5.

2.2.2.2 Origin of the electromechanical and optomechanical coupling strength

Electromechanical device In the design we introduced above (cf. fig. 2.5), we realize such a coupling between a planar microwave resonator and a mechanical resonator. The displacement from the mechanical oscillations modifies the capacitance and thereby creates a coupling between both resonators. We increased this effect by using a tuning fork geometry for the mechanical resonator that allows us to constructively modulate two parallel capacitors by one mechanical resonator.
The coupling strength between them or single-photon EM coupling rate $g_{0,\mathrm{e}} = 2x_{\mathrm{zpf}}g_{\mathrm{em}}$[18] is composed of the zero-point amplitude of the mechanical displacement $x_{\mathrm{zpf}} = \sqrt{\hbar/(2m_{\mathrm{eff}}\omega_{\mathrm{m}})}$ and the microwave frequency shift per displacement g_{em} [Fink et al., 2016]. x_{zpf} determines the amplitude of the quantum fluctuations of the displacement field as a consequence of Heisenberg's uncertainty principle and, thus, in absence of any classical, thermal excitation. In order to increase this amplitude, it is required to reduce the effective mass or motional mass m_{eff} which is the mass of the oscillator weighted by its displacement. In practice, we achieve that by reducing the volume of our resonator to strings of a few $\mathrm{\mu m}$ length, only $\sim 100\,\mathrm{nm}$ width and $220\,\mathrm{nm}$ thickness. This results in a motional mass of only $1.3\,\mathrm{pg}$ and a zero-point amplitude of the mechanical displacement of $24.5\,\mathrm{fm}$.
The induced frequency shift per displacement is defined as [Arnold et al., 2020]

$$g_{\mathrm{em}} = -\eta \frac{\omega_{\mathrm{e}}}{2}\frac{1}{2C_{\mathrm{m}}}\frac{\partial C}{\partial u} = -\frac{2C_{\mathrm{m}}}{2C_{\mathrm{m}} + C_{\mathrm{s}}}\frac{\omega_{\mathrm{e}}}{2}\frac{1}{2C_{\mathrm{m}}}\frac{\partial C}{\partial u}, \tag{2.48}$$

The first part marks the electrical participation ratio $\eta = \frac{2C_{\mathrm{m}}}{2C_{\mathrm{m}}+C_{\mathrm{s}}}$. It represents the fraction of the modulated capacitance with respect to the total capacitance of the circuit. Consequently, the stray capacitance C_{s} needs to be minimized to enhance the EM coupling. The last term describes the change in the capacitance by a normalized displacement u. For a parallel plate capacitor $\frac{1}{C_{\mathrm{m}}}\frac{\partial C}{\partial u}$ reduces to $1/d$ with the nominal gap size d. For a real device the ratio $\frac{\partial C}{\partial u}$ is derived from numerical simulations calculating the effect of a shift of a dielectric boundary. [Johnson et al., 2002] derive the effect of small pertubations from a moving dielectric boundary on eigensolutions of Maxwell equations $E^{(0)}$

$$\frac{\partial C}{\partial u} = \frac{\left\langle E^{(0)}\middle|\Delta\epsilon\middle|E^{(0)}\right\rangle}{\langle E^{(0)}|\epsilon|E^{(0)}\rangle} = \frac{\oint_S \mathbf{U}\cdot\mathbf{n}(\Delta\epsilon\mathbf{E}_{||}^2 - \Delta(\epsilon^{-1})\mathbf{D}_{\perp}^2)\,dS}{\int_V \mathbf{E}\cdot\mathbf{D}\,dV} \tag{2.49}$$

$\mathbf{U}\cdot\mathbf{n}$ is the component of the displacement field, which is perpendicular to the surface, i.e. multiplied by the normal vector of the surface. It is also normalized by the maximum displacement $\mathbf{U} = \tilde{\mathbf{U}}/\max|\tilde{\mathbf{U}}|$. $\mathbf{E}_{||}$ is the electric field component parallel to the surface and

---

[18] The factor of 2 stems from the fact that we use two mechanically compliant capacitors in parallel.

$\mathbf{D}_\perp$ is the perpendicular electric displacement field. $\Delta\epsilon = \epsilon_1 - \epsilon_2$ and $\Delta(\epsilon^{-1}) = \epsilon_1^{-1} - \epsilon_2^{-1}$ are defined by the different dielectric functions of the two materials on each side of the boundary. As our capacitor comprises a silicon string with metal electrodes on top (cf. fig. 2.5), we have to calculate eq. 2.2.2.2 for the silicon-air and metal-air interface.
Interestingly, the simulated moving boundary contribution to the EM coupling of the silicon-air interface is larger than for the actual metal-air interface in the nano-gap capacitor. The reason is that the electric field between the two electrodes extends to the silicon gap and the dielectric function of silicon is relatively high. The larger fraction of silicon $(220\,\mathrm{nm})$ on the gap surface compared to aluminum $(60\,\mathrm{nm})$ outweighs the slightly weaker electric field and smaller dielectric function (in simulations we use $\epsilon_{\mathrm{al}} = 10^{12}$). As a consequence, we refrained from angled evaporation of aluminum to create vacuum gap capacitors [Zemlicka et al., 2023] where the gap is completely covered by aluminum. Since 1) angled evaporation decreases the reliability of fabrication ultra-narrow gap capacitors without creating short circuits 2) the silicon also significantly contributes to the moving boundary effect creating the EM coupling, 3) the EM coupling rate depends strongly on the gap size with $g_{0,\mathrm{e}} \propto d^{-1.5}$ and 4) the fabrication of the device was already extensive and comprised six layers, we decided to rather aim for smallest possible gap sizes $<70\,\mathrm{nm}$ with high yield.

Optomechanical device The OM cavity comprising the optical resonator in fig. 2.2 and the mechanical mode in fig. 2.5d reveals a single-photon OM coupling strength of $g_{0,\mathrm{o}} = 660\,\mathrm{kHz}$ as shown in paragraph Optomechanical device . The main origin of the coupling between optical and mechanical field for this specific design is - as for the EM device above (paragraph Electromechanical device) - the shifting silicon-air boundary as a consequence of the mechanical motion [Johnson et al., 2002]. Thus, the frequency shift of the optical cavity per unit displacement g_{om} takes a very similar form as in eq. 2.2.2.2

$$g_{\mathrm{om}} = \frac{\partial\omega_{0,\mathrm{o}}}{\partial u} = -\frac{\omega_{\mathrm{o}}}{2}\frac{\oint_S \mathbf{U}\cdot\mathbf{n}(\Delta\epsilon\mathbf{E}_{\|}^2 - \Delta(\epsilon^{-1})\mathbf{D}_{\perp}^2)\,dS}{\int_V \mathbf{E}\cdot\mathbf{D}\,dV} \tag{2.50}$$

and the single-photon OM coupling strength can be calculated as $g_{0,\mathrm{o}} = x_{\mathrm{zpf}}g_{\mathrm{om}} = g_{\mathrm{om}}\sqrt{\frac{\hbar}{2m_{\mathrm{eff}}\omega_{\mathrm{m}}}}$.
In silicon with its high refractive index a significant contribution to the OM coupling often originates from the photoelastic effect, which scales with the fourth power of the refractive index. This mechanical mode, however, is spread across the device and does not induce a significant localized deformation such as a $\sim\mathrm{GHz}$ breathing mode [Chan et al., 2012]. Thus, the photoelastic effect for this device is more than three orders of magnitude smaller than the moving boundary contribution to the OM coupling rate.

2.2.3 Dynamic response of an electrooptic device

Besides the mechanical systems described above in 2.2.1, we also worked with an EO device that couples directly microwave and optical fields by the Pockels effect where an electric field influences the refractive index of the optical mode. As the Pockels effect is a second order $(\chi^{(2)})$ nonlinearity, it requires a non-centrosymmetric crystal as the used Z-cut $\mathrm{LiNbO_3}$. The device comprises an optical (2.1.1.2) and microwave (2.1.2.2) whispering gallery mode (WGM) with a maximized field overlap between optical and electrical field. This is achieved by using the EO $\mathrm{LiNbO_3}$ as a dielectric in the capacitor of the microwave cavity as well as the dielectric medium that hosts the optical mode. The electro-optic coupling constant for a three wave-mixing process involving a strong pump, an optical and an electrical mode can be generally written as

$$g_{0,\mathrm{eo}} = 2\epsilon_0 \chi^{(0)} \sqrt{\frac{\hbar\omega_1\omega_2\omega_3}{8\epsilon_1\epsilon_2\epsilon_3 V_1 V_2 V_3}} \int_V \psi_1 \psi_2^\dagger \psi_3^\dagger \, dV \tag{2.51}$$

with ψ_i as the spatial mode distribution of mode $\hat{a}_\mathrm{i}$ with frequency ω_i, and V_i is the effective volume with dielectric function ϵ_i. A detailed description of the device and the EO coupling can be found in [Rueda Sanchez, 2018; Hease et al., 2020; Sahu et al., 2023].

Comparing the OM and EM model in fig. 2.6a-c) with the model of the EO device in fig. 2.7a), the first conspicuous difference is the occurrence of several identical optical modes separated by $\nu_\mathrm{FSR} = \omega_\mathrm{b}$. The Stokes and Antistokes sideband scatter to distinct optical modes at frequency ω_s and ω_as respectively.
Fundamentally, however, it still comprises two coupled harmonic oscillators. Under a strong coherent pump tone on mode $\hat{a}$ the interaction Hamiltonian between the microwave field $\hat{b}$ and the two sideband modes $\hat{a_\mathrm{s}}$ and $\hat{a_\mathrm{as}}$ has the same form as in eq. 2.29 with colors highlighting again the amplification and beamsplitter interaction:

$$H_\mathrm{int} \simeq \hbar g_0 \sqrt{\bar{n}_\mathrm{a}} (\underbrace{\hat{a}_\mathrm{s}{}^\dagger \hat{b}^\dagger + \hat{a}_\mathrm{s}\hat{b}}_{\text{amplification}} + \underbrace{\hat{a}_\mathrm{as}^\dagger \hat{b} + \hat{a}_\mathrm{as}\hat{b}^\dagger}_{\text{beamsplitter}}) \tag{2.52}$$

Nevertheless, as the sidebands of the pump are now different resonator modes as well, we write the quantum Langevin equations as [Sahu et al., 2022]

$$\frac{d}{dt}\hat{a}(t) = \left(i\Delta_\mathrm{a} - \frac{\kappa_\mathrm{a}}{2}\right)\hat{a}(t) - ig_0\left(\hat{b}^\dagger \hat{a}_\mathrm{as} + \hat{a}_\mathrm{s}\hat{b}\right) + \sqrt{\kappa_\mathrm{ex,a}}(\lambda\bar{\xi}_\mathrm{a} + \hat{a}_{ex}) + \sqrt{\kappa_\mathrm{in,a}}\hat{a}_{in} \tag{2.53a}$$

$$\frac{d}{dt}\hat{a}_\mathrm{as}(t) = \left(i\Delta_\mathrm{as} - \frac{\kappa_\mathrm{as}}{2}\right)\hat{a}_\mathrm{as}(t) - ig_0\hat{a}^\dagger\hat{b} + \sqrt{\kappa_\mathrm{ex,as}}(\lambda\bar{\xi}_\mathrm{as} + \hat{a}_\mathrm{as,ex}) + \sqrt{\kappa_\mathrm{in,as}}\hat{a}_\mathrm{as,in} \tag{2.53b}$$

$$\frac{d}{dt}\hat{a}_\mathrm{s}(t) = \left(i\Delta_\mathrm{as} - \frac{\kappa_\mathrm{s}}{2}\right)\hat{a}_\mathrm{s}(t) - ig_0\hat{a}\hat{b}^\dagger + \sqrt{\kappa_\mathrm{ex,s}}(\bar{\alpha}_\mathrm{s} + \hat{a}_\mathrm{s,ex}) + \sqrt{\kappa_\mathrm{in,s}}\hat{a}_\mathrm{s,in} \tag{2.53c}$$

$$\frac{d}{dt}\hat{b}(t) = \left(i\Delta_\mathrm{b} - \frac{\kappa_\mathrm{b}}{2}\right)\hat{b}(t) - ig_0\left(\hat{a}\hat{a}_\mathrm{s}^\dagger + \hat{a}^\dagger\hat{a}_\mathrm{as}\right) + \sqrt{\kappa_\mathrm{ex,b}}(\bar{\xi}_\mathrm{b} + \hat{b}_{ex}) + \sqrt{\kappa_\mathrm{in,b}}\hat{b}_{in} \tag{2.53d}$$

We adjusted the standard equations of motion to achieve the best possible description of our device:

- λ is the mode matching factor that accounts for the non-perfect mode overlap between the optical mode in the fiber and the mode in the WGM. It is an additional loss factor to the actual coupling efficiency between fiber and resonator $\eta_j = \kappa_{\mathrm{ex},j}/\kappa_j$. This mode factor is not included in the microwave description.

- We used this device for conversion between microwave and optical fields using the beam splitter interaction. Thus, the applied coherent fields $\hat{\xi}_\mathrm{a}, \hat{\xi}_\mathrm{as}$ and $\hat{\xi}_\mathrm{b}$ correspond to the optical pump and the two signals to convert the anti-Stokes sideband mode and the microwave resonator mode. The amplitude of the coherent input field is given by the square root of the photon input flux $|\hat{\xi}_j| = \sqrt{P_{\mathrm{in}/(\hbar\omega_j)}}$

- While in [Sahu et al., 2022] the unwanted Stokes process was suppressed by strongly coupling the Stokes sideband to a fifth mode of different polarization to allow for conversion in the quantum regime, we did not have this constraint because we converted a coherent signal from a superconducting qubit-cavity system (section 4).
- While we changed to a frame rotating with the drive frequency in the OM case and the only important detuning was the frequency difference between drive and the resonator mode Δ_a, here we introduce several detunings:
    1. the detuning between the optical pump and its resonator mode $\Delta_\mathrm{a} = \omega_{\xi_\mathrm{a}} - \omega_\mathrm{a}$,
    2. the detuning between the anti-Stokes sideband mode and the upper optical sideband signal$\Delta_\mathrm{as} = \omega_{\xi_\mathrm{a}} + \omega_{\xi_\mathrm{b}} - \omega_\mathrm{as}$
    3. the detuning between the Stokes sideband mode and the lower optical sideband signal$\Delta_\mathrm{s} = \omega_{\xi_\mathrm{a}} - \omega_{\xi_\mathrm{b}} - \omega_\mathrm{s}$
    4. the detuning between the microwave tone and the microwave mode $\Delta_\mathrm{b} = \omega_{\xi_\mathrm{b}} - \omega_\mathrm{b}$

  ω_{ξ_a} and ω_{ξ_b} are the frequencies of the optical pump and microwave source respectively. The latter is either used to send a microwave signal to mode $\hat{b}$ or to create a sideband of the optical pump used as an optical signal with $\omega_{\xi_\mathrm{as}} = \omega_{\xi_\mathrm{a}} + \omega_{\xi_\mathrm{b}}$ or $\omega_{\xi_\mathrm{s}} = \omega_{\xi_\mathrm{a}} - \omega_{\xi_\mathrm{b}}$

The noise terms have again the correlation functions

$$\langle \hat{a}_{\mathsf{ext},j}(t)\hat{a}^\dagger_{\mathsf{ext},j}(t')\rangle = \langle \hat{a}^\dagger_{\mathsf{ext},j}(t)\hat{a}_{\mathsf{ext},j}(t')\rangle + \delta(t-t') = (\bar{n}_{\mathsf{ext},j}+1)\delta(t-t'), \tag{2.54a}$$

$$\langle \hat{a}_{\mathsf{in},j}(t)\hat{a}^\dagger_{\mathsf{in},j}(t')\rangle = \langle \hat{a}^\dagger_{\mathsf{in},j}(t)\hat{a}_{\mathsf{in},j}(t')\rangle + \delta(t-t') = (\bar{n}_{\mathsf{in},j}+1)\delta(t-t') \tag{2.54b}$$

As we used the electro-optic device in the classical limit for the conversion of coherent signals, we may simplify eq. 2.53 after the linearization of the external input fields $\hat{a}_j \to \bar{\alpha}_j + \hat{a}_j$ for $j = as, s$ and $\hat{b} \to \bar{\beta} + \hat{b}$

$$\frac{d}{dt}\bar{\alpha}(t) = \left(i\Delta_\mathrm{a} - \frac{\kappa_\mathrm{a}}{2}\right)\bar{\alpha}(t) - ig_0\left(\bar{\beta}^*\bar{\alpha}_\mathrm{as} + \bar{\alpha}_\mathrm{s}\bar{\beta}\right) + \sqrt{\kappa_\mathrm{ex,a}}\lambda\bar{\xi}_\mathrm{a} \tag{2.55a}$$

$$\frac{d}{dt}\bar{\alpha}_\mathrm{as}(t) = \left(i\Delta_\mathrm{as} - \frac{\kappa_\mathrm{as}}{2}\right)\bar{\alpha}_\mathrm{as}(t) - ig_0\bar{\alpha}\,\bar{\beta} + \sqrt{\kappa_\mathrm{ex,as}}\lambda\bar{\xi}_\mathrm{as} \tag{2.55b}$$

$$\frac{d}{dt}\bar{\alpha}_\mathrm{s}(t) = \left(i\Delta_\mathrm{as} - \frac{\kappa_\mathrm{s}}{2}\right)\bar{\alpha}_\mathrm{s}(t) - ig_0\bar{\alpha}\bar{\beta} \tag{2.55c}$$

$$\frac{d}{dt}\bar{\beta}(t) = \left(i\Delta_\mathrm{b} - \frac{\kappa_\mathrm{b}}{2}\right)\bar{\beta}(t) - ig_0\left(\bar{\alpha}^*\bar{\alpha}_\mathrm{as} + \bar{\alpha}\hat{\alpha}^*_\mathrm{s}\right) + \sqrt{\kappa_\mathrm{ex,b}}\bar{\xi}_\mathrm{b} \tag{2.55d}$$

If all resonators are coupled reflectively the output fields are calculated by $\bar{a}_{\mathrm{out},j}(t) = \sqrt{\kappa_\mathrm{ex,j}}\lambda\bar{a}_j - \xi_j(t)$ and $\bar{b}_\mathrm{out} = \sqrt{\kappa_\mathrm{ex,b}}\bar{b} - \xi_b$ for microwave and optical mode respectively. These equations can be numerically integrated to model the system response to various input field. Inserting the measured microwave input pulse to the microwave resonator mode (fig. 2.7b) in eq. (2.55)d, the reflected microwave pulse shape can be accurately predicted (gray line in fig. 2.7c). If an additional optical pump is sent simultaneously to the optical resonator (fig. 2.7c), the induced parametric enhancement of the beamsplitter interaction in eq.2.52 converts a considerable fraction of the microwave input photons to the optical domain. The converted signal at the anti-Stokes sideband $|\bar{a}_\mathrm{out,as}|^2(t)$ (fig. 2.7e) depends on the microwave input signal and the optical pump alike.

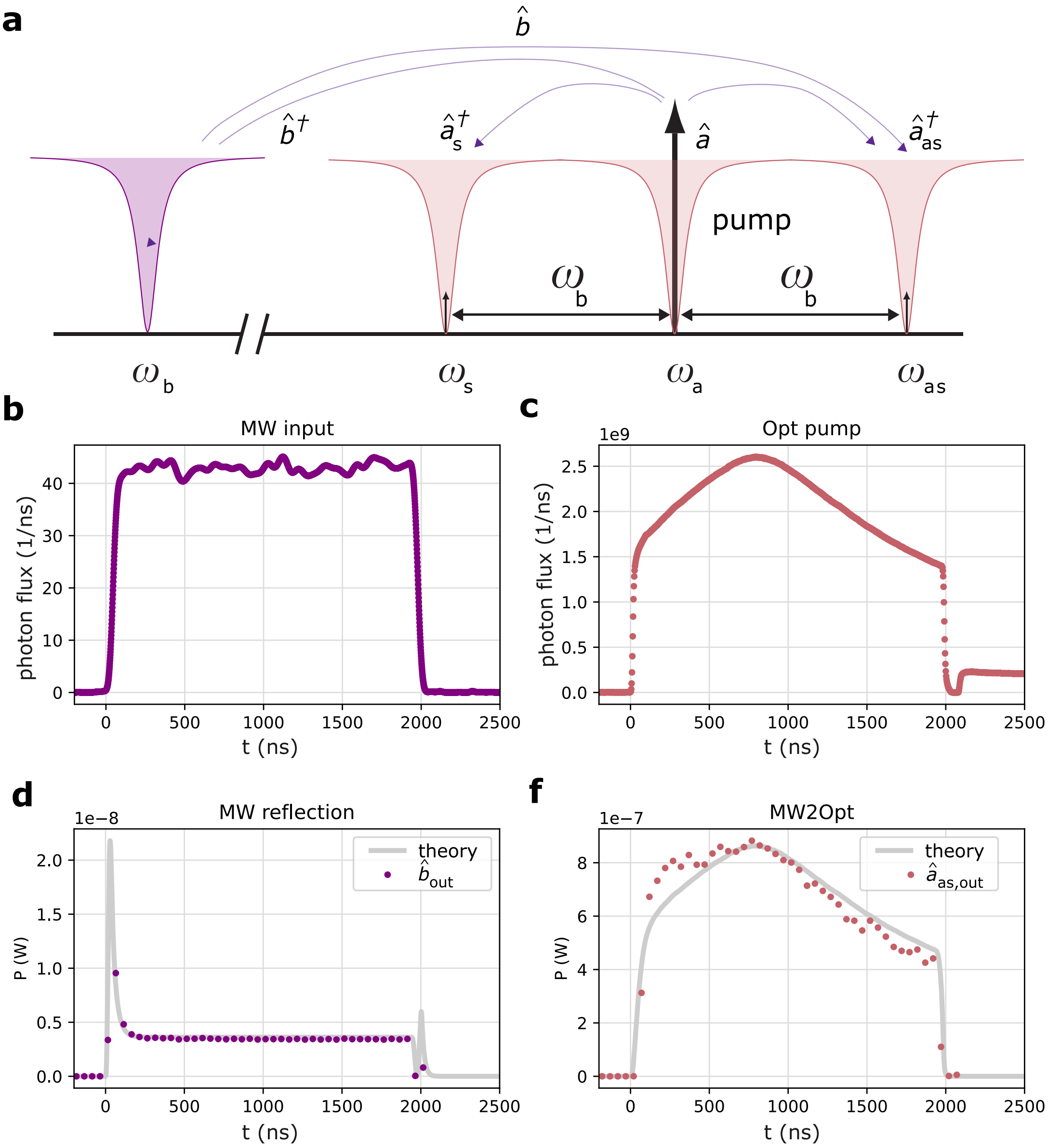

Figure 2.7: **Electrooptic device a**, EO model with a pump mode $\hat{a}$, the (anti-)Stokes sideband $\hat{a_{\rm a}}$ ($\hat{a_{\rm as}}$) and the microwave mode $\hat{b}$. The amplification three-wave-mixing process $\hat{b}^\dagger\,\hat{a}\,\hat{a}_{\rm s}^\dagger$ and the beamsplitter process $\hat{b}\,\hat{a}\,\hat{a}_{\rm as}^\dagger$ are indicated by arrows. One of the parametric processes can be suppressed by a split mode [Sahu et al., 2022] or detuned optical pump [Rueda Sanchez, 2018]. **b** Measured microwave pulse sent to mode $\hat{b}$. **c** Optical pump sent to mode $\hat{b}$. **d** Microwave reflection $|b_{\rm out}|^2$ according to eq. 2.55d. **e** Optical output of the converted microwave signal reflection $|a_{\rm out,as}|^2$ according to eq. 2.55b. Panels d,e are adjusted from [Arnold et al., 2023].

2.3 From weak to strong coupling

In the considerations above we discussed a regime where the linearized interaction Hamiltonian 2.28 between two bosonic modes can sufficiently describe the physical system, i.e. by quadratic interactions such as $\delta\hat{a}\hat{b}$ or $\delta\hat{a}^\dagger\hat{b}$. This applies as long as a strong pump parametrically enhances the interaction between the two modes, and fluctuations of the fields are small compared to the pump, and the interaction rate is much weaker than the loss rates in the system. If the drive power is strong enough, that is, $g_0\sqrt{n_{\rm d}} > \kappa_{\rm i}$, one enters the strong-coupling regime between the two oscillators. At these interaction strengths the amplification process or

Stokes scattering would be beyond the stability criterion. Thus, the only stable interaction is given by anti-Stokes scattering process used for coherent conversion and sideband cooling. In the strong-coupling regime, the fact that the rate of interaction exceeds the decay rates of the system leads to *normal-mode splitting*. The Anti-Stokes peak hybridizes to two split eigenmodes resulting from the fluctuations of the pump field $\hat{a}$ and the second resonator $\hat{b}$ [Aspelmeyer et al., 2014]. This has been achieved in EM [Teufel et al., 2011a] by microwave photon enhanced coupling and static electric field enhancement [Bozkurt et al., 2023], in EO for optical pumps [Sahu et al., 2022] and microwave pumps [Rueda et al., 2019; Hease et al., 2020], and OM devices using optical drives [Thompson et al., 2008; Gröblacher et al., 2009; Verhagen et al., 2012], partly with the more stringent requirement of $g_0\sqrt{n_\mathrm{d}} > \kappa_\mathrm{i}\bar{n}_\mathrm{i,th}$. In this regime coherent conversion of fragile quantum states is possible because the mutual exchange between the two modes exceeds the infiltration of thermal noise with rate $\kappa_\mathrm{i}\bar{n}_\mathrm{i,th}$, i.e. the so-called thermal decoherence rate with mean thermal occupation $\bar{n}_\mathrm{i,th}$.
A substantially more challenging regime is the regime of single-photon strong coupling with $g_0 > \kappa_\mathrm{i}$. Normal-mode splitting is observed here without the parametric enhancement of the coupling by a strong drive. In fact, a single photon entering a resonator shifts the equilibrium of the second resonator by more than its linewidth. Thus, single excitations can be resolved and phenomena such as photon-blockade become visible [Rabl, 2011]. Additionally, the non-linearity in the interaction allows for the creation of non-Gaussian states from a Gaussian input, a task that is of high relevance for quantum communication and computing. Although this regime is currently out-of-reach, non-classical states can still be produced in the linearized interaction regime. First, externally created non-classical states can be used as an input state to the OM, EO or EM device [Reed et al., 2017; Ma et al., 2021]. On the other hand, measurement based protocols are a well-investigated way to create non-classical states in a probabilistic manner via single photon detectors [Riedinger et al., 2018]. In linear optics, the application of single-photon sources and single-photon detectors serves a similar purpose [Aspelmeyer et al., 2014].
In contrast, a superconducting qubit is an anharmonic oscillator and an exciting pulse addresses only a single transitions if the pulse is longer than the inverse of the anharmonicity. Therefore, quantum states or Fock state excitations are instrinic to these devices. Additionally, superconducting qubits and microwave resonator are coupled systems that are routinely operating in the single photon strong-coupling regime [Wallraff et al., 2004], allowing to exploit the nonlinearity of the qubit to generate a Fock state in the harmonic microwave resonator. Thus, this system offers the full spectrum of desired possibilities mentioned above.

In the next chapter, we quickly introduce the model of such a coupled qubit-resonator system and characterize the specific device used for the experiments demonstrated in chapter 4.

2.4 Strong coupling between a harmonic and a nonlinear oscillator - qubit-cavity interaction

Superconducting circuits have emerged as a promising platform for realizing qubits, the essential components of quantum processors. The superconductivity provides a dissipation-free system, and a superconducting nonlinear oscillator establishes the quasi-two-level-nature presenting the two basic states of the qubit. The nonlinearity of these circuits is a consequence of a Josephson tunnel junction (JJ) consisting of a thin ($\sim \mathcal{O}(1\,\mathrm{nm})$) insulating layer between two superconducting electrodes. Cooper pairs in the superconductor can tunnel across the JJ without fundamental dissipation. The voltage drop across the junction is related to the change in supercurrent [19]

$$V = \frac{\Phi_0}{2\pi I_\mathrm{c} \cos\phi} \frac{dI}{dt} \tag{2.56}$$

with $\Phi_0 = h/2e$ as the superconducting flux quantum and I_c the critical current above which the JJ is not free of dissipation. The similarity in eq. 2.56 to an inductor $V = L\frac{dI}{dt}$ leads to the widely used description of the JJ as a nonlinear inductor, even though a JJ does not create a magnetic field when the supercurrent passes through it. Instead, the energy depending on the phase difference ϕ between the two superconducting electrodes

$$E(\phi) = -\frac{\Phi_0 I_\mathrm{c}}{2\pi} \cos\phi = -E_\mathrm{j} \cos\phi \tag{2.57}$$

is stored inside the JJ. The second decisive parameter besides E_j is the charging energy

$$E_\mathrm{c} = \frac{e^2}{2C_{\sum}} \tag{2.58}$$

with the elementary charge e and the circuit capacitance. Both parameters can be widely controlled by the circuit and physical JJ geometry.

2.4.1 The transmon regime

In our experiments we used a transmission line shunted plasma oscillation qubit (Transmon), where the JJ is shunted by a large capacitor. This reduces the charging energy to ratios $E_\mathrm{j}/E_\mathrm{c} \geq 50$. The energy dispersion with respect to the number of charges for low lying energy levels becomes flat and, hence, the sensitivity to charge noise is decreased [Koch et al., 2007; Schreier et al., 2008]. At the same time, the frequency difference between neighboring levels is approximated by

$$\omega_\mathrm{n-1,n} = \omega_\mathrm{n} - \omega_\mathrm{n-1} \simeq (\sqrt{8E_\mathrm{j}E_\mathrm{c}} - nE_\mathrm{c})/\hbar \tag{2.59}$$

This still allows to selectively address individual transitions, i.e. it preserves the quasi-two-level-characteristic due to the anharmonicity $\approx E_\mathrm{c}$. The exact value of $\approx E_\mathrm{c}$, however, places a lower bound on the qubit control pulse duration because the anharmonicity has to exceed the spectral width of the applied pulse in order to avoid multi-level excitation.

Our qubit design is based on [Paik et al., 2011] requiring simply two electrodes connected by a thin wire of length $400\,\mathrm{nm}$ interrupted in its center by an $Al/AlO_x/Al$ JJ of area 200 x $300\,\mathrm{nm}$. The large 330 x $550\,\mathrm{\mu m}$ electrodes form the shunting capacitor of the transmon ($C_{\sum} = 93\,\mathrm{fF}$) with a simulated charging energy of $E_\mathrm{c} = 206\,\mathrm{MHz}$. Together with the Josephson energy of $E_\mathrm{j} = 24\,\mathrm{GHz}$ this enables the desired $E_\mathrm{j}/E_\mathrm{c} \gg 1$ regime with a reduced sensitivity against charge noise. The qubit transition frequency between the ground and first excited state without the AC Stark shift due to resonator occupation (cf. eq. 2.67) is measured as $\omega_{01} = 6.251\,\mathrm{GHz}$.

---

[19] The dissipationless current in a superconductor

2.4.2 The Jaynes-Cummings Hamiltonian

The design described above was chosen because we wanted to make use of the large frequency and bandwidth tuning range of our tunable waveguide cavity 2.4. Due to the extended mode volume in such a three-dimensional cavity compared to an integrated approach, the large electrodes of this qubit geometry are required to increase the dipole moment in order to reach strong coupling between qubit and resonator. In this regime, the coupling is larger than the individual loss rates ($g > \kappa, \gamma$) but not comparable to the transition frequencies ($g \ll \omega_{01}, \omega_{\mathrm{e}}$). The qubit couples with a rate of $g/(2\pi) = 326\,\mathrm{MHz}$ to the cavity field with a tunable power decay rate of $0.4 - 20\,\mathrm{MHz}$.

From a mathematical point of view, the microwave cavity with the Hamiltonian of an harmonic oscillator

$$H_{\mathrm{e}} = \hbar\omega_{\mathrm{e}}\hat{a}^{\dagger}\hat{a} \tag{2.60}$$

couples to the transmon qubit, essentially an oscillator with nonlinear energy levels introduced by the JJ [Blais et al., 2020]

$$H_{\mathrm{q}} \approx \hbar\omega_{\mathrm{q}}\hat{q}^{\dagger}\hat{q} - \frac{E_{\mathrm{c}}}{2}\hat{q}^{\dagger}\hat{q}^{\dagger}\hat{q}\hat{q} \tag{2.61}$$

The energy in the first term is given by the transition frequency between the first two levels in eq. 2.59, the second term can be interpreted as a Kerr nonlinearity with Kerr factor $-E_{\mathrm{c}}/(2\hbar)$. Thus, the qubit as an anharmonic oscillator experiences a negative frequency shift of $E_{\mathrm{c}}/\hbar$ per excitation. [20]

Neglecting other resonator modes under the assumption, that the qubit frequency ω_{q} is significantly closer to the nearest cavity frequency than any other cavity modes ("single-mode approximation"), the coupled system in the strong coupling regime and under rotating-wave-approximation is described by

$$H \approx H_{\mathrm{e}} + H_{\mathrm{q}} + \hbar g(\hat{q}^{\dagger}\hat{a} + \hat{q}\hat{a}^{\dagger}) \tag{2.62}$$

This beam-splitter interaction or exchange of excitation between the involved modes also describes specific cases of the OM, EM and EO interaction (cf. section 2.2, 2.2.1, and 2.2.3). The coupling constant g between excitations of the transmon and the resonator is given by [Blais et al., 2021]:

$$g = \omega_{\mathrm{e}}\frac{C_{\mathrm{g}}}{C_{\sum}}\left(\frac{E_{\mathrm{J}}}{2E_{\mathrm{J}}}\right)^{1/4}\sqrt{\frac{\pi Z_{\mathrm{e}}}{R_{\mathrm{q}}}} \tag{2.63}$$

which can be rewritten as the the dipole moment coupled to the field of the resonator from the perspective of the qubit. The participation ratio $C_{\mathrm{g}}/C_{\sum}$ accounts for the fact that the coupling capacitance is not the only capacitance in the circuit. $(E_{\mathrm{J}}/2E_{\mathrm{J}})^{1/4}$ relates e.g. to the magnitude of the charge zero-point-fluctuations or the dipole moment of the transmon. The final term with the resistance quantum $R_{\mathrm{q}} = h/e^2$ can be rewritten as $\sqrt{2\pi\alpha\frac{Z_{\mathrm{e}}}{Z_{\mathrm{vac}}}}$

---

[20] In [Blais et al., 2021] the Hamiltonian of eq. 2.61 is rewritten to make the analogy to the Kerr-effect even more visible: $H_{\mathrm{q}} \approx \hbar\tilde{\omega}_{\mathrm{q}}(\hat{q}^{\dagger}\hat{q})^2$ with excitation dependent frequencies $\tilde{\omega}_{\mathrm{q}}(\hat{q}^{\dagger}\hat{q}) = \omega_{01} - E_{\mathrm{c}}/(2\hbar)(\hat{q}^{\dagger}\hat{q} - 1)$

to show the dependence on the circuit impedance normalized by the vacuum impedance $Z_\mathrm{vac} = \sqrt{\mu_0/\epsilon_0} = \mu_0 c \approx 377\,\Omega$.

The commonly used Jaynes-Cummings Hamiltonian [Jaynes and Cummings, 1963; Bernardot et al., 1992; Wallraff et al., 2004] is recovered when restricting the qubit creation and annihilation operators to the ground state and first excited state of the transmon. $\hat{q}^\dagger \rightarrow |1\rangle\langle 0| := \hat{\sigma}_+$, $\hat{q} \rightarrow |0\rangle\langle 1| := \hat{\sigma}_-$ and $\hat{\sigma}_\mathrm{z} := |1\rangle\langle 1| - \rightarrow |0\rangle\langle 0|$ leads to [Blais et al., 2004]

$$H_\mathrm{JC} = H_\mathrm{e} + \hbar\frac{\omega_\mathrm{q}}{2}\hat{\sigma}_\mathrm{z} + \hbar g\left(\hat{a}^\dagger\hat{\sigma_-} + \hat{a}\hat{\sigma_+}\right) \tag{2.64}$$

2.4.3 Dispersive qubit readout

The exchange of excitations between resonator and qubit can be used e.g. for single photon generation by tuning the qubit after the state preparation in resonance with the resonator [Eichler et al., 2011]. [21] However, it is often advantageous to work in the so-called dispersive regime, where the direct exchange of excitation is suppressed because it is off-resonant, $|\Delta| = |\omega_\mathrm{q} - \omega_\mathrm{e}| \gg g$. First, qubit and resonator are only weakly entangled and allow for a quantum-non-demolition readout of the qubit state. On resonance, i.e. $\Delta = 0$, the qubit-cavity system is maximally entangled and the qubit is never in a well-defined state [Blais et al., 2021]. Secondly, the resonator is a band-pass filter and, thus, shields the detuned qubit from e.g. vacuum noise. In this regime, the qubit can be approximated by

$$H_\mathrm{disp} \approx \hbar\tilde{\omega}_\mathrm{e}\hat{a}^\dagger\hat{a} + \hbar\frac{\tilde{\omega}_\mathrm{q}}{2}\hat{\sigma}_\mathrm{z} + \hbar\chi\hat{a}^\dagger\hat{a}\hat{\sigma}_\mathrm{z} \tag{2.65}$$

The first obvious difference to the Jaynes-Cunning Hamiltonian is the absence of the ladder operators $\hat{\sigma}_\pm$ that change the qubit state. It reveals that the resonator cannot induce a direct state flip of the qubit in the dispersive regime as $\Delta \gg g$. Nevertheless, as a consequence of the strong coupling, the bare frequencies of both resonator and transmon experience a significant shift due the vacuum fluctuations (Lamb-shift):

$$\tilde{\omega}_\mathrm{q} = \omega_\mathrm{q} + \frac{g^2}{\Delta} \tag{2.66a}$$

$$\tilde{\omega}_\mathrm{e} = \omega_\mathrm{e} - \frac{g^2}{\Delta - E_\mathrm{C}/\hbar} \tag{2.66b}$$

Additionally, the last term in eq. 2.65 contains the dispersive shift

$$\chi = -\frac{g^2 E_\mathrm{C}/\hbar}{\Delta\left(\Delta - E_\mathrm{C}/\hbar\right)} \tag{2.67}$$

and represents both a qubit-state dependent shift of the cavity frequency and the AC-Stark shift of the qubit frequency depending on the number of photons in the resonator $\hat{a}^\dagger\hat{a}$. The former is used to detect the state of the qubit ("*dispersive readout*"), the latter provides a

---

[21] In recent years, also the preparation of complex resonator states has been performed with a large detuning between cavity and qubit, i.e. in the dispersive regime [Pechal et al., 2014; Kurpiers et al., 2018; Campagne-Ibarcq et al., 2018]

usefull tool to quantify the number of photons in the resonator for weak coherent input fields to the resonator ("*AC Stark shift calibration*").

It is instructive to add two points: First, the appearance of E_C in the frequency corrections accounts for the fact that the multi-level system of the transmon is taken into account in the derivation of the dispersive Hamiltonian (eq. 2.65). Hence, it cannot be directly derived from eq. 2.64 but rather from eq. 2.61. The reason is that the exchange of excitations between resonator and transmon is still possible by virtual photons, even though the direct exchange is suppressed. These virtual processes can take place via higher levels of the transmon. Secondly, the dispersive regime breaks down for higher resonator photon numbers or qubit excitations. The readout photon number should be well below the so-called critical photon number. For the first two qubit levels, this bound is: [Blais et al., 2021]

$$n_\mathrm{crit,0} = \left(\frac{\Delta}{2g}\right)^2, n_\mathrm{crit,1} = \frac{1}{2}\left(\frac{(\Delta - E_\mathrm{C}/\hbar)^2}{4g^2} - 1\right). \tag{2.68}$$

Comprehensive insight into the dynamics of measurement induced transitions of a transmon qubit with useful advises how to minimize these unwanted excitations can be found in [Khezri et al., 2023; Dumas et al., 2024].

For our qubit parameters (section 2.4.1), the cavity with decay rates from fig. 2.1 and a bare resonator frequency of $8.806\,\mathrm{GHz}$, a power sweep of the resonator drive yields the frequency spectrum shown in 2.8a (b) with the qubit prepared in the $|0\rangle$ ($|1\rangle$) state. At low powers, i.e. in the dispersive regime, the resonator frequency shows a dispersive shift depending on the qubit state (cf. fig. 2.8d) of $\pm\chi$ resulting in a total separation of $6.6\,\mathrm{MHz}$. In agreement with eq. 2.68 we used 12 ($< n_\mathrm{crit,0}$) and 7 ($< n_\mathrm{crit,1}$) readout photons for the qubit in ground and excited state, indicated as dashed lines in fig. 2.8a and b.
At high powers, the measured resonator frequency switches to the bare resonance with a Lamb shift of $26\,\mathrm{MHz}$. In this regime, the nonlinearity from the Jaynes-Cummings interaction can be employed for a measurement of the qubit state with high signal-to-noise ratio (SNR) [Reed et al., 2010]. The high power, however, is destructive, i.e. the measurement does not preserve the projected quantum state in contrast to the quantum non-demolition (QND) dispersive readout at low readout powers. The measurement effectively makes use of the qubit-induced cavity anharmonicity depending on the cavity drive power for higher occupations. In combination with the dispersive shift χ_{01} of the cavity at low drive powers this leads to a shift of the cavity resonance to its bare frequency f_{bare} at different drive power levels for different qubit states. Hence, at a specific drive power, e.g. $-10\,\mathrm{dBm}$ or $\approx$ 28000 photons in this device (cf. dashed lines in fig. 2.8a and b), one can infer the qubit state with a high SNR. Phenomenologically, the cavity shows a resonance at its bare resonator frequency ($|1\rangle$) or is completely off-resonant ($|0\rangle$). In this specific experimental setup which has been used for an all optical readout of a qubit state, cf. section 4, another microwave cavity from an electro-optic transducer was tuned to f_{bare}, too. Thus, one observes either this second cavity alone or the qubit readout cavity on resonance with the microwave cavity of the electro-optic transducer by means of cascaded cavities (fig.2.8c) [Arnold et al., 2023].
Theoretically, the behavior at high powers is modelled by either including higher qubit levels [Boissonneault et al., 2010] or a semi-classical treatment for large cavity-qubit detunings and drive power-dependent anharmonicities [Bishop et al., 2010]. Both models qualitatively agree with the frequency spectrum in fig. 2.8.

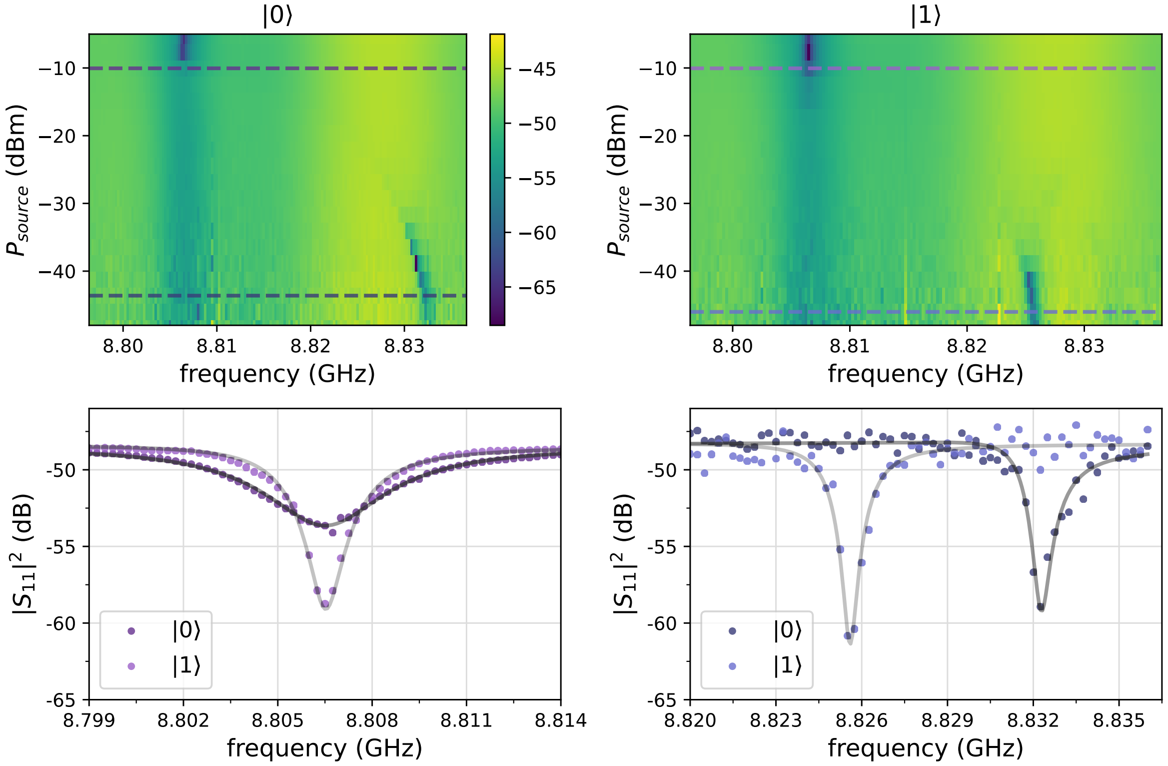

Figure 2.8: **Jaynes-Cummings readout.** **a**, Microwave reflection spectrum from a power sweep of the cascaded cQED-EO cavities with the qubit in ground state, the electro-optic transducer cavity at $\omega_e/(2\pi) = 8.806\ \mathrm{GHz}$, and additionally the cQED cavity switches to $\omega_{bare} = \omega_e$ at high readout powers. **b**, Similar spectrum to **a** with the qubit prepared in the excited state. The increased contrast due to the cQED cavity being resonant with the transducer cavity happens at slightly lower powers than for the ground state. **c**, Microwave reflection for both qubit states at the hight microwave readout power used for the Jaynes-Cummings readout indicated as a dashed line in the top panels. The contrast difference allows to detect the qubit states at high powers at the bare cQED cavity frequency. **d**, Microwave reflection for both qubit states at low microwave readout power for a QND dispersive readout, indicated again as a dashed line in the top panels. The frequency shift between both resonators is given by 2χ.

CHAPTER 3

An integrated electrooptomechanical converter

Acknowledgements I want to thank Matthias Wulf for the constructive and harmonic teamwork throughout the project and Elena Redchenko for her valuable help at the fabrication of the tightly packed coils. The chapter is based on the work presented in [Arnold et al., 2020].

The EM device characterized in 2.2.2.1 and the OM device introduced in 2.2.2.1 were actually both coupled to the same mechanical resonator, as can bee seen by the SEM image in fig. 2.5a. The mechanical resonator comprises strings that are a moving plate of a capacitor driven by their thermal and quantum fluctuations as well as moving beams of a photonic crystal cavity. If one applies microwave and optical pumps at the same time, this device enables the coupling between both frequency domains by a mechanical mediator. It represents the first integrated realization of such an EOM platform that has achieved impressive results in a bulk device [Higginbotham et al., 2018] and therefore can satisfy the requirements of a high package density. Miniaturization of such microwave-optic converters is a fundamental prerequisite to distribute entanglement between a large number of microwave-based qubits, i.e. superconducting qubits or many spin qubits, required to unlock the full potential of e.g. distributed or edge quantum computing.

The compact device enables the first detailed study of the impact of high energy optical photons on nearby superconducting circuits and mechanical oscillators at mK temperatures. As such qubits are restricted to this temperature regime it is crucial to operate the microwave-optic interface also $<100\,\mathrm{mK}$. Firstly, this temperature regime has not been explored with previous integrated microwave-optic converters [Vainsencher et al., 2016; Fan et al., 2018; Jiang et al., 2020]. Additionally, these works have only focused on the efficiency of the microwave-optic transduction but left the noise aspect aside. For the conversion of quantum signals, however, the noise aspect is of even higher importance because limited efficiency can be compensated by heralding schemes using, e.g. optical single photon detectors [Hong et al., 2017]. However, if a quantum signal has been corrupted by thermal noise, though, it is lost beyond recall.

The prior investigations of optical heating on mechanical oscillators in photonic crystal cavities [Meenehan et al., 2014, 2015] and the slightly surprising occurence of microwave noise at high intracavity photon numbers in integrated microwave circuits [Higginbotham et al., 2018] has motivated a design with maximum coupling for the OM and EM parts. Consequently, we were able to achieve satisfactory parametrically enhanced coupling rates and a total microwave-optic transduction efficiency of 1.2 % with pump powers of only $1\,\mathrm{nW}$ for each the microwave and optical pump. The is equivalent to a record-low V_π of only $16\,\mu$V.

However, there were two major drawbacks in this design. First, we could not reduce the optical cavity linewidth sufficiently to achieve the sideband resolved regime ($\kappa_\mathrm{o} < 4\omega_\mathrm{m}$). Hence, this microwave-optic transduction lacks the suppression of the unwanted amplification interaction 2.29. Instead, it amplifies the converted signal by two orders of magnitude. This is advantageous for classical conversion but prohibits the coherent conversion of quantum signals because the amplification process adds noise. A strategy to overcome this constraint has been tested and is discussed in section 3.7.
Secondly, the bandwidth of the transduction process is dominated by the EM and OM coupling rates. Due to the heating-related limit of the optical pump power, we were limited to a transduction bandwidth of $< 1\,\mathrm{kHz}$.

3.1 Modelling the coupling between three harmonic oscillators

While we introduced the coupling between two bosonic modes of harmonic oscillators in 2.2, we expand this now to three oscillators, that is an optical, a mechanical and a microwave resonator as schematically shown in fig. 3.1a. An optical drive and a microwave drive is applied to the respective resonator with frequencies $\omega_{\mathsf{d},j} = \omega_j - \Delta_j$, where Δ_j are the detunings from the respective resonance frequency ω_j, with $j =$ e,o. This results in parametrically enhanced photon-phonon coupling rates $g_{0,j}\sqrt{\hat{n}_j/\kappa_j}$ (fig. 3.1b). Since the optical resonator is not sideband resolved, a signal at the upper and lower optical sideband is created upon the transduction of an applied microwave signal (right panel in fig. 3.1b).

Please note that in the current chapter we use the indices o, e, m for optical, microwave (electrical), and mechanical parameters. In the previous sections we referred to the two harmonic oscillators with the general indeces a and b to highlight the fundamental similarity between an OM/EM and EO system in the theoretical description.

Intrinsic losses for the microwave resonator and optical cavity are denoted as $\kappa_{\mathsf{in},j}$, and the waveguide-cavity coupling rates are $\kappa_{\mathsf{ex},j}$. The total resonator decay rates are $\kappa_j = \kappa_{\mathsf{in},j} + \kappa_{\mathsf{ex},j}$. The full Hamiltonian is given by [Lauk et al., 2020]

$$\hat{H} = \hbar\omega_\mathsf{m}\hat{b}^\dagger\hat{b} + \hbar\sum_{j=\mathsf{e,o}}\Big[\omega_j\hat{c}_j^\dagger\hat{c}_j + g_{0,j}(\hat{b}^\dagger + \hat{b})\hat{c}_j^\dagger\hat{c}_j + iE_j(\hat{c}_j^\dagger e^{-i\omega_{\mathsf{d},j}t} - \hat{c}_j e^{i\omega_{\mathsf{d},j}t})\Big], \tag{3.1}$$

the annihilation operator of the mechanical mode remains $\hat{b}$, as in section 2.2.2, the optical and microwave resonator are represented by the annihilation operator $\hat{c}_j$ for resonator $j =$ e,o. The coupling rate to the mechanical resonator is $g_{0,j}$. The respective drive strength for resonator j is $E_j = \sqrt{\kappa_{\mathsf{ex},j}\,P_j/\hbar\omega_{\mathsf{d},j}}$, where P_j is the power of the driving field.

In the interaction frame with respect to $\hbar\sum_{j=\mathsf{e,o}}\omega_{\mathsf{d},j}c_j^\dagger c_j$ and neglecting terms oscillating at $\pm 2\omega_{\mathsf{d},j}$, the system Hamiltonian reduces to

$$\hat{H} = \hbar\omega_\mathsf{m}\hat{b}^\dagger\hat{b} + \hbar\sum_{j=\mathsf{e,o}}\Big[\Delta_j + g_{0,j}(\hat{b}^\dagger + \hat{b})\Big]\hat{c}_j^\dagger\hat{c}_j + \hat{H}_\mathsf{d}, \tag{3.2}$$

where the Hamiltonian associated with the driving fields is $\hat{H}_\mathsf{d} = i\hbar\sum_{j=\mathsf{e,o}}E_j(\hat{c}_j^\dagger - \hat{c}_j)$.

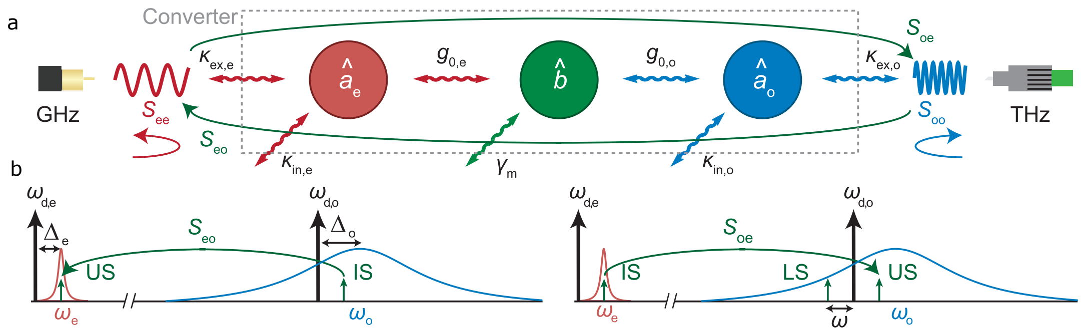

Figure 3.1: **EOM transducer scheme**. **a** Diagram showing the microwave ($\hat{a}_\mathrm{e}$), mechanical ($\hat{b}$), and optical ($\hat{a}_\mathrm{o}$) mode, and the relevant coupling and loss rates of the device. Scattering parameters S_{ij} characterizing the transducer performance are indicated. **b**, Schematic showing the frequencies of the coherent signals involved in the conversion process (green arrows). On the left an optical input signal (IS) is converted to an upper sideband (US) of the microwave pump signal whereas in the microwave-to-optics conversion on the right also the lower sideband (LS) is created. The bidirectional transduction ζ is only evaluated between the upper sidebands at $\omega_{\mathrm{d},j} + \omega_\mathrm{m}$. Figure adjusted from [Arnold et al., 2020].

Linearizing the Hamiltonian in (3.2) in by expanding the microwave and optical mode fluctuations around their steady-state field amplitudes, $\hat{a}_j \rightarrow \hat{c}_j - \bar{c}_j$, with $\bar{c}_j = \sqrt{\bar{n}_{\mathrm{d},j}}$ and $\bar{n}_{\mathrm{d},j} = |E_j|^2/(\kappa_j^2/4 + \Delta_j^2)$ as the mean number of intra-cavity photons induced by the microwave and optical pumps. Δ_j are the effective resonator and cavity detunings. The linearized Hamiltonian becomes

$$\hat{H} = \hbar\omega_\mathrm{m}\hat{b}^\dagger\hat{b} + \hbar\sum_{j=\mathrm{e,o}}\Big[\Delta_j\hat{a}_j^\dagger\hat{a}_j + G_j(\hat{b}+\hat{b}^\dagger)(\hat{a}_j^\dagger + \hat{a}_j)\Big], \tag{3.3}$$

where the parametrically enhanced photon-phonon coupling strength $G_j = g_{0,j}\sqrt{n_{\mathrm{d},j}}$

3.1.1 Equations of motion

Analog to chapter 2.2, the system can be treated quantum mechanically by adding the quantum noise fluctuations to the Heisenberg equations of motion. The noise acting on the mechanical resonator is ($\hat{b}_\mathrm{in}$ with damping rate γ_m), resonator and cavity input fluctuations ($\hat{a}_{\mathrm{ex},j}$, for $j =$ e,o, with rates $\kappa_{\mathrm{ex},j}$), and the intrinsic bath noises of the resonator and cavity modes ($\hat{a}_{\mathrm{in},j}$, for $j =$ e,o, with loss rates $\kappa_{\mathrm{in},j}$). These fluctuations have the correlation functions

$$\langle\hat{a}_{\mathrm{ext},j}(t)\hat{a}^\dagger_{\mathrm{ext},j}(t')\rangle = \langle\hat{a}^\dagger_{\mathrm{ext},j}(t)\hat{a}_{\mathrm{ext},j}(t')\rangle + \delta(t-t') = (\bar{n}_{\mathrm{ext},j}+1)\delta(t-t'), \tag{3.4a}$$

$$\langle\hat{a}_{\mathrm{in},j}(t)\hat{a}^\dagger_{\mathrm{in},j}(t')\rangle = \langle\hat{a}^\dagger_{\mathrm{in},j}(t)\hat{a}_{\mathrm{in},j}(t')\rangle + \delta(t-t') = (\bar{n}_{\mathrm{in},j}+1)\delta(t-t'), \tag{3.4b}$$

$$\langle\hat{b}_\mathrm{in}(t)\hat{b}^\dagger_\mathrm{in}(t')\rangle = \langle\hat{b}^\dagger_\mathrm{in}(t)\hat{b}_\mathrm{in}(t')\rangle + \delta(t-t') = (\bar{\mathrm{n}}_m+1)\delta(t-t'), \tag{3.4c}$$

where $\bar{n}_{\mathrm{ext},j}$, $\bar{n}_{\mathrm{in},j}$, and $\bar{n}_\mathrm{m}$ are the Planck-law thermal occupancies of each bath with $j =$ e,o. The resulting Langevin equations corresponding to Hamiltonian (3.3) are

$$\frac{d\hat{a}_j}{dt} = -(\frac{\kappa_j}{2} + i\Delta_j)\hat{a}_j - iG_j(\hat{b}+\hat{b}^\dagger) + \sqrt{\kappa_{\mathrm{ext},j}}\hat{a}_{\mathrm{ex},j} + \sqrt{\kappa_{\mathrm{in},j}}\hat{a}_{\mathrm{in},j}, \tag{3.5a}$$

$$\frac{d\hat{b}_j}{dt} = -(\frac{\gamma_\mathrm{m}}{2} + i\omega_\mathrm{m})\hat{b} - i\sum_{j=\mathrm{e,o}} G_j(\hat{a}_j + \hat{a}_j^\dagger) + \sqrt{\gamma_\mathrm{m}}\hat{b}_\mathrm{in} \tag{3.5b}$$

We again move to the Fourier space to be able to solve the system and substitute Eqs. (3.5a)–(3.5b) into the corresponding input-output relation, i.e., $\hat{a}_{\mathrm{out},j} = \sqrt{\kappa_{\mathrm{ex},j}}\hat{a}_j - \hat{a}_{\mathrm{ex},j}$. The scatterimg matrix $\mathbf{\Upsilon}(\omega)$

$$\mathbf{S}_{\mathrm{out}}(\omega) = \mathbf{\Upsilon}(\omega)\mathbf{S}_{\mathrm{in}}(\omega), \tag{3.6}$$

is defined the same way as in 2.2.1 by $\mathbf{\Upsilon}(\omega) = \Big(\mathbf{C}.[-i\omega\mathbf{I} - \mathbf{A}]^{-1}.\mathbf{B} - \mathbf{D}\Big)$ with **I** as the identity matrix. The complete list of resonator output operators is $\mathbf{S}_{\mathrm{out}} = [\hat{a}_{\mathrm{out,e}}, \hat{a}_{\mathrm{out,o}}, \hat{a}^\dagger_{\mathrm{out,e}}, \hat{a}^\dagger_{\mathrm{out,o}}]^T$, the inputs are $\mathbf{S}_{\mathrm{in}} = [\hat{a}_{\mathrm{ext,e}}, \hat{a}_{\mathrm{in,e}}, \hat{a}_{\mathrm{ext,o}}, \hat{a}_{\mathrm{in,o}}, \hat{b}_{\mathrm{in}}, \hat{a}^\dagger_{\mathrm{ext,e}}, \hat{a}^\dagger_{\mathrm{in,e}}, \hat{a}^\dagger_{\mathrm{ext,o}}, \hat{a}^\dagger_{\mathrm{in,o}}, \hat{b}^\dagger_{\mathrm{in}}]^T$. The matrices now include one more mode as in 2.2 and while microwave and optical resonator have both a waveguide port and the coupling to an intrinsic bath, the mechanical mediator cannot be controlled externally but modelled by a single bath.

$$\mathbf{A} = \begin{bmatrix} -(\frac{\kappa_\mathrm{e}}{2} + i\Delta_\mathrm{e}) & 0 & -iG_\mathrm{e} & 0 & 0 & -iG_\mathrm{e} \\ 0 & -(\frac{\kappa_\mathrm{o}}{2} + i\Delta_\mathrm{o}) & -iG_\mathrm{o} & 0 & 0 & -iG_\mathrm{o} \\ -iG_\mathrm{e} & -iG_\mathrm{o} & -(\frac{\gamma_\mathrm{m}}{2} + i\omega_\mathrm{m}) & -iG_\mathrm{e} & -iG_\mathrm{o} & 0 \\ 0 & 0 & iG_\mathrm{e} & -(\frac{\kappa_\mathrm{e}}{2} - i\Delta_\mathrm{e}) & 0 & iG_\mathrm{e} \\ 0 & 0 & iG_\mathrm{o} & 0 & -(\frac{\kappa_\mathrm{o}}{2} - i\Delta_\mathrm{o}) & iG_\mathrm{o} \\ iG_\mathrm{e} & iG_\mathrm{o} & 0 & iG_\mathrm{e} & iG_\mathrm{o} & -(\frac{\gamma_\mathrm{m}}{2} - i\omega_\mathrm{m}) \end{bmatrix}, \tag{3.7}$$

$$\mathbf{B} = \begin{bmatrix} \sqrt{\kappa_\mathrm{e}\eta_\mathrm{e}} & \sqrt{\kappa_\mathrm{e}(1-\eta_\mathrm{e})} & 0 & 0 & 0 & 0 & 0 & 0 & 0 & \\ 0 & 0 & \sqrt{\kappa_\mathrm{o}\eta_\mathrm{o}} & \sqrt{\kappa_\mathrm{o}(1-\eta_\mathrm{o})} & 0 & 0 & 0 & 0 & 0 & \\ 0 & 0 & 0 & 0 & \sqrt{\gamma_\mathrm{m}} & 0 & 0 & 0 & 0 & \\ 0 & 0 & 0 & 0 & 0 & \sqrt{\kappa_\mathrm{e}\eta_\mathrm{e}} & \sqrt{\kappa_\mathrm{e}(1-\eta_\mathrm{e})} & 0 & 0 & \\ 0 & 0 & 0 & 0 & 0 & 0 & 0 & \sqrt{\kappa_\mathrm{o}\eta_\mathrm{o}} & \sqrt{\kappa_\mathrm{o}(1-\eta_\mathrm{o})} & \\ 0 & 0 & 0 & 0 & 0 & 0 & 0 & 0 & 0 & \surd \end{bmatrix} \tag{3.8}$$

$$\mathbf{C} = \begin{bmatrix} \sqrt{\kappa_\mathrm{e}\eta_\mathrm{e}} & 0 & 0 & 0 & 0 & 0 \\ 0 & \sqrt{\kappa_\mathrm{o}\eta_\mathrm{o}} & 0 & 0 & 0 & 0 \\ 0 & 0 & 0 & \sqrt{\kappa_\mathrm{e}\eta_\mathrm{e}} & 0 & 0 \\ 0 & 0 & 0 & 0 & \sqrt{\kappa_\mathrm{o}\eta_\mathrm{o}} & 0 \end{bmatrix}, \tag{3.9}$$

$$\mathbf{D} = \begin{bmatrix} 1 & 0 & 0 & 0 & 0 & 0 & 0 & 0 & 0 & 0 \\ 0 & 0 & 1 & 0 & 0 & 0 & 0 & 0 & 0 & 0 \\ 0 & 0 & 0 & 0 & 0 & 1 & 0 & 0 & 0 & 0 \\ 0 & 0 & 0 & 0 & 0 & 0 & 0 & 1 & 0 & 0 \end{bmatrix}, \tag{3.10}$$

with $\eta_j = \kappa_{\text{ext,j}}/\kappa_j$. The total output fields are then

$$\begin{aligned}\hat{a}_{\text{out,e}} &= (\eta_\text{e}\alpha_{\text{e,e}} - 1)\hat{a}_{\text{ext,e}} + \sqrt{\eta_\text{e}}\Big[\sqrt{1-\eta_\text{e}}\alpha_{\text{e,e}}\hat{a}_{\text{int,e}} + \sqrt{\eta_\text{o}}\alpha_{\text{e,o}}\hat{a}_{\text{ext,o}} + \sqrt{1-\eta_\text{o}}\alpha_{\text{e,o}}\hat{a}_{\text{int,o}} + \alpha_{\text{e,m}}\hat{b}_{\text{in}} \\ &\quad + \sqrt{\eta_\text{e}}\tilde{\alpha}_{\text{e,e}}\hat{a}^\dagger_{\text{ext,e}} + \sqrt{1-\eta_\text{e}}\tilde{\alpha}_{\text{e,e}}\hat{a}^\dagger_{\text{int,e}} + \sqrt{\eta_\text{o}}\tilde{\alpha}_{\text{e,o}}\hat{a}^\dagger_{\text{ext,o}} + \sqrt{1-\eta_\text{o}}\tilde{\alpha}_{\text{e,o}}\hat{a}^\dagger_{\text{int,o}} + \tilde{\alpha}_{\text{e,m}}\hat{b}^\dagger_{\text{in}}\Big], \quad (3.11\text{a})\end{aligned}$$

$$\begin{aligned}\hat{a}_{\text{out,o}} &= (\eta_\text{o}\alpha_{\text{o,o}} - 1)\hat{a}_{\text{ext,o}} + \sqrt{\eta_\text{o}}\Big[\sqrt{1-\eta_\text{o}}\alpha_{\text{o,o}}\hat{a}_{\text{int,o}} + \sqrt{\eta_\text{e}}\alpha_{\text{o,e}}\hat{a}_{\text{ext,e}} + \sqrt{1-\eta_\text{e}}\alpha_{\text{o,e}}\hat{a}_{\text{int,e}} + \alpha_{\text{o,m}}\hat{b}_{\text{in}} \\ &\quad + \sqrt{\eta_\text{o}}\tilde{\alpha}_{\text{o,o}}\hat{a}^\dagger_{\text{ext,o}} + \sqrt{1-\eta_\text{o}}\tilde{\alpha}_{\text{o,o}}\hat{a}^\dagger_{\text{int,o}} + \sqrt{\eta_\text{e}}\tilde{\alpha}_{\text{o,e}}\hat{a}^\dagger_{\text{ext,e}} + \sqrt{1-\eta_\text{e}}\tilde{\alpha}_{\text{o,e}}\hat{a}^\dagger_{\text{int,e}} + \tilde{\alpha}_{\text{o,m}}\hat{b}^\dagger_{\text{in}}\Big], \quad (3.11\text{b})\end{aligned}$$

with $\hat{a}^{(\dagger)}_{\text{ext},j}$ and $\hat{a}^{(\dagger)}_{\text{int},j}$ referring to modes in the waveguide and bath respectively and the coefficients

$$\alpha_{\text{e,e}} = \frac{\kappa_\text{e}\,\chi_\text{e}\Big(1 + G_\text{o}^2(\chi_\text{o} - \chi_\text{o}^*) - G_\text{e}^2\chi_\text{e}^*\Big)\Big[-\chi_\text{m} + \chi_\text{m}^*\Big]}{1 + [\chi_\text{m} - \chi_\text{m}^*]\Big[G_\text{e}^2(\chi_\text{e} - \chi_\text{e}^*) + G_\text{o}^2(\chi_\text{o} - \chi_\text{o}^*)\Big]}, \tag{3.12a}$$

$$\alpha_{\text{o,o}} = \frac{\kappa_\text{o}\,\chi_\text{o}\Big(1 + G_\text{e}^2(\chi_\text{e} - \chi_\text{e}^*) - G_\text{o}^2\chi_\text{o}^*\Big)\Big[-\chi_\text{m} + \chi_\text{m}^*\Big]}{1 + [\chi_\text{m} - \chi_\text{m}^*]\Big[G_\text{e}^2(\chi_\text{e} - \chi_\text{e}^*) + G_\text{o}^2(\chi_\text{o} - \chi_\text{o}^*)\Big]}, \tag{3.12b}$$

$$\alpha_{\text{e,o}} = \alpha_{\text{o,e}} = \frac{\sqrt{\kappa_\text{e}\kappa_\text{o}}\,\chi_\text{e}\chi_\text{o}G_\text{e}G_\text{o}\Big[-\chi_\text{m} + \chi_\text{m}^*\Big]}{1 + [\chi_\text{m} - \chi_\text{m}^*]\Big[G_\text{e}^2(\chi_\text{e} - \chi_\text{e}^*) + G_\text{o}^2(\chi_\text{o} - \chi_\text{o}^*)\Big]}, \tag{3.12c}$$

$$\alpha_{j,\text{m}} = -\frac{i\,\sqrt{\kappa_j\gamma_\text{m}}\,G_j\chi_j\chi_\text{m}}{1 + [\chi_\text{m} - \chi_\text{m}^*]\Big[G_\text{e}^2(\chi_\text{e} - \chi_\text{e}^*) + G_\text{o}^2(\chi_\text{o} - \chi_\text{o}^*)\Big]}, \tag{3.12d}$$

$$\tilde{\alpha}_{j,j} = \frac{\kappa_j\,\chi_j\chi_j^*G_j^2\Big[-\chi_\text{m} + \chi_\text{m}^*\Big]}{1 + [\chi_\text{m} - \chi_\text{m}^*]\Big[G_\text{e}^2(\chi_\text{e} - \chi_\text{e}^*) + G_\text{o}^2(\chi_\text{o} - \chi_\text{o}^*)\Big]}, \tag{3.12e}$$

$$\tilde{\alpha}_{\text{e,o}} = \frac{\sqrt{\kappa_\text{e}\kappa_\text{o}}\,\chi_\text{e}\chi_\text{o}^*G_\text{e}G_\text{o}\Big[-\chi_\text{m} + \chi_\text{m}^*\Big]}{1 + [\chi_\text{m} - \chi_\text{m}^*]\Big[G_\text{e}^2(\chi_\text{e} - \chi_\text{e}^*) + G_\text{o}^2(\chi_\text{o} - \chi_\text{o}^*)\Big]}, \tag{3.12f}$$

$$\tilde{\alpha}_{\text{o,e}} = -\frac{\sqrt{\kappa_\text{e}\kappa_\text{o}}\,\chi_\text{e}^*\chi_\text{o}G_\text{e}G_\text{o}\Big[-\chi_\text{m} + \chi_\text{m}^*\Big]}{1 + [\chi_\text{m} - \chi_\text{m}^*]\Big[G_\text{e}^2(\chi_\text{e} - \chi_\text{e}^*) + G_\text{o}^2(\chi_\text{o} - \chi_\text{o}^*)\Big]}, \tag{3.12g}$$

$$\tilde{\alpha}_{j,\text{m}} = -\frac{i\,\sqrt{\kappa_j\gamma_\text{m}}\,G_j\chi_j\chi_\text{m}^*}{1 + [\chi_\text{m} - \chi_\text{m}^*]\Big[G_\text{e}^2(\chi_\text{e} - \chi_\text{e}^*) + G_\text{o}^2(\chi_\text{o} - \chi_\text{o}^*)\Big]}, \tag{3.12h}$$

with $j =$ e,o. We also define the individual susceptibilities of the optical cavity and microwave resonator $\chi_j^{-1} = \chi_j(\omega)^{-1} = i(\Delta_j - \omega) + \kappa_j/2$ and the mechanical susceptibility $\chi_\text{m}^{-1} = \chi_\text{m}(\omega)^{-1} = i(\omega_\text{m} - \omega) + \gamma_\text{m}/2$ and $\chi_k^* = \chi_k(-\omega)^*$ $k =$ e,o,m. Note that the commutation relation $[\hat{a}_{\text{out},j}(\omega), \hat{a}^\dagger_{\text{out},j}(\omega')] = \delta(\omega - \omega')$ imposes the following constrains

$$\begin{aligned}1 &= |\eta_\text{e}\alpha_{\text{e,e}} - 1|^2 + \eta_\text{e}(1-\eta_\text{e})|\alpha_{\text{e,e}}|^2 - \eta_\text{e}|\tilde{\alpha}_{\text{e,e}}|^2 \\ &\quad + \eta_\text{e}(|\alpha_{\text{e,o}}|^2 - |\tilde{\alpha}_{\text{e,o}}|^2) + \eta_\text{e}(|\alpha_{\text{e,m}}|^2 - |\tilde{\alpha}_{\text{e,m}}|^2) \qquad (3.13\text{a}) \\ 1 &= |\eta_\text{o}\alpha_{\text{o,o}} - 1|^2 + \eta_\text{o}(1-\eta_\text{o})|\alpha_{\text{o,o}}|^2 - \eta_\text{o}|\tilde{\alpha}_{\text{o,o}}|^2 \\ &\quad + \eta_\text{o}(|\alpha_{\text{o,e}}|^2 - |\tilde{\alpha}_{\text{o,e}}|^2) + \eta_\text{o}(|\alpha_{\text{o,m}}|^2 - |\tilde{\alpha}_{\text{o,m}}|^2) \qquad (3.13\text{b})\end{aligned}$$

3.1.2 Conversion efficiency and gain

From eq. (3.6) we can directly calculate all elements of the scattering matrix including the reflection parameters and transduction efficiency. The *effective* microwave-to-optical transduction efficiency is given by

$$\begin{aligned}\zeta(\omega) &:= |\Upsilon_{2,1}|^2 = |\Upsilon_{1,2}|^2 \\ &= \left| \frac{\sqrt{\kappa_{\mathrm{ex,e}}\kappa_{\mathrm{ex,o}}} G_{\mathrm{e}} G_{\mathrm{o}} \chi_{\mathrm{e}}(\omega)\chi_{\mathrm{o}}(\omega)\Big[-\chi_{\mathrm{m}}(\omega)+\chi_{\mathrm{m}}(-\omega)^*\Big]}{1+[\chi_{\mathrm{m}}(\omega)-\chi_{\mathrm{m}}(-\omega)^*]\Big[G_{\mathrm{e}}^2(\chi_{\mathrm{e}}(\omega)-\chi_{\mathrm{e}}(-\omega)^*)+G_{\mathrm{o}}^2(\chi_{\mathrm{o}}(\omega)-\chi_{\mathrm{o}}(-\omega)^*)\Big]} \right|^2 .\end{aligned} \tag{3.14}$$

The above equation contains the pure conversion efficiency and the gain due to the unresolved sideband condition of the optical mode. We can separate these two effects by rewriting eq. (3.14) in terms of the electro- and OM damping rates $\Gamma_j = G_j^2\Big[\frac{\kappa_j}{(\Delta_j-\omega)^2+\kappa_j^2/4} - \frac{\kappa_j}{(\Delta_j+\omega)^2+\kappa_j^2/4}\Big]$. This then gives $\zeta(\omega) = \theta \times \mathcal{G}$, where

$$\theta = \left| \frac{2\sqrt{\eta_{\mathrm{e}}\eta_{\mathrm{o}}}\,\sqrt{\Gamma_{\mathrm{e}}\Gamma_{\mathrm{o}}}}{2i(\omega-\omega_{\mathrm{m}}') + \gamma_{\mathrm{m}} + \Gamma_{\mathrm{e}} + \Gamma_{\mathrm{o}}} \right|^2, \tag{3.15}$$

is the pure bidirectional optical-to-microwave conversion efficiency with $\omega_{\mathrm{m}}' = \omega_{\mathrm{m}} - \delta_\omega(\omega_{\mathrm{m}})$ and $\delta_\omega(\omega_{\mathrm{m}}) = \sum_{j=\mathrm{e,o}} \mathrm{Im}(G_j^2(\chi_j^* - \chi_j))$ being the electro- and OM frequency shifts while $\mathcal{G} = \mathcal{G}_{\mathrm{o}}\mathcal{G}_{\mathrm{e}}$ is the amplification gain of the converter where

$$\mathcal{G}_{\mathrm{e}} = \left(\frac{|\chi_{\mathrm{e}}|^2}{4\Delta_{\mathrm{e}}\omega_{\mathrm{m}}}\right)\Big[(\Delta_{\mathrm{e}}-\omega)^2+\kappa_{\mathrm{e}}^2/4\Big]\Big[(\Delta_{\mathrm{e}}+\omega)^2+\kappa_{\mathrm{e}}^2/4\Big], \tag{3.16a}$$

$$\mathcal{G}_{\mathrm{o}} = \left(\frac{|\chi_{\mathrm{o}}|^2}{4\Delta_{\mathrm{o}}\omega_{\mathrm{m}}}\right)\Big[(\Delta_{\mathrm{o}}-\omega)^2+\kappa_{\mathrm{o}}^2/4\Big]\Big[(\Delta_{\mathrm{o}}+\omega)^2+\kappa_{\mathrm{o}}^2/4\Big], \tag{3.16b}$$

are the gains attributed to the unresolved sideband condition of the optical cavity and the microwave resonator. For our system $\delta_\omega \ll \omega_{\mathrm{m}}$, as such we consider $\omega = \omega_{\mathrm{m}}' \simeq \omega_{\mathrm{m}}$, resulting in

$$\mathcal{G}_{\mathrm{e}} = \left(\frac{(\Delta_{\mathrm{e}}+\omega_{\mathrm{m}})^2+\kappa_{\mathrm{e}}^2/4}{4\Delta_{\mathrm{e}}\,\omega_{\mathrm{m}}}\right), \tag{3.17a}$$

$$\mathcal{G}_{\mathrm{o}} = \left(\frac{(\Delta_{\mathrm{o}}+\omega_{\mathrm{m}})^2+\kappa_{\mathrm{o}}^2/4}{4\Delta_{\mathrm{o}}\,\omega_{\mathrm{m}}}\right). \tag{3.17b}$$

Note that $\Delta_{\mathrm{e}} = \omega_{\mathrm{m}}$ and considering the fact that in our system the microwave resonator is in the resolved sideband regime $\omega_{\mathrm{m}} \gg \kappa_{\mathrm{e}}$ entails $\mathcal{G}_{\mathrm{e}} \simeq 1$. The total gain, therefore, reduces to $\mathcal{G} \simeq \mathcal{G}_{\mathrm{o}} = 1 + \langle n\rangle_{\mathrm{min}}$ where

$$\langle n\rangle_{\mathrm{min}} = \frac{(\Delta_{\mathrm{o}}-\omega_{\mathrm{m}})^2+\kappa_{\mathrm{o}}^2/4}{4\Delta_{\mathrm{o}}\omega_{\mathrm{m}}} \tag{3.18}$$

is the minimum phonon number of the mechanical resonator induced by the OM quantum backaction when the mechanical resonator is decoupled from its thermal bath [Marquardt et al., 2007; Wilson-Rae et al., 2007]. At the optical detuning $\Delta_{\mathrm{o}} = \kappa_{\mathrm{o}}/2$ the phononic occupation number at absence of thermal noise reaches its minimum $\langle n\rangle_{\mathrm{min}} \simeq \kappa_{\mathrm{o}}/4\omega_{\mathrm{m}} \gg 1$. In this regime the backaction cooling of the mechanical resonator to its ground state is prohibited.

We can rewrite Eqs. (3.12) in terms of the system gains

$$\begin{aligned}\eta_{\mathsf{e}}\eta_{\mathsf{o}}|\tilde{\alpha}_{\mathsf{e,o}}|^2 &= \theta\mathcal{G}_{\mathsf{e}}(\mathcal{G}_{\mathsf{o}}-1),\\ \eta_{\mathsf{e}}\eta_{\mathsf{o}}|\tilde{\alpha}_{\mathsf{o,e}}|^2 &= \theta\mathcal{G}_{\mathsf{o}}(\mathcal{G}_{\mathsf{e}}-1),\\ \eta_{\mathsf{e}}\eta_{\mathsf{o}}|\alpha_{\mathsf{e,o}}|^2 &= \eta_{\mathsf{e}}\eta_{\mathsf{o}}|\alpha_{\mathsf{o,e}}|^2 = \theta\mathcal{G}_{\mathsf{o}}\mathcal{G}_{\mathsf{e}}.\end{aligned} \tag{3.19}$$

Using the above equation we can simplify Eqs. (3.11) to

$$\hat{a}_{\text{out,e}}/\sqrt{\theta} = \mathcal{G}_{\text{e}}(\sqrt{\mathcal{G}_{\text{o}}}\hat{a}_{\text{ext,o}} + \sqrt{\mathcal{G}_{\text{o}}-1}\hat{a}^{\dagger}_{\text{ext,o}}) + \sum_{j=e,o}\sum_{i=e,o,m} F_{\text{e}}(\alpha_{j,i}/\sqrt{\theta},\hat{O}), \tag{3.20a}$$

$$\hat{a}_{\text{out,o}}/\sqrt{\theta} = \mathcal{G}_{\text{o}}(\sqrt{\mathcal{G}_{\text{e}}}\hat{a}_{\text{ext,e}} + \sqrt{\mathcal{G}_{\text{e}}-1}\hat{a}^{\dagger}_{\text{ext,e}}) + \sum_{j=e,o}\sum_{i=e,o,m} F_{\text{o}}(\alpha_{j,i}/\sqrt{\theta},\hat{O}). \tag{3.20b}$$

The terms inside the brackets on the right hand side of the above equations describe the amplification of the quantum fluctuation $\hat{a}_{\text{ext,o(e)}}$ at the input port of the optical cavity (microwave resonator) with corresponding gain $\mathcal{G}_{\text{o(e)}}$ [Caves, 1982]. Here, $F_{\text{e(o)}}(\alpha_{i,j}/\sqrt{\theta},\hat{O})$ show the contribution of the quantum fluctuation at the input of the microwave resonator (optical cavity) and mechanical resonator.

At the resonance condition $\omega = \Delta_j = \omega_{\mathsf{m}}$, the total gain simplifies to $\mathcal{G} = \mathcal{G}_{\mathsf{o}}\mathcal{G}_{\mathsf{e}} = [1 + (\kappa_{\mathsf{o}}/4\omega_{\mathsf{m}})^2][1+(\kappa_{\mathsf{e}}/4\omega_{\mathsf{m}})^2]$. If electro- and OM cavity are additionally in the resolved sideband regime ($\omega_{\mathsf{m}} \gg \kappa_j$) all contributions from counter-rotating terms in the Hamiltonian (3.3) become negligible, resulting in $\mathcal{G} = 1$ and the effective conversion efficiency (3.14) reduces to

$$\zeta_{\text{sbr}}(\omega_{\mathsf{m}}) = \frac{4\eta_{\mathsf{e}}\eta_{\mathsf{o}}\Gamma_{\mathsf{e}}\Gamma_{\mathsf{o}}}{(\gamma_{\mathsf{m}}+\Gamma_{\mathsf{e}}+\Gamma_{\mathsf{o}})^2} = \frac{4\eta_{\mathsf{e}}\eta_{\mathsf{o}}\mathcal{C}_{\mathsf{e}}\mathcal{C}_{\mathsf{o}}}{(1+\mathcal{C}_{\mathsf{e}}+\mathcal{C}_{\mathsf{o}})^2}, \tag{3.21}$$

where Γ_j simplifies to $\Gamma_j = \frac{4g_{0,j}^2 n_{\mathsf{d},j}}{\kappa_j} = \frac{4G_j^2}{\kappa_j} = \mathcal{C}_j\gamma_{\mathsf{m}}$ with the OM cooperativity $\mathcal{C}_j$.

3.1.3 Conversion bandwidth

The bandwidth of the conversion process can be calculated from the denominator of eq. (3.14). In our experiment the microwave resonator is in the resolved sideband regime $4\omega_{\mathsf{m}} \gg \kappa_{\mathsf{e}}$, while the optical cavity goes beyond this regime $\omega_{\mathsf{m}} \ll \kappa_{\mathsf{o}}$. As such for $\omega = \Delta_j = \omega_{\mathsf{m}} \gg \gamma_{\mathsf{m}}$ we have $\chi_{\mathsf{e}} \to 2/\kappa_{\mathsf{e}}$, $\chi_{\mathsf{o}} \simeq \chi_{\mathsf{o}}^* \to 2/\kappa_{\mathsf{o}}$, $\chi_{\mathsf{m}} \to 2/\gamma_{\mathsf{m}}$, and $\{\chi_{\mathsf{e}}^*, \chi_{\mathsf{m}}^*\} \to 0$ which gives the following bandwidth

$$\Gamma_{\mathsf{conv}} \approx \Gamma_{\mathsf{e}} + \gamma_{\mathsf{m}}. \tag{3.22}$$

Its dependence on the OM damping rate $\Gamma_{\mathsf{o}} \ll \Gamma_{\mathsf{e}}$ is negligible because the unresolved sideband condition of the optical cavity significantly limits Γ_{o} due to equal photon scattering to the red and blue sidebands.

3.1.4 Added noise

The total noise added during conversion including the vibrational noise of the mechanics and the resonators' noises can be calculated with the spectral density of the output fields

$$2\pi\,\mathbf{S}_{\mathsf{SD}}(\omega)\delta(\omega-\omega') = \langle \mathbf{S}_{\mathsf{out}}(\omega')^{\dagger}\mathbf{S}_{\mathsf{out}}(\omega)\rangle. \tag{3.23}$$

The input signals for the noise are thermal states with bath occupations $\mathbf{N} = \mathrm{diag}[\bar{n}_{\mathsf{ext,e}}, \bar{n}_{\mathsf{int,e}}, \bar{n}_{\mathsf{ext,o}}, \bar{n}_{\mathsf{int,o}}, \bar{n}_{\mathsf{m}}]$. The spectral density (not symmetrized) can then be written as

$$\mathbf{S}_{\mathsf{SD}}(\omega) = \mathbf{\Upsilon}^{*}(\omega)\mathbf{\Sigma}\mathbf{\Upsilon}^{T}(\omega). \tag{3.24}$$

with

$$\mathbf{\Sigma} = \begin{bmatrix} \mathbf{N} & 0 \\ 0 & \mathbf{N}+1 \end{bmatrix}. \tag{3.25}$$

Using eq. (3.11), the total noises added to the output of the microwave resonator and optical cavity are given by

$$\begin{aligned} n_{\mathsf{add,e}} = {} & |\eta_{\mathsf{e}}\alpha_{\mathsf{e,e}} - 1|^2\bar{n}_{\mathsf{ext,e}} + \eta_{\mathsf{e}}\Big[(1-\eta_{\mathsf{e}})|\alpha_{\mathsf{e,e}}|^2\bar{n}_{\mathsf{int,e}} + \eta_{\mathsf{o}}|\alpha_{\mathsf{e,o}}|^2\bar{n}_{\mathsf{ext,o}} + (1-\eta_{\mathsf{o}})|\alpha_{\mathsf{e,o}}|^2\bar{n}_{\mathsf{int,o}} \\ & + |\alpha_{\mathsf{e,m}}|^2\bar{n}_{\mathsf{m}} + \eta_{\mathsf{e}}|\tilde{\alpha}_{\mathsf{e,e}}|^2(\bar{n}_{\mathsf{ext,e}}+1) + (1-\eta_{\mathsf{e}})|\tilde{\alpha}_{\mathsf{e,e}}|^2(\bar{n}_{\mathsf{int,e}}+1) + \eta_{\mathsf{o}}|\tilde{\alpha}_{\mathsf{e,o}}|^2(\bar{n}_{\mathsf{ext,o}}+1) \\ & + (1-\eta_{\mathsf{o}})|\tilde{\alpha}_{\mathsf{e,o}}|^2(\bar{n}_{\mathsf{int,o}}+1) + |\tilde{\alpha}_{\mathsf{e,m}}|^2(\bar{n}_{\mathsf{m}}+1)\Big], \end{aligned} \tag{3.26a}$$

$$\begin{aligned} n_{\mathsf{add,o}} = {} & |\eta_{\mathsf{o}}\alpha_{\mathsf{o,o}} - 1|^2\bar{n}_{\mathsf{ext,o}} + \eta_{\mathsf{o}}\Big[(1-\eta_{\mathsf{o}})|\alpha_{\mathsf{o,o}}|^2\bar{n}_{\mathsf{int,o}} + \eta_{\mathsf{e}}|\alpha_{\mathsf{o,e}}|^2\bar{n}_{\mathsf{ext,e}} + (1-\eta_{\mathsf{e}})|\alpha_{\mathsf{o,e}}|^2\bar{n}_{\mathsf{int,e}} \\ & + |\alpha_{\mathsf{o,m}}|^2\bar{n}_{\mathsf{m}} + \eta_{\mathsf{o}}|\tilde{\alpha}_{\mathsf{o,o}}|^2(\bar{n}_{\mathsf{ext,o}}+1) + (1-\eta_{\mathsf{o}})|\tilde{\alpha}_{\mathsf{o,o}}|^2(\bar{n}_{\mathsf{int,o}}+1) + \eta_{\mathsf{e}}|\tilde{\alpha}_{\mathsf{o,e}}|^2(\bar{n}_{\mathsf{ext,e}}+1) \\ & + (1-\eta_{\mathsf{e}})|\tilde{\alpha}_{\mathsf{o,e}}|^2(\bar{n}_{\mathsf{int,e}}+1) + |\tilde{\alpha}_{\mathsf{o,m}}|^2(\bar{n}_{\mathsf{m}}+1)\Big]. \end{aligned} \tag{3.26b}$$

The noise terms can be simplified in the vacuum condition in which the thermal occupations of the microwave resonator $\bar{n}_{\mathsf{ext,e}} = \bar{n}_{\mathsf{int,e}} = 0$, optical cavity $\bar{n}_{\mathsf{ext,o}} = \bar{n}_{\mathsf{int,o}} = 0$, and mechanical resonator $\bar{n}_{\mathsf{m}} = 0$ are negligible,

$$n_{\mathsf{add,e}} = \eta_{\mathsf{e}}\Big(|\tilde{\alpha}_{\mathsf{e,e}}|^2 + |\tilde{\alpha}_{\mathsf{e,o}}|^2 + |\tilde{\alpha}_{\mathsf{e,m}}|^2\Big), \tag{3.27a}$$

$$n_{\mathsf{add,o}} = \eta_{\mathsf{o}}\Big(|\tilde{\alpha}_{\mathsf{o,o}}|^2 + |\tilde{\alpha}_{\mathsf{o,e}}|^2 + |\tilde{\alpha}_{\mathsf{o,m}}|^2\Big). \tag{3.27b}$$

We can write the noise added to the output of the transducer in terms of the EM and OM gain introduced in Eqs. (3.16). By considering $|\tilde{\alpha}_{\mathsf{e(o),m}}|^2_{\omega=\omega_{\mathsf{m}}} \ll \{|\tilde{\alpha}_{\mathsf{e,o}}|^2, |\tilde{\alpha}_{\mathsf{e,o}}|^2, |\tilde{\alpha}_{j,j}|^2\}$ (since $\chi_{\mathsf{m}}(\omega_{\mathsf{m}}) \gg \chi^{*}_{\mathsf{m}}(-\omega_{\mathsf{m}})$ for $\omega_{\mathsf{m}} \gg \gamma_{\mathsf{m}}$) the Eqs. (3.27) reduce to

$$n_{\mathsf{add,e}} \simeq \theta/\eta_{\mathsf{o}}\,\mathcal{G}_{\mathsf{e}}\Big[\Big(\frac{\Gamma_{\mathsf{e}}}{\Gamma_{\mathsf{o}}}\Big)(\mathcal{G}_{\mathsf{e}}-1) + (\mathcal{G}_{\mathsf{o}}-1)\Big], \tag{3.28a}$$

$$n_{\mathsf{add,o}} \simeq \theta/\eta_{\mathsf{e}}\,\mathcal{G}_{\mathsf{o}}\Big[\Big(\frac{\Gamma_{\mathsf{o}}}{\Gamma_{\mathsf{e}}}\Big)(\mathcal{G}_{\mathsf{o}}-1) + (\mathcal{G}_{\mathsf{e}}-1)\Big]. \tag{3.28b}$$

The above equations can be simplified further and written in terms of the added noises of the optical and microwave amplifier models introduced in Eqs. (3.20). The resolved sideband condition of either the microwave resonator or optical cavity, respectively, results in $\mathcal{G}_{\mathrm{e}} \simeq 1$ or $\mathcal{G}_{\mathrm{o}} \simeq 1$, as such Eqs. (3.28) reduce to

$$\begin{aligned} n_{\mathrm{amp,e}} &= \frac{n_{\mathrm{add,e}}}{\theta} \simeq \mathcal{G}_{\mathrm{o}} - 1, \\ n_{\mathrm{amp,o}} &= \frac{n_{\mathrm{add,o}}}{\theta} \simeq \mathcal{G}_{\mathrm{e}} - 1, \end{aligned} \tag{3.29a}$$

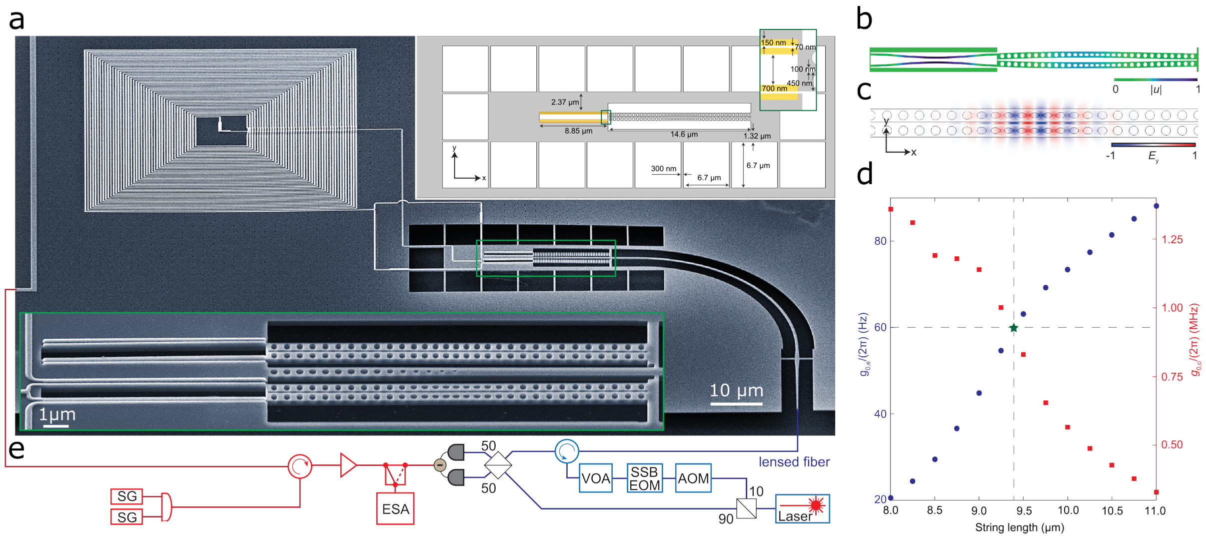

Figure 3.2: **EOM**. **a** SEM of the microwave resonator circuit, the photonic crystal resonator and the mechanical oscillator coupling to both. Insets show a closeup of the mechanical part and the exact dimensions. **b**, Simulation of the mechanical mode. **c**, Optical field distribution of the y-component (transverse to the beam-axis. **d**, Influence of the capacitor string length on the EM and OM coupling rate. Figure adapted from [Arnold et al., 2020].

representing the added noise at the output of quantum limited amplifiers with gains $\mathcal{G}_\mathrm{o}$ and $\mathcal{G}_\mathrm{e}$ considering vacuum noise at the input ports, in agreement with Eqs. (3.20).

For the special case of $\Delta_\mathsf{e} = \omega_\mathsf{m}$ and considering the microwave resonator being in the resolved sideband condition i.e. $\mathcal{G}_\mathsf{e} \simeq 1$, we can rewrite Eqs. (3.28) in terms of the phononic occupancy $\langle n \rangle_\mathsf{min}$, as

$$n_\mathsf{add,e} \simeq \theta/\eta_\mathsf{o}\,(\mathcal{G}_\mathsf{o} - 1) = \theta/\eta_\mathsf{o}\,\langle n \rangle_\mathsf{min}, \tag{3.30a}$$

$$n_\mathsf{add,o} \simeq \theta/\eta_\mathsf{e}\,(\mathcal{G}_\mathsf{o} - 1)\mathcal{G}_\mathsf{o}\left(\frac{\Gamma_\mathsf{o}}{\Gamma_\mathsf{e}}\right) = \theta/\eta_\mathsf{e}\,\langle n \rangle_\mathsf{min}\Big(\langle n \rangle_\mathsf{min} + 1\Big)\left(\frac{\Gamma_\mathsf{o}}{\Gamma_\mathsf{e}}\right). \tag{3.30b}$$

Note that for $\theta = 1$ and therefore also $\eta_j = 1$, the added noises in eq. (3.30)a represents the amplification of the vacuum noise with gain $\mathcal{G}_\mathsf{o}$ which is the direct result of the quantum backaction induced phononic occupation $\langle n \rangle_\mathsf{min} = \mathcal{G}_\mathsf{o} - 1$.

We want to stress that we use microwave and optical heterodyne detection in this experiment. Thus, the outgoing field is detected after interference with a reference beam and the detection is therefore sensitive to emission and absorption of photons from this field [Weinstein et al., 2014]. Consequently the measured quantity is correctly described by the single-sided and symmetrized power spectral density given by

$$\mathbf{S}_\mathsf{SD,sym}(\omega) = \boldsymbol{\Upsilon}^*(\omega)\boldsymbol{\Sigma}_\mathsf{sym}\boldsymbol{\Upsilon}^T(\omega). \tag{3.31}$$

with

$$\boldsymbol{\Sigma}_\mathsf{sym} = \begin{bmatrix} \mathbf{N} + 1/2 & 0 \\ 0 & \mathbf{N} + 1/2 \end{bmatrix}. \tag{3.32}$$

3.2 Device

3.2.1 Device design and parameters

The basic principles of the device design have already been introduced in section 2.1.1.3 and 2.2.2.2. The full circuit of the EOM converter can be seen in fig 3.2a comprising the rectangular coil as part of the microwave resonator and the the tuning fork geometry of the mechanical resonator, combining two beams as parallel plate capacitor components and two beams for the photonic crystal zipper cavity [Safavi-Naeini et al., 2013]. The insets show a zoom in on the transduction element with the mechanical resonator and a drawing with the central dimensions. The design aims at achieving maximum coupling of microwave and optical domain to the mechanical mediator. Fig 3.2b shows the differential in-plane mechanical oscillations where EM and OM part oscillate out-of-phase (cf. section 2.1.3), and panel c the optical cavity field used for this experiment (antisymmetric along the beam). As both OM and EM coupling depend on the geometrical moving boundary effect (eq. 2.2.2.2) and not e.g. on the photoelastic effect where strong couplings can be achieved with a tightly constrained mechanical "breathing" mode [Chan et al., 2012], we had to design the involved beams with sufficient length with $\approx 9\,\mu\mathrm{m}$ and $\approx 14\,\mu\mathrm{m}$ for the capacitor and photonic crystal beams respectively, in order to create a large displacement and consequently a large EM and OM coupling. The longer beams reduce the fundamental mechanical eigenfrequencies to only $\omega_\mathrm{m} \approx 10\,\mathrm{MHz}$ which has two drawbacks: 1) typical sample temperatures in a the dilution refrigerator environment between $50\,\mathrm{mK}$ and $100\,\mathrm{mK}$ lead to a thermal equilibrium population in the mechanical oscillator of more than 100 phonons according to the Bose-Einstein distribution $(e^{(\frac{\hbar\omega_\mathrm{m}}{k_\mathrm{b}T})}-1)^{-1}$. Consequently, active OM and EM cooling is necessary for quantum transduction. 2) The optical photonic crystal resonator linewidth is much larger than the mechanical frequency and the OM system is deep in the unresolved sideband regime. This leads to an insufficient suppression of the undesired amplification process (eq. 2.28) which adds inevitably quantum noise to the transduction process, even if the resonator would be in the thermal ground state. This amplification is discussed in detail in chapter 3.4. Combining the two remarks above leads ironically to the inconvenient situation, that the mechanical resonator will be thermally excited by its surrounding bath, and simultaneously, OM sideband cooling is impossible because the sideband unresolved regime with $\kappa_\mathrm{o} \gg 4\omega_\mathrm{m}$ prohibits to sufficiently favor the beam splitter or cooling interaction over the amplification or heating mechanism. However, the EM part is sideband-resolved and allows to apply sideband cooling on the total mechanical oscillator including also the OM part.

Although the mechanical mode is hybridized, slight adjustments of the relative lengths between the capacitors strings and the photonic crystal beams can tend to favor the EM and OM coupling respectively. This behavior is illustrated in fig. 3.2d showing simulations of the mechanical mode from fig. 3.2b for various lengths of the capacitor strings and a fixed length of the photonic crystal beams. Depending on this length either the EM (blue) or OM coupling (red) is emphasized. This trend for the mechanical mode with antisymmetric oscillations between the OM and the EM part is inverse for the symmetric mode at approximately $13\,\mathrm{MHz}$ (cf. 2.5). As both couplings are important to reach high transduction efficiency (cf. chapter 3.3) but also for the noise added to the conversion process, we chose a balanced configuration where the effective mass of the capacitor and the photonic crystal part are equal. This situation is visible as dashed lines in fig. 3.2. The influence of both couplings on the thermal noise can be understood in the following: A strong EM couplings allows for a stronger sideband-cooling of the device, while a large opto-mechanical (OM) coupling achieves a high parametrically enhanced interaction with optical drives of comparably lower powers. This is crucial because

the high energy optical photons are the dominant source of thermal heating. The noise performance of the device and the influence on various device parameters is investigated in chapter 3.5).
All important device parameters used for the experiment are summarized in Table 3.1. For each parameter the design value from simulation as well as the experimentally extracted value is listed, if available.

Parameter	Simulated value		Measured value	
$\omega_\mathsf{o}/(2\pi)$	193.874	THz	198.081	THz
$\Delta_\mathsf{o}/(2\pi)$	-	-	126	MHz
$\kappa_{\mathsf{ex,o}}/(2\pi)$	2.15	GHz	0.18	GHz
$\kappa_{\mathsf{in,o}}/(2\pi)$	0.02	GHz	1.42	GHz
$\omega_\mathsf{e}/(2\pi)$	10.387	GHz	10.497 ($P_\mathsf{o} = 0\,$pW) 10.490 ($P_\mathsf{o} = 92\,$pW) 10.478 ($P_\mathsf{o} = 1556\,$pW)	MHz
$\Delta_\mathsf{e}/(2\pi)$	-	-	11.84	MHz
$\kappa_{\mathsf{ex,e}}/(2\pi)$	0.9	MHz	1.15	MHz
$\kappa_{\mathsf{in,e}}/(2\pi)$	-	-	1.6 ($P_\mathsf{o} = 0\,$pW) 6.1 ($P_\mathsf{o} = 92\,$pW) 13.9 ($P_\mathsf{o} = 1556\,$pW)	MHz
L_coil	59.8	nH	-	-
C_s	3.0	fF	-	-
C_m	0.9	fF	-	-
$\omega_\mathsf{m}/(2\pi)$	10.9	MHz	11.84	MHz
$\gamma_\mathsf{m}/(2\pi)$	-	-	15 ($P_\mathsf{o} = 0\,$pW) 164 ($P_\mathsf{o} = 92\,$pW) 355 ($P_\mathsf{o} = 1556\,$pW)	Hz
x_zpf	24.5	fm	-	-
m_eff	1.3	pg	-	-
$g_{\mathsf{0,o}}/(2\pi)$	893	kHz	662	kHz
$g_{\mathsf{0,e}}/(2\pi)$	60	Hz	67	Hz

Table 3.1: Summary of important device parameters.

3.2.2 Fabrication

The EOM device is fabricated using a robust multi-step recipe including electron beam lithography, silicon etching, aluminum thin-film deposition and HF vapor acid etching. It is based on the recipes described in detail in Ref. [Dieterle et al., 2016; Fink et al., 2016; Barzanjeh et al., 2019; Redchenko, 2022].

3.2.3 Setup

The full measurement setup used for characterizing the microwave-to-optics converter is shown in detail in fig. 3.3a. It consists of two parts, namely an optical (blue color) and a

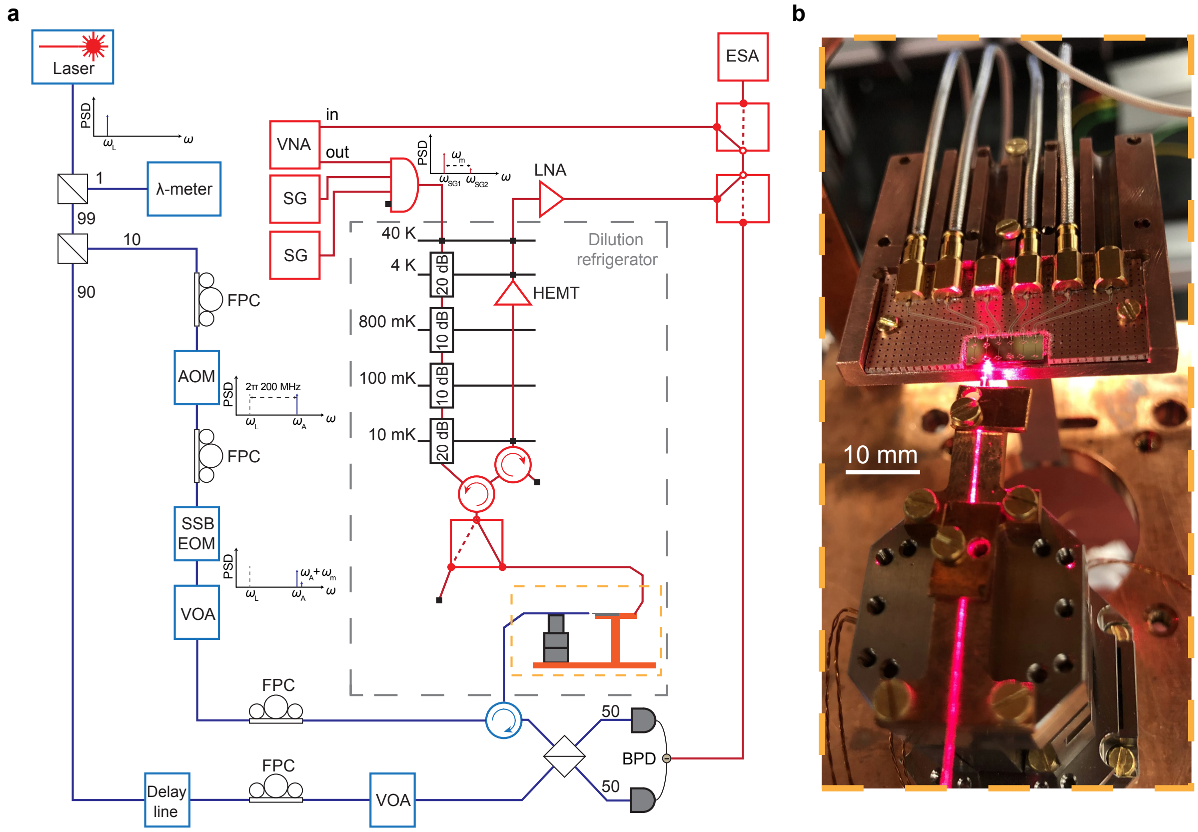

Figure 3.3: **EOM device design a**, Schematic of the optical (blue) and microwave (red) setup used for characterizing the microwave-to-optics converter. In the optical setup the laser light is split into two branches, a high-power local oscillator and a low-power signal arm, for building a high-sensitive heterodyning setup. In the signal arm an AOM is used for shifting the light frequency and a SSB EOM is applied for generating a single weak frequency-shifted probe tone. The light reflected from the sample is recombined with the strong local oscillator and measured on a BPD. In the microwave setup the output of the VNA is combined with the output of two SGs and the signals are sent through a cable in the dilution refrigerator to the sample. The microwave signal reflected from the sample is amplified by a HEMT and a LNA. Two microwave switches allow to choose: first if the reflected microwave or the electrical response from the BPD is analyzed and second if the reflected signal is sent to the VNA or the ESA. The spectral position of all signals are indicated schematically at important positions in the setup, i.e. ω_L for the laser frequency and ω_A for the AOM shifted frequency. Acronyms: wavemeter (λ-meter), fiber polarization controller (FPC), acousto-optic modulator (AOM), single-sideband electro-optic modulator (SSB EOM), variable optical attenuator (VOA), balanced photodetector (BPD), vector network analyzer (VNA), microwave signal generator (SG), high-electron-mobility transistor (HEMT), low-noise amplifier (LNA), electronic spectrum analyzer (ESA). **b**, Photograph showing the alignment of the lensed fiber to the chip using the stack of piezo nanopositioners and the mounting of the chip on the printed circuit board in the dilution refrigerator. 650 nm laser light was sent through the optical measurement system instead of telecom wavelengths to achieve visibility of the optical path to the sample. Figure adapted from [Arnold et al., 2020].

microwave (red color) reflection setup. The converter is mounted on a stage made out of OFC (oxygen-free copper) attached to the mixing chamber plate of a dilution refrigerator (Bluefors LD250) which is kept at a temperature of ∼50 mK, if not specified differently, e.g. in section 2.2.2.1 and 2.2.2.1.

As light source for our optical setup we use a fiber-coupled tunable external-cavity diode laser (Santec TSL-550 type A) operated around a frequency of $\omega_\mathrm{o}/(2\pi) = 198.0815\,\mathrm{THz}$. Using a 99:1 fiber coupler a small fraction of the light is sent to a wavemeter (λ-meter, Newport WM-1210) for frequency stabilization. The remaining light is divided by a 90:10 fiber coupler into two branches, a low-power signal and a high-power local oscillator arm, required for building an optical heterodyning setup. In the signal arm an acousto-optic modulator (Gooch & Housego T-M200-0.1C2J-3-F2P) is used to shift the light frequency by 200 MHz. Afterwards the light is sent through an single-sideband electro-optic modulator (SSB EOM, Thorlabs LN86S-FC) to generate a single small (approximately 20 dB smaller) optical probe tone detuned by the mechanical frequency $\omega_\mathrm{m}/(2\pi)$. Note that the SSB EOM is operated in such a way that the carrier is not suppressed. Subsequently, the optical signal passes through a variable optical attenuator (VOA, HP8156A) to control the light level that is sent to the sample. Finally, the light is sent to a circulator which routes the light into the dilution refrigerator where a lensed fiber mounted on a stack of attocube® piezo nanopositioners is used for end-fire coupling to the desired device on the mounted chip with a single-pass coupling efficiency of 64 % (see fig. 3.3b). The light reflected by the sample is recombined on a 50:50 fiber coupler with the local oscillator signal whose amplitude is kept at roughly $800\,\mu\mathrm{W}$ with an additional variable optical attenuator. Important to note is that the length of both arms were matched to achieve the lowest noise level. The recombined signal is measured eventually on a balanced photodetector (BPD, Thorlabs PDB470C-AC).

In the microwave setup the signals of three devices, i.e. the output port of a vector network analyzer (VNA, Rohde & Schwarz ZNB 20) and two microwave signal sources (SG, Rohde & Schwarz SGS 100A and Rohde & Schwarz SMA 100B), are first combined by a power combiner and then sent together through a cable to the sample in the dilution refrigerator. The signal is attenuated at every temperature stage to eliminate Johnson-Nyquist noise. Using a circulator the microwave signal is routed to the sample which is mounted on a printed circuit featuring coplanar microwave waveguides to direct the RF signal to the chip (see fig. 3.3b), or alternatively to a low-temperature 50 Ohm termination by employing a microwave switch mounted also at the mixing chamber plate. On the output side a second circulator is used to isolate the sample from thermal noise coming from the hotter stages above. After this isolator the reflected microwave signal is sent to two amplifiers, i.e. a HEMT (Low-noise factory LNC6-20C) mounted at the 4K-stage in the refrigerator and a low-noise amplifier (LNA, Agile AMT-A0067) positioned outside of the cryostat.

Two microwave switches allow us to decide which signal we want to analyze. The first switch grants us the possibility to choose between the reflected microwave signal or the electronic response of the balanced photodetector. The second switch routes this signal then either to the input port of the VNA or to an electronic spectrum analyzer (ESA, Rohde & Schwarz FSW 26). In conclusion, this allows us to make three types of measurements: 1. measure the microwave resonator with the VNA, 2. spectrally analyze the reflected microwave signal or 3. spectrally analyze the reflected optical signal.

3.3 Conversion measurements

To perform coherent photon conversion, red-detuned microwave and optical tones with powers $P_{\mathrm{e(o)}}$ are applied to the microwave and the optical resonator. These drive tones establish the linearized electro- and OM interactions, which results in the conversion of a weak microwave (optical) signal tone to the optical (microwave) domain measured in our setup as shown in fig. 3.2e. We experimentally characterize the transducer efficiency by measuring the normalized

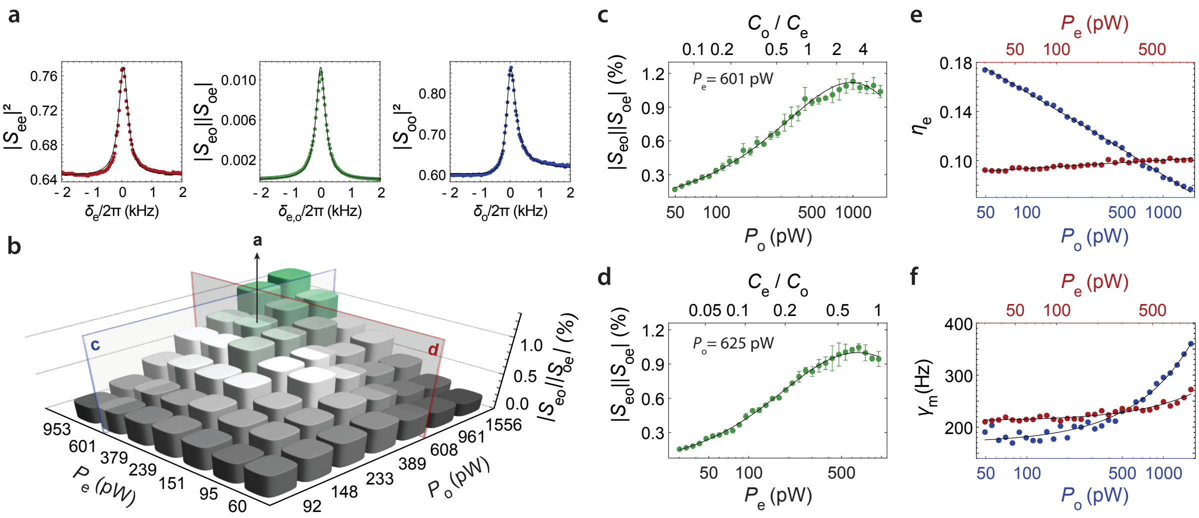

Figure 3.4: **Coherent scattering parameter measurements.** **a**, The reflection $|S_{jj}|^2$ ($j=$ e,o) and bidirectional transduction $\zeta := |S_{\text{eo}}||S_{\text{oe}}|$ parameters as a function of signal tone detuning $\delta_j = \omega - (\omega_{\text{d},j} + \omega_{\text{m}})$ for fixed pump powers $P_{\text{e}} = 601\,\text{pW}$ and $P_{\text{o}} = 625\,\text{pW}$. The dots represent the experimental data while the solid lines show the theoretical prediction with γ_{m} as the only fit parameter. **b**, Measured photon number transduction efficiency as a function of microwave and optical pump powers. **c**, Measured transduction efficiency with respect to optical pump power for fixed $P_{\text{e}} = 601\,\text{pW}$. **d**, Measured transduction efficiency with respect to microwave pump power for fixed $P_{\text{o}} = 625\,\text{pW}$. In **c** and **d**, the error bars are the standard deviation of three independent measurement runs and solid lines are theory with interpolated γ_{m} (from panel **f**) and no other free parameters. **e**, The coupling efficiency of the microwave resonator to the waveguide $\eta_{\text{e}} = \kappa_{\text{ex,e}}/\kappa_{\text{e}}$, extracted from broad band reflection measurements, as a function of optical (blue, $P_{\text{e}} = 601\,\text{pW}$) and microwave (red, $P_{\text{o}} = 625\,\text{pW}$) pump tones. **f**, Intrinsic mechanical decoherence rate γ_{m} versus optical (blue, $P_{\text{e}} = 601\,\text{pW}$) and microwave (red, $P_{\text{o}} = 625\,\text{pW}$) pump powers extracted from **c** and **d** with eq. (3.34) and γ_{m} as only fit parameter. Solid lines in panel (**f**) are linear fits to the data. Figure adapted from [Arnold et al., 2020].

reflection $|S_{jj}|^2$ ($j=$ e,o) and the bidirectional transmission $\zeta := |S_{\text{eo}}||S_{\text{oe}}|$ coefficients as a function of signal detuning δ. As shown in fig. 3.4a, for drive powers $P_{\text{e}} = 601\,\text{pW}$ and $P_{\text{o}} = 625\,\text{pW}$ with drive frequencies $\omega_{d,j}$ and detunings $\Delta_j = \omega_j - \omega_{\text{d},j}$ of $\Delta_{\text{e}} = \omega_{\text{m}}$ and $\Delta_{\text{o}}/(2\pi) = 126\,\text{MHz}$ leading to intracavity photon numbers of $n_{\text{d,e}} \approx 9\times10^5$ and $n_{\text{d,o}} \approx 0.2$ with cooperativities $\mathcal{C}_{\text{e}} \approx 0.57$ and $\mathcal{C}_{\text{o}} \approx 0.9$, the measured total (waveguide to waveguide) photon transduction efficiency is $\approx\ 1.1\,\%$ corresponding to $96.7\,\%$ internal (resonator to resonator) photon transduction efficiency over the total bandwidth of $\Gamma_{\text{conv}}/(2\pi) \approx 0.37\,\text{kHz}$. In the case of $\kappa_{\text{o}} > 4\omega_{\text{m}}$ and $\kappa_{\text{e}} < 4\omega_{\text{m}}$, the bandwidth is given by $\Gamma_{\text{conv}} \approx (\mathcal{C}_{\text{e}}+1)\gamma_{\text{m}}$ because the non-sideband resolved OM cavity does not induce mechanical broadening. The signal tone adds 17(10^{-3}) photons to the microwave resonator (optical cavity).

Here we use a self-calibrated measurement scheme that is independent of the gain and loss of the measurement lines as described in Ref. [Andrews et al., 2014] and we only take into account transduction between the upper two sidebands at $\omega_{\text{d},j} + \omega_{\text{m}}$ as shown in fig. 3.1b. Neglecting the lower optical sideband that is generated due to the non-sideband resolved situation $\kappa_{\text{o}}/4\omega_{\text{m}} \approx 30$ reduces the reported mean bidirectional efficiencies by $\sqrt{2}$ compared to the actually achieved total transduction efficiency between microwave and optical fields. The observed reflection peaks indicate that both resonators are under-coupled, equivalent to an impedance mismatch for incoming signal light. All scattering parameters are obtained from measured coherent tones whose linewidths are given by the chosen resolution bandwidth

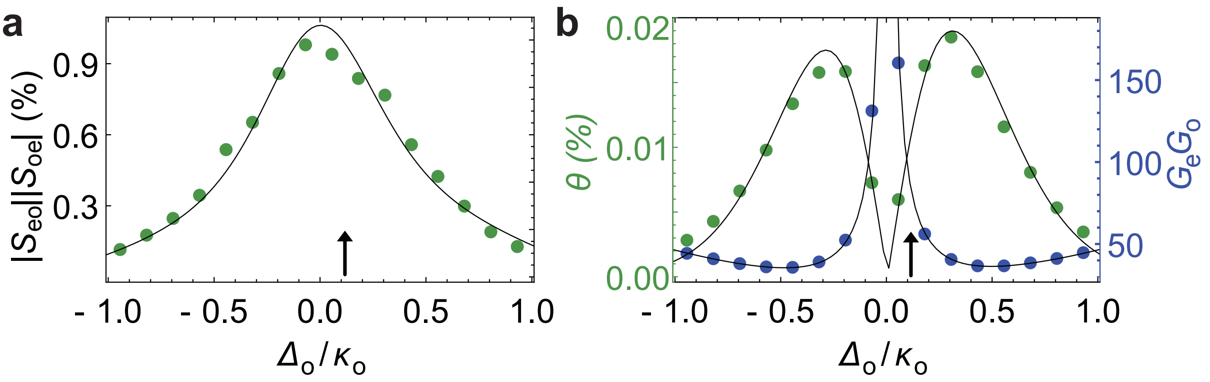

Figure 3.5: **Pure and amplified conversion.** **a**, Measured total transduction efficiency $\zeta := |S_{\text{eo}}||S_{\text{oe}}|$ with respect to pump detuning Δ_{o} of the non-sideband resolved optical cavity for a constant intra-cavity photon number $n_{\text{d,o}} = 0.185$. **b**, Pure and - in the absence of thermal noise - noiseless conversion θ (green dots) as well as the total conversion gain $\mathcal{G}$ (blue dots) that gives rise to amplified vacuum noise. θ is extracted from panel a by dividing the measured total transduction by the calculated gain using Eqs. 3.14 and 3.16. While $\mathcal{G}_{\text{o}}$ diverges for $\Delta_{\text{o}} \to 0$, the OM damping rate drops to zero and leads to a vanishing pure conversion θ. The arrows in both panels indicate the detuning used in Figs. 3.4 and 3.6. Figure adapted from [Arnold et al., 2020].

and the stability of the heterodyne setup. While this does not explicitly show long term phase stability of the conversion we find that these results are in excellent agreement with our coherent conversion theory model (solid lines) with γ_{m} as the only free fit parameter.

Figure 3.4b shows the total transduction efficiency for different pump power combinations with microwave and optical pump powers ranging from 30 to 953 pW and 48 to 1561 pW, respectively. Figure 3.4c (3.4d) shows the efficiency versus P_{o} (P_{e}) for fixed microwave (optical) pump power $P_{\text{e}} = 601$ $(P_{\text{o}} = 625)$ pW. As expected, the transduction efficiency rises with increasing pump powers and reaches a maximum of $\zeta = 1.2\,\%$. The internal transduction efficiency is significantly higher $(\zeta/(\eta_{\text{o}}\eta_{\text{e}}) \leq 135\,\%)$ because both the microwave resonator as well as the optical cavity are highly under-coupled with coupling ratios of $\eta_{\text{o}} = 0.11$ and η_{e} ranging between $0.07 - 0.18$ when both pumps are on. The increase in the intrinsic loss rate of microwave $\kappa_{\text{in,e}}$ and mechanical resonator γ_{m} at higher pump powers are shown in fig. 3.4e and fig. 3.4f caused by considerable heating related to (especially optical) photon absorption. This results in the degradation of the microwave and mechanical quality factors and consequently reduces the waveguide coupling efficiency, the cooperativities and the total transduction efficiency (cf. section 3.1.2).

3.4 Amplification and sideband resolution

In the non-sideband resolved limit (cf. 3.1.2) the contribution of the counter-rotating term of the Hamiltonian $\hat{H}_{\text{CR,o}}$ is not negligible, resulting in a transduction process that cannot be fully noise-free. This interesting effect can be correctly described by introducing an amplification of the signal tone with (in the absence of thermal noise) quantum limited gain $\mathcal{G}_{\text{o}}$ (see eq. 3.16). In contrast, the microwave resonator is in the resolved-sideband condition $4\omega_{\text{m}} > \kappa_{\text{e}}$, so that the signal tone amplification due to EM interaction is negligible $\mathcal{G}_{\text{e}} \simeq 1$. This results in the total, power independent, bidirectional conversion gain of $\mathcal{G} = \mathcal{G}_{\text{e}}\mathcal{G}_{\text{o}} \simeq \mathcal{G}_{\text{o}}$, which turns out to be directly related to the minimum reachable phonon occupation (eq. 3.18)

$$\langle n \rangle_{\mathsf{min}} = \frac{(\Delta_{\mathsf{o}} - \omega_{\mathsf{m}})^2 + \kappa_{\mathsf{o}}^2/4}{4\Delta_{\mathsf{o}}\omega_{\mathsf{m}}} = \mathcal{G}_{\mathsf{o}} - 1 \tag{3.33}$$

induced by OM quantum backaction when the mechanical resonator is decoupled from its thermal bath [Aspelmeyer et al., 2014]. Due to this amplification process the measured transduction efficiency in fig. 3.4a is about 110 times larger than one would expect from a model that does not include gain effects for the chosen detuning, and adds the equivalence of at least one half of a vacuum noise photon to the input of the transducer in our case of heterodyne detection (for $\eta_j = 1$ and $\mathcal{G} \gg 1$). However, it turns out that this noise limitation, which might in principle be overcome with efficient feedforward [Higginbotham et al., 2018], sideband suppression [Asjad et al., 2016; Lau and Clerk, 2020], or sideband resolution [Kalaee et al., 2019], accounts for only about $0.1\,\%$ of the total conversion noise observed in our system.

The total transduction (including gain) can be written in terms of the susceptibilities of the electromagnetic modes $\chi_j^{-1}(\omega) = i(\Delta_j - \omega) + \kappa_j/2$ and the mechanical resonator $\chi_{\mathsf{m}}^{-1}(\omega) = i(\omega_{\mathsf{m}} - \omega) + \gamma_{\mathsf{m}}/2$ as

$$\zeta = \left| \frac{\sqrt{\kappa_{\mathsf{ex,e}}\kappa_{\mathsf{ex,o}}} G_{\mathsf{e}} G_{\mathsf{o}} \chi_{\mathsf{e}} \chi_{\mathsf{o}} \Big[-\chi_{\mathrm{m}} + \tilde{\chi}_{\mathsf{m}} \Big]}{1 + [\chi_{\mathsf{m}} - \tilde{\chi}_{\mathsf{m}}] \Big[G_{\mathsf{e}}^2(\chi_{\mathsf{e}} - \tilde{\chi}_{\mathsf{e}}) + G_{\mathsf{o}}^2(\chi_{\mathsf{o}} - \tilde{\chi}_{\mathsf{o}} \Big]} \right|^2, \tag{3.34}$$

where $\tilde{\chi}_j(\omega) = \chi_j(-\omega)^*$.

Equation (3.34) can be decomposed into a product of the conversion gain $\mathcal{G}$ and the pure conversion efficiency θ, i.e. $\zeta := \mathcal{G} \times \theta$, for frequencies in the vicinity of ω_{m} (see section 3.1.2). Equation (3.33) shows that the signal amplification depends only on the resonator linewidth and the detuning and is not directly related to the $\propto \hat{a}^\dagger \hat{b}^\dagger$ interaction term or the pump power [Andrews et al., 2014]. This can be understood by the alternative interpretation that the gain represents the ratio of the transduced upper sideband to the difference between upper and lower sideband at each cavity (cf. also 3.6). Therefore, it is instructive to measure the transducer parameters as a function of optical pump detuning as shown in fig. 3.5a. While changing the optical detuning, we also vary the pump power in order to keep the optical intra-cavity photon number constant at $n_{\mathsf{d,o}} = 0.185 \pm 0.015$. This way it is possible to investigate the influence of Δ_{o} at a constant OM coupling $G_{\mathsf{o}} = g_{0,\mathsf{o}}\sqrt{n_{\mathsf{d,o}}}$. The measured total transduction efficiency is shown in fig. 3.5a and reaches $\approx 1\%$ at $\Delta_{\mathsf{o}} \approx 0$ for the chosen pump powers in agreement with fig. 3.4c and 3.4d. We can now separate the measured transduction (eq. (3.34)) into conversion gain and pure conversion, as shown in fig. 3.5b. The gain shows the expected steep increase at $\Delta_{\mathsf{o}} \to 0$ where the pure conversion θ approaches zero for equal cooling and amplification rates. Around $\Delta_{\mathsf{o}} = \kappa_{\mathsf{o}}/2$ on the other hand, where $\langle n \rangle_{\mathsf{min}}$ reaches its minimum of roughly $\kappa_{\mathsf{o}}/4\omega_{\mathsf{m}} \approx 30$, also the gain reaches its minimum and the noiseless part (at zero temperature) of the total (internal) conversion process shows its highest efficiency of $\theta = 0.019\%$ ($\theta/(\eta_{\mathsf{e}}\eta_{\mathsf{o}}) = 1.6\%$).

3.5 Noise measurements

Another important figure of merit, not only for quantum applications, is the amount of added noise quanta [Zeuthen et al., 2020], usually an effective number referenced to the input of the

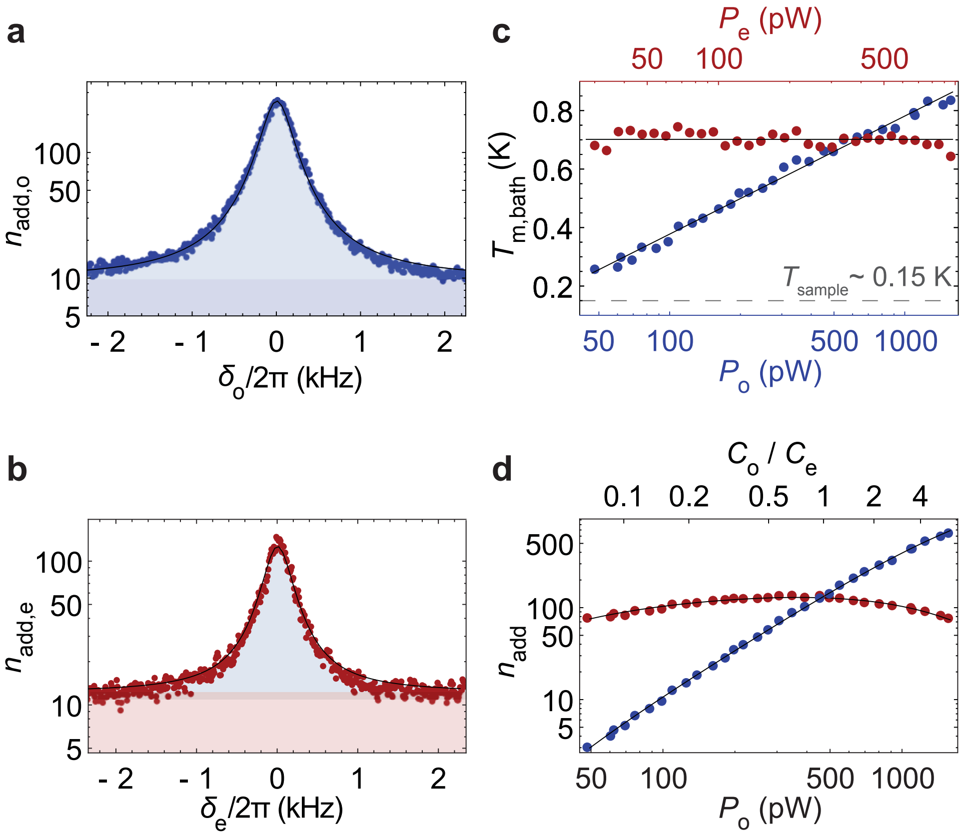

Figure 3.6: **Conversion noise properties.** Measured noise spectra at the device output for the optical cavity (**a**) and the microwave resonator (**b**) as a function of the signal tone detuning $\delta_j = \omega - (\omega_{\mathsf{d},j} + \omega_{\mathsf{m}})$ at fixed pump powers $P_{\mathsf{e}} = 601$ pW and $P_{\mathsf{o}} = 625$ pW in units of added noise quanta. **a**, The dark blue region represents the two-quadrature noise added by the optical measurement chain; the light blue region indicates the thermal mechanical noise added to the converted optical output signal. **b**, Bottom light red region represents the two-quadrature background noise from the microwave measurement chain. The central dark red region indicates a small amount of broad band resonator noise and the light blue region the transduction noise due to the thermal population of the mechanical mode. In both panels, fits to one common mechanical bath n_{m} are shown in black. **c** Mechanical bath temperature $T_{\mathsf{m,bath}}$ extracted as only fit parameter from fits to the measured output noise as in panels **a** and **b** with respect to optical (blue dots, $P_{\mathsf{e}} = 601$ pW) and microwave (red dots, $P_{\mathsf{o}} = 625 \pm 19$ pW) pump power. Black lines show fits to the data with the logarithmic growth function $0.18 \log_{\mathsf{e}}(P_{\mathsf{o}}) - 0.47$ and $T_{\mathsf{m,bath}} = 0.70$ K respectively. The dashed line indicates the thermalized mechanical mode temperature T_{sample} when both pumps are off. **d**, Microwave (red, $n_{\text{add,e}}$) and optical (blue, $n_{\text{add,o}}$) added noise photons at the output with respect to optical pump power ($P_{\mathsf{e}} = 601$ pW). The full theory based on an interpolation of $T_{\mathsf{m,bath}}$ from panel **c** is shown as black lines. Figure adapted from [Arnold et al., 2020].

device. For clarity with regards to the physical origin and the actual measurement of the noise power, in the following we define the total amount of added noise quanta $n_{\mathsf{add},j}$ added to the input signal $S_{\mathsf{in},j}$ after the transduction process as $S_{\mathsf{out},j} = \zeta S_{\mathsf{in},j} + n_{\mathsf{add},j}$. Figures 3.6a and 3.6b show the measured conversion noise $n_{\mathsf{add},j}$ as a function of frequency δ_j for the same powers and detunings as in fig. 3.4a. At these powers our device adds $n_{\mathsf{add,o(e)}} = 224(145)$ noise quanta to the output of the microwave resonator (optical cavity), corresponding to an effective input noise of $n_{\mathsf{add},j}/\zeta$. The noise floor originates from the calibrated measurement system and in case of the microwave port to a small part also from an additional broadband resonator noise, cf. fig. 3.6b. The solid lines are fits to the theory with the mechanical bath occupation $\bar{n}_\mathrm{m}$ as the only fit parameter (fig. 3.4).

The fitted effective mechanical bath temperature as a function of pump powers is shown in fig. 3.6c. It reveals the strong optical pump dependent mechanical mode heating (blue), while the microwave pump (red) has a negligible influence on the mechanical bath. Figure 3.6d shows the measured total added noise at the output of the microwave resonator and optical cavity as a function of optical pump power. The noise added to the optical output (blue) increases with pump power due to absorption heating and increasing OM coupling rate G_o, while the degradation of the resonator-waveguide coupling efficiency η_e explains the decreasing $n_\mathrm{add,e}$ at higher optical powers for the microwave output noise (red), see fig. 3.4e. The intersection of the two noise curves occurs at $\mathcal{C}_\mathrm{e} \simeq \mathcal{C}_\mathrm{o}$ with cooperativities C_j as defined above, and shows that the optical and microwave resonators share the same mechanical thermal bath. The power dependence is in full agreement with theory (solid lines) and demonstrates that the thermal mechanical population is the dominating origin of the added transducer noise.

3.6 Comparing gain in electrooptic and electrooptomechnanical conversion

As previously described (e.g. in 2.2.2.1, 3.1.2, 3.1.4), amplification necessarily adds noise to the coherent conversion between e.g. photonon and phonons 2.2.1 or optical and microwave photons 2.2.3. This originates from an insufficient suppression of the corresponding amplification interaction in the linearized Hamiltonian between two coupled harmonic oscillators. However, despite the equivalence of the OM and EM interaction on the one hand (2.29), and the EO interaction on the other hand (2.52), the added noise shows a different dependency on the system parameters for the two cases. Despite the equivalent interaction Hamiltonian, there is a subtle but decisive difference between them:

The mechanical mode has no accessible output port.

In other words: while we can measure both the microwave and optical output of an EO transducer, this is usually not the case in the fields of OM or EM. It is important to note that this situation is not necessarily the case. There have been fantastic achievements in using travelling phonons for communication, such as creation and detection of single phonons (as weak coherent states) via the OM interaction [Riedinger et al., 2016], single phonons in a single-mode waveguide [Zivari et al., 2022], a phononic beam splitter [Qiao et al., 2023] and mechanical oscillators in conjuction with superconducting qubits [Bienfait et al., 2019; Ma et al., 2021]. In many of these situations, the mechanical resonator coupling can be separated into an intrinsic loss channel and an external waveguide coupling. However, in the devices used throughout this thesis and all other microwave-optic converters with a mechanical mediator, mechanical losses in the **EM** or **OM** device parts couple only to the surrounding mechanical bath and not to a separate mechanical waveguide for further processing of the information encoded in the phonons. Thus, the mechanical state in **OM** or **EM** devices is manipulated AND probed by optical or microwave photons respectively. The second category one can introduce in the investigated devices is to distinguish between dual-stage conversion and single-stage conversion. In the following we will therefore compare the differences in gain and transduction efficiency between a single-stage EO converter with two measurable output ports, a single-stage converter with a non-directly accessible mechanical resonator (EM and OM device), and a dual-stage EOM transducer with a mechanical mediator.

Starting with the conversion efficiency of an EOM transducer, it is understandable that the intrinsic loss rate of the intermediate mechanical resonator should be minimal in order to get the most efficient microwave-optic conversion. The OM and EM scattering rates should exceed the intrinsic linewidth (i.e. loss rate) of the mechanical resonator as much as possible, or in other words, the photon-phonon cooperativities $C_\mathrm{e}, C_\mathrm{o} \rightarrow \infty$. The impedance matching or rate matching condition is achieved by $C_\mathrm{e} \approx C_\mathrm{o}$.
In the EO case, however, photons converted between the microwave and optical domain can be directly accessed at the respective output port. Consequently, maximum internal conversion is achieved for $C_\mathrm{eo} = 1$, i.e. matched loss and coupling rates. The cooperativity has in this case a slightly different meaning. While it is in the EOM device described above the ratio between the OM and EM photon-phonon scattering rate and the undesired intrinsic and inaccessible mechanical loss, where this ratio has to be maximized, it is here the electro-optic scattering rate over the out-coupling rate from the device to the target waveguide. The latter is ideally matched.

This intuitive approach to understand the meaning of the cooperativity and it's implication for the maximum conversion efficiency of dual-stage and single-stage microwave-optic converters using an EOM and an EO device, will be put in a mathematical form below and visualised in fig. 3.7a. The amount of amplification, however, does not follow the same classification. Here it is the non-accessible mechanical port in the OM and EM interaction that leads to a different behavior for both dual-stage transducers (EOM) but also single-stage processes (EM and OM) compared to the EO case with two accessible output ports, as will be shown below and in fig. 3.7b.

Please note that we intentionally neglect the non-ideal coupling ratio of the output ports, i.e. $\eta = \kappa_\mathrm{ex}/(\kappa_\mathrm{ex} + \kappa_\mathrm{in})$. An ideal output port for a microwave-optic transducer is under all circumstances predominantly coupled to the corresponding waveguide, i.e. $\kappa_\mathrm{ex} \gg \kappa_\mathrm{in}$.

OM case The gain of an OM ($\mathcal{G}_\mathrm{o}$) or EM system ($\mathcal{G}_\mathrm{e}$) is described by eq. 3.17 [Andrews et al., 2014] with the minimum occupation of the mechanical resonator by photon backaction being $n_\mathrm{min} = \mathcal{G}_j - 1$. First, this relation intuitively describes the connection between added noise and amplification. Secondly, it is clear from eq. 3.17 that the gain depends only on the position of the pump and the photon resonator's linewidth with respect to the mechanical frequency. The EM or OM gain, in the following just referred to as $\mathcal{G}$, can herein be related to the ratio between both sideband processes

$$\mathcal{G} = 1 + \langle n \rangle_\mathrm{min} = 1 + \frac{\Gamma^+}{\Gamma^- - \Gamma^+} = \frac{\Gamma^-}{\Gamma^- - \Gamma^+} = \left(1 - \frac{\Gamma^+}{\Gamma^-}\right)^{-1} \tag{3.35}$$

with the Anti-Stokes rate Γ^- and the Stokes rate Γ^+. Inserting the rates [1]

$$\Gamma^\pm = G^2 \frac{\kappa}{\kappa^2 + (\Delta \pm \omega_\mathrm{m})^2} \tag{3.36}$$

into eq. 3.35 yields the explicit expressions for the gain and minimum occupation consistent eq. 3.17 and eq. 3.18 in section 3.1.2.

In turn, the sideband suppression can also be expressed in terms of the gain

---

[1] As a reminder, the detuning is defined as $\Delta = \omega_\mathrm{cav} - \omega_\mathrm{pump}$ and a cooling or Anti-Stokes scheme refers to a detuning of $\Delta = \omega_\mathrm{m}$

$$\Gamma^+/\Gamma^- = \left(1 - \frac{1}{G}\right)^{-1} \tag{3.37}$$

.

The OM and EM conversion for $\Delta = \omega_\mathrm{m}$, the usual configuration for the beam-splitter interaction, is then

$$\zeta_\mathrm{om,em} = \mathcal{G}\frac{4C}{(1+C)^2} \simeq \left[1 + \left(\frac{\kappa}{4\omega_\mathrm{m}}\right)^2\right]\frac{4C}{(1+C)^2} \tag{3.38}$$

Combining OM and EM relation gives the full microwave-optic conversion for $\Delta_\mathrm{e} = \Delta_\mathrm{o} = \omega_\mathrm{m}$

$$\zeta_\mathrm{eom} = \mathcal{G}_\mathrm{e}\mathcal{G}_\mathrm{o}\frac{4C_\mathrm{e}C_\mathrm{o}}{(1+C_\mathrm{e}+C_\mathrm{o})^2} \simeq \left[1 + \left(\frac{\kappa_\mathrm{e}}{4\omega_\mathrm{m}}\right)^2\right]\left[1 + \left(\frac{\kappa_\mathrm{o}}{4\omega_\mathrm{m}}\right)^2\right]\frac{4C_\mathrm{e}C_\mathrm{o}}{(1+C_\mathrm{e}+C_\mathrm{o})^2} \tag{3.39}$$

If one selects now a typical sideband scattering ratio in the sideband resolved regime between beam-splitter and amplification interaction of $\Gamma^+/\Gamma^- = 0.9/0.1$ for both EM and OM interaction, the total EOM transduction efficiency in eq. 3.39 increases for larger cooperativities $C = C_\mathrm{e} = C_\mathrm{o}$ as shown in green in fig. 3.7a. As described above, this behavior is a consequence of the multi-step conversion process with an intermediate mechanical oscillator, whose intrinsic loss should be small compared to the EM and OM scattering rate. Ignoring the amplification interaction and the corresponding gain ("eom pure", light green), the total transduction is reduced because it is free of amplification but also free of quantum noise (ignoring classical noise from thermal excitation). fig. 3.7b shows the ratio of both curves and reveals that the gain is independent of the actual transduction efficiency.
Reducing the scheme to a single stage process, e.g. a OM or EM conversion, fig. 3.7a reveals that such a process reaches the ideal conversion without amplification at a cooperativity $C = 1$ (light purple). The total photon-phonon transduction including gain from Γ^+ (eq. 3.38, gray in panel a) can reach a maximum conversion efficiency larger than 1 and reaches the maximum at cooperativities sligthly below 1. Despite this different optimum, one can see in fig. 3.7b that the gain is again independent of the cooperativity, as for EOM transduction.

EO case The case for an EO device is similar but subtle differences result in the completely different behavior that the gain depends on the conversion efficiency and thus the parametric pump power. In our device, we deal with an optical resonator with multiple modes, i.e. both sidebands are distinct optical modes and are thereby enhancing the scattering rates of anti-Stokes and Stokes sideband or the beam splitter and the amplification interaction respectively. We assume now that the optical linewidth is smaller than the microwave resonance frequency, the EO device is therefore always in the sideband-resolved regime. This is a fair assumption, given that the microwave resonator is in the regime of a few GHz, whereas mechanical resonators, which are not necessarliy sidebanrd-resolved, typically range from kHz [Gröblacher et al., 2009; Weis et al., 2010; Safavi-Naeini et al., 2011] to GHz [Chan et al., 2012; Qiu et al., 2020; Forsch et al., 2020]. Nevertheless, as the interaction Hamiltonian is the same (eq. 2.52), we can also find a very similar form as in eq. 3.38.

Now we define the suppression of the unwanted sideband as [Sahu et al., 2022]

$$\Gamma^+/\Gamma^- = (1 + C_\mathrm{S})^{-1}. \tag{3.40}$$

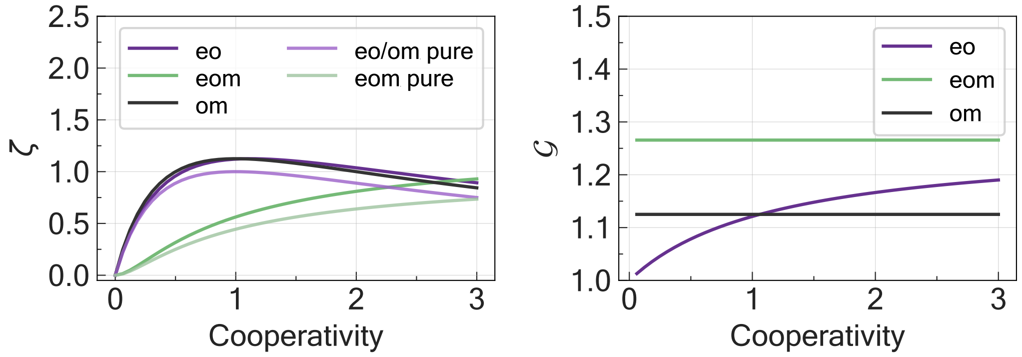

Figure 3.7: **Gain comparison** between a single-stage EO conversion and a single-stage and double-stage conversion process with a mechanical resonators involved. **a**, Conversion efficiency including and excluding (legend entry 'pure') the unwanted amplification interaction with respect to the cooperativity defined as the interaction rate divided by the linewidths of the involved resonators, and a fixed ratio between Stokes and Anti-Stokes scattering rate of $\Gamma^+/\Gamma^- = 0.1/0.9$. We assume $C_{\mathrm{om}} = C_{\mathrm{em}} = C_{\mathrm{eo}}$. While the 'pure' EO/OM conversion reaches its peak conversion efficiency at a cooperativity of 1 and cannot go beyond $\zeta = 1$, this behavior changes if the amplification interaction is taken into account. **b**, The gain $\mathcal{G}$ calculated as the ratio between ζ in panel a) and the respective 'pure' conversion considering only the Anti-Stokes scattering. While OM and EOM gain are only defined by the ratio between Stokes and Anti-Stokes scattering, the EO gain increases with increasing cooperativity.

C_{S} is herein the cooperativity of the coupling between a spurious mode and the unwanted Stokes mode. If the cooperativity is greater unity, the unwanted Stokes modes splits and the is consequently suppressed. Relating this to the relations from the OM case, one obtains

$$\frac{1}{C_{\mathrm{S}}} = \frac{\Gamma^+}{\Gamma^- - \Gamma^+} = \langle n \rangle_{\mathrm{min}} = \mathcal{G} - 1 \tag{3.41}$$

The microwave-optic conversion efficiency in this case is given by

$$\zeta_{\mathrm{eo}} = \frac{4\,C_{\mathrm{eo}}\,(1 + C_{\mathrm{s}}^{-1})^2}{(1 + C_{\mathrm{eo}} + C_{\mathrm{s}}^{-1})^2} = \mathcal{G}^2 \frac{4\,C_{\mathrm{eo}}}{(1 + C_{\mathrm{eo}} + C_{\mathrm{s}}^{-1})^2} \tag{3.42}$$

The occurrence of C_{s}^{-1} in the denominator is the only difference to eq. 3.38 but makes a decisive difference

- $C_{\mathrm{s}} \to \infty$ (minimum gain):
  In case of complete splitting of the unwanted sideband, the Stokes scattering is infinitely suppressed, $\mathcal{G} = 1$ and we have perfect quantum limited conversion
  $$\zeta_{\mathrm{eo}} \underset{C_{\mathrm{s}} \to \infty}{=} \frac{4 C_{\mathrm{eo}}}{(1 + C_{\mathrm{eo}})^2} \tag{3.43}$$
  with a maximum at $C_{\mathrm{eo}} \to 1$
- $C_{\mathrm{s}} \to 0$ (maximum gain):
  In case of equal scattering rates between Stokes and anti-Stokes sideband, the , $\mathcal{G} \to \infty$ and the conversion efficiency scales linearly with the cooperativity following
  $$\zeta_{\mathrm{eo}} \underset{C_{\mathrm{s}} \to 0}{\simeq} 4\,C_{\mathrm{eo}} \tag{3.44}$$

Consequently, for moderate cooperativites, i.e. $C_{\mathrm{eo}} \ll 1$, there is little influence of the unwanted Stokes scattering process and eq. 3.43 and eq. 3.44 show similar results. This is visible in fig. 3.7b (purlple) which shows a clear increase of the EO gain with respect to the cooperativity, in contrast to the OM, EM, and EOM case . Panel (a) shows again the maximum transduction efficiency at $C \approx 1$ (dark purple).

In summary, one can draw to main conclusions: 1) the maximum transduction for a multistage conversion is achieved for $C_{\mathrm{e}} \approx C_{\mathrm{o}} \to \infty$ such as in the EOM transducer, in a single-stage process the maximum transduction is reached for $C_{\mathrm{e}}, C_{\mathrm{o}}, C_{\mathrm{eo}} \approx 1$ (OM, EM, EO). 2) the gain is power-dependent if both resonators are coupled to the waveguide outputs (cf. EO transducer). However, if one of the resonators has only a single intrinsic loss channel (EOM, OM, EM), the gain is independent of the cooperativity and depends only on the ratio of Stokes and Antistokes scattering rate. .

3.7 Conclusion and outlook

In conclusion, we demonstrated an efficient bidirectional and chip-scale microwave-to-optics transducer using pump powers orders of magnitude lower than comparable all-integrated [Fan et al., 2018; Jiang et al., 2020; Forsch et al., 2020] approaches. Low pump powers are desired to limit the heat load of the cryostat and to minimize on-chip heating, which is particularly important for integrated devices because of their limited heat dissipation at millikelvin temperatures. Due to the standard material choice involving only silicon and aluminum, our device can be easily integrated with other elements of superconducting circuits and silicon photonic and phononic devices in the future.

The two main challenges ahead are the reduced pure conversion efficiency and the optical heating that adds incoherent noise to the converted signal. We expect that both can be solved with design improvements in combination with new measurement techniques. Specifically, starting from the observed pure efficiency of 0.019% a factor of up to nearly two orders of magnitude could be gained with better waveguide coupling geometries in combination with fabrication optimization, e.g. by using surface cleaning and the reduction of humidity [Sekoguchi et al., 2014]. Improving the sideband resolution by increasing the mechanical frequency [Kalaee et al., 2019] could yield another factor of up to 25 assuming the same cooperativities can be achieved. Going to the high cooperativity limit would then yield the remaining fraction needed for unity total conversion efficiency. This will certainly require a very effective mitigation of the optical pump power dependent mechanical heating and the associated linewidth degradation that is also required for noise-free conversion. Nevertheless, with better chip thermalization, reduced optical absorption and low duty cycle pulsed measurements this should be feasible. Moreover, it has already been shown that pulsed pump-probe type experiments together with high efficiency heralding measurements can be used for post-selecting rare successful conversion or entanglement generation events for low-noise low-efficiency devices [Forsch et al., 2020; Zhong et al., 2020].

In terms of near-term classical receiver and modulation applications, an important figure of merit is the voltage required to induce an optical phase shift of π. We are able to reach a value as low as $V_\pi = 16\,\mu$V, comparable with typical zero point fluctuations in superconducting circuits and nearly a factor 9 lower than the previously reported record [Bagci et al., 2014]. It is also almost 10^{12} times more power efficient than commercial passive and wide-band unidirectional electro-optic modulators at X band gigahertz frequencies.

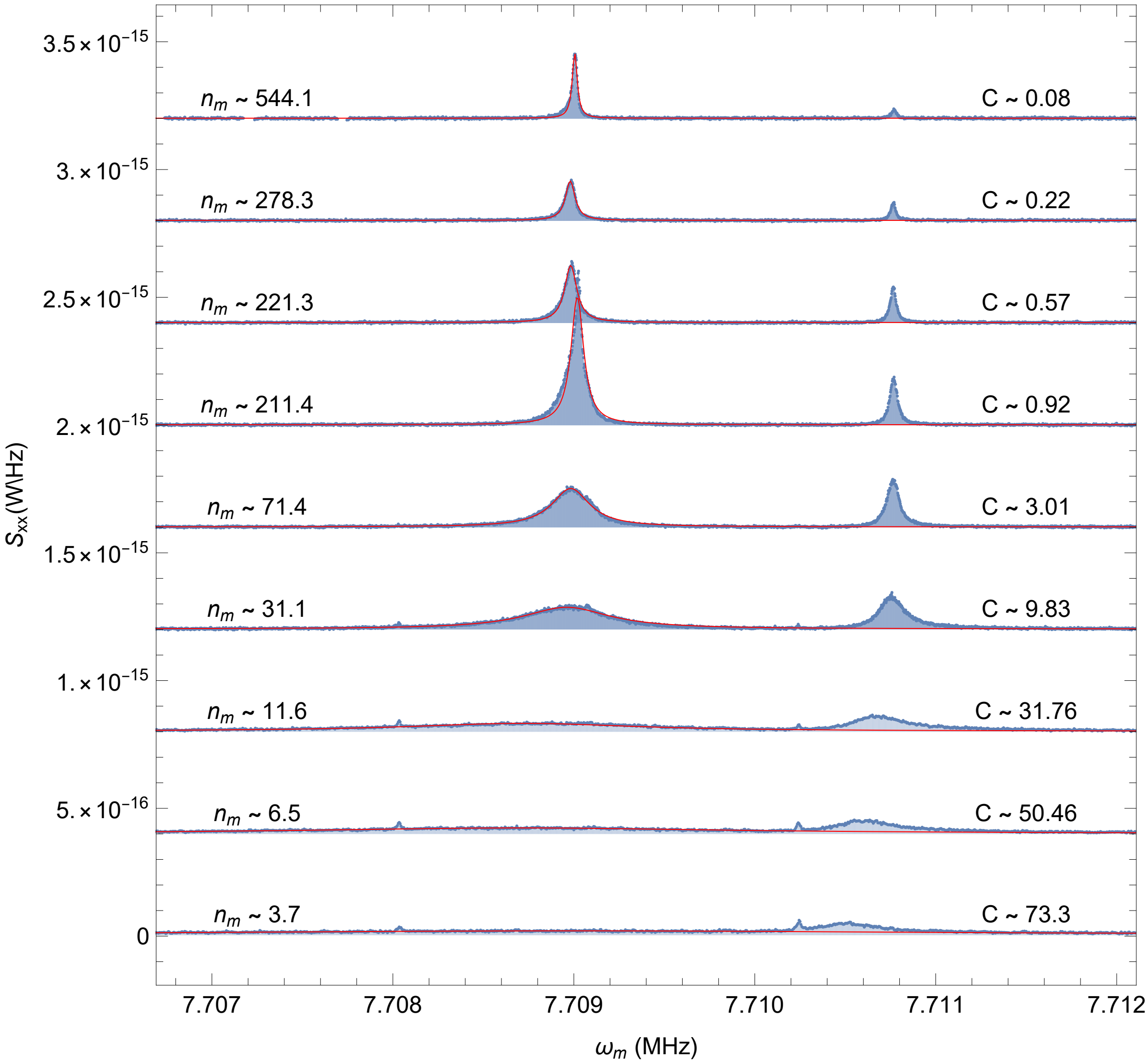

Figure 3.8: **Cooling of an EOM device with $g_{0,\mathrm{em}}/(2\pi) = 160\,\mathrm{Hz}$.** The main in-plane differential mode at $\omega_\mathrm{m}/(2\pi) = 7.709\,\mathrm{MHz}$ is cooled for increasing cooperativities resulting in a reduced area of the mechanical noise spectrum S_xx and an increased total linewidth $\gamma_\mathrm{m}+\Gamma_\mathrm{em}$. For high cooperativities and Γ_em respectively, the increased linewidth starts to overlap to a spurious neighbouring mode with lower EM coupling. This spurious mode at higher temperature eventually prevents ground state cooling with the available drive powers.

3.8 Overcoming the sideband-unresolved-limitation in the converter

Several methods have been proposed to overcome the fundamental problem of OM cavities not operating in the sideband-resolved regime, e.g. the usage of squeezed pumps [Lau and Clerk, 2020] or Floquet engineering [Qiu et al., 2020]. Due to the limited squeezing and applicable pump strength because of absorption-induced heating effects, we followed a different strategy tailored to our converter in order to account for the non-sideband resolved cavity of our converter.

One important goal of such microwave-optic converters is - besides the efficient conversion of signals between optical and microwave frequencies - the creation of remote entanglement between distant microwave quantum nodes in different cryogenic units. A well-known protocol

to establish such an entanglement is to create entanglement between a microwave qubit and a travelling microwave photon, converting such a microwave photon to optical frequencies, sending it to the second node, converting it there again to microwave frequencies and mapping the state on a qubit in the second node ('*direct conversion entanglement protocol*', see also section 5.1.1). This deterministic protocol requires a total minimum efficiency of 50% and an added noise of < 0.5, whereas the added noise is referred to the input added noise after the creation of the initial microwave photon. These conditions are out-of-reach for all currently available platforms. However, a probabilistic protocol with less stringent requirements on the performance of the microwave-optic interface produces entangled or two-mode-squeezed (TMS) microwave-optic photon pairs at both cryogenic nodes. The optical photons are interfered on a beam splitter and measured on optical single photon detectors. For low success rates and therefore a low probability to detect two optical photons at the same time, a single click erases the 'which-path' information and entangles the microwave photons at each nodes. This entanglement is transferred towards a qubit-qubit entanglement ('*TMS-based entanglement protocol*', section 5.1.3).
Consequently, a crucial feature of a microwave-optic interface is the creation of TMS microwave-optic photon pairs. In our EOM device, we can make use of the fact that the EM part is sideband-resolved and could therefore cool the mechanical oscillator to the ground state. If then an optical, not sideband resolved pump pulse arrives further cooling or Anti-Stokes scattering is prohibited because the device is already in the quantum ground state. Hence, the optical pulse creates entangled microwave-optic photon pairs as needed for the TMS-based entanglement protocol.

Ground-state cooling The theoretical minimal occupation is given by eq. 3.18 and becomes for a microwave drive detuned by $\Delta = \omega_\mathrm{m}$ applied to this specific device with the parameters from tab. 3.1 and a maximum photon number of 10^5 photons $\langle n\rangle_\mathrm{min} < 0.01$ phonons. Thus, the sideband resolution of the microwave-optical interface is sufficient to cool the device into its ground state. However, the device is exposed to a finite thermal environment despite the cooling capacities of the dilution refridgerator. Since the device did not perfectly thermalize to the base plate of the dilution unit at a temperature of $<10\,\mathrm{mK}$ (fig. 2.6g-h), the temperature of the mechanical mode is higher and we extracted a bath temperature of $150\,\mathrm{mK}$. In such a regime, the final occupation of an electromechanically sideband cooled mechanical oscillator [2] is [Aspelmeyer et al., 2014]:

$$\langle n\rangle = \frac{\Gamma_\mathrm{em}\langle n\rangle_\mathrm{min} + \gamma_\mathrm{m}\bar{n}_\mathrm{th}}{\Gamma_\mathrm{em} + \gamma_\mathrm{m}} \tag{3.45}$$

with the mechanical coupling rate γ_m to the thermal bath with occupation $\bar{n}_\mathrm{th}$ and the EM damping rate $\Gamma_\mathrm{em} = \Gamma^- - \Gamma^+$ with Stokes and anti-Stokes scattering rate $\Gamma^\pm$ as defined in eq. 3.36. The final mechanical occupation becomes then $\langle n\rangle \approx 20$ photons, again for a intra-cavity drive photon number of $\bar{n}_{cav} = 10^5$. There are now several options to reduce the mechanical occupation that can be controlled by the experimental parameters or the design. They may include but are not limited to

- Improve the thermalization to the fridge and thereby reduce the bath temperature
- Increase the microwave drive power

---

[2] it naturally applies also to OM sideband cooling

- Reduce the mechanical coupling to the bath
- Increase the EM coupling strength g_0

We successfully reduced the bath temperature to $70\,\mathrm{mK}$ but this reduces the final phonon occupation to only $\langle n \rangle \approx 9$ phonons. Even a theoretically achievable bath temperature of $10\,\mathrm{mK}$ does not allow ground state cooling with $\langle n \rangle \approx> 1$. Consequently, this is one important but not sufficient improvement.

Our microwave circuits on superconducting thin film aluminum showed an increase in the intrinsic linewidth κ_{in} for drive photon numbers $\bar{n}_{cav} > 10^5$. This is usually attributed to self-heating effects due to the dissipated fraction of the drive κ_{in}/κ [Mittal et al., 2024] which is particularly a problem for samples with a weak thermal link to the refrigerator base plate or small thermal conductivity. Both applies to our SOI sample at the mK environment. Since other materials with more resilience to heating such as niobium or niobium titanium nitride were not available at that time in our nanofabricaiton facility, we kept being limited to $\bar{n}_{cav} > 10^5$.

We tried to reduce mechanical losses already by the tuning fork geometry in our design, which minimizes the clamping losses. A further reduction involving a phononic shield for MHz frequencies [Tsaturyan et al., 2014; Yu et al., 2014] was found to be impractical in connection with the additional circuit elements because of the large dimensions and a further reduced mechanical stability of the $220\,\mathrm{nm}$ thick silicon membrane with an enhanced risk of bending and coupling to undesired out-of-plane mechanical modes.

The last option was an improvement of the EM coupling strength. This is particularly advantageous because the EM scattering rate Γ_{em} in eq. 3.45 exhibits a quadratic dependence on it (eq. 3.36). The strong dependence on the capacitor plate distance with $x^{-1.5}$ [Barzanjeh et al., 2019] could not be exploited because the typical gap width of $70\,\mathrm{nm}$ is already the lower bound without sacrificing the fabrication yield due to shortened capacitors. Secondly, the thickness of the capacitor plates was more or less set by the desired thickness of the aluminum electrodes and the top silicon layer of our SOI waver. Hence, we extended the length of the capacitor strings to increase the EM coupling. This increase also overcompensates the concomitant reduction in mechanical frequency and, thus, the increase in mechanical occupation at a given temperature. While former increased to $g_{0,\mathrm{em}}/(2\pi) = 160\,\mathrm{Hz}$ and thereby by a factor 2.4, the mechanical frequency decreased to $\omega_{\mathrm{m}}/(2\pi) \approx 7.7\,\mathrm{MHz}$ equivalent to a reduction of 35 % which relates to a similar increase in the thermal-equillibrium occupation to the bath temperature.

Fig. 3.8 shows a typical cooling spectrum for such a high $g_{0,\mathrm{em}}$ device. The increase in total mechanical linewidth $\gamma_{\mathrm{m}} + \Gamma_{\mathrm{em}}$ is evident. As a consequence of the cooling tone due to the beam splitter interaction (eq. 2.29), the area proportional to the $\sqrt{T_{\mathrm{m}}}$ gets reduced. Unfortunately, besides the expected modes (cf. fig. 2.5d) we see spurious modes in close proximity. We attribute this splitting to hybrid out-of-plane coupling due to a slight bending of the membrane, which is also visible in optical microscopy and SEM. These spurious modes that were observed in all devices to different extend eventually prohibited a successful ground state cooling and the application of a TMS-based entanglement protocol to create entangled photon pairs in the microwave and optical domain with further application in the establishement of remote entanglement between superconducting qubits.

Finally, another constraint of this device, the only moderate bandwidth, could not be resolved due to the limited pump power. Higher optical and microwave pump pulses both led to a decrease of the microwave resonator quality factor. The maximum microwave-optic conversion bandwidth comprising the intrinsic linewidth, EO and OM damping rate (cf. 3.1.3) was still limited to $10\,\mathrm{kHz}$. This number is still hardly compatible with typical qubit lifetimes and especially orders of magnitude above typical time scales for gate pulse lengths in superconducting qubit architectures.

CHAPTER 4

All-optical state readout of a superconducting qubit with an electrooptic interface

Acknowledgements As this project combines almost all aspects of the Fink group from superconducting qubits, microwave-optic transducers and optical setups and measurements, I would like to thank the whole team to enable this experiment in an collaborative effort. Special thanks to my colleague Thomas for his unwavering calmness combined with his rigorous way of working.

Superconducting qubits have demonstrated fantastic achievements and are one of the most mature platform for quantum computers. However, a significant drawback is the requirement for ultra-low temperature environments. Today's cryogenic technology can routinely provide these environments, but the available cooling power drops significantly at lower temperatures. In our commercial dilution refrigerator, a Bluefors LD250, the cooling power of $0.5\,\mathrm{mW}$ at $100\,\mathrm{mK}$ reduces to $20\,\mathrm{\mu W}$ at $20\,\mathrm{mK}$. There are impressive efforts to build modular systems and use several cooling units. The power of each unit, however, cannot be drastically increased. This becomes a serious limitation for current qubit systems with multiple logical qubits accompanying an exponential scaling with the number of actual physical qubits and the number of control lines.
Consequently, besides the creation of remote entanglement between separate dilution units, such microwave-optic interfaces may also find application for readout and control of superconducting qubits.

The increasing demand for higher data transfer rates and energy efficiency alike has set the path to replacing electrical components by their optical counterparts. This is because of the substantially larger bandwidth of optical signals and the exceptionally low transmission loss in fibers at telecom wavelengths. Recently, this transition affects not only long-distance communication but also short-range links within data centers [Cheng et al., 2018] or even on a single chip [Sun et al., 2015]. Moving the processors into a cryogenic environment can decrease the power consumption of computation even further [Holmes et al., 2013], increase the sensitivity of detection systems [de Cea et al., 2020], and interface classical control systems with cryogenic quantum processors directly [Pauka et al., 2021]. However, such an approach is also susceptible to transmission losses and related heating in electrical wires and thus might also benefit from a suitable, low-loss and low thermal conductivity optical [Shen et al., 2024] or contactless [Wang et al., 2023] links.

Quantum processors, such as superconducting platforms that operate at ultra-low temperatures of a few millikelvin, have particularly demanding I/O requirements. In stark contrast to classical processors, herein the number of external control and readout lines scales linearly with the number of qubits. Currently, the most powerful quantum processors utilize more than 100 qubits requiring hundreds of high-bandwidth coaxial cables with appropriate signal conditioning [Kim et al., 2023], i.e. attenuation and careful thermalization on the input as well as isolation and low noise amplification on the output, see fig. 4.1a. Considering the limited cooling power of dilution refrigerators, this architecture might allow for thousands of qubits [Krinner et al., 2019] given that advanced multiplexing strategies are employed [Chen et al., 2012; Heinsoo et al., 2018; Acharya et al., 2023]. This is - ignoring space and financial constraints - still orders of magnitudes beneath the millions of qubits expected to be required for fault-tolerant universal quantum computing [Gidney and Ekerå, 2021; Bravyi et al., 2022; Hoefler et al., 2023].

Searching for ways to overcome these barriers, photonic links [Youssefi et al., 2021; Lecocq et al., 2021; Joshi and Moazeni, 2022] were identified as a promising alternative to conventional [Krinner et al., 2019], cryo-CMOS [Pauka et al., 2021] or single flux quantum control [Liu et al., 2023] of cryogenic quantum computing platforms. The first optical interconnect with a superconducting qubit detected the average optical power emitted from the qubit - a destructive measurement that prevented further use of the qubit state [Mirhosseini et al., 2020]. Low back-action qubit readout has also recently been shown with a mechanically mediated electro-optical interconnect [Delaney et al., 2022] in a scheme comparable to fig. 4.1b, but this relatively low bandwidth method necessitates additional microwave pumps with the associated heat load and isolation requirements. Ultra-high bandwidth readout of an electro-mechanical system has been demonstrated with a commercial electro-optic modulator operated at 4 K but with limited efficiency and noise performance [Youssefi et al., 2021]. On the input side, high-speed photodetectors have been used to demodulate microwave control and readout signals [Lecocq et al., 2021]. This is a promising approach for multiplexed control but necessarily dissipative and does not allow to convert the readout signals back to the optical domain.

4.1 Superconducting qubit readout schemes

4.1.1 Microwave readout model

We model the microwave system consisting of the cQED cavity and the transducer microwave cavity as two cascaded cavities with reflective ports (coupling $\eta\kappa$) and intrinsic loss rates $(1-\eta)\kappa$. Specifically, the microwave readout field from the cQED cavity $\hat{a}_{c,\mathrm{out}}(t)$ travels through superconducting cables of efficiency $\eta_{e,c}$ and delay τ, and enters the microwave cavity of the electro-optical transducer with $\hat{a}_{e,\mathrm{in}}(t) = \eta_{e,c}\hat{a}_{c,\mathrm{out}}(t+\tau)$ [Gardiner, 1993].

If we send the specific readout power to the cQED device, at which the Jaynes-Cummings nonlinearity allows to detect the qubit state (cf. chapter 2.4.3 and specifically fig. 2.8c), the cQED cavity is either on-resonant with the transducer cavity ($\omega_e = \omega_c$, excited state) or completely reflective (ground state). We model the latter by a detuning χ_0. Hence, the equations of motion for the transducer microwave cavity and the microwave cavity coupled to the qubit can be written as

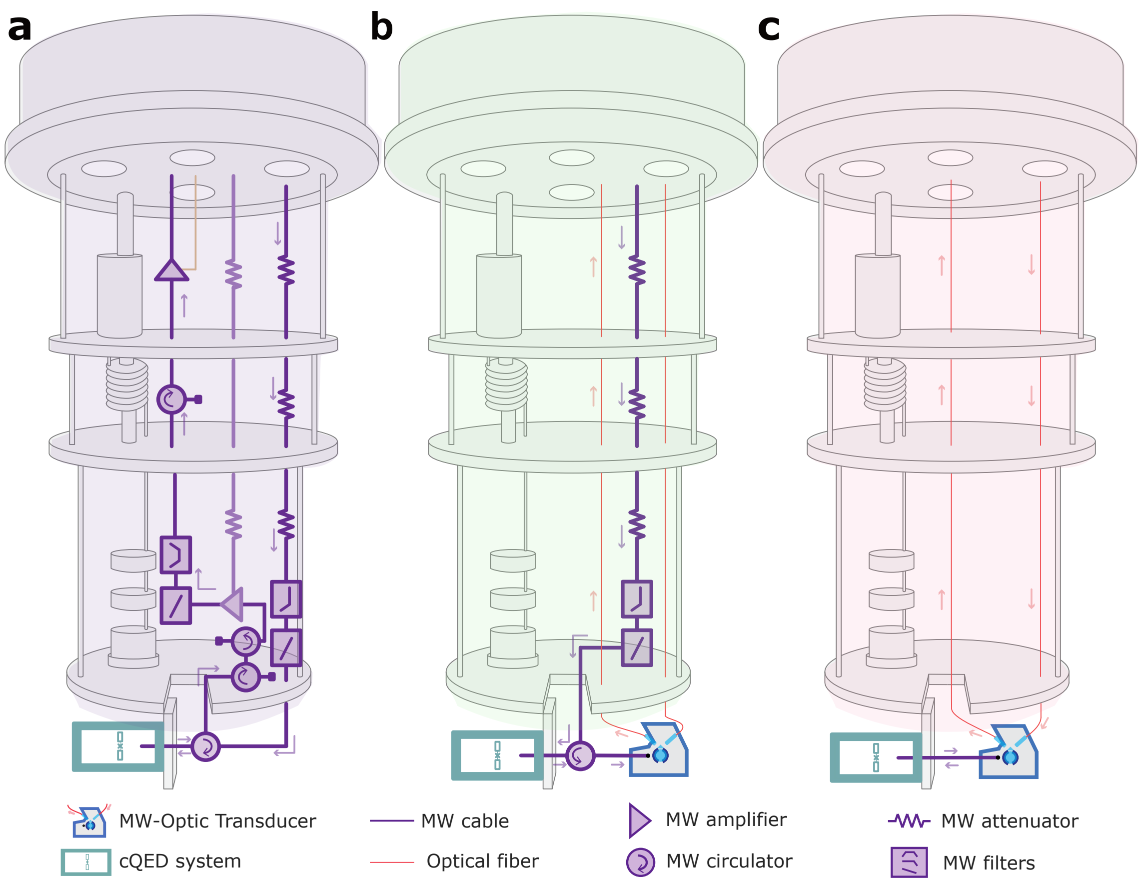

Figure 4.1: **Comparison of conventional and optical qubit readout setups in a dilution refrigerator.** **a**, microwave in - microwave out: Typical setup consisting of carefully thermalized coaxial cables, attenuators, filters, circulators, a directional coupler, a driven parametric amplifier, and a dc-biased high-electron-mobility-transistor amplifier, all of which are approximately wavelength sized (centimeters). **b**, microwave in - optics out: Reduced readout setup replacing the active microwave output components with an optically driven, resonant electro-optic transceiver. **c**, optics in - optics out: all-optical, circulator-free qubit readout based on simultaneous microwave down- and up-conversion of an optical carrier. Here, all cryogenic microwave components are replaced by a single electro-optic transceiver. Figure adapted from [Arnold et al., 2023].

$$\frac{d\hat{a}_e}{dt} = -\frac{\kappa_e}{2}\hat{a}_e + \sqrt{\eta_e\kappa_e}\eta_{e,c}\hat{a}_{c,\mathrm{out}}, \tag{4.1}$$

$$\frac{d\hat{a}_c}{dt} = \left[-i\frac{\chi_0}{2}(\langle\hat{\sigma_z}\rangle + 1) - \frac{\kappa_c}{2}\right]\hat{a}_c + \sqrt{\eta_c\kappa_c}\hat{a}_{c,\mathrm{in}}. \tag{4.2}$$

We model the system using decoupled equations assuming the signal propagation is unidirectional. This is a reasonable assumption because of the microwave circulator between both cavities. We want to stress again that this is only a phenomenological model to describe the behavior of the system at the specific power chosen for the Jaynes-Cummings readout.

4.1.2 Microwave-optical readout model

The microwave-optical readout of the qubit state is enabled by converting the microwave field from the cQED system into the optical domain using the electro-optic transducer. This allows for efficient conversion from microwave to optical fields. The electro-optic device is driven by a resonant optical pump pulse, with dynamics given by,

$$\frac{d\bar{a}_p}{dt} = \left(i\Delta_p - \frac{\kappa_p}{2}\right)\bar{a}_p + \sqrt{\eta_p\kappa_p}\bar{a}_{p,\mathrm{in}}, \tag{4.3}$$

The dynamics of the multi-mode electro-optic device can be described by the quantum Langevin equation,

$$\begin{aligned}
\frac{d\hat{a}_e}{dt} &= -\frac{\kappa_e}{2}\hat{a}_e - ig\hat{a}_o - ig^*\hat{a}_s^\dagger + \sqrt{\eta_e\kappa_e}\hat{a}_{e,\mathrm{in}}, && (4.4)\\
\frac{d\hat{a}_o}{dt} &= \left(i\delta_o - \frac{\kappa_o}{2}\right)\hat{a}_o - ig\hat{a}_e, && (4.5)\\
\frac{d\hat{a}_s}{dt} &= \left(i\delta_s - \frac{\kappa_s}{2}\right)\hat{a}_s - ig^*\hat{a}_e^\dagger - iJ\hat{a}_{\mathrm{tm}}, && (4.6)\\
\frac{d\hat{a}_{\mathrm{tm}}}{dt} &= \left(i\delta_{\mathrm{tm}} - \frac{\kappa_{\mathrm{tm}}}{2}\right)\hat{a}_{\mathrm{tm}} - iJ\hat{a}_s. && (4.7)
\end{aligned}$$

where $a_{e,in}$ denotes again the output field from the cQED cavity and $g(t) = \bar{a}_p(t)g_0$ the cavity enhanced electro-optical coupling rate. We note that, $J \ll \kappa_s$ in our device. The qubit state is verified by the converted optical Stokes output field from the electro-optic device,

$$\hat{a}_{o,\mathrm{out}}(t) = -\sqrt{\kappa_{o,\mathrm{ex}}}\hat{a}_o(t). \tag{4.8}$$

4.1.3 All optical readout model

The full optical readout of the superconducting qubit is realized by sending an optical signal together with an optical pulse to the electro-optic transducer. The converted microwave signal is used for qubit readout and reflected back to the electro-optic transducer. The reflected microwave field is subsequently converted again into the optical domain. The dynamics of the electro-optic device from eq. 4.4-4.7 is now related to the cQED system by

$$\begin{aligned}
\hat{a}_{e,\mathrm{in}}(t) &= \eta_{e,c}\hat{a}_{c,\mathrm{out}}(t), && (4.9)\\
\hat{a}_{c,\mathrm{in}}(t) &= \eta_{c,e}\hat{a}_{e,\mathrm{out}}(t). && (4.10)
\end{aligned}$$

The superconducting qubit state thus can be verified from the reflected optical anti-Stokes field,

$$\hat{a}_{o,\mathrm{out}}(t) = \hat{a}_{o,\mathrm{in}}(t) - \sqrt{\kappa_{o,\mathrm{ex}}}\hat{a}_o(t). \tag{4.11}$$

4.2 Dynamics and single-shot fidelity

4.2.1 Comparison of microwave, microwave-optic and all-optical readout

We start with a comparison of the three different readout methods schematically depicted in fig. 4.1: (i) *all-microwave readout* (fig. 4.2a) with a microwave tone sent through coaxial cables to the cQED system and detected with a standard microwave heterodyne setup, (ii) *microwave-optic readout* with optical detection of the same microwave signal as in (i) from the cQED component after using it for the modulation of laser light via the EO transceiver

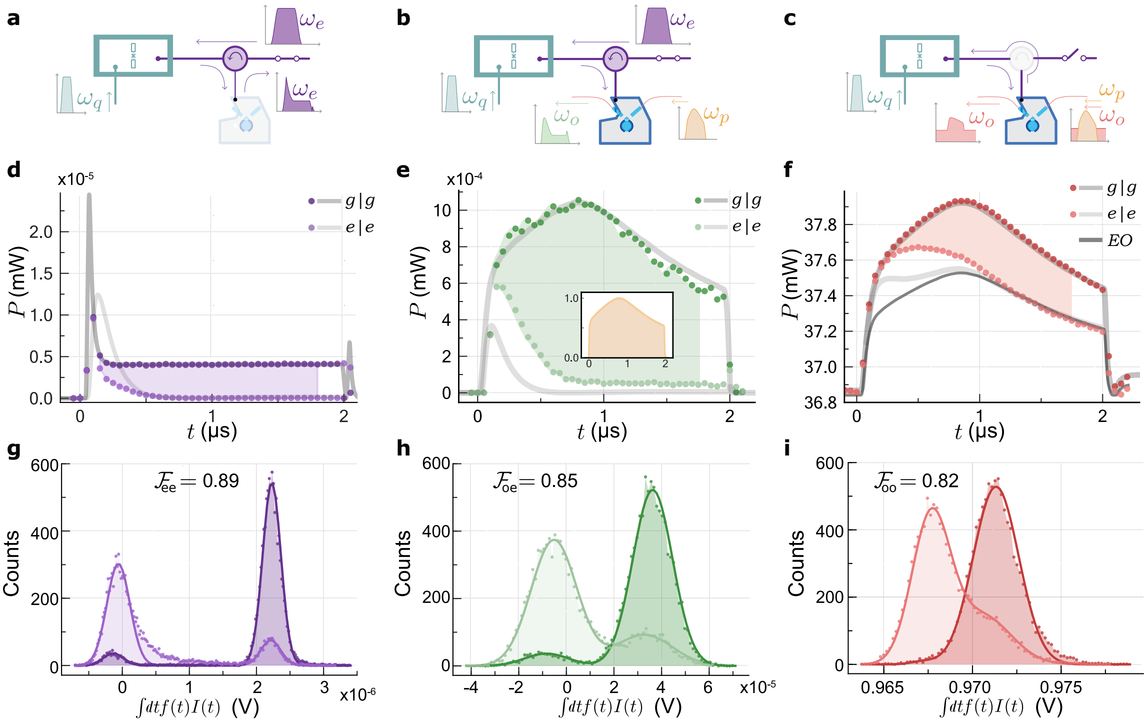

Figure 4.2: **Conventional and optical single-shot readout of a superconducting qubit. a,b,c**, Sketches of the different readout schemes involving a microwave cavity with bare resonance frequency ω_c and dispersively coupled to a transmon qubit (cQED system in jade) and the electro-optical transceiver, consisting of a second microwave cavity (blue/gray) at $\omega_e = \omega_c$ coupled to an optical whispering gallery mode resonator (light blue). The qubit state is prepared via a separate port at ω_q. The electro-optic transceiver is operated with an optical pump pulse at ω_p to parametrically enhance the interconversion of microwave ω_e and optical ω_o signals. **a**, Conventional microwave readout: a microwave pulse probes the cQED system and is detected via microwave heterodyne detection. **b**, Optical detection of a microwave readout tone: the microwave pulse reflected from the cQED system is upconverted to the optical domain and detected with optical heterodyne detection. **c**, All-optical readout: a modulated optical carrier is converted to the microwave domain to probe the cQED system. Its reflection is simultaneously converted back to the optical domain and detected with an optical heterodyne setup. **d, e, f**, Averaged time traces of the correspondingly measured heterodyne signal powers postselected on successful measurements of the prepared qubit state ($g|g$ and $e|e$) based on 15,000 independent trials. Gray lines show theoretical predictions which are expected to deviate for $|e\rangle$ before steady state is reached (see text and SI). The inset in **e** is a normalized measurement of the optical pump power. **f** shows additionally the simulated optical response of the electro-optic converter without the reflection from the cQED system ('EO'). The shaded area highlights the difference between both qubit state readouts, which serves as the weighting function $f_q = q_e - q_g$ with $q \in Q, I$ for the temporal quadrature integration. **g, h, i**, Corresponding histograms of 15,000 single-shots obtained by integrating the weighted in-phase quadrature $f(t)I(t)$ with the corresponding state assignment fidelities $\mathcal{F}_{ij}$. Figure adapted from [Arnold et al., 2023].

(fig. 4.2b), and (iii) *all-optical readout*: We send modulated light to the EO transceiver. The demodulated microwave pulse enters the cQED system and its reflection is converted back into the optical domain using the same EO transceiver before being analyzed with an optical heterodyne detector at room temperature (fig. 4.2c). All three schemes can be realized without setup changes except for the state of a cryogenic RF switch, as shown in fig. 4.2a-c. While the first two methods can be performed simultaneously, opening the RF switch prevents the optically demodulated microwave signal in the all-optical readout from entering the microwave output line, which also effectively removes the circulator.

The operation frequency of the photonic link is determined by its optical free-spectral range $\omega_{\mathrm{FSR}}/(2\pi) = 8.8065$ GHz set by the diameter of the $\mathrm{LiNbO_3}$ resonator. To achieve a triply-resonant configuration that maximizes the transduction efficiency, we tune the electro-optic microwave cavity in resonance $\omega_{\mathrm{e}} = \omega_{\mathrm{FSR}}$ [Rueda et al., 2016]. Similarly, to maximize the dispersive qubit readout efficiency [Wallraff et al., 2005] we also tune the cQED cavity to the same frequency $\omega_{\mathrm{c}} = \omega_{\mathrm{FSR}}$. Both are implemented with a piezoelectric actuator.

The transmon qubit with anharmonicity $\nu/(2\pi) = 201$ MHz is alternately prepared in its first excited state $|e\rangle$ or thermalized in its ground state $|g\rangle$ by selectively applying a flat-top-Gaussian microwave pulse of duration 104 ns at the qubit transition frequency $\omega_{\mathrm{q}}/(2\pi) = 6.625$ GHz via a dedicated drive line, as shown in fig. 4.2a-c. The readout tone, on the other hand, is either applied via filtered and attenuated input coaxial lines (fig. 4.2a-b) or directly generated by the electro-optic transceiver (fig. 4.2c) via resonantly enhanced optical down-conversion [Sahu et al., 2022]. The readout amplitude corresponding to approximately $\sqrt{n_{\mathrm{meas}}} = 122\ \mathrm{photons}^{1/2}$ in the cavity is chosen to optimally benefit from the Jaynes-Cummings nonlinearity of the qubit-cavity system [Bishop et al., 2010; Boissonneault et al., 2010] that maps the qubit-state-dependent dispersive frequency shift of the resonator $\chi/(2\pi) = 6.6$ MHz into a large readout amplitude difference at the bare cQED cavity frequency ω_e, see fig. 2.8 for details. The latter allows for single-shot readout of the the standard Transmon qubit state with an increased signal-to-noise ratio and without a quantum limited amplifier [Reed et al., 2010].

Figure 4.2d shows the averaged reflected amplitude in power units postselected on measuring the prepared state from heterodyne detection for the all-microwave readout. The measured dynamics with the qubit initialized in its ground state is in excellent agreement with the input-output relations of the transducer microwave cavity reflection alone (dark gray line), revealing that the cQED cavity does not exhibit a resonance at the readout frequency ω_{e}. In contrast, when the qubit is prepared in the excited state, the cQED cavity resonance appears at the bare resonance frequency with $\omega_{\mathrm{c}} \approx \omega_{\mathrm{e}}$ and the reflected power decreases (light gray line). While the initial dynamics are out of reach to be modeled given the high photon numbers, we adopt a simple cascaded cavity model between the cQED cavity and the EO microwave cavity [Gardiner, 1993], cf. also chapter 2.4.3 and fig. 2.8 for more details. This accurately predicts the steady-state result after times $> 1.0\ \mu$s without free parameters (light gray) and consequently the readout contrast between both states. We then use these averaged measurements to optimize the quadrature rotation and the integration weights as the difference between the response of both states (shaded region in fig. 4.2d) to maximize the distinguishability for the single-shot-readout.

The corresponding single-shot histograms from 1.5×10^4 independent measurements for each qubit state are shown in fig. 4.2g with double-Gaussian fits to extract the relevant errors [Walter et al., 2017]. The maximum state assignment fidelity of $\mathcal{F}_{ee} = 1 - (P(e|g) + P(g|e))/2 = 0.89 \pm 0.01$, is reached after an integration time of 1.8 μs, with $P(x|y)$ being the probability to measure the qubit in state $|x\rangle$ after preparation of state $|y\rangle$. The clear separation between the two distributions indicates a negligible overlap error ($\epsilon_{ol,e} < 10^{-10}$). The ground state error ($\epsilon_{g,e} \approx\ 7\ \%$) originates partly from thermal excitation ($1.5\ \%$ as quantified below), while the rest is attributed to transitions induced by the comparably long high power readout pulse [Sank et al., 2016]. The excited state readout results in an error of $\epsilon_{e,e} \approx\ 16\ \%$. Interestingly, the asymmetric tail in the excited state Gaussian towards the ground state distribution originates from switching before steady-state is reached and not from qubit decay due to the limited coherence as in the low-power limit (cf. chapter 4.2.2).

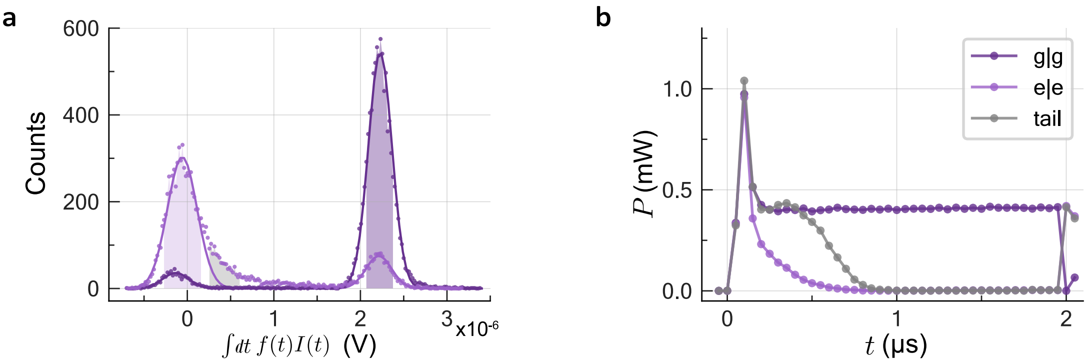

Figure 4.3: **Skewed excited state distribution.** **a**, The histograms of a Jaynes-Cummings microwave readout from fig. 2g in the main text. Shaded regions mark selections for prepared and measured excited states (light purple), excited and measured ground states (purple) and the region (gray) where it significantly deviates from double-Gaussian fits (lines). **b**, Averaged coherent power for the respective selection highlighted in panel a. The skewness of the excited state population histogram arises from 'double' or 'delayed' switching of the cavity reflection which initially follows the ground state response before switching to the excited state cavity reflection.

For a direct comparison, we simultaneously also read out a small part of the reflected microwave readout tone optically, as shown in fig. 4.2b. After resonantly enhanced microwave to optical conversion [Sahu et al., 2022], in which about 3% of the intra-cavity microwave photons are converted, we perform optical heterodyne detection, which yields the averaged time traces shown in fig. 4.2e. In comparison to the microwave readout, we find slower dynamics due to the limited conversion bandwidth of ≈ 10 MHz for the optical readout signal at $\omega_o/(2\pi) = 193.4$ THz. Additionally, the shape of the optical pump pulse with peak power ≈ 140 mW at frequency $\omega_p = \omega_o - \omega_{\mathrm{FSR}}$ (inset in fig. 4.2e) is therefore imprinted on the optical readout signal because it parametrically enhances the microwave-optic transduction in very good agreement with theory for the ground state (dark gray line). We attribute the deviation of the steady-state coherent power for the excited state (light gray line) to imperfections in our optical phase correction for weaker optical powers. The separation between the single-shot state distributions decreases (fig. 4.2h), resulting in a larger overlap error of $\epsilon_{ol,eo} = 2\%$ and a slightly reduced microwave-optical state assignment fidelity of $\mathcal{F}_{oe} = 0.85 \pm 0.01$.

Finally, also in case of the all-optical readout the optically demodulated microwave tone (corresponding to $\sqrt{n_{\mathrm{meas}}} = 116\ \mathrm{photons}^{1/2}$ in the cQED cavity) results in well-distinguished state dependent trajectories as shown in fig. 4.2f. The large optical background signal is due to the cumulative reflection of the optical input e.g. at the coupling prism. The bandwidth of the EO transceiver now also slows down the dynamics of the build-up of microwave readout photons. Additionally, electro-optically induced transparency [Qiu et al., 2023b] raises the signal levels during the optical pulse, visualized as the simulated optical reflection of this EO transducer if there was no cQED system connected (dark line "EO"). In total, this leads to excellent agreement between the measured data and theory (light gray and gray lines). The moderate reduction of fidelity $\mathcal{F}_{oo} = 0.82 \pm 0.01$ can be fully attributed to the larger overlap error between the state distributions shown in fig. 4.2i. This result proves the feasibility of an isolator-free qubit readout without cryogenic microwave components.

4.2.2 Time-dynamics and errors in the Jaynes-Cummings readout

Before we investigate time - resolved qubit measurements, we want to discuss novel insights into the Jaynes-Cummings readout, which have - to the best of our knowledge - not been

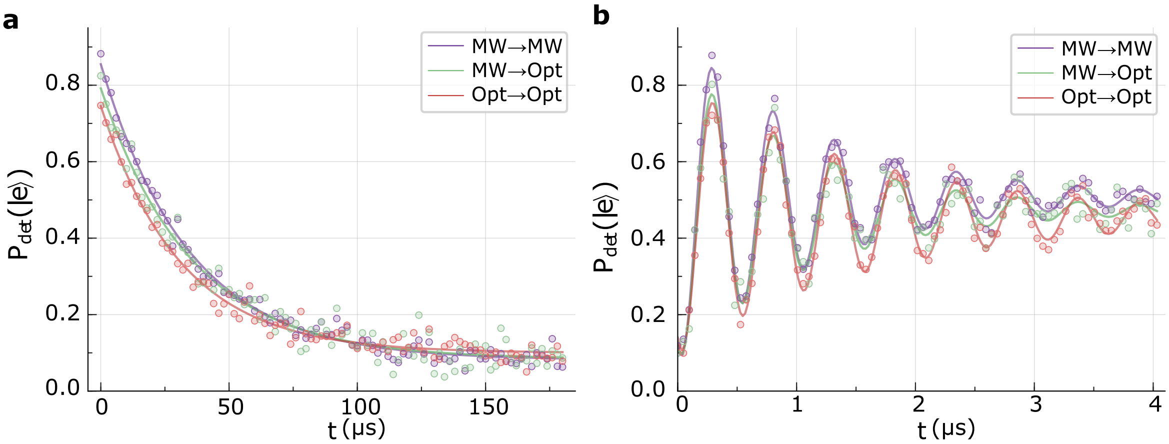

Figure 4.4: **Qubit coherence for different readout methods.** **a**, Measured excited state detection probability $P_{\mathrm{det}}(|e\rangle)$ after a π pulse for varying measurement delays t using the three different readout methods shown in fig. 4.2. **b**, Measured Ramsey oscillations using two $\pi/2$ pulses separated by a variable delay t and detuned by ≈ 2 MHz from the qubit transition for the three readout methods. Figure adapted from [Arnold et al., 2023].

presented yet. The histograms for the excited state measurements in the Jaynes-Cummings readout reveal an asymmetric distribution which is particularly visible for the well-separated peaks in the all-microwave readout (fig. 4.3a, cf. also fig. 4.2g). In the dispersive low-power readout, such an asymmetry arises typically from decays during the readout due to a limited longitudinal coherence time T_1. The high power Jaynes-Cummings readout, however, is latching and remains in its states until the readout tone is switched off. Thus, the response should not suffer from the exponential qubit decay. fig. 4.3b shows the averaged time traces for three distinct regions in the histograms shaded by the corresponding color in panel a: 1) single-shot readout traces of a qubit prepared in the ground state that yielded a value within the FWHM of the corresponding peak (purple), 2) Values that fall within the FWHM of the excited state histogram peak after the qubit was prepared in the excited state (light purple), and 3) single-shot traces that form the asymmetric tail of the excited state histogram. Interestingly, the asymmetric tail in the excited state histogram arises from a deviation at the beginning of the readout pulse rather than the end which is typical for a standard low-power dispersive readout. The averaged response for these cases (excited qubit state prepared) approaches first the ground-state readout response and switches then later irreversibly to the excited state readout signal. Further investigations are necessary to gain more insights in this behavior. While the frequency spectrum has been qualitatively predicted by theoretical models [Bishop et al., 2010; Boissonneault et al., 2010], the temporal dynamics of the Jaynes-Cummings readout are still theoretically and experimentally rather unexplored.

4.3 Time-dependent qubit measurements

We use all three readout methods to extract the longitudinal T_1 and transverse relaxation time T_2^* of the superconducting qubit, based on 2,000 preparations with a 10 Hz repetition rate. Figure 4.4a shows the energy relaxation after a π-pulse yielding a consistent T_1 of 31.1 to 35.4 μs for the three readout types. The observed differences are in line with expected T_1 variability over the course of days. The individual signal-to-noise ratio and resulting confidence level is very similar for all three measurements and the slightly reduced contrast is expected due to the previously extracted $\mathcal{F}_{ij}$.

Similar conclusions can be drawn from the measured exponential decay of the Ramsey oscillations shown in fig. 4.4b. The fitted mean transverse decays for all three measurements, $T_2^* = 1.16 - 1.73\ \mu$s, are comparable. The all-optical readout yields the longest coherence. The comparably low T_2^* is limited by shot noise from residual cavity photons [Clerk and Utami, 2007; Rigetti et al., 2012] owed to the strong qubit-cavity coupling and small detuning. We attribute the remaining discrepancy to the theoretical limit ($T_{2,max}^* \approx 4\ \mu$s) to fabrication and design-related issues, as a Hahn-echo measurement of $T_{2,\text{echo}} = (1.40 \pm 0.09)\ \mu$s, 3σ fit confidence interval, excludes a low frequency, e.g. mechanical, noise origin. Moreover, we observe the same coherence times when the readout laser is turned off, or when the optical pulse is applied during the qubit state preparation, as discussed below. Our measurements, therefore, clearly demonstrate the integrity of superconducting qubit coherence using a photonic readout.

Origin of the high qubit dephasing rate

In follow-up measurements, which are only qualitatively comparable due to setup changes, we identified the temperature of the microwave input line as one major contribution to the effective thermal occupation of the resonator resulting in photon shot noise dephasing of the qubit. By varying the extrinsic coupling of the microwave resonator and performing Hahn-echo measurements [Sears et al., 2012], we could not only calculate an effective resonator temperature for each η_e assuming that thermal shot noise dephasing limited $T_{2,\text{echo}}$, but also disentangle the temperature of the microwave waveguide port and the intrinsic cavity port. This yielded a temperature of $\sim 50\,\text{mK}$ for the internal port (i.e. the cavity material itself) and $\sim 120\,\text{mK}$ for the external waveguide port. Thus, further filtering and thermalized attenuation is necessary to reduce the thermal occupation of the microwave input line to the qubit-cavity system to increase the achievable T_2 and make the qubit-cavity system more sensitive for measurements of potential impacts on the qubit coherence from the strong optical pump.

4.4 Impact of optical absorption heating quantified with quantum-non-demolition measurements

While the previous measurements have shown that reliable qubit characterization is feasible with a strong optical readout pulse, a more sensitive method is required to fully quantify the potential radiative [Barends et al., 2011; Houzet et al., 2019] and thermal [Hease et al., 2020] impact of high energy pump photons. In the following, we use a near-quantum-limited non-degenerate Josephson parametric amplifier [Winkel et al., 2020] to perform a low power, dispersive, and non-destructive qubit readout to quantify such effects.

First, we measure the alternately prepared qubit states two times back to back, the first one in the presence of the previously used optical pump pulse and for comparison also when the laser is off. Figure 4.5a shows the extracted assignment fidelity $\mathcal{F}$ of the first (second) measurement in cyan (green) for increasing optical pulse repetition rates. The observed dependence on the resulting applied average optical power (top axis) is in excellent agreement with theory (lines and 3σ confidence bands) for spontaneous emission scaling with $1 - e^{-t/T_1}$ and the independently measured thermal excitation of the qubit, cf. fig. 4.5c. The remaining discrepancy is fitted to be $\leq 1\%$ and attributed to either measurement (or optical radiation) induced transitions or state preparation errors.

The quantum-non-demolition (QND) metric is defined as the fraction of measurements, where two consecutive readouts yield the same qubit state [Touzard et al., 2019], i.e.

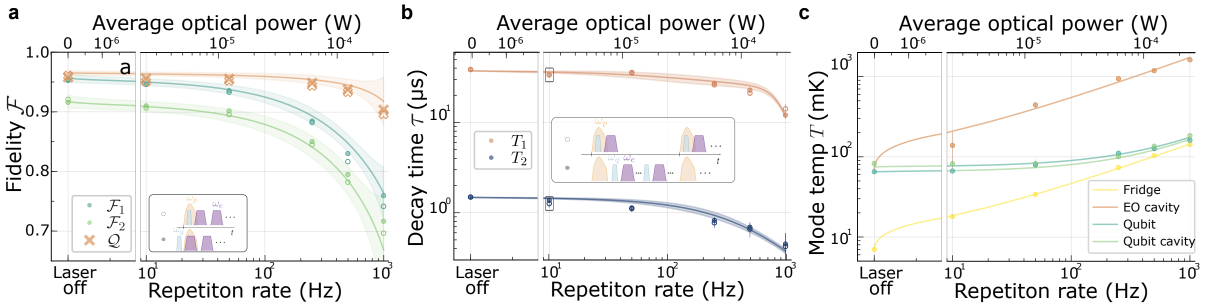

Figure 4.5: **Impact of the optical pump.** **a**, Measured state assignment fidelities $\mathcal{F}_1$ and $\mathcal{F}_2$ of two consecutive JPA-assisted microwave measurements (full circles) and corresponding QND metric (crosses) obtained in the presence of a 2 μs long optical pump pulse of ≈ 0.14 W applied during the first readout as a function of repetition rate and calculated dissipated optical power (top axis) together with theory (lines and 3σ confidence bands). Approximately $1-(1-2\eta_o)^2 \approx 69\%$ of the average optical power sent to the sample are dissipated in the device. Empty circles (mostly overlapping with full circles) denote measurements where the optical pump was applied also during state preparation. Statistical errors of data points are $\sim 1\%$ and smaller than the marker size. The insets show pulse sequences for the differently triggered measurements. Qubit preparation, readout and optical pump are denoted by ω_q, ω_e and ω_p, respectively. **b**, Measured qubit coherence times when the optical pulse is synchronized with each qubit preparation and readout pulse (empty circles) and for a free-running measurement sequence (full circles) vs. optical pulse repetition rate. Squares indicate the mean of the optical readout results in fig. 4.4. The decrease in T_1 and T_2 is accurately modelled with theory (red and blue line with 3σ confidence band), the measured thermal occupancy shown in panel c, the expected quasiparticle distribution and Purcell decay (red line). Data error bars show the 90% confidence interval of the mean according to a student-t distribution for 5 measurements (cf. fig. 4.4). **c**, Measured temperature of the mixing chamber (yellow dots) and the different microwave modes (dots) together with power law fits as a guide to the eye. Error bars stem from 3σ confidence bands of the respective fit and corresponding error propagation calculations. Figure adapted from [Arnold et al., 2023].

$\mathcal{Q} = \left(P(g_2|g_1) + P(e_2|e_1)\right)/2$ and therefore probes the impact of an applied readout tone. Importantly, $\mathcal{Q}$ (orange) is comparable for moderate repetition rates and a dark measurement without laser light, which implies a minimal (if any) direct impact of the optical pulse on the qubit. This interpretation is supported by additional measurements where the same optical pulse is applied also already during the qubit state preparation (open circles in fig. 4.5a), which mostly overlap with the solid circles, c.f. pulse sequence in inset. The theoretical prediction of $\mathcal{Q}$ is based on spontaneous emission.

Figure 4.5b shows coherence times as a function of optical pulse repetition rate with optical pulses sent simultaneously with qubit preparation and the readout pulses (closed circles) together with free-running measurements where the optical pulse is not synchronized with the microwave measurements ($\approx$ 5 kHz repetition rate, full circles). The latter method cannot induce an instantaneous radiation-based impact, e.g. via the generation of quasiparticles. The very close agreement between the two types of measurements, the small difference between low repetition rates and laser-off measurements, and the very good agreement with the coherence times obtained with the (all-)optical readout of fig. 4.4 (black squares) indicates the absence of such radiative effects.

The measured increase in the longitudinal decay rate $\gamma_1 = 1/T_1$ as a function of applied average optical power compared to the "cold" decay rate without laser light, γ_1^0, is in excellent agreement with a prediction of thermal effects due to optical absorption heating in the EO transducer

$$\gamma_1 = \gamma_1^0 \left(1 + 2n_{\mathrm{th}} + \frac{\sqrt{2\pi k_{\mathrm{B}} T_{\mathrm{q}}/\Delta_{\mathrm{sc}}}}{x_{\mathrm{qp}}^0} e^{-\frac{\Delta_{\mathrm{sc}}}{k_{\mathrm{B}} T_{\mathrm{q}}}}\right) + \frac{g_{\mathrm{qc}}^2}{\Delta_{\mathrm{qc}}^2} \Delta_{\kappa_{\mathrm{c}}} \tag{4.12}$$

as shown in fig. 4.5b (red line and 3σ confidence band). eq. 4.12 only takes into account direct qubit excitation from blackbody radiation n_{th} [Córcoles et al., 2011] at temperature T_{q}, thermal equilibrium quasiparticles with a superconducting gap Δ_{sc} of 205 μeV as well as a typical nonequilibrium quasiparticle density of $x_{\mathrm{qp}}^0 = 1.6 \times 10^{-7}$ [Serniak et al., 2018], and an increase in the Purcell rate with qubit-cavity coupling g_{qc} and detuning Δ_{qc}. Using the independently measured qubit temperature T_{q} shown in fig. 4.5c and measurements of the slightly broadened cQED cavity linewidth $\Delta_{\kappa_{\mathrm{c}}} = \kappa_{\mathrm{c}} - \kappa_{\mathrm{c}}^0$ of up to 240 kHz at higher repetition rates (temperatures), $\gamma_1^0 = 37$ μs remains as the only fit parameter.

In a similar manner, the relative dependence of the transverse decay T_2^* (fig. 4.5b, blue) is fully consistent with the increased dephasing rate from thermal photon shot noise due to the rising qubit cavity temperature (fig. 4.5c) and the increase in γ_1 as described above. $T_{2,\mathrm{echo}}$ and T_2^* show again no measureable difference. Quasiparticles are also not believed to have a dominating effect on dephasing in transmon qubits [Catelani et al., 2012; Zanker and Marthaler, 2015; Ristè et al., 2013].

Finally, we investigate the average temperature distribution of the different components, which is used for the theory in fig. 4.5a and b. fig. 4.5c shows the measured base plate temperature from a calibrated rutenium oxide sensor, as well as the mode temperature of the superconducting qubit as obtained from thermally excited $|e\rangle \leftrightarrow |f\rangle$ Rabi oscillations [Jin et al., 2015]. The temperature of the cQED cavity is extracted from populated Ramsey oscillations [Dassonneville et al., 2021], and the EO microwave cavity temperature is calculated from the measured power spectral density at its output [Hease et al., 2020]. These measurements were performed free-running but with the same optical pulse applied to the transducer.

When the laser is off, all components thermalize to a temperature of $\approx$ 75 mK, while the refrigerator reaches a base temperature of $\approx$ 7 mK, see fig. 4.5c. When the optical pump is on, it acts as a localized heat source that increases the EO microwave mode temperature (orange). The proportionality to the time-averaged applied optical power of $\propto \bar{P}_{\mathrm{opt}}^{0.54}$ agrees with previous findings for continuous wave optical pumps [Hease et al., 2020].

The EO transceiver is in very good thermal contact to the refrigerator's base plate, which heats up the refrigerator with the same power law (yellow) fundamentally originating from the dependence of the mixing chamber cooling power on its temperature $\sqrt{P_{\mathrm{MXC}}} \propto T_{\mathrm{MXC}}$ [Betts, 1989]. The resilience of the cQED system to radiation and heating at moderate repetition rates (cf. fig. 4.5a and b) is reflected again in the mode temperature of the qubit and the dispersively coupled cavity. Their temperature increases only slightly compared to the laser-off situation for moderate repetition rates. One reason for this behavior is the detuning between the transducer cavity mode and the cQED system by the Lamb shift $\chi_0/(2\pi) = 26$ MHz except for the moment when the high power readout pulse is applied. Other reasons are the careful thermalization of all components and the large heat capacity and thermal contact area of the bulk EO transducer compared to integrated photonics approaches. However, as the cQED system is thermally connected to the mixing chamber as well, its mode temperature rises as soon as the fridge temperature approaches the thermalization temperature of the cQED unit (cyan and light green). This behavior is consistent with the sharp decline in the qubit coherence and readout fidelity for higher repetition rates in fig. 4.5a and b.

4.5 Heat load comparison

A main motivation of this work was the fact that 1) microwave input lines need more than $60\,\mathrm{dB}$ of attenuation and therefore dissipate an overwhelming fraction of the original signal power in the dilution refrigerator, 2) microwave amplifiers in the output line such as a HEMT need a dissipative DC supply and 3) microwave amplifiers also add - except for quantum limited amplifiers such as Josephson-parametric amplifiers or travelling-wave parametric amplifiers with JJs - additional thermal noise equivalent to the effective noise temperature. Optical input and output lines can offer advantages: 1) Optical signals do not require thermalization at lower temperature stages because the occupation is negligible even at room temperature. 2) microwave-optic transducers require only a parametric pump for operation that fundamentally does not need to be dissipative. The power dissipation arises from the intrinsic losses of the resonator. 3) After microwave-optic transduction which can happen with very low added noise at mK temperatures, no further amplification is needed before the optical detection at room temperature. We will separately compare the heat load for the input signal reaching the device under test on the mixing chamber stage and the output signal emitted from the sample. [1]

4.5.1 Input

As the mixing chamber is the stage with the smallest cooling power and in order to allow for a fair comparison, we want to compare the dissipated heat at the mixing chamber stage with respect to the microwave signal power that is available for further processing, e.g. can be used for qubit state readout, a qubit gate pulse, or a pump for a quantum-limited amplifier. The comparison includes a standard microwave setup (fig. 4.1a) with a final attenuation of $30\,\mathrm{dB}$ at the mixing chamber, a cryogenic avalanche photodetector, that converts the dissipated optical power to an electrical current (*EO power conversion*), and a microwave-optic converter that uses a parametric pump to achieve an efficient conversion between microwave and optical photons (*EO photon number conversion*). We focus our analysis on the mixing chamber stage because the low temperature environment is particularly demanding for the heating budget due to the limited cooling power available.

Microwave input signal on an attenuator

A microwave signal needs to be attenuated by cold attenuators in order to reduce the thermal noise in the signal. The number of noise photons after attenuation A at temperature T is

$$n_{out}(\omega) = \frac{n_{in}(\omega)}{A} + \frac{A-1}{A}\frac{1}{e^{\frac{\hbar\omega}{k_B T}}-1} \tag{4.13}$$

where $n_{in}(\omega)$ is the noise photon occupation at a specific frequency and the last term is the Bose-Einstein distribution. Please note that $A \leq 1$ and denotes the factor by which the input signal is attenuated. [2] For a cascaded input attenuation chain with $20\,\mathrm{dB}$ of

---

[1] Phase-insensitive quantum-limited amplifiers add noise, too, but only the minimum amount of 0.5 photons over the amplification bandwidth

[2] a widely used unit that is convenient in the experimental practice, where each device and instrument has a certain bandwidth or resolution bandwidth that needs to be accounted for, is *photons/s/Hz*. This photon flux (or power) per frequency interval $1\,\mathrm{Hz}$ is also dimensionless, as the Bose-Einstein-distribution.

attenuation at the $4\,\mathrm{K}$ stage and the cold plate respectively, a further attenuation of $30\,\mathrm{dB}$ thermalized to the base plate temperature of $10\,\mathrm{mK}$ reduces the thermal occupation at typical microwave frequencies $\omega/(2\pi) \approx 5\,\mathrm{GHz}$ to $\bar{n}_{\mathrm{mxc}} < 10^{-3}$. In practice, however, qubit control lines have been recently identified to radiate a spectrum equivalent to a black body at $\sim 70\,\mathrm{mK}$ towards the superconducting qubit [Simbierowicz et al., 2024]. Nevertheless, the power that is dissipated by an attenuator with attenuation A with respect to the achieved output power P_{out} after the attenuator is

$$\bar{P}_{\mathrm{diss,mw}} = \bar{P}_{\mathrm{out,mw}}(A-1) \tag{4.14}$$

For a $30\,\mathrm{dB}$ attenuation, it is apparent that $99.9\,\%$ of the incoming signal gets dissipated. fig. 4.6a shows the dissipated power of such an attenuator (purple) for various $\bar{P}_{\mathrm{out,mw}}$. Dashed, vertical lines show typical power values for qubit readout ($-117\,\mathrm{dBm}$), qubit gate pulses ($-66\,\mathrm{dBm}$), and a drive for a parametric amplifier ($-50\,\mathrm{dBm}$). The horizontal dashed line marks the cooling power of our Bluefors LD250 dilution refrigerator at $10\,\mathrm{mK}$ ($20\,\mu\mathrm{W}$).

Optical input signal on a photodetector

If a modulated optical tone with modulation frequency ω_{mw} is sent to a photodiode, the resulting photocurrent will oscillate with the modulation frequency. We can also exploit the familiar picture from previous sections where an optical pump and an optical signal at frequency $\omega_{\mathrm{sb}} = \omega_{\mathrm{pump}} + \omega_{\mathrm{mw}}$ are sent to a photodiode. Only recently was it demonstrated for the first time that a microwave signal, generated from dissipated optical tones in a photodiode, can be used to control the state of a superconducting qubit or serve as a readout signal [Lecocq et al., 2021]. A quantitative investigation of the quality of such a microwave signal generated by optical transmission and cryogenic photodetectors found a single-qubit gate error <0.0015 via cross-entropy benchmarking [Li et al., 2024]. The latter work also used an integrated laser diode chip at room temperature, where the microwave modulation signal could be directly applied to, instead of an external electro-optic modulator.

In the following, we will follow the description of [Lecocq et al., 2021] to assess the optical power that is dissipated in order to generate a specific microwave power. The optical power dissipated in the active area of the photodetector and thereby generating multiple electron-hole pairs and a subsequent photocurrent is given by

$$\bar{P}_{\mathrm{diss,PD}} = \sqrt{\frac{2\bar{P}_{\mathrm{out,mw}}}{m^2\mathcal{R}^2 Z}} \tag{4.15}$$

Z is the impedance and m is the relative strength between carrier and sideband, i.e. the incident optical power is of the from $P_{\mathrm{diss,PD}}(t) = \bar{P}_{\mathrm{diss,PD}}(1 + m\cos(\omega_{\mathrm{mw}}t + \phi)$. The responsivity $\mathcal{R}$ relates the incident optical power of the photodiode to the generated photocurrent. The photodiode used in [Lecocq et al., 2021] featured $\mathcal{R} = 0.5\,\mathrm{AW}^{-1}$ at the fridge base temperature. We assumed here a unity transfer function for the photodiode. fig. 4.6a (cyon) shows the dissipated power with respect to the achieved microwave output power for the parameters in [Lecocq et al., 2021] and a modulation strength of $m = 1$. A striking difference to eq. 4.14 is the square-root dependence of the dissipated power with respect to the generated microwave power. This can offer advantages for higher $\bar{P}_{\mathrm{out}}$, however, in the power range of qubit control and readout signals, the dissipated power at the mixing chamber is still higher than that of a 30dB attenuator in a microwave input line (purple). The benefits are a decreased passive heat load due to the lower thermal conductivity of an optical fiber and the potentially simpler wiring from room temperature to the temperature stage of the photo-diodes.

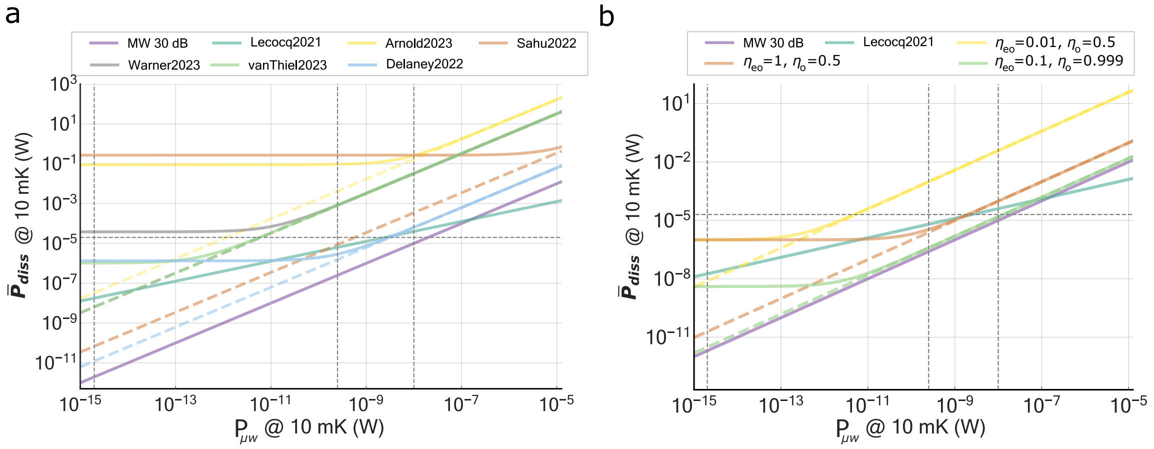

Figure 4.6: **Comparison of the power dissipation at the base plate.** **a**, Dissipated power with respect to the microwave power available for the device for a $30\,\mathrm{dB}$ micowave attenuator (purple), the photodetector scheme (cyan), and various microwave-optic converter platforms. Dashed lines show the dissipated input signal power, solid lines the total dissipated power including the parametric pump for the converter schemes **b**, Dissipated power for various hypothetical converter parameters. The optical pump power is fixed at $1\,\mathrm{\mu W}$ and thus in the range of integrated microwave-optic transducers. The current performance of these devices is shown in yellow, and compared to improvements in conversion efficiency (red) and optical coupling ratio (green, $\eta_\mathrm{o} = 0.999$) Only such a high coupling ratio can compensate the energy mismatch $\omega_\mathrm{o}/\omega_\mathrm{e}$ and make the optically dissipated power comparable to the absorbed power in a conventional microwave input line with a $30\,\mathrm{dB}$ attenuator. For both plots, vertical dashed lines mark typical microwave powers for qubit readout ($-117\,\mathrm{dBm}$), qubit control ($-66\,\mathrm{dBm}$), and a parametric microwave amplifier ($-50\,\mathrm{dBm}$). The horizontal dashed line visualizes the cooling power of a Bluefors LD250 or XLD400 dilution unit ($20\,\mathrm{\mu W}$ at $20\,\mathrm{mK}$).

Optical input signal on a microwave-optic converter

Due to the plethora of different approaches for microwave-optic conversion, we try to formulate a very general model for these devices: In order to create a microwave tone from an optical input signal, the device features

- an optical pump that is reflectively coupled to an optical resonator
- an optical signal sent to the same optical resonator as the pump
- a specific photon number conversion efficiency between an incoming optical signal and the generated microwave signal

The reflected field from a reflectively coupled resonator is $S_{11} = 1 - \frac{\kappa_\mathrm{ex}}{\kappa/2 - i\Delta}$ (eq. 2.3). We denote the reflected power from an optical cavity then as $|S_\mathrm{oo}|^2$. We assume that all remaining power, which is not reflected from the device and collected into the optical waveguide or optical fiber, is dissipated somewhere in the dilution unit. If we neglect the comparably small amount of pump photons that are annihilated in the conversion process, the dissipated optical pump power is

$$\bar{P}_{\mathrm{diss,eo_{pump}}} = (1 - |S_\mathrm{oo,pump}|^2)\bar{P}_\mathrm{pump} \tag{4.16}$$

The optical pump power in practice sets the parametrically enhanced conversion efficiency between microwave and optical photons in the respective waveguide $|S_\mathrm{eo}|^2$. This determines the optical signal power we need to send to the converter in order to generate a certain microwave power at its output.

$$\bar{P}_{\mathrm{eo}_{\mathrm{signal}}} = \frac{\bar{P}_{\mathrm{out,mw}}}{\eta_{\mathrm{eo}}} \frac{\omega_{\mathrm{opt}}}{\omega_{\mathrm{mw}}} \tag{4.17}$$

A fraction of those optical photons is again reflected back into the optical waveguide, $|S_{\mathrm{oo,signal}}|^2$. Another fraction of the optical signal gets converted either directly to microwave photons in case of an EO transducer or phonons when using a mechanical mediator. Either way, the efficiency of these processes is given by $\eta_{\mathrm{o}} 4C_{\mathrm{o}}/(1+C_{\mathrm{o}})^2$ where the cooperativity is defined between optical and microwave fields or optical and mechanical fields respectively. We neglect here the mechanical or microwave dissipation because its contribution to heating is negligible compared to optical absorption. The remaining fraction besides the sum of reflected and converted part is then assumed to be dissipated in the optical resonator so that the total optical power that is turned into heat with respect to the generated microwave power becomes

$$\bar{P}_{\mathrm{diss,eo}} = \left(1 - \underbrace{|S_{\mathrm{oo,pump}}|^2}_{\text{reflected}}\right) \bar{P}_{\mathrm{pump}} + \left(1 - \underbrace{|S_{\mathrm{oo,signal}}|^2}_{\text{reflected}} - \underbrace{\eta_{\mathrm{o}} \frac{4C_{\mathrm{o}}}{(1+C_{\mathrm{o}})^2}}_{\text{converted}}\right) \underbrace{\frac{\bar{P}_{\mathrm{out,mw}}}{|S_{\mathrm{eo}}|^2} \frac{\omega_{\mathrm{opt}}}{\omega_{\mathrm{mw}}}}_{\bar{P}_{\mathrm{signal}}} \tag{4.18}$$

In contrast to $|S_{\mathrm{oo,pump}}|^2$ where we use eq. 2.3 for a single resonator, the optical signal mode is exposed to dynamical backaction from coupling to a microwave mode for an EO converter and to a mechanical resonance for a transducers with a mechanical mediator between microwave and optical photons. Thus, $|S_{\mathrm{oo,signal}}|^2 = (1 - 2\eta_{\mathrm{o}}/(1+C))^2$. This is the reflected power at the signal mode with the pump being red-detuned in the sideband resolved regime, i.e. for an Anti-Stokes scattering process with a suppressed Stokes sideband [Safavi-Naeini et al., 2011].

Hence, with the general expression in eq. 4.18 we can calculate the dissipated optical power $\bar{P}_{\mathrm{diss,eo}}$ for microwave-optic transducer on various platforms including for example electro-optic converters [Arnold et al., 2023; Warner et al., 2023], electro-opto-mechanical converters [Delaney et al., 2022; Arnold et al., 2020] and piezo-optomechanical converters [Weaver et al., 2024; Meesala et al., 2023; Blésin et al., 2021; Jiang et al., 2023].

In fig. 4.6a we plot the the dissipated total power of optical pump and optical signal (solid lines) according to 4.18 and the dissipated optical signal power to visualize the scaling (dashed lines). As described above, the reference of a standard microwave input is the power dissipated in a 30dB attenuator (eq. 4.14) in purple. In the region of interest up to microwave powers of $-50\,\mathrm{dBm}$, a conventional microwave input with thermalized attenuators still has the lowest power dissipation. If one compares now the dissipated signal power, i.e. the dashed lines, the best performing devices with the smallest dissipation are also the ones with the highest conversion efficiency (0.2 for [Delaney et al., 2022] and 0.3 for [Sahu et al., 2022]). The latter shows a slightly higher power dissipation because the coupling ratio of the optical cavity is lower and, hence, the fraction of dissipated power is increased. The other three converters all show a conversion efficiency between $\sim$ 0.1 and $\sim$ 1% and need higher optical input power (more dissipated power) to achieve a given microwave strength.

The largest part of the heating power, however, stems from the parametric pump, that is also sent to the optical cavity. The horizontal region of the corresponding solid lines (yellow to blue) refers to dissipated power of the (constant) optical pump. Converters with a large parametric amplification (i.e. direct EO devices such as [Sahu et al., 2022; Arnold et al., 2023; Warner et al., 2023]) have a larger power dissipation than the available cooling power (horizontal dashed gray line) and require therefore a pulsed operation even for a single device in order to keep the base temperature of the dilution unit around $10\,\mathrm{mK}$.

In order to achieve a heating performance comparable to a microwave readout, it is important to improve both the conversion efficiency but also - and this is even more important - the losses in the optical resonator. fig. 4.6b shows the influence of improvements in both parameters on the heating performance. While the current performance of integrated converter with pump powers of $\simeq 1\,\mu\mathrm{W}$ is shown as a reference (yellow), achieving unity internal conversion efficiency reduces the power dissipated by the signal because a smaller signal power is required (red curve), but the overall dissipation remains unchanged because it is dominated by the pump. Consequently, it is crucial to reduce the dissipation from the pump which depends inversely on the coupling ratio η_o. Only an almost unity coupling ratio of $\eta_\mathrm{o} = 0.999$ can reduce the dissipated optical power enough to become comparable to the microwave power dissipated in a 30dB attenuator. Every optical photon that is absorbed, dissipates $\omega_\mathrm{o}/\omega_\mathrm{e} > 10^4$ times more energy than a microwave photon.

It is also important to note that this is the standard regime for parametric interactions, i.e. where the pump power is much larger than the signal power. Above that, the linearization of the interaction breaks down and the mathematical description is not valid any more. The pump power in 4.5 is taken from the parameters of the respective experiment. If the dashed line merges with the solid line, the signal would have a similar or higher power than the pump and the pump power would need to be adjusted accordingly so that the actual dissipation will be above the dashed line.

Please note that electro-opto-mechanical converter that use the radiation pressure force to create the electro-mechanical interaction, require a strong microwave pump. Thus, it is highly demanding to use such a device for the generation of microwave signals that are used for e.g. the excitation or readout of a qubit because the microwave pump needs to be filtered out. In [Delaney et al., 2022], where a microwave signal from a low-power dispersive readout of a qubit is optically detected after frequency conversion, they operate the device exclusively in the microwave-to-optic direction and shield the microwave pump from the qubit by three circulators in series. This would naturally suppress any microwave signal generated by optic-to-microwave conversion as well. Instead, such a platform would require narrow-band filtering around the microwave signal which again sets a limit on the available minimal signal pulse length. Consequently, an electro-mechanical interaction that exploits the piezoelectric effect or a direct electro-optic transducer is highly advantageous for this specific purpose because both do not require a microwave pump for parametric enhancement.

4.5.2 Output

The drawback of optic-to-microwave photon number conversion for the generation of microwave signals from a power-efficiency perspective, i.e. the optical power sent to the transducer has to be at least $\frac{\omega_\mathrm{o}}{\omega_\mathrm{m}} > 10^4$ times higher than the generated microwave signal power, can be turned into an advantage for the reverse conversion process. The power of a low-power microwave signals can be increased by orders of magnitudes when converting the photons to optical frequencies which 1) reduces the thermal background noise and 2) brings the signal to the optical domain with quantum limited detectors available. In such a configuration with an optical interferometric detection scheme, which acts as a quantum-limited detector itself when the shot noise from the local oscillator surpasses classical, e.g. electronic, noise sources, it was possible to optically detect the signal change resulting from different qubit states for a strongly coupled microwave cavity with a coherent occupation of only 361 photons [Delaney et al., 2022].

Nevertheless, similar to chapter 4.5.1 an attempt for a fair comparison of the heat load between a standard microwave output line and an output line converting the microwave signal to optical frequencies shall be conducted.

4.5.2.1 Power dissipation

Dissipation in a microwave output chain A typical microwave output chain consists of a quantum-limited amplifier (cavity-based or travelling wave parametric amplifier) and a HEMT (cf. also fig. 4.1). While the power dissipation associated with the quantum limited amplifier is dominated by the dissipation of the parametric microwave pump and was therefore considered in the previous chapter 4.5.1, the HEMT dissipation originates from the source-drain current I_{ds} and source-drain voltage V_{ds} of the transistor. In the following, we will use the specification of the HEMT LNF-LNC4-16C used in the experiments in the previous sections of chapter 4 as a representative example with $I_{\mathrm{ds}} = 18\,\mathrm{mA}$ and V_{ds} =1.1 V when operated at $4\,\mathrm{K}$. This results in a power dissipation of

$$\bar{P}_{\mathrm{diss,hemt}} \approx V_{\mathrm{ds}} I_{\mathrm{ds}} \tag{4.19}$$

accumulating to $22\,\mathrm{mW}$ or 13.3 dBm (fig. 4.7a). This is a lower bound because we only account for the static power dissipation due to the DC supply and neglect the dynamic dissipation during RF signal operation. The cooling power of the corresponding 4K stage in a Bluefors XLD400 dilution refrigerator is around $1.5\,\mathrm{W}$ at $4.2\,\mathrm{K}$ [Krinner et al., 2019], highlighted as horizontal line in fig. 4.7a. Considering the heat budget alone and neglecting space constraints, this limits the number of parallel HEMT amplifiers to ~50, or in case of the more efficient LNF-LNC4-8C HEMT to a maximum of 100. Even considering multiplexed readout - but accounting for the necessary frequency separation between readout qubits of $\geq$ 200 MHz [Heinsoo et al., 2018] which results in $\sim$ 10 multiplexed qubits per readout line - the power dissipation of HEMT amplifiers at the $4\,\mathrm{K}$ stage may be a major bottleneck in scaling up quantum processors. It has to be mentioned, though, that it is generally less challenging to increase the cooling power at a temperature of $4\,\mathrm{K}$ compared to lower temperature stages of $\leq 1\,\mathrm{K}$. All these estimates are based on current dilution refrigerators and are likely to change in the future.

Dissipation in a microwave-optic output chain The dissipated power of around $20\,\mathrm{mW}$ by a HEMT amplifier in a microwave output line shall be compared to the dissipated optical pump power of various microwave-optic transducer, described again by eq. 4.18 as in the previous section. As the coupling strategies from fiber to chip or device vastly differ for the different experiments and the coupling losses range from $1\,\mathrm{dB}$ to $12\,\mathrm{dB}$ but can be optimized to $<1\,\mathrm{dB}$ for all devices, these losses are neglected in the following. The horizontal lines in fig.4.7a highlight the cooling power of various temperature stages in a commercial Bluefors XLD400 dilution unit. It is clearly visible that the power dissipation for the macroscopic transducer

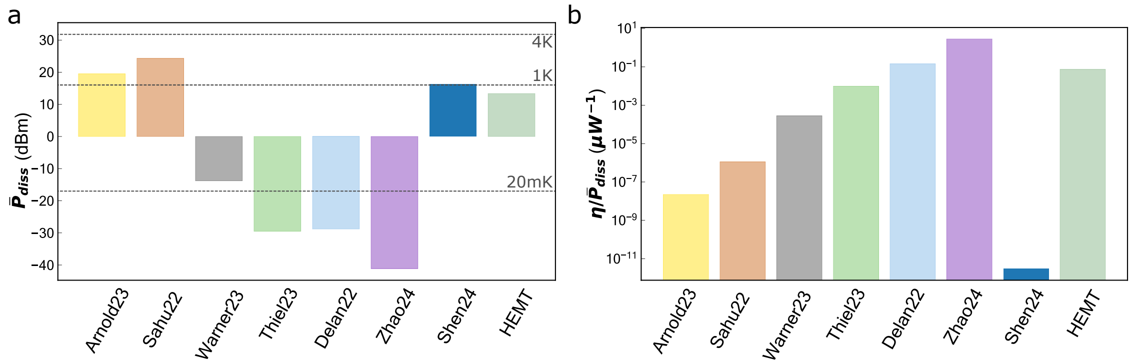

Figure 4.7: **Comparison of power dissipation and power efficiency for the output line.** **a**, Dissipated power of the optical parametric pumps in continuous operation for various converter devices in comparison with the electrical power dissipation of a HEMT. Horizontal lines indicate the cooling power of a Bluefors XLD400 dilution unit for various temperature stages. **b**, power efficiency of the device as the ratio between coherent photon number change $n_{\mathrm{coh,out}}/n_{\mathrm{coh,in}}$ and the dissipated power $\bar{P}_{\mathrm{diss}}$ from the optical pumps or electrical power supply of the HEMT. Coupling losses from optical fibers or free space to the device/chip are not taken into account for better comparison between different devices. Data extracted from [Arnold et al., 2023; Sahu et al., 2022; Warner et al., 2023; van Thiel et al., 2023; Delaney et al., 2022; Zhao et al., 2024; Shen et al., 2024] and a characterized LNF-LNC4-16C HEMT.

used in chapter 4 and [Arnold et al., 2023] or related previous work [Sahu et al., 2022] is not a scalable approach because of the large optical pump power, which is mainly dissipated due to the intrinsic loss of the optical resonator. As the dissipated power is larger than the available cooling power at the $1\,\mathrm{K}$ and mixing chamber ($20\,\mathrm{mK}$) stage, these transducers require pulsed operation on those low temperature stages. Moreover, the power dissipation for a single device with a bandwidth of 10-$20\,\mathrm{MHz}$ is larger than the power dissipated by a HEMT with a bandwidth of several GHz allowing for multiplexed signals. A traveling-wave electro-optic transducer operated at $5.6\,\mathrm{K}$ that exhibits a bandwidth of $17\,\mathrm{GHz}$ and thereby even larger than a HEMT, dissipates only slightly more power than the microwave benchmark ([Shen et al., 2024]).

In contrast, the dissipated power of integrated electro-optic [Warner et al., 2023] electrooptomechanical transducers [van Thiel et al., 2023; Zhao et al., 2024], and a macroscopic electrooptomechanical transducer [Delaney et al., 2022] dissipate up to five orders of magnitudes less power than a HEMT. Although the limited bandwidth of these transducers precludes multiplexing, the usage of multiple efficient microwave-optic transducers in the readout line instead of HEMTs can therefore lead to an overall reduction in heating, considering again that a single output line with one HEMT cannot multiplex more than 10-20 qubit readout signals to avoid frequency crowding. In practice, it naturally has to be taken into account that each of these transducers requires optical and microwave connections as well as optical and sometimes microwave parametric pumps, which can result in significant challenges for the control infrastructure of arrays of these devices.

4.5.2.2 Power efficiency

Although a HEMT and a microwave-optic transducer both achieve a power gain, they work fundamentally differently. While the former is an amplifier in which the large DC current between drain and source of the transistor is leveraged to increase the input signal power, microwave-optic transducers convert microwave photons to the optical domain without increasing the number of photons but their frequency. Please note, that this is true as long as the transducer is operated in the conventional conversion scheme with a red-detuned parametric pump initiating the beam splitter interaction, cf. section 2.2.1. In case of blue-detuned pumps a microwave-optic transducer can increase the number and frequency of the input microwave signal. The energy for these processes stems from the pump itself. Thus, while a HEMT is usually characterized by a gain $\gg 1$, an important metric for the microwave-optic transducer's performance is the photon-number conversion efficiency ≤ 1. fig. 4.7a considers the bare amount of the dissipated power $\bar{P}_{\mathrm{diss}}$ to relate it to the cooling power of refrigerators. In contrast, in fig. 4.7b we combine the change of number of photons by the respective device η and the dissipated power to $\eta/\bar{P}_{\mathrm{diss}}$ with $\bar{P}_{\mathrm{diss}}$ resulting again from the dissipation of the parametric pump tones ($\bar{P}_{\mathrm{diss,eo}}$ as in eq. 4.18) or the DC power supply of the HEMT ($\bar{P}_{\mathrm{diss,hemt}}$), cf. eq. 4.19. Even though the HEMT has a characterized gain of $32\,\mathrm{dB}$, the most power-efficient converters with $\eta \leq -3\,\mathrm{dB}$ still outperform the high-end microwave amplifier.

4.5.2.3 Power gain

In the next step, we will now also consider the energy increase of the photons due to microwave-optic conversion. The signals from a quantum system are generally rather weak, e.g. a single photon for quantum communication or $\simeq$ 10 photons for non-destructive qubit readout. Consequently, it is decisive how much the signal differs from the (thermal) noise background. We assess this situation from the power gain, defined by the product of the change in photon number between device input and output, i.e. η in fig. 4.7b, and the change of each photon's energy proportional to $\omega_{\mathrm{out}}/\omega_{\mathrm{in}}$. Fig. 4.8a demonstrates that the vast frequency difference between optical and microwave domain with $\omega_{\mathrm{o}}/\omega_{\mathrm{e}} \geq 40\,\mathrm{dB}$ is of the same order of magnitude as the impressive gain of HEMTs. Thus, the power gain between signal input and device output of the most efficient microwave-optic transducers with $\eta \simeq 0.2$ [Sahu et al., 2022; Delaney et al., 2022; Zhao et al., 2024] surpasses the gain of the herein considered HEMT of $32\,\mathrm{dB}$. In both cases, the signal power is raised to or above the thermal background at ambient conditions. While the HEMT achieves this by amplification of the input signal (thermal occupation at $300\,\mathrm{K}$ and $5\,\mathrm{GHz}$ $n_{300\mathrm{K},5\mathrm{GHz}} \approx 1250$), the conversion to optical frequencies around $193\,\mathrm{THz}$ makes the thermal background at room temperature negligible ($n_{300\mathrm{K},193\mathrm{THz}} \approx 0$). These considerations, however, do not account for noise that is added by the device, which will be discussed in the following.

4.5.2.4 Added noise and effective noise temperature

While the investigations above focus on the signal evolution along the output chain and consider the efficiency of microwave-optic transducers and gain of the HEMT respectively, an equally important specification for the final SNR is the added noise or the related noise temperature of the devices. The latter describes the temperature which would produce Johnson-Nyquist noise $k_{\mathrm{B}}T$ per unit bandwidth of equivalent noise power. Fig. 4.8b shows the effective noise temperature in Kelvin. It should be noted that the comparison may appear slightly incongruous at first sight, because two devices are operated at higher temperatures of $5.6\,\mathrm{K}$ [Shen et al., 2024] and $5\,\mathrm{K}$ (according to the HEMT data sheet), while the remaining microwave-optic transducers are mounted on the base plate of a dilution refrigerator with temperatures $\simeq 10\,\mathrm{mK}$. However, both devices operated at higher temperatures are in their current realization incompatible with lower temperature stages. While the static dissipation of the HEMT exceeds the heat budget of lower temperature plates (4.7a), the traveling-wave electro-optic transducer could in principle be operated in pulsed mode to sufficiently

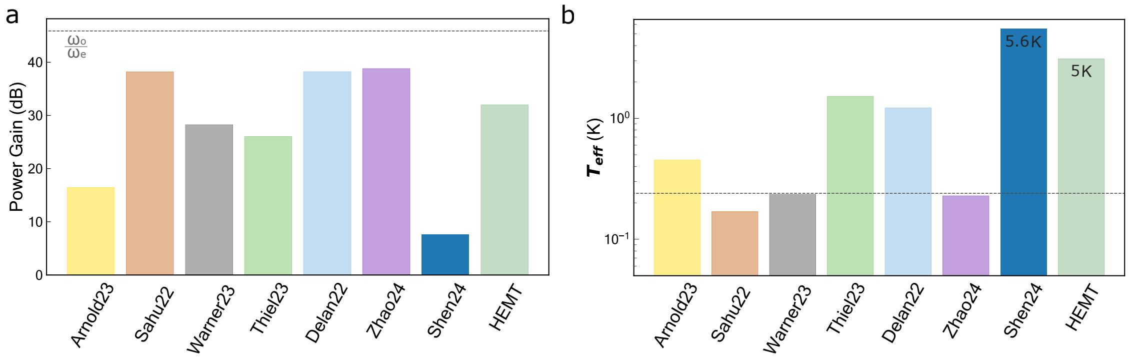

Figure 4.8: **Comparison of power gain and effective noise temperature for the output line.** **a**, The power gain defined as the product of change in coherent photon number and photon energy, $\frac{n_{\mathrm{coh,out}}}{n_{\mathrm{coh,in}}}\frac{\omega_{\mathrm{coh,out}}}{\omega_{\mathrm{coh,in}}}$, for various converter devices in comparison with a HEMT. The horizontal line indicates the power gain for a microwave-optic transducer with unity conversion. **b**, Noise temperature of the various components with the horizontal line being the equivalent temperature of 1 photon input-referred added noise at $5\,\mathrm{GHz}$. If not indicated otherwise, the devices are operated at the base plate of a dilution refrigerator at $\approx 10\,\mathrm{mK}$. Data extracted from [Arnold et al., 2023; Sahu et al., 2022; Warner et al., 2023; van Thiel et al., 2023; Delaney et al., 2022; Zhao et al., 2024; Shen et al., 2024] and a characterized LNF-LNC4-16C HEMT.

decrease the dissipated power. However, the device achieved the necessary index-matching between microwave and optical group index, required for efficient transduction, at these temperatures around $5.6\,\mathrm{K}$. Thus, the mutual dependencies between heat budget, signal gain and added noise lead to a relatively narrow range of operation parameters and the effective noise temperature remains a valuable metric to characterize electrical amplifiers such as the HEMT and microwave-optic transducers alike.

The horizontal line in fig. 4.8b refers to an input-referred added noise of 1 photon expressed as the effective noise temperature at $5\,\mathrm{GHz}$. This constitutes a widely used upper bound for the quantum-enabled regime, where entanglement of the input signal can be preserved. Only two devices mentioned here [Sahu et al., 2022; Zhao et al., 2024], and to the best of my knowledge two other microwave-optic transducers [Mirhosseini et al., 2020; Meesala et al., 2024] and one mm-wave to optical transducer [Kumar et al., 2023] achieved this challenging regime for transduction between vastly different frequency domains, where quantum operations become feasible. This reveals another constraint specifically related to quantum applications. If entanglement between microwave and optical frequency components should be feasible, e.g. to create remote entanglement between microwave qubits (cf. chapter 5), it is ultimately required to operate at the lowest environmental temperature. At the same time, even the cooling power for the currently most powerful dilution unit (Bluefors KIDE, $90\,\mu\mathrm{W}$), limits the number of continuously operating microwave-optic transducers to around 100 devices for the most power-efficient devices to date. Taking into account the probabilistic nature of such a process with efficiencies below $50\,\%$, it remains unclear if a sufficient generation rate of entangled microwave-optic pairs can be achieved with this comparably low number of ∼100 microwave-optic transducers - even neglecting the problem of storing them via quantum memories for now - to be able to integrate on-demand entangled pairs in larger-scale quantum processors with gate operations of ns gate times and fidelities exceeding $99\,\%$.

This condition becomes relaxed for e.g. large-scale qubit readout, where weak coherent tones of a few photons are used. In order to compete with the HEMT noise temperature of 1 - $3\,\mathrm{K}$, microwave-optic transducers have to be mounted at the $1\,\mathrm{K}$ stage or below. However, even an rather smaller dilution unit (e.g. Bluefors XLD400) with a cooling power of $40\,\mathrm{mW}$ allows to host more than 10000 microwave-optic transducers with typical pump powers of $\simeq 1\,\mu\mathrm{W}$ for integrated devices.

4.5.2.5 Signal detection

In the final stage, we want to briefly include also the potential detection of the signal traveling along the refrigerator output line. This is only intended as a brief overview and makes no claim to be an exhaustive list of all potential noise sources for the respective detection scheme. The goal is to point out differences between microwave and optical signal detection with a focus on microwave-optic transducers.

microwave heterodyne detection
The most common way to detect microwave signals after amplification with low-noise amplifiers is a microwave-heterodyne detection scheme (chapter 3.2.3) where the signal is mixed with a strong local oscillator (LO). The detected signal is then proportional to a mixed term $\sqrt{P_{\mathrm{sig}} P_{\mathrm{LO}}}$. This scheme allows to detect both phase and amplitude quadrature. The dominant noise source in the microwave regime is thermal noise ($k_{\mathrm{B}T}$) which is mitigated by the use of amplifiers at lower temperatures, i.e. HEMT. For large gain the total noise is dominated by the first amplifier noise (and the signal loss between sample and first amplifier). In conjunction with quantum-limited microwave amplifiers at temperatures $\leq 1\,\mathrm{K}$ the total detection chain can work close to the quantum limit. Even noiseless amplification of a chosen quadrature is theoretically possible with phase-sensitive amplifiers.

optical heterodyne detection
In section 4.5.2.3 we discussed how the higher photon energy of optical photons compared to microwave photons makes the signal resilient to the thermal background noise at room temperature. A comprehensive view on this topic requires, however, to also take the detection into account. Optical heterodyne detection is indeed typically insensitive to thermal noise, but features a quantum noise effect called *shot noise*. It is an intrinsic property of the optical field as it is composed of discrete photons. In the typical operation regime of optical heterodyne detection the following aspects contribute to the measurable SNR:

- Strong LO for shot-noise limited detection
  The optical power of the LO, typically $\geq 1\,\mathrm{mW}$ and orders of magnitudes larger than the signal from the device, is large enough so that the shot noise exceeds the electronic (e.g. thermal) noise of the optical detector. The shot noise power spectral density of the photocurrent generated in the photodetector is proportional to the mean current and optical power respectively

  $$S_{\mathrm{I}} = 2e\bar{I} \propto \bar{P}_{\mathrm{o}} \approx \bar{P}_{\mathrm{o,LO}} \tag{4.20}$$

  as $\mathrm{Var}(n) = \bar{n}$ following Poissonian statistics. In this regime, optical heterodyne detection is quantum-limited and the measurement of both conjugate quadratures adds half a noise photon due to quantum field fluctuations.[3] Referenced to the input of the microwave-optic transducer the added noise becomes

---

[3] A common convention is also to define the noise of an ideal heterodyne detection as 1 photon instead of 0.5. The quantum efficiency of the detection in this convention is then ideally 1 and simply given by $\eta_{\mathrm{q}} = \eta_{\mathrm{het}}/1$.

$$n_{\mathrm{add,het}} = \frac{1}{2}\frac{1}{\eta_{\mathrm{eo}}\eta_{\mathrm{het}}} \tag{4.21}$$

with η_{eo} being again the photon-number conversion efficiency between microwave and optical domain as above and η_{het} as the optical loss in the detection chain as well as imperfections such as limited mode overlap in the heterodyne detection. Considering typical values of most efficient transducers $\eta_{\mathrm{eo}} \simeq 0.1$ and losses in the optical detection path $\eta_{\mathrm{het}} \simeq 0.1$, we arrive at $n_{\mathrm{add,het}} > 50$ referenced to the microwave-optic transducer input. Thus, even though the high energy makes optical photons resilient to environmental thermal noise in contrast to microwave heterodyne detection, quantum shot noise arises as a fundamental noise limit that can only be mitigated by other quantum mechanisms such as squeezed light for interferometric detection (heterodyne/homodyne) or single-photon detection, which is insensitive to losses in the optical path.

- Signal of the microwave-optic transducer
  In contrast to optical fields, signals in the GHz regime before the transduction process can be corrupted by the thermal environment. According to fig. 4.8b, the added thermal noise to the detected signal is for most state-of-the-art microwave-optic transducers $n_{\mathrm{add,th}} \approx 1 - 10$ photons referenced again to the transducer input. The combined added noise of the microwave-optic detection setup referenced to the converter input comprises the thermal noise added by the transducer, the finite transduction efficiency and subsequent optical loss and imperfections in the heterodyne detection:

$$n_{\mathrm{add}} = \frac{1/2}{\eta_{\mathrm{eo}}\eta_{\mathrm{het}}} + n_{\mathrm{add,th}} \tag{4.22}$$

  Please not that this is in disagreement with the formulation of the quantum efficiency in [Delaney et al., 2022], $1/\eta_{\mathrm{q}} = \frac{1+N_{\mathrm{t}}}{\eta_{\mathrm{loss}}}$, where N_{t} defines the transducer added noise, η_{loss} includes all losses along the detection chain, i.e. in the discussion above only $\eta_{\mathrm{eo}}\eta_{\mathrm{het}}$, and the noise of an ideal heterodyne detector defined as unity with a single-quadrature noise of 0.5[4]. The discrepancy, besides the factor of 2 in the definition of the vacuum fluctuation, originates from the point of reference. While eq. 4.22 refers to the input of the transducer, $1 + N_{\mathrm{t}}$ in [Delaney et al., 2022] is the noise right before an ideal optical detector.

- Optical pump of the microwave-optic transducer
  The SNR in heterodyne detection schemes normally rises linearly with the signal power. The optical signal from a transducer, however, consists of two components: The *optical pump*, which is a by-product of the parametric enhancement of the microwave-optic conversion and the actually converted *transducer input signal*. This is an unusual situation and implies several consequences. First of all, the conversion efficiency η_{eo} is proportional to the optical pump power. Thus, an increasing pump power decreases the noise contribution from heterodyne detection $n_{\mathrm{add,het}}$, cf. eq. 4.21. On the other hand, as the optical pump is an undesired "signal" that gets amplified by the LO and is typically orders of magnitudes stronger than the transducer input signal, it can create a significant shot noise contribution when the relation $P_{\mathrm{pump}} \ll P_{\mathrm{LO}}$ breaks down. In order to be able to increase the conversion efficiency without increasing the shot noise

---

[4] In this thesis, the single quadrature noise is chosen to be 1/4 and the two-quadrature noise as 1/2, being consistent with the Heisenberg uncertainty relation and e.g. the zero-point energy of a harmonic oscillator

contribution from the pump, the optical signal should be cleaned from the pump with appropriate filtering. In experiments with strong optical pump powers even exceeding the LO power this is anyways a prerequisite [Arnold et al., 2023; Sahu et al., 2022].

- Pump phase noise
  Phase fluctuations in the optical pump directly impact the SNR of the heterodyne detection. In fact, in the experiments of chapter 4 an averaged readout signal without phase correction would have been completely unfeasible as the phase of the optical pump imprinted on the detected signal would completely randomize between two consecutive readout pulses. Along this line, fluctuations in the low-frequency system coupled to optical cavity will also be reflected on the optical pump after interaction with the coupled electrooptic or optomechanical system. [Delaney et al., 2022].

- Limited transduction bandwidth The transduction bandwidth of many transducers is currently in the MHz range. However, some transducers with the highest efficiencies are limited to an instantaneous bandwidth of 10-100kHz [Brubaker et al., 2022; Zhao et al., 2024], while state-of-the-art qubit readout pulses are on the order of $\sim 50\,\mathrm{ns}$ [Walter et al., 2017]. This bandwidth mismatch between the readout pulse Γ_p and the transduction bandwidth Γ_eo reduces the readout efficiency by [Delaney et al., 2022]

$$\eta_\mathrm{BW} \approx 1 - 2\frac{1 - e^{\Gamma_\mathrm{eo}\Gamma_\mathrm{p}/2}}{\Gamma_\mathrm{eo}\Gamma_\mathrm{p}}. \tag{4.23}$$

The above discussion points out, that despite the resilience to thermal noise after microwave-optic transduction, other effects come into play. As the output signal is never amplified (in terms of photon numbers) but experiences its power gain only via the frequency increase from microwave-optic conversion, the occurrence of shot noise in conjunction with losses during microwave-optic transduction and the optical detection path constitutes a non-negligible, fundamental noise source.

4.6 Conclusions and prospects

4.6.1 On the current experiment

One major motivation for this experiment is to demonstrate a potential simplification of the cryogenic measurement setup by eliminating bulky and costly microwave components that are also the source of a significant heat load and limits the number of addressable qubits [Krinner et al., 2019]. In contrast, even the smallest cooling power at the mixing chamber plate can handle the passive heat load of millions of fibers [Lecocq et al., 2021] and their small cross-section mitigates the problem of space constraints raised by mm-sized coaxial cables. Nevertheless, the active heat load of this proof-of-principle all-optical readout limits the duty cycle and prevents a direct scaling-up to many readout-out lines. In the present case, the low optical coupling efficiency of $\eta_o = 0.22$ causes the absorption of the majority of the parametric pump power at the mixing chamber, leading to the observed temperature increase associated degradation of the qubit coherence shown in fig. 4.5. In the future, the optical coupling efficiency is therefore a critical parameter to improve, and optimized devices will also need to out-couple the majority of the reflected light to avoid absorption in the refrigerator. On the other hand, the power efficiency is another critical parameter that could theoretically be improved dramatically with integrated photonic devices. One example are electro-opto-mechanical device yielding cooperativities $C \approx 1$ for 10^{-9} times lower optical pump power [Arnold et al., 2020; Delaney et al., 2022] albeit with lower bandwidth and noise performance. The aforementioned improvements are necessary to ultimately gain - besides the drastic setup simplifications - an actual heat load advantage compared to standard microwave cabling or the use of cryogenic photodetectors [Lecocq et al., 2021]. While a microwave readout with thermalized attenuators on the input line fundamentally generates a heat load on the dilution unit, the dissipation of the readout presented here depends only on the efficiency and is, hence, subject to device engineering.

One of the limitations of the presented optical readout is the need for a comparably large number of readout photons n_{meas}. Scaling the histograms in fig. 4.2g-i with the corresponding readout amplitude $\sqrt{n_{\mathrm{meas}}}$ yields the quantum efficiency $\eta_{\mathrm{det}} = \sigma_0^2/\sigma_{\mathrm{det}}^2$ with the Gaussian variance of the measured histogram σ_{det}^2 and the variance of an ideal phase insensitive amplifier $\sigma_0^2 = 0.5$ [Hatridge et al., 2013]. For the conventional microwave readout (without JPA) we extract $\eta_{\mathrm{det,mw}} \approx 1.3 \times 10^{-3}$. This is consistent with a comparably large amount of loss between the cQED system and the first amplifier (transmission of only $< 3\%$) due to the extra circuit elements such as the EO converter with reflectivity $(1-2\eta_e)^2 = 0.09$, with the microwave coupling efficiency η_e. For the two optical readouts on the other hand we find $\eta_{\mathrm{det,opt}} \approx 1.5 \times 10^{-4}$, which agrees with the moderate total electro-optic device conversion efficiency $\eta_{eo} = 0.3\%$ and optical losses. This is in the same ballpark as recent experiments with an electro-opto-mechanical system using a longer ($15\ \mu s$) readout pulse [Delaney et al., 2022]. Importantly, even with just the original performance of this device [Sahu et al., 2022] (we observed optical Q degradation in repeated cooldowns) a quantum-non-demolition single-shot readout without electronic amplifiers and readout times of $\approx 1\ \mu$s would be within reach. With further realistic improvements of in/out coupling and transmission losses close to quantum limited detection efficiencies for photonic RF sensing [Botello et al., 2018] as well as high bandwidth and high fidelity qubit readout comparable to the state of the art [Walter et al., 2017] will be possible.

In summary, we have demonstrated a circulator-free superconducting qubit readout with an all-optical scheme that relies only on optical (de-)modulation and optical heterodyne detection. Such a platform significantly reduces the number of necessary cryogenic components as the optical signal is already resilient to thermal noise and only optical fibers alone act as link to the cryogenic environment. Somewhat surprisingly we found that the comparably high power optical pulse in the $100\,\mathrm{mW}$ range does not have a detrimental effect on the qubit coherence, despite the absence of shielding elements. This result, when combined with recent integrated photonics demonstrations of more power-efficient and higher repetition rate devices for optical control [Warner et al., 2023] and readout [van Thiel et al., 2023] of planar superconducting qubits, provides a viable path towards all-integrated photonic operation of superconducting quantum processors.

4.6.2 On the general application of optical components for control and readout of superconducting qubits

Section 4.5 tried to assess the opportunities and challenges for electro-optic components as part of the hardware infrastructure for superconducting quantum processors to gain an advantage in heat load or noise performance. While microwave-optic transducers can in principle operate without any dissipation, current platforms dissipate most of the power that is sent to these device, predominantly because of intrinsic optical losses such as optical absorption.

On the device input side (cf. section 4.5.1), optic-microwave photon number conversion as fundamental mechanism of the transduction process makes the application of transducer unfavorable, as the absolute optical power sent to the devices has to exceed the generated microwave power by at least $\omega_\mathrm{o}/\omega_\mathrm{e} \leq 10^4$. Photodetectors, however, make use of this energy difference by fully absorbing the high energy optical photon to generate electrical fields. This makes this process inherently dissipative, but the square root scaling of the dissipated optical power with respect to the generated microwave power can create a heat load advantage for higher microwave signals compared to the linear dependence between dissipated and eventually delivered microwave power in microwave attenuators (fig. 4.6). The moderate powers required for current microwave applications such as dispersive qubit readout, qubit drive pulses, as well as parametric pumps are (slightly) below the crossover point, though. Thus, it appears challenging to create a significant advantage for the mixing chamber heat budget compared to a standard microwave input line. An alternative bottleneck such as the passive heat load at higher temperature stages or bandwidth and space constraints might show stronger indication for the usage of electro-optic components for microwave signal delivery.
An analysis of the detection chain also revealed challenges to create an advantage in the measurement SNR for e.g. qubit readout, by replacing microwave components with their optical counterparts. In particular, the noise from heterodyne fluctuations referenced to the device at the beginning of the output line (section 4.5.2.5) exceeds typical effective system noise temperatures and added noise photons respectively for conventional microwave setups (fig. 4.8b). On the other hand, first estimates suggest that microwave-optic transducer mounted on the $1\,\mathrm{K}$ stage potentially offer a drastically improved scaleup compared to HEMT amplifiers at $4\,\mathrm{K}$, solely considering the dissipated power and the currently available heat budget (fig. 4.7). In practice, the packaging and operation of microwave-optic transducer arrays with individual optical control can represent an additional complication. In this regard, traveling-wave electro-optic transducers with a single optical pump and up to $17\,\mathrm{GHz}$ bandwidth [Shen et al., 2024] may offer simplified packaging and control and much faster optical pulses compared to transducer arrays of $\simeq 10\,\mathrm{MHz}$ bandwidth. The large bandwidth seems to be particularly appealing as the probability of a further pulse length reduction for state-of-the-art qubit readout from currently $50\,\mathrm{ns}$ is high, considering the increasing demand for mid-circuit measurements in quantum error correction [Bengtsson et al., 2024]. Unfortunately, the efficiency of these traveling-wave electro-optic modulators needs to still be improved. Currently, it is mainly limited by the optical propagation loss.

All in all, while some aspects indicate a potential improvement by electro-optic devices such as microwave-optic transducers or photodiodes over a pristine microwave setup, the immediate usage is not immanent. Microwave setups would probably need to experience an insurmountable barrier that prohibits further scaling of quantum processors to replace them with an electro-optic interface for qubit readout or control. The current development in classical data centers, where electrical components and mid-range connections are replaced by optical counterparts for larger bandwidth, less transmission loss and lower heating [Cheng et al., 2018] may reach quantum networks or connected quantum computer in the future, but the bandwidth of microwave-optic transducers need to be highly improved to be able to fully exploit the larger data rates offered by optical fibers. In my opinion, the connection of microwave quantum systems with optical links and the related generation of remote entanglement remains the most important application of microwave-optic transducers within the framework of superconducting quantum computers. As the deterministic operation of transducers is currently out of reach but it needs to be compatible with superconducting qubit algorithms with fast gate operations and fidelities exceeding $99\,\%$, a more feasible application seems to be the continuous generation

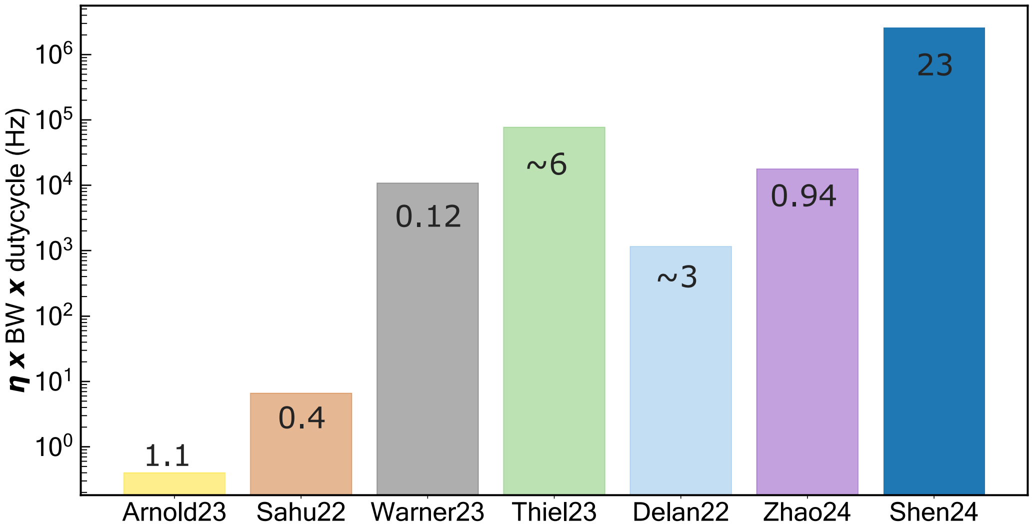

Figure 4.9: **Comparison of the transducer throughput as the product of efficiency, bandwidth and duty cycle.** Numbers on the bars indicate the input referred added noise. Data extracted from [Arnold et al., 2023; Sahu et al., 2022; Warner et al., 2023; van Thiel et al., 2023; Delaney et al., 2022; Zhao et al., 2024; Shen et al., 2024].

and temporary storage of entangled microwave-optical photon pairs with quantum memories to make them available on-demand. For the generation of these entangled pairs with high rates the transducer throughput is a suitable metric besides the input-referred added noise < 1 [Zeuthen et al., 2020]. Fig. 4.9 shows the transducer throughput as the product of transduction efficiency, conversion bandwidth and duty cycle (expressed as decimal instead of percentage). The duty cycle is one if the transducer is operated continuously. If the optical pump is pulsed, the duty cycle is the product of pulse length and repetition rate. The two devices with the largest product of all cavity-enhanced transduction systems [van Thiel et al., 2023; Zhao et al., 2024] work in continuous operation while the throughput gets significantly reduced for power-inefficient devices, where the large optical pump dissipation requires a low duty cycle in cryogenic environments to avoid temperature increase [Arnold et al., 2023; Sahu et al., 2022]. Similar to above, the traveling-wave electrooptic modulator [Shen et al., 2024] demonstrates its potential due to the large bandwidth, but both the efficiency and noise performance need to be improved for quantum operations. The numbers show the input referred added noise of each platform which needs to be below 1 to preserve entanglement during transduction.

In the next section, we will take a closer look at quantum network protocols involving microwave-optic transducers and the generation of remote entanglement between superconducting qubits connected via an optical link.

CHAPTER 5

Future directions and conclusions

Besides the application of electro-optic links for microwave signal delivery and readout as described in chapter 4, the most powerful application is the distribution of coherent quantum information and entanglement between distant locations. While the former can be seen as an alternative approach to cryogenic microwave engineering, optical interconnects are generally perceived as the only possible realization of the latter. Despite the advancements of distributed entanglement between superconducting qubits with cryogenic links of up to $30\,\mathrm{m}$ [Magnard et al., 2020] and the development of modular cooling systems, the usage of optical photons for long-range quantum networks is essential due to its low loss of down to $0.2\,\mathrm{dB/km}$ for telecom photons in optical fibers [1] , high bandwidth and the resilience to thermal noise at room temperature due to the high photon energy [2]. Microwave-optic converters can therefore not only create distributed quantum communication and operation of superconducting qubits, but they might also enable the transfer of quantum information between different qubits. This would give access to the individual strengths of various qubit platforms such as cold atoms, trapped ions, superconducting circuits, semiconductor defect center, photonic qubits, and quantum dots in a hybrid quantum network. Without touching the plethora of potential applications of a quantum network for secure communication and authentification, enhanced sensing or fundamental science, the establishment of efficient, low-noise frequency converters allows remarkable applications within the framework of quantum computing.[Wehner et al., 2018; Awschalom et al., 2021]

- *Blind quantum computing:* If qubits can be deterministically transmitted and relayed between a client device and a central quantum computer by exploiting a local quantum memory, the client device can remotely run computations on the quantum computer. This way, the client can keep his data, the performed algorithm, and the gained result private.
- *Edge quantum computing:* In the classical domain, edge computing refers to the decentralized computation of data close to its source instead of a central cloud. In the

---

[1] This corresponds to the inherent propagation loss. In commercial fiber networks such as the Boston-Area Quantum Network (BARQNET), a propagation loss of 0.5-$1\,\mathrm{dB/km}$ at a wavelength of $1350\,\mathrm{nm}$ has been found as a consequence of spliced connections in the existing fiber infrastructure [Bersin et al., 2024]. Additionally, depending on the used encoding, polarization drifts, phase noise and time-of-flight delays have to be taken into account.

[2] In shear numbers, the Bose-Einstein occupation of a bosonic mode from a thermal environment at $300\,\mathrm{K}$ is $n_{5GHz} \approx 1250$ for a typical microwave signal and $n_{200THz} \approx 10^{-14}$ in case of an optical telecom photon.

quantum realm, entanglement can be used as a resource to compute the data e.g. from a quantum sensor at the "edge" of a network.

- *Distributed quantum computing:* The computational space is exponentially enlarged by the coherent connection between individual nodes and the addition of remote operations.

While a hybrid quantum network including quantum sensors and processors opens a plethora of exciting opportunities, it is beyond the scope of this thesis. Instead, the focus is on the transfer of quantum information between two remote superconducting processors. This application, however, sets the highest requirement on the interconnect because it needs to be compatible in speed and fidelity with local operations in order to create an actual advantage in the presence of limited coherence times of qubits and quantum memories. The software stack, or to be more specific the compiler, has to balance the application of local and remote operations for a specific algorithm depending on the execution time and fidelity of the local qubit gates and the iternode connections. In [Ang et al., 2022], the authors investigate this situation for several benchmarks (e.g. the distribution of a GHZ state or the quantum Fourier transform) and an internode link fidelity of ca. 0.8, a remote gate time of $1\,\mu\mathrm{s}$ (10 times longer than the local gate time) and a repetition rate of $1\,\mathrm{MHz}$ operating in a deterministic fashion. They also show, that a interconnect with this moderate fidelity compared to locally operating qubits can already outperform two separated local system connected by a classical communication channel and the advantage scales exponentially with higher fidelity of the interconnect.

In the following, I will discuss several approaches to accomplish the first step towards, distributed entanglement of two qubits. It is worth mentioning such a remote entanglement has already been demonstrated for qubit platforms with optical transitions such photonic qubits, trapped ions, or defect centers (e.g. [Giustina et al., 2015; Hensen et al., 2015; Yin et al., 2017; Krutyanskiy et al., 2023; Knaut et al., 2024] among others), partly with bidirectional conversion from optical to telecom frequencies. Recently, remote entanglement and a loophole free Bell-test has been shown also for superconducting micorwave qubits with a cryogenic microwave link over $30\,\mathrm{m}$ [Magnard et al., 2020; Storz et al., 2023]. One remaining challenge is the remote entanglement of microwave qubits connected to a room-temperature optical fiber via microwave-optic transducers, which will be the focus of the next section.

5.1 Distributed microwave qubit entanglement

The performance of microwave-optic links used for the considerations in [Ang et al., 2022] on distributed quantum computing are still far beyond current devices. The best microwave-optic conversion efficiency to-date of $47\,\%$ is still slightly below the minimum threshold required for deterministic quantum operations [Higginbotham et al., 2018]. Additionally, a decisive parameter for microwave-optic transducers operating in the quantum regime besides the signal conversion efficiency is the noise added by the conversion process [Zeuthen et al., 2020]. The active parametric pump tones that are usually exploited for these high-efficiency converters to enhance the interaction between these vastly different frequency domains, induce absorption and thermal noise in the conversion process (cf. chapters 2.2.2,3.1.4,4). Outside the deterministic regime, where there is only a certain probability for an interconnect operation to succeed, an important metric that combines both aspects is the added noise referred to the corresponding input port or input-referred added noise. Practically speaking, it means that the noise at the converter output is divided by the non-unity transmission (or conversion efficiency). It is, thus, related to the decrease of SNR in the transduction process. If this parameter is below

1 photon the transduction process allows to preserve entanglement in the input field, even if the efficiency is low [Kumar et al., 2023]. This marks the so-called *quantum-enabled regime*, where heralding schemes can detect the successful transduction events and thereby allow for the transduction of quantum signals. The maturity of optical single-photon detectors with high efficiencies above $90\,\%$ at the desired wavelength of $1550\,\mathrm{nm}$ and dark count rates below $10\,\mathrm{Hz}$ makes optical heralding an excellent tool to enable quantum communication protocols in the presence of moderate microwave-to-optical conversion efficiency. In the following, we will describe three approaches to create such an entanglement with decreasing requirements on the performance of the respective microwave-optic transducer.

5.1.1 Direct conversion based entanglement

A widely used method for local microwave networks [Kurpiers et al., 2018; Campagne-Ibarcq et al., 2018] or short-range connections [Magnard et al., 2020; Qiu et al., 2023a] between qubits is the generation of entanglement between the qubit-state and the emission of a microwave-photon at node A, the transfer of the microwave photon to node B and capturing the photon at node B. The entanglement between a superconducting qubit and a travelling photon can be achieved in several ways (cf. Tab. 5.1). A resonant excitation transfer between qubit and cavity is a fast method ($\tau^{\pi}_{\mathrm{ge}} \approx 20\,\mathrm{ns}$, $\tau^{\pi/2}_{\phi} = \pi/(4g) \approx 2\,\mathrm{ns}$) but requires a flux-tunable qubit and precise flux control [Eichler et al., 2012b]. A dispersively coupled qubit-resonator system ($\Delta > g$) can be used as well, either using the blue-sideband transition (a Raman-type two-photon transition, [Wallraff et al., 2007; Campagne-Ibarcq et al., 2018]), or a higher-order transition of the qubit-cavity system [Egger et al., 2018; Magnard et al., 2018; Campagne-Ibarcq et al., 2018]. The former drives transitions between the qubit-resonator states $|g0\rangle \leftrightarrow |e1\rangle$ by two off-resonant drives with the resonance condition $\tilde{\omega}_{\mathrm{r}} + \tilde{\omega}_{\mathrm{q}} = \omega_{\mathrm{d1}} + \omega_{\mathrm{d2}}$. The latter applies a microwave drive at the difference frequency of the second excited qubit state and the resonator frequency $\omega_{\mathrm{d}} = \omega_{\mathrm{ge}} + \omega_{\mathrm{ef}} - \omega_{\mathrm{r}}$. In both cases, the effective coupling for both transitions is decreased but Rabi rates of $10\,\mathrm{MHz}$ are easily achievable with increased microwave drive power.

Table 5.1: **Various approaches to create entanglement between the state of a superconducting qubit and a travelling photon.**

	[Eichler et al., 2012b]	[Kurpiers et al., 2018]	[Campagne-Ibarcq et al., 2018]
photon excitation	Resonant excitation transfer	higher-order transition	two-photon sideband transition
final state	$(\lvert g1\rangle + \lvert e0\rangle)/\sqrt{2}$	$(\lvert g1\rangle + \lvert e0\rangle)/\sqrt{2}$	$(\lvert g0\rangle + \lvert e1\rangle)/\sqrt{2}$
pulse sequence	$R^{\pi}_{\mathrm{ge}} + \phi^{\pi/2}_{e\rightarrow 1}$	$R^{\pi}_{\mathrm{ge}} + R^{\pi/2}_{\mathrm{ef}} + R^{\pi}_{\mathrm{f0g1}}$	$R^{\pi/2}_{\mathrm{ge}} + R^{\pi}_{\mathrm{g0e1}}$

Consequently, a qubit-photon entanglement is encoded in the Fock state basis, where the emission of a photon is correlated with the qubit state. A substantial challenge for Fock-space encoding is the sensitivity to photon loss because the loss of the emitted photon transforms one basis state into the other, that is no photon was emitted. Hence, loss in the photon transmission or microwave-optic photon conversion directly reduces the fidelity [3].

---

[3] Time-bin encoding has the advantage that the vacuum state is not part of the encoding basis, thus, loss can be identified by the absence of a detection event [Beukers et al., 2024]

The discovery of the low loss in pure aluminium coaxial cables down to $0.15\,\mathrm{dB/km}$ at $10\,\mathrm{mK}$ [Niu et al., 2023] - similar to the previously unprecedented transmission in optical fibers - has enabled the remote entanglement between qubits separated by a $64\,\mathrm{m}$ long coaxial cable with a state fidelity of $94\,\%$ [Qiu et al., 2023a]. Even though the low loss in optical fibers down to $0.2\,\mathrm{dB/km}$ would also provide the ideal prerequisites to apply such an approach over long distances with room temperature interconnects, the moderate conversion efficiency of microwave-optic transducers puts such a protocol out of reach for quantum communication or distributed entanglement for current state-of-the-art transducers. The maximally allowed photon loss for such a deterministic protocol is $50\,\%$, in addition to the previously introduced limit for the input-referred added noise. The total loss for such an optical interconnect includes the internal microwave resonator loss at nodes A and B, microwave transmission loss to the microwave-optic transducer and from the optic-microwave transducer, microwave-optic and optic-microwave conversion efficiency, and the optical fiber transmission. Achieving a total loss $< 50\,\%$ requires a drastic increase of microwave-optic conversion efficiency with concomitant low thermal noise because the noise added by the microwave-optic converters decreases the fidelity, in addition to photon loss and limited qubit coherence.

Nevertheless, current microwave-optic converters have proven to work in the quantum-enabled regime as described above [Mirhosseini et al., 2020; Sahu et al., 2022; Meesala et al., 2024; Zhao et al., 2024]. Exploiting optical heralding and therefore the post-selection of successful events, this allows for the application of heralded remote quantum communication and entanglement.

5.1.2 Heralded direct-conversion based entanglement

5.1.2.1 Measurement-induced entanglement swapping

Instead of a "pitch-and-catch" sequence as described above, the entangled pair of a qubit and a microwave photon can be generated at both nodes A and B. We assume in the following an entangled qubit-photon state of the form $\left(|g0\rangle + |e1\rangle\right)/\sqrt{2}$ although other maximally entangled states can be generated as well, cf. Tab. 5.1. The joint state of both nodes is given by

$$\Psi_{0,\mathrm{AB}} = \left(|g_\mathrm{A} g_\mathrm{B}\rangle|0_\mathrm{A}0_\mathrm{B}\rangle + |e_\mathrm{A}e_\mathrm{B}\rangle|1_\mathrm{A}1_\mathrm{B}\rangle + |g_\mathrm{A}e_\mathrm{B}\rangle|0_\mathrm{A}1_\mathrm{B}\rangle + |e_\mathrm{A}g_\mathrm{B}\rangle|1_\mathrm{A}0_\mathrm{B}\rangle\right)/2 \tag{5.1}$$

Then, The travelling microwave photons are converted to optical frequencies using microwave-optic conversion. Assuming that the optical photons are indistinguishable, interfering them on an optical 50:50 beam splitter with subsequent detection of one photon on a single-photon detector erases the information if the photon was produced in node A or B. The detected photon state $\left(|0_\mathrm{A}1_\mathrm{B}\rangle \pm e^{-i\phi}|1_\mathrm{A}0_\mathrm{B}\rangle\right)/\sqrt{2}$ simultaneously projects the two qubits at node A and B via entanglement swapping onto the state $\left(|g_\mathrm{A}e_\mathrm{B}\rangle \pm e^{-i\phi}|e_\mathrm{A}g_\mathrm{B}\rangle\right)/\sqrt{2}$. This protocol thereby creates remote heralded entanglement between separated microwave qubits.
In practice, however, there are several sources of imperfections that decrease the fidelity of the final state. In the following we will omit the indices for the nodes A and B for simplicity.

Distinguishable photons If the two optical photons arriving at the beam splitter prior to detection are not perfectly indistinguishable, a complete path-erasure is not possible and the fidelity decreases. Typical experimental imperfections that lead to distinguishable photons are:

- Difference in frequency (i.e. optical transducer resonance frequency)

- Difference in arrival time (path length)
- Different probability to arrive at the detector

Photons with different frequencies. The frequency of the optical photons are determined by the optical mode frequency of the microwave-optic transducer. Ideally, the separation between the optical resonances of the two transducers at node A and B is not larger than their linewidth. However, a time-resolved measurement of the photon detection event can recover the indistinguishability. The frequency difference of the two photons $\Delta\omega_{12} = \omega_{\mathrm{o},2} - \omega_{\mathrm{o},1}$ leads to an oscillating phase in the entangled state. If the photon is detected at time t_{d}, the corresponding state is $\left(|ge\rangle \pm e^{-i\Delta\omega_{12}t_{\mathrm{d}}}|eg\rangle\right)/\sqrt{2}$. Applying an appropriate pulse on one of the qubits $R_{\mathrm{ge}}^{\phi_{\mathrm{c}}}$ with phase $\phi_{\mathrm{c}} = \Delta\omega_{12}t_{\mathrm{d}}$ compensates the frequency difference and recover the maximally entangled state [Zhao et al., 2014]. Because the detection time t_{d} is stochastic, the corrected phase of the active feed-forward protocol is different for each entanglement generation. Additionally, this correction can also be applied for a double-pulse-sequence (cf. 5.1.2.2)[Ruskuc et al., 2024]. Lastly, in [Levonian et al., 2022] the authors use a phase EO-modulator to combine photons at two different frequencies at a single output port. This enables the generation of heralded entanglement between quantum emitters with detuned optical transitions by detection of a single photon in a common optical path. In contrast to differences in the temporal mode arising from unequal frequencies which requires a precise control of the absolute optical resonator frequency, the temporal envelopes of the emitted microwave and optical photon are expected to be identical. They can be efficiently controlled by the applied microwave gate and optical pump pulses.

Path length differences While systematic path length differences can be corrected by a calibrated delay in the initial qubit-photon entanglement generation, small fluctuations in the path length of the order of a wavelength change the phase ϕ in the state $\left(|ge\rangle \pm e^{-i\phi}|eg\rangle\right)/\sqrt{2}$. Consequently, the paths need to be actively stabilized. Otherwise one measures a statistical mixture of the entangled states. Another related constraint is a negligible detector time jitter.

Different detection probability In order to avoid a bias in the detection probability from one of the nodes, a convenient method to adjust for differences in photon transmission or microwave-optic coupling is the corresponding adaption of the parametric optical pump pulse strength and therefore the microwave-optic conversion efficiency.

Limited qubit coherence From the form of the entangled qubit state, it is obvious that both qubit decay and dephasing decrease or even destroy the entangled state.

Two-photon-excitation While the detection of a photon carves out the contribution from $|gg\rangle|00\rangle$ in eq. 5.1, it cannot exclude an initial state of $|ee\rangle|11\rangle$ in the presence of photon loss and limited detection efficiency. Thus, it reduces the fidelity of the target state $\left(|ge\rangle \pm e^{-i\phi}|eg\rangle\right)/\sqrt{2}$.

5.1.2.2 Heralding against two-photon-excitation

Many of the experimental imperfections above can be mitigated by a sequence based on Barrett and Kok [Barrett and Kok, 2005]. If the qubit-photon entanglement with subsequent detection is followed by a R_{ge}^{π} pulse and another photon emission dependent on the qubit state, i.e. in other words a qubit-photon CNOT gate. A detection of one photon after each qubit-photon pulse heralds the protocol against the state $|ee\rangle|11\rangle$ because this necessitates $|gg\rangle|00\rangle$ without photon emission in the other time bin. Additionally, as long as the sample frequencies are constant and the (optical) setup is stable on the order of the optical wavelength ($1550\,\mathrm{nm}$) during the pulse-sequence i.e. between the two arrival times, the phase ϕ transforms into a global phase and the measured state becomes $\Psi^{\pm} = (|ge\rangle \pm |eg\rangle)/\sqrt{2}$ [Bernien et al., 2013]. The two antisymmetric Bell states can be further distinguished by measuring both outputs of the beam splitter and taking into account if both photon detection events occurred in the same (Ψ^{+}) or different detectors (Ψ^{-}). Moreover, the feed-forward correction for distinguishable photon frequencies can be expanded to this two-photon protocol by applying a pulse $R_{\mathrm{ge}}^{\phi_{\mathrm{c}}}$ with $\phi_{\mathrm{c}} = \Delta\omega_{12}(t_0 - t_1)$ to the second qubit with the arrival times of the two consecutive pulses t_0 and t_1. And lastly, the intermittent R_{ge}^{π} pulse acts as an Echo-sequence and protects the qubit from low-frequency dephasing. The disadvantage of the double pulse sequence is that the success probability is limited to $50\,\%$ even with ideal detection efficiency and the absence of photon loss. Secondly, experimentally unavoidable photon loss enters the success probability squared because two photons need to be detected in consecutive pulses.

Fig. 5.1 compares the fidelity and success probability of the single and two-photon protocol with respect to transducer thermal noise as a highly critical parameter because it determines the fidelity of the upconverted optical photon together with the losses between the cQED resonator that produces the single photon and the transducer microwave resonator. The echo sequence with two pulse sequences achieves a better fidelity due to the advantages described above, namely the protection against double excitations and the improved qubit phase coherence due to the echo sequence. The qubit parameters and pulse lengths are the experimental values from our samples and summarized in Tab. 5.2. However, as it requires the arrival of two photons in consecutive pulses the measurement time scales with the square of the photon losses throughout.

Table 5.2: **Sample parameters used for the simulations in fig. 5.1 and fig. 5.2.**

Longitudinal decay rate	T1	$18\,\mu\mathrm{s}$
Transversal decay rate	T2*	$10\,\mu\mathrm{s}$
Transversal decay rate	T2	$19\,\mu\mathrm{s}$
Pulse length	$R_{ge}^{\pi} = R_{ef}^{\pi}$	$50\,\mathrm{ns}$
Pulse length	R_{f0e1}^{π}	$100\,\mathrm{ns}$
Coupling ratio cQED resonator	η_c	0.79
Waveguide transmission	η_{wg}	0.8
Coupling ratio transducer resonator	η_e	0.55
Transduction efficiency	η_{eo}	0.1
Optical detection efficiency	η_{det}	0.2

5.1.3 TMS entanglement generation based

In the above method, the relevant limit is the added noise of the transducer referenced to the source of the single microwave photons, i.e. the qubit or strongly-coupled qubit cavity system. Therefore, both the thermal noise n_{th} of the transducer and the transmission loss between the microwave single photon source and the transducer, η_{mw}, need to be minimized and $n_{\mathrm{th}}/\eta_{\mathrm{mw}} < 1$ has to be fulfilled. Consequently, it can be advantageous to create the microwave photon directly at the transducer so that the photon does not experience transmission loss

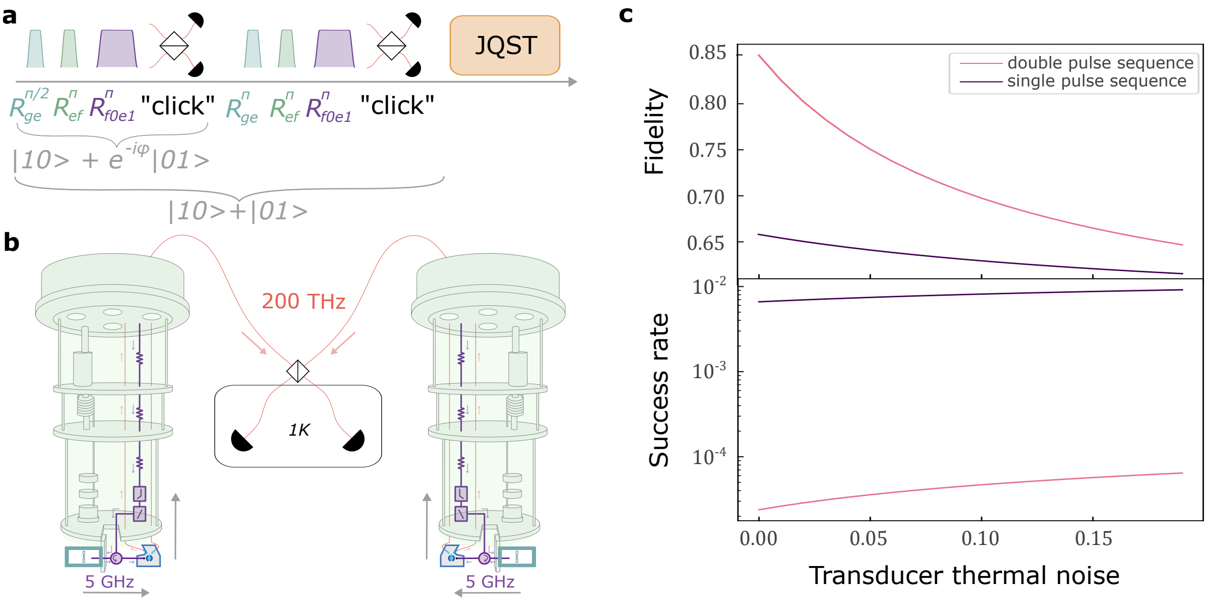

Figure 5.1: **Optically heralded remote qubit entanglement via microwave-optic conversion** **a**, Qubit and travelling microwave photon are prepared in the entangled state $1/\sqrt{2}(|g0\rangle + |e1\rangle)$ at each node. After microwave-optic conversion the indistinguishable optical photons are interfered on a beam-splitter. If the probability to detect two optical photons simultaneously is low, the measurement-induced entanglement between the photons $1/\sqrt{2}(|01\rangle + e^{-i\phi}|10\rangle)$ is swapped on the two qubit into $1/\sqrt{2}(|ge\rangle + e^{-i\phi}|eg\rangle)$. In a second round, the qubit state is inverted and another qubit-photon entanglement, optical photon interference and detection is performed. A single click in each round carves out the simultaneous emission of two photons and transforms the phase into a global phase. The final remotely entangled qubit state is $1/\sqrt{2}(|ge\rangle + |eg\rangle)$. **b** Simplified setup showing the essential microwave and optical components: Qubit-cavity system with microwave, microwave-optic transducer, optical beam splitter and optical single photon detector. **c** Fidelity and success rate of the remotely entangled qubit state with respect to the thermal noise of the transducer for the measured sample parameters T1 $= 18$ μs, T2 $= 10$ μs, T2* $= 19$ μs, and a total microwave transmission between cQED cavity and transducer microwave cavity of 55%, a microwave-optic conversion efficiency of 10% and an optical detection efficiency of 20% due to the multiple filter cavities to suppress the strong optical pump.

before it is corrupted by the thermal population in the microwave-optic transducer mode. The creation of an entangled microwave-optic photon pair in a transducer via spontaneous parametric downconversion [Sahu et al., 2023] enables such a protocol. The entangled microwave-optic photon pairs are again created at both cryogenic nodes by two transducers. If the optical photons from both nodes are indistinguishable and interfered on a symmetric beam splitter, the detection of one optical photon heralds the generation of an entangled microwave-optic photon pair. If the creation in each node is controlled to occur with equal probability, the 'which-path' information is erased and entanglement between the two microwave photons in both cryogenic nodes is established by entanglement swapping. As the state of microwave photons can be mapped on qubits, e.g. by direct absorption [Leung et al., 2019; Niu et al., 2023] or a suitable off-resonant transition [Kurpiers et al., 2018; Campagne-Ibarcq et al., 2018], this protocol establishes the remotely entangled state $\Psi^{\pm} = \left(|ge\rangle e^{-i\phi}|eg\rangle\right)/\sqrt{2}$ between qubits at the two distant cryogenic nodes (fig. 5.2a and b). The phase ϕ depends on the optical path length differences and needs to be actively stabilized or fed-forward [Lago-Rivera et al., 2021a]. Despite the aforementioned advantage of this protocol, that is that the thermal noise in the transducer is mixed with the photon right at its creation without prior attenuation as for

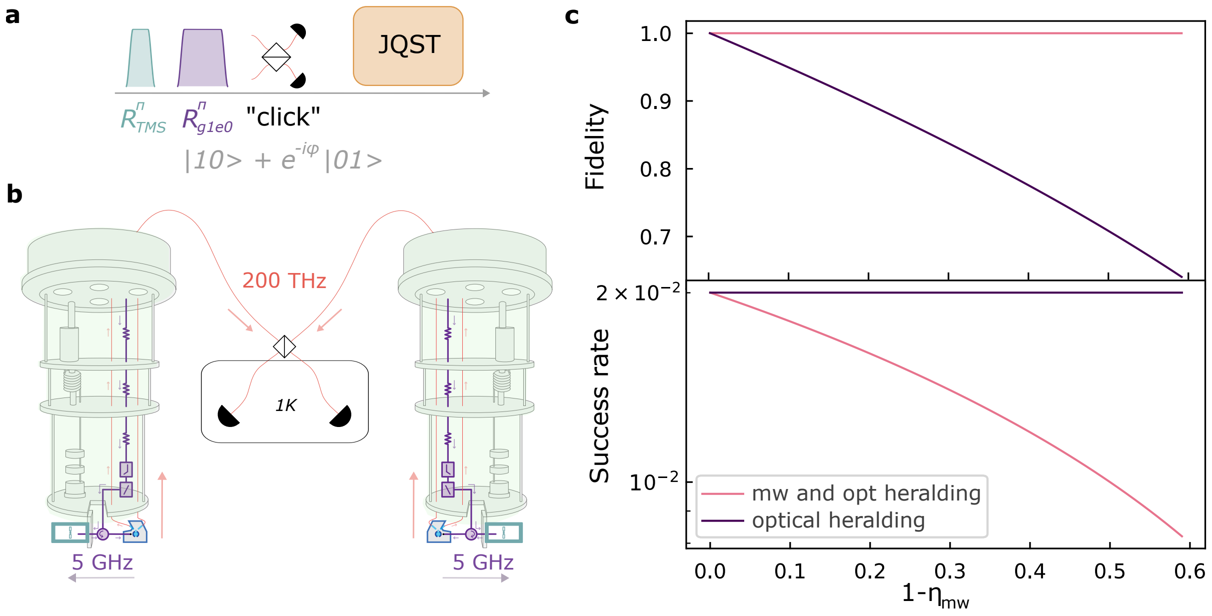

Figure 5.2: **Heralded remote qubit entanglement via two-mode squeezed microwave-optical photon pairs a**, After the generation of the entangled microwave-optic qubit pairs, and the optical detection of exactly one photon which swaps the entanglement on the two microwave photons, the photon excitation is swapped on the dispersively coupled qubit and the state $1/\sqrt{2}(|ge\rangle + e^{-i\phi}|eg\rangle)$ is created between the distant qubits. **b** Simplified experimental setup. The starting point is the electro-optic transducer that creates the entangled microwave-optical photon pairs. They propagate to the qubit and optical single photon detector at each node. **c** Fidelity and success rate of the protocol with respect to the microwave loss $1-\eta_{\mathrm{mw}}$ between the transducer resonator and the qubit. While a photon detection at the optical SNSPD heralds the generation of a microwave-optic hole pair, loss in the microwave line can alter the measured qubit state and therefore decrease the fidelity. By employing microwave heralding to detect photon loss one can maintain the high fidelity.

a qubit-photon entangled state (cf. 5.1.2, the optical detection only heralds the generation of a microwave-optical photon pair and not the entanglement of superconducting qubits. Thus, the fidelity of this protocol depends on the success probability that a created microwave photon in the transducer is mapped successfully on the superconducting qubit. Fig. 5.2c shows the fidelity of the created entangled state between the superconducting qubits with respect to the microwave loss $1-\eta_{\mathrm{mw}}$ between the transducer microwave mode and the qubit. This comprises outcoupling losses from the microwave transducer device, transmission losses in the cable, and losses in 'catching' the photon, i.e. the state transfer from the microwave photon to the qubit. In the protocol described above, this loss significantly affects the fidelity of the remotely entangled qubit state (purple curve).

Protection agains microwave photon loss Nevertheless, it is possible to protect the entangled state from the influence of microwave photon loss by employing microwave heralding in addition to the optical heralding described above. A drawback, however, is a decreased entanglement generation rate because the protocol relies on time-bin superposition of a single photon. The underlying strategy is to relate photon loss to a qubit state outside the entanglement subspace $|g\rangle, |e\rangle$. Such a protocol has been demonstrated in [Kurpiers et al., 2019], where the detection of photon loss was associated with a detection of the qubit in the second excited state, $|f\rangle$. Even though the improvement of fidelity was calculated in post-selection based on single-shot readout of the qutrit states $|g\rangle$, $|e\rangle$, and $|f\rangle$, a quantum non-demolition readout of the $|f\rangle$ state alone detects photon loss and simultaneously prevents measuring within the entanglement subspace $|g\rangle, |e\rangle$. Thus, the quantum information transmitted via the travelling microwave photon remains not affected.

Weak coherent tones as "single photons" As efficient microwave-optic transducers consist of harmonic oscillators and lack a non-linearity required for single excitation of a two-level-system and a pure Fock state generation, the produced photon-pairs in spontaneous parametric downconversion are essentially weak coherent tones with a small mean photon number and success probabilities. The blue detuned parameteric pump enhances the interaction $H_{int} \propto \hat{a}^\dagger\hat{b}^\dagger + \hat{a}\hat{b}$ (cf. 2.2 and creates the joint microwave-optic state $\Psi_{eo} \propto |00\rangle + \sqrt{p}|11\rangle + p|22\rangle + \mathcal{O}(p^{3/2})$ with p as the excitation probability [Hong et al., 2017]. Thus, the corrupting two-photon component $|22\rangle$ can only be neglected for low excitation probabilities which are typically chosen to be around 1%. Otherwise it reduces the fidelity of the finally achieved qubit-photon entangled state because photon loss of one of the two photons in the $|2\rangle$ state is equivalent to information leakage to the environment [Beukers et al., 2024]. Therefore, despite the higher resilience to thermal transducer noise, such a protocol is limited by the trade-off between the achieved entanglement generation rate and the entanglement fidelity and intrinsically excludes high success rates towards the deterministic generation of remotely entangled qubit states.

5.1.4 Conclusions

Heralded entanglement protocols substantially lower the performance requirements for the generation of remote entanglement between microwave qubits in separate refrigerators. Especially the generation via two-mode-squeezed microwave-optic photon pairs (cf. section 5.1.3 appears to be an experimental realization that is in reach considering recent results [Sahu et al., 2023; Meesala et al., 2024, 2023]. Nevertheless, this approach necessitates a low success probability for a high entanglement fidelity and is therefore an approach that prevents efficient scale-up. The generation of entanglement between a qubit and a travelling microwave photon (cf. section 5.1.2) can be achieved with both high quality and yield in various ways (Tab. 5.1). Ignoring the limited microwave-optic transduction efficiency, the exploited optical Bell-state measurement to swap the entanglement between the qubit-photon pair onto entangled qubits is bound to a $50\,\%$ success rate and therefore probabilistic. [4] Thus, only a direct conversion based approach in the spirit of a "pitch-and-catch" excitation transfer between the remote qubits via travelling microwave and optical photons including both microwave-optic and optic-microwave conversion (section 5.1.1) can ultimately achieve deterministic entanglement between superconducting qubits over large distances in separate cryogenic environments. However, significant improvement in the current device performance of microwave-optic transducers is needed to enter this regime.

In general, the future role of microwave-optic transducers for superconducting quantum processors heavily depends on the achieved performance of these devices. A long-term goal, for example, is to perform qubit state teleportation or remote gate teleportation between distant superconducting qubit via microwave-optic transducers. The room-temperature optical link would allow for disaggregation into separate cryogenic modules while still benefiting from the large computational space spanned by the qubits in these separate cryostats. Both operations can be performed only with local gates, if qubits at each computational node are remotely entangled (communication qubits) as proposed in [Jiang et al., 2007]. Quantum

---

[4] The efficiency of a Bell measurement can be theoretically increased to $75\,\%$ by exploiting single photon ancillae [Ewert and van Loock, 2014]

state teleportation performs after the creation of remote entanglement an entangling (local) two-qubit gate at e.g. node A between one of the distantly entangled communication qubits and the qubit whose state should be teleported, followed by a (single shot) Bell measurement. The outcome is then fed-forward to the distant communication qubit at node B to perform the appropriate qubit rotation. A non-local CNOT gate requires local CNOT operations between each qubit of the distantly entangled pair of communication qubits and a local qubit, followed by unitary rotations and projective measurements in the Z and X basis. This sequence realizes a CNOT gate between the two local qubits without any direct interaction between them. Gate teleportation has been achieved within the same physical device [Chou et al., 2018]. Superconducting resonators with high dimensional modes served in this experiment as data qubits and transmons (section 2.4.1) acted as communication qubits, entangled by a qubit-state dependent phase induced by the AC-Stark shift due to a resonator coupled to both qubits. The reported full process fidelity was $68\,\%$ with a total gate time of $4.6\,\mu s$. The finite transmon coherence ($T_2 \sim 15\,\mu s$) was identified as the main error source. [Wan et al., 2019] use ion-shuttling for the communication to teleport a gate between separate locations within the same trap with an entanglement fidelity of the remote CNOT gate of $\sim 85\,\%$. While single and two-qubit gates were performed within 10-20 and $\sim 200\,\mu s$) respectively, the shuttling processes ($570\,\mu s$)) and ion cooling ($\sim 1\,ms$) consume the majority of the process time. Gate teleportation between distant modules separated by $60\,m$ has been achieved with a final Bell state fidelity of $\sim 76\,\%$ via travelling photons for trapped Rubidium atoms [Daiß et al., 2021]. The two atoms are entangled by the photons being reflected from the two cavities coupled to the respective atom which conveniently creates the entanglement on-the-fly but the gate teleportation was probabilistic with a relatively low success rate of $0.6\,\%$ due to the use of weak coherent pulses with a dominant vacuum contribution (cf. section 5.1.3) and losses in the communication channel. While the remote gate itself can be performed within $22\,\mu s$, the initialization takes $\sim 200\,\mu s$. What these experiments above have in common is the high fidelity of the created remotely entangled state. Deterministic gate teleportation over distance had been prevented from the loss in the communication channel though. Even for deterministic remote entanglement demonstration [Kurpiers et al., 2018; Campagne-Ibarcq et al., 2018], the loss in the connection between the two sites has limited the fidelities to $80\,\%$. Only the discovery of low-loss coaxial cables from superconducting aluminum has enabled the first deterministic remote gate teleportation between distant qubits connected via a $64\,m$ long fiber with a loss of only $0.3\,dB/km$ [Qiu et al., 2023b]. The reported process fidelity for this *deterministic* gate teleportation is $70\,\%$ [5] Comparing these works with a communication channel that includes microwave-optic converters (cf. fig. 5.1 and fig. 5.2), we are facing three challenges:

- *current and near-term microwave-optic transducers work probabilistic*. Nevertheless, success rates on the order of $1\,\%$ should be achievable in the near future with the current approaches.[Daiß et al., 2021]
- *current and near-term microwave-optic transducers have a limited fidelity*. Every transducer platform is facing detrimental optical absorption heating that limits the achievable entanglement fidelity.
- The bandwidth of current and near-term microwave-optic transducers is $\simeq 10\,MHz$. This will ultimately limit the bandwidth of the photons in the communication channel but is currently the least severe constraint.

---

[5] This work is currently under peer-review.

Overall, it will be crucial to minimize the thermal added noise, e.g. below 0.1 and minimize the losses between the qubit and the microwave-optic converter (cf. fig. 5.1). While the former could be achieved by e.g. two-dimensionsonal OM crystals with larger heat capacity [Povey et al., 2024; Mayor et al., 2024; Sonar et al., 2024] or a spatial separation between the GHz resonator mode and the optical resonator [Warner et al., 2023], the usage of superconducting aluminum coaxial cable [Niu et al., 2023; Qiu et al., 2023b] could provide spatial separation between the optical resonator and the sensitive superconducting qubit in a modular architecture [Delaney et al., 2022; Arnold et al., 2023; Meesala et al., 2024; van Thiel et al., 2023] to avoid degradation of the qubit coherence by optical radiation while keeping the loss of information between these two components minimal. As another fundamental limitation for the achieved fidelity is always phase coherence and relaxation of the qubit, it is also crucial to use highly coherent qubits.

Closing this section with my personal view, remote qubit-qubit entanglement and quantum communication seem to be the most important applications of microwave-optic transducers within the framework of quantum computing, despite recent demonstrations for qubit readout and control [Lecocq et al., 2021; Delaney et al., 2022; Warner et al., 2023; van Thiel et al., 2023; Arnold et al., 2023]. As laid out in section 4.6.2, it seems to be rather challenging to offer sufficient advantage over all-microwave drive and readout to position microwave-optic qubit control and readout as a beneficial alternative, unless an all-microwave readout faces an unavoidable barrier in scaling, e.g. the heat budget associated with HEMT amplifiers. In the case of the generation of entangled qubits, it seems important in the long term to reach the deterministic transduction regime so that remote, long-range qubit-qubit entanglement can be created on demand. It is currently not assessable which platform has the capacity to reach a quantum limited conversion efficiency with an added noise < 0.5 at a transduction bandwidth compatible with superconducting qubit time scale, that is $\sim\mathrm{MHz}$. Otherwise, it will be interesting to see if smart compilers and algorithms manage to beneficially implement a probabilistic process within the framework of superconducting qubits. The development of long-living quantum memories might represent a key component for this task, as well as for entanglement purification and distillation to increase the fidelity of the remotely entangled qubit state. A significant increase of the entanglement generation rate has been achieved by asynchronous Bell-state measurements for qubits in the range of visible light connected via a fiber link and visible-telecom optic conversion [Bhaskar et al., 2020].

Despite these challenges and as microwave-optic transducers can be such crucial devices for large-scale superconducting quantum processors, the distribution of quantum resources and hybrid quantum networks as well as considering the radical improvements that have been achieved only over the last few years, it is exciting to work on further enhancing the performance and worth to invest more resources in the development of future quantum transducers.

Bibliography

S. Abel, F. Eltes, J. E. Ortmann, A. Messner, P. Castera, T. Wagner, D. Urbonas, A. Rosa, A. M. Gutierrez, D. Tulli, et al. Large pockels effect in micro-and nanostructured barium titanate integrated on silicon. *Nature materials*, 18(1):42–47, 2019.

R. Acharya, S. Brebels, A. Grill, J. Verjauw, T. Ivanov, D. P. Lozano, D. Wan, J. Van Damme, A. M. Vadiraj, M. Mongillo, B. Govoreanu, J. Craninckx, I. P. Radu, K. De Greve, G. Gielen, F. Catthoor, and A. Potočnik. Multiplexed superconducting qubit control at millikelvin temperatures with a low-power cryo-CMOS multiplexer. *Nature Electronics*, Sept. 2023. ISSN 2520-1131.

A. Akhiezer. On the sound absorption in solids. *J. Phys. (USSR)*, 1:277–287, 1939.

P. Anand, E. G. Arnault, M. E. Trusheim, and D. R. Englund. Microwave single-photon detection using a hybrid spin-optomechanical quantum interface. *arXiv preprint arXiv:2401.10455*, 2024.

R. W. Andrews, R. W. Peterson, T. P. Purdy, K. Cicak, R. W. Simmonds, C. A. Regal, and K. W. Lehnert. Bidirectional and efficient conversion between microwave and optical light. *Nature physics*, 10(4):321–326, 2014.

J. Ang, G. Carini, Y. Chen, I. Chuang, M. A. DeMarco, S. E. Economou, A. Eickbusch, A. Faraon, K.-M. Fu, S. M. Girvin, M. Hatridge, A. Houck, P. Hilaire, K. Krsulich, A. Li, C. Liu, Y. Liu, M. Martonosi, D. C. McKay, J. Misewich, M. Ritter, R. J. Schoelkopf, S. A. Stein, S. Sussman, H. X. Tang, W. Tang, T. Tomesh, N. M. Tubman, C. Wang, N. Wiebe, Y.-X. Yao, D. C. Yost, and Y. Zhou. Architectures for Multinode Superconducting Quantum Computers. *arXiv*, 2022.

G. Arnold, M. Wulf, S. Barzanjeh, E. S. Redchenko, A. Rueda, W. J. Hease, F. Hassani, and J. M. Fink. Converting microwave and telecom photons with a silicon photonic nanomechanical interface. *Nature Communications*, 11(1):4460, Sept. 2020. ISSN 2041-1723.

G. Arnold, T. Werner, R. Sahu, L. N. Kapoor, L. Qiu, and J. M. Fink. All-optical single-shot readout of a superconducting qubit. *arXiv preprint arXiv:2310.16817*, 2023. accepted for publication in Nature Physics under https://doi.org/10.1038/s41567-024-02741-4.

F. Arute, K. Arya, R. Babbush, D. Bacon, J. C. Bardin, R. Barends, R. Biswas, S. Boixo, F. G. S. L. Brandao, D. A. Buell, B. Burkett, Y. Chen, Z. Chen, B. Chiaro, R. Collins, W. Courtney, A. Dunsworth, E. Farhi, B. Foxen, A. Fowler, C. Gidney, M. Giustina, R. Graff, K. Guerin, S. Habegger, M. P. Harrigan, M. J. Hartmann, A. Ho, M. Hoffmann, T. Huang, T. S. Humble, S. V. Isakov, E. Jeffrey, Z. Jiang, D. Kafri, K. Kechedzhi, J. Kelly, P. V. Klimov, S. Knysh, A. Korotkov, F. Kostritsa, D. Landhuis, M. Lindmark, E. Lucero, D. Lyakh, S. Mandrà, J. R. McClean, M. McEwen, A. Megrant, X. Mi, K. Michielsen, M. Mohseni,

J. Mutus, O. Naaman, M. Neeley, C. Neill, M. Y. Niu, E. Ostby, A. Petukhov, J. C. Platt, C. Quintana, E. G. Rieffel, P. Roushan, N. C. Rubin, D. Sank, K. J. Satzinger, V. Smelyanskiy, K. J. Sung, M. D. Trevithick, A. Vainsencher, B. Villalonga, T. White, Z. J. Yao, P. Yeh, A. Zalcman, H. Neven, and J. M. Martinis. Quantum supremacy using a programmable superconducting processor. *Nature*, 574(7779):505–510, Oct. 2019. ISSN 1476-4687.

M. Asjad, S. Zippilli, and D. Vitali. Mechanical einstein-podolsky-rosen entanglement with a finite-bandwidth squeezed reservoir. *Physical Review A*, 93(6):062307, 2016.

M. Aspelmeyer, T. J. Kippenberg, and F. Marquardt. Cavity optomechanics. *Reviews of Modern Physics*, 86(4):1391–1452, Dec. 2014.

D. Awschalom, K. K. Berggren, H. Bernien, S. Bhave, L. D. Carr, P. Davids, S. E. Economou, D. Englund, A. Faraon, M. Fejer, S. Guha, M. V. Gustafsson, E. Hu, L. Jiang, J. Kim, B. Korzh, P. Kumar, P. G. Kwiat, M. Lončar, M. D. Lukin, D. A. Miller, C. Monroe, S. W. Nam, P. Narang, J. S. Orcutt, M. G. Raymer, A. H. Safavi-Naeini, M. Spiropulu, K. Srinivasan, S. Sun, J. Vučković, E. Waks, R. Walsworth, A. M. Weiner, and Z. Zhang. Development of Quantum Interconnects (QuICs) for Next-Generation Information Technologies. *PRX Quantum*, 2(1):36, 2021. ISSN 26913399.

K. Azuma, S. E. Economou, D. Elkouss, P. Hilaire, L. Jiang, H.-K. Lo, and I. Tzitrin. Quantum repeaters: From quantum networks to the quantum internet. *Reviews of Modern Physics*, 95(4):045006, 2023.

T. Bagci, a. Simonsen, S. Schmid, L. G. Villanueva, E. Zeuthen, J. Appel, J. M. Taylor, a. Sørensen, K. Usami, a. Schliesser, and E. S. Polzik. Optical detection of radio waves through a nanomechanical transducer. *Nature*, 507(7490):81–5, 2014. ISSN 1476-4687.

R. Barends, J. Wenner, M. Lenander, Y. Chen, R. C. Bialczak, J. Kelly, E. Lucero, P. O'Malley, M. Mariantoni, D. Sank, H. Wang, T. C. White, Y. Yin, J. Zhao, A. N. Cleland, J. M. Martinis, and J. J. Baselmans. Minimizing quasiparticle generation from stray infrared light in superconducting quantum circuits. *Applied Physics Letters*, 99(11):2009–2012, 2011. ISSN 00036951.

S. D. Barrett and P. Kok. Efficient high-fidelity quantum computation using matter qubits and linear optics. *Physical Review A—Atomic, Molecular, and Optical Physics*, 71(6):060310, 2005.

J. G. Bartholomew, J. Rochman, T. Xie, J. M. Kindem, A. Ruskuc, I. Craiciu, M. Lei, and A. Faraon. On-chip coherent microwave-to-optical transduction mediated by ytterbium in yvo4. *Nature communications*, 11(1):3266, 2020.

S. Barzanjeh, E. S. Redchenko, M. Peruzzo, M. Wulf, D. P. Lewis, G. Arnold, and J. M. Fink. Stationary entangled radiation from micromechanical motion. *Nature*, 570(7762):480–483, 2019.

J. S. Bell. On the Einstein Podolsky Rosen paradox. *Physics Physique Fizika*, 1:195–200, Nov 1964.

A. Bengtsson, A. Opremcak, M. Khezri, D. Sank, A. Bourassa, K. J. Satzinger, S. Hong, C. Erickson, B. J. Lester, K. C. Miao, A. N. Korotkov, J. Kelly, Z. Chen, and P. V. Klimov. Model-Based Optimization of Superconducting Qubit Readout. *Physical Review Letters*, 132, 2024.

F. Bernardot, P. Nussenzveig, M. Brune, J. Raimond, and S. Haroche. Vacuum rabi splitting observed on a microscopic atomic sample in a microwave cavity. *Europhysics Letters*, 17(1): 33, 1992.

H. Bernien, B. Hensen, W. Pfaff, G. Koolstra, M. S. Blok, L. Robledo, T. H. Taminiau, M. Markham, D. J. Twitchen, L. Childress, and R. Hanson. Heralded entanglement between solid-state qubits separated by three metres. *Nature*, 497(7447):86–90, May 2013. ISSN 1476-4687.

E. Bersin, M. Grein, M. Sutula, R. Murphy, Y. Q. Huan, M. Stevens, A. Suleymanzade, C. Lee, R. Riedinger, D. J. Starling, P. J. Stas, C. M. Knaut, N. Sinclair, D. R. Assumpcao, Y. C. Wei, E. N. Knall, B. Machielse, D. D. Sukachev, D. S. Levonian, M. K. Bhaskar, M. Lončar, S. Hamilton, M. Lukin, D. Englund, and P. B. Dixon. Development of a Boston-area 50-km fiber quantum network testbed. *Physical Review Applied*, 21(1), 2024. ISSN 23317019.

D. S. Betts. *An Introduction to Millikelvin Technology*. Cambridge University Press, Cambridge, 1989. ISBN ISBN-10 0-521-34456-5.

H. K. Beukers, M. Pasini, H. Choi, D. Englund, R. Hanson, and J. Borregaard. Remote-entanglement protocols for stationary qubits with photonic interfaces. *PRX Quantum*, 5(1): 010202, 2024.

M. K. Bhaskar, R. Riedinger, B. Machielse, D. S. Levonian, C. T. Nguyen, E. N. Knall, H. Park, D. Englund, M. Lončar, D. D. Sukachev, and M. D. Lukin. Experimental demonstration of memory-enhanced quantum communication. *Nature*, 580(7801):60–64, 2020.

A. Bienfait, K. J. Satzinger, Y. Zhong, H.-S. Chang, M.-H. Chou, C. R. Conner, É. Dumur, J. Grebel, G. A. Peairs, R. G. Povey, et al. Phonon-mediated quantum state transfer and remote qubit entanglement. *Science*, 364(6438):368–371, 2019.

L. S. Bishop, E. Ginossar, and S. M. Girvin. Response of the Strongly Driven Jaynes-Cummings Oscillator. *Physical Review Letters*, 105(10):100505, Sept. 2010.

A. Blais, R.-S. Huang, A. Wallraff, S. M. Girvin, and R. J. Schoelkopf. Cavity quantum electrodynamics for superconducting electrical circuits: An architecture for quantum computation. *Physical Review A*, 69(6):062320, 2004.

A. Blais, S. M. Girvin, and W. D. Oliver. Quantum information processing and quantum optics with circuit quantum electrodynamics. *Nature Physics*, 16(3):247–256, 2020.

A. Blais, A. L. Grimsmo, S. M. Girvin, and A. Wallraff. Circuit quantum electrodynamics. *Reviews of Modern Physics*, 93(2):025005, May 2021.

T. Blésin, H. Tian, S. A. Bhave, and T. J. Kippenberg. Quantum coherent microwave-optical transduction using high-overtone bulk acoustic resonances. *Physical Review A*, 104(5): 052601, 2021.

M. Boissonneault, J. M. Gambetta, and A. Blais. Improved Superconducting Qubit Readout by Qubit-Induced Nonlinearities. *Physical Review Letters*, 105(10):100504, Sept. 2010.

M. Borselli, T. J. Johnson, and O. Painter. Measuring the role of surface chemistry in silicon microphotonics. *Applied Physics Letters*, 88(13), 2006. ISSN 00036951.

G. S. Botello, F. Sedlmeir, A. Rueda, K. A. Abdalmalak, E. R. Brown, G. Leuchs, S. Preu, D. Segovia-Vargas, D. V. Strekalov, L. E. G. M. noz, and H. G. L. Schwefel. Sensitivity limits of millimeter-wave photonic radiometers based on efficient electro-optic upconverters. *Optica*, 5(10):1210–1219, Oct 2018.

D. Bouwmeester, J.-W. Pan, K. Mattle, M. Eibl, H. Weinfurter, and A. Zeilinger. Experimental quantum teleportation. *Nature*, 390(6660):575–579, 1997.

A. Bozkurt, H. Zhao, C. Joshi, H. G. LeDuc, P. K. Day, and M. Mirhosseini. A quantum electromechanical interface for long-lived phonons. *Nature Physics*, 19(9):1326–1332, 2023.

S. Bravyi, O. Dial, J. M. Gambetta, D. Gil, and Z. Nazario. The future of quantum computing with superconducting qubits. *Journal of Applied Physics*, 132(16):160902, Oct. 2022. ISSN 0021-8979.

S. Bravyi, A. W. Cross, J. M. Gambetta, D. Maslov, P. Rall, and T. J. Yoder. High-threshold and low-overhead fault-tolerant quantum memory. *Nature*, 627, 2024. ISSN 14764687.

T. Brecht, M. Reagor, Y. Chu, W. Pfaff, C. Wang, L. Frunzio, M. H. Devoret, and R. J. Schoelkopf. Demonstration of superconducting micromachined cavities. *Applied Physics Letters*, 107(19), 2015.

I. Breunig, B. Sturman, F. Sedlmeir, H. Schwefel, and K. Buse. Whispering gallery modes at the rim of an axisymmetric optical resonator: Analytical versus numerical description and comparison with experiment. *Optics express*, 21(25):30683–30692, 2013.

A. Broadbent, J. Fitzsimons, and E. Kashefi. Universal blind quantum computation. In *2009 50th Annual IEEE Symposium on Foundations of Computer Science*, pages 517–526, 2009.

B. M. Brubaker, J. M. Kindem, M. D. Urmey, S. Mittal, R. D. Delaney, P. S. Burns, M. R. Vissers, K. W. Lehnert, and C. A. Regal. Optomechanical ground-state cooling in a continuous and efficient electro-optic transducer. *Phys. Rev. X*, 12:021062, 2022.

M. J. Burek, C. Meuwly, R. E. Evans, M. K. Bhaskar, A. Sipahigil, S. Meesala, B. Machielse, D. D. Sukachev, C. T. Nguyen, J. L. Pacheco, E. Bielejec, M. D. Lukin, M. Lončar, and J. A. Paulson. Fiber-Coupled Diamond Quantum Nanophotonic Interface. *Physical Review Applied*, 8(2), 2017.

P. Campagne-Ibarcq, E. Zalys-Geller, A. Narla, S. Shankar, P. Reinhold, L. Burkhart, C. Axline, W. Pfaff, L. Frunzio, R. J. Schoelkopf, and M. H. Devoret. Deterministic Remote Entanglement of Superconducting Circuits through Microwave Two-Photon Transitions. *Physical Review Letters*, 120(20), 2018.

G. Catelani, S. E. Nigg, S. M. Girvin, R. J. Schoelkopf, and L. I. Glazman. Decoherence of superconducting qubits caused by quasiparticle tunneling. *Physical Review B*, 86(18): 184514, Nov. 2012.

C. M. Caves. Quantum limits on noise in linear amplifiers. *Phys. Rev. D*, 26:1817–1839, 1982.

J. Chan, A. H. Safavi-Naeini, J. T. Hill, S. Meenehan, and O. Painter. Optimized optomechanical crystal cavity with acoustic radiation shield. *Applied Physics Letters*, 101(8), 2012.

M. Chen, J. C. Owens, H. Putterman, M. Schäfer, and O. Painter. Phonon engineering of atomic-scale defects in superconducting quantum circuits. *Science Advances*, 10(37): eado6240, 2024.

Y. Chen, D. Sank, P. O'Malley, T. White, R. Barends, B. Chiaro, J. Kelly, E. Lucero, M. Mariantoni, A. Megrant, C. Neill, A. Vainsencher, J. Wenner, Y. Yin, A. N. Cleland, and J. M. Martinis. Multiplexed dispersive readout of superconducting phase qubits. *Applied Physics Letters*, 101(18):182601, Nov. 2012. ISSN 0003-6951.

Q. Cheng, M. Bahadori, M. Glick, S. Rumley, and K. Bergman. Recent advances in optical technologies for data centers: a review. *Optica*, 5(11):1354, 2018. ISSN 23342536.

K. S. Chou, J. Z. Blumoff, C. S. Wang, P. C. Reinhold, C. J. Axline, Y. Y. Gao, L. Frunzio, M. H. Devoret, L. Jiang, and R. J. Schoelkopf. Deterministic teleportation of a quantum gate between two logical qubits. *Nature*, 561(7723):368–373, 2018. ISSN 14764687.

A. A. Clerk and D. W. Utami. Using a qubit to measure photon-number statistics of a driven thermal oscillator. *Physical Review A*, 75(4):042302, Apr. 2007.

J. F. Cochran and D. Mapother. Superconducting transition in aluminum. *Physical Review*, 111(1):132, 1958.

A. D. Córcoles, J. M. Chow, J. M. Gambetta, C. Rigetti, J. R. Rozen, G. A. Keefe, M. B. Rothwell, M. B. Ketchen, and M. Steffen. Protecting superconducting qubits from radiation. *Appl. Phys. Lett.*, 99(18):181906, 2011.

J. P. Covey, H. Weinfurter, and H. Bernien. Quantum networks with neutral atom processing nodes, 2023. ISSN 20566387.

K. D. Crowley, R. A. Mclellan, A. Dutta, N. Shumiya, A. P. Place, X. H. Le, Y. Gang, T. Madhavan, M. P. Bland, R. Chang, N. Khedkar, Y. C. Feng, E. A. Umbarkar, X. Gui, L. V. Rodgers, Y. Jia, M. M. Feldman, S. A. Lyon, M. Liu, R. J. Cava, A. A. Houck, and N. P. De Leon. Disentangling Losses in Tantalum Superconducting Circuits. *Physical Review X*, 13(4), 2023. ISSN 21603308.

S. Daiß, S. Langenfeld, S. Welte, E. Distante, P. Thomas, L. Hartung, O. Morin, and G. Rempe. A quantum-logic gate between distant quantum-network modules. *Science*, 371(6529): 614–617, 2021. ISSN 10959203.

R. Dassonneville, R. Assouly, T. Peronnin, A. A. Clerk, A. Bienfait, and B. Huard. Dissipative Stabilization of Squeezing beyond 3 dB in a Microwave Mode. *PRX Quantum*, 2(2):20323, 2021. ISSN 26913399.

M. de Cea, E. E. Wollman, A. H. Atabaki, D. J. Gray, M. D. Shaw, and R. J. Ram. Photonic readout of superconducting nanowire single photon counting detectors. *Scientific Reports*, 10(1):9470, 2020.

R. D. Delaney, M. D. Urmey, S. Mittal, B. M. Brubaker, J. M. Kindem, P. S. Burns, C. A. Regal, and K. W. Lehnert. Superconducting-qubit readout via low-backaction electro-optic transduction. *Nature*, 606(7914):489–493, June 2022. ISSN 1476-4687.

Y. A. Demchenko and M. L. Gorodetsky. Analytical estimates of eigenfrequencies, dispersion, and field distribution in whispering gallery resonators. *JOSA B*, 30(11):3056–3063, 2013.

P. B. Dieterle, M. Kalaee, J. M. Fink, and O. Painter. Superconducting cavity electromechanics on a silicon-on-insulator platform. *Phys. Rev. Applied*, 6(1):014013, July 2016.

M. F. Dumas, B. Groleau-Paré, A. McDonald, M. H. Muñoz-Arias, C. Lledó, B. D'Anjou, and A. Blais. Unified picture of measurement-induced ionization in the transmon. 2024.

D. J. Egger, M. Werninghaus, M. Ganzhorn, G. Salis, A. Fuhrer, P. Müller, and S. Filipp. Pulsed reset protocol for fixed-frequency superconducting qubits. *Physical Review Applied*, 10(4):044030, 2018.

C. Eichler, D. Bozyigit, C. Lang, L. Steffen, J. Fink, and A. Wallraff. Experimental State Tomography of Itinerant Single Microwave Photons. *Phys. Rev. Lett.*, 106(22):220503, jun 2011.

C. Eichler, D. Bozyigit, and A. Wallraff. Characterizing quantum microwave radiation and its entanglement with superconducting qubits using linear detectors. *Physical Review A - Atomic, Molecular, and Optical Physics*, 86(3):1–14, 2012a.

C. Eichler, C. Lang, J. M. Fink, J. Govenius, S. Filipp, and A. Wallraff. Observation of entanglement between itinerant microwave photons and a superconducting qubit. *Physical Review Letters*, 109(24):1–5, 2012b. ISSN 00319007.

A. Einstein, B. Podolsky, and N. Rosen. Can Quantum-Mechanical Description of Physical Reality Be Considered Complete? *Physical Review*, 47(10):777–780, May 1935.

F. Ewert and P. van Loock. 3/4-efficient bell measurement with passive linear optics and unentangled ancillae. *Physical review letters*, 113(14):140403, 2014.

L. Fan, C.-L. Zou, R. Cheng, X. Guo, X. Han, Z. Gong, S. Wang, and H. X. Tang. Superconducting cavity electro-optics: A platform for coherent photon conversion between superconducting and photonic circuits. *Science Advances*, 4(8):eaar4994, 2018.

A. Faraon, C. Santori, Z. Huang, V. M. Acosta, and R. G. Beausoleil. Coupling of nitrogen-vacancy centers to photonic crystal cavities in monocrystalline diamond. *Physical review letters*, 109(3):033604, 2012.

T. Faust, J. Rieger, M. J. Seitner, J. P. Kotthaus, and E. M. Weig. Signatures of two-level defects in the temperature-dependent damping of nanomechanical silicon nitride resonators. *Physical Review B*, 89(10):100102, 2014.

X. Fernandez-Gonzalvo, S. P. Horvath, Y.-H. Chen, and J. J. Longdell. Cavity-enhanced raman heterodyne spectroscopy in er 3+: Y 2 sio 5 for microwave to optical signal conversion. *Physical Review A*, 100(3):033807, 2019.

J. M. Fink, M. Kalaee, A. Pitanti, R. Norte, L. Heinzle, M. Davanço, K. Srinivasan, and O. Painter. Quantum electromechanics on silicon nitride nanomembranes. *Nature Communications*, 7:12396, aug 2016.

M. Forsch, R. Stockill, A. Wallucks, I. Marinković, C. Gärtner, R. A. Norte, F. van Otten, A. Fiore, K. Srinivasan, and S. Gröblacher. Microwave-to-optics conversion using a mechanical oscillator in its quantum ground state. *Nature Physics*, 16(1):69–74, 2020.

G. Gagliardi and H.-P. Loock. *Cavity-enhanced spectroscopy and sensing*, volume 179. Springer, 2014.

B. T. Gard, K. Jacobs, R. McDermott, and M. Saffman. Microwave-to-optical frequency conversion using a cesium atom coupled to a superconducting resonator. *Physical Review A*, 96(1):013833, 2017.

C. W. Gardiner. Driving a quantum system with the output field from another driven quantum system. *Physical Review Letters*, 70(15):2269–2272, Apr. 1993.

C. W. Gardiner and M. J. Collett. Input and output in damped quantum systems: quantum stochastic differential equations and the master equation. *Phys. Rev. A*, 31(6):3761–3774, 1985.

A. H. Ghadimi, S. A. Fedorov, N. J. Engelsen, M. J. Bereyhi, R. Schilling, D. J. Wilson, and T. J. Kippenberg. Elastic strain engineering for ultralow mechanical dissipation. *Science*, 360(6390):764–768, may 2018. ISSN 0036-8075.

C. Gidney and M. Ekerå. How to factor 2048 bit RSA integers in 8 hours using 20 million noisy qubits. *Quantum*, 5:433–464, 2021. ISSN 2521327X.

M. Giustina, M. A. Versteegh, S. Wengerowsky, J. Handsteiner, A. Hochrainer, K. Phelan, F. Steinlechner, J. Kofler, J.-Å. Larsson, C. Abellán, et al. Significant-loophole-free test of bell's theorem with entangled photons. *Physical review letters*, 115(25):250401, 2015.

M. L. Gorodetsky, A. D. Pryamikov, and V. S. Ilchenko. Rayleigh scattering in high-q microspheres. *JOSA B*, 17(6):1051–1057, 2000.

D. Gottesman, T. Jennewein, and S. Croke. Longer-baseline telescopes using quantum repeaters. *Phys. Rev. Lett.*, 109:070503, Aug 2012.

S. Gröblacher, K. Hammerer, M. R. Vanner, and M. Aspelmeyer. Observation of strong coupling between a micromechanical resonator and an optical cavity field. *Nature*, 460: 724–727, aug 2009.

S. Gröblacher, J. T. Hill, A. H. Safavi-Naeini, J. Chan, and O. Painter. Highly efficient coupling from an optical fiber to a nanoscale silicon optomechanical cavity. *Applied Physics Letters*, 103(18):1–4, 2013.

J. Han, T. Vogt, C. Gross, D. Jaksch, M. Kiffner, and W. Li. Coherent microwave-to-optical conversion via six-wave mixing in rydberg atoms. *Physical review letters*, 120(9):093201, 2018.

X. Han, W. Fu, C. Zhong, C.-L. Zou, Y. Xu, A. A. Sayem, M. Xu, S. Wang, R. Cheng, L. Jiang, et al. Cavity piezo-mechanics for superconducting-nanophotonic quantum interface. *Nature communications*, 11(1):3237, 2020.

X. Han, W. Fu, C.-L. Zou, L. Jiang, and H. X. Tang. Microwave-optical quantum frequency conversion. *Optica*, 8(8):1050–1064, Aug. 2021. ISSN 2334-2536.

R. F. Harrington and J. L. Harrington. *Field computation by moment methods*. Oxford University Press, Inc., 1996.

M. Hatridge, S. Shankar, M. Mirrahimi, F. Schackert, K. Geerlings, T. Brecht, K. M. Sliwa, B. Abdo, L. Frunzio, S. M. Girvin, R. J. Schoelkopf, and M. H. Devoret. Quantum back-action of an individual variable-strength measurement. *Science*, 339(6116):178–181, jan 2013. ISSN 10959203.

W. Hease, A. Rueda, R. Sahu, M. Wulf, G. Arnold, H. G. Schwefel, and J. M. Fink. Bidirectional Electro-Optic Wavelength Conversion in the Quantum Ground State. *PRX Quantum*, 1(2): 020315, Nov. 2020.

J. Heinsoo, C. K. Andersen, A. Remm, S. Krinner, T. Walter, Y. Salathé, S. Gasparinetti, J.-C. Besse, A. Potočnik, A. Wallraff, and C. Eichler. Rapid high-fidelity multiplexed readout of superconducting qubits. *Phys. Rev. Appl.*, 10:034040, Sep 2018.

B. Hensen, H. Bernien, A. E. Dréau, A. Reiserer, N. Kalb, M. S. Blok, J. Ruitenberg, R. F. Vermeulen, R. N. Schouten, C. Abellán, et al. Loophole-free bell inequality violation using electron spins separated by 1.3 kilometres. *Nature*, 526(7575):682–686, 2015.

S. L. N. Hermans, M. Pompili, H. K. C. Beukers, S. Baier, J. Borregaard, and R. Hanson. Qubit teleportation between non-neighbouring nodes in a quantum network. *Nature*, 605 (7911):663–668, May 2022. ISSN 1476-4687.

A. P. Higginbotham, P. S. Burns, M. D. Urmey, R. W. Peterson, N. S. Kampel, B. M. Brubaker, G. Smith, K. W. Lehnert, and C. A. Regal. Harnessing electro-optic correlations in an efficient mechanical converter. *Nature Physics*, 14(10):1038–1042, 2018. ISSN 1745-2481.

J. T. Hill, A. H. Safavi-Naeini, J. Chan, and O. Painter. Coherent optical wavelength conversion via cavity optomechanics. *Nature Communications*, 3:1196, jun 2012.

R. Hisatomi, A. Osada, Y. Tabuchi, T. Ishikawa, A. Noguchi, R. Yamazaki, K. Usami, and Y. Nakamura. Bidirectional conversion between microwave and light via ferromagnetic magnons. *Physical Review B*, 93(17):174427, 2016.

T. Hoefler, T. Häner, and M. Troyer. Disentangling hype from practicality: On realistically achieving quantum advantage. *Commun. ACM*, 66(5):82–87, apr 2023. ISSN 0001-0782.

D. S. Holmes, A. L. Ripple, and M. A. Manheimer. Energy-Efficient Superconducting Computing—Power Budgets and Requirements. *IEEE Transactions on Applied Superconductivity*, 23(3):1701610–1701610, 2013. ISSN 1051-8223.

S. Hong, R. Riedinger, I. Marinković, A. Wallucks, S. G. Hofer, R. A. Norte, M. Aspelmeyer, and S. Gröblacher. Hanbury Brown and Twiss interferometry of single phonons from an optomechanical resonator. *Science*, 358(6360):203–206, 2017.

M. Houzet, K. Serniak, G. Catelani, M. H. Devoret, and L. I. Glazman. Photon-assisted charge-parity jumps in a superconducting qubit. *Physical Review Letters*, 123(10):107704, 2019.

S. S. Iyer and R. N. Candler. Mode-and direction-dependent mechanical energy dissipation in single-crystal resonators due to anharmonic phonon-phonon scattering. *Physical Review Applied*, 5(3):034002, 2016.

C. Javerzac-Galy, K. Plekhanov, N. R. Bernier, L. D. Toth, A. K. Feofanov, and T. J. Kippenberg. On-chip microwave-to-optical quantum coherent converter based on a superconducting resonator coupled to an electro-optic microresonator. *Phys. Rev. A*, 94:053815, Nov 2016.

E. T. Jaynes and F. W. Cummings. Comparison of quantum and semiclassical radiation theories with application to the beam maser. *Proceedings of the IEEE*, 51(1):89–109, 1963.

L. Jiang, J. M. Taylor, A. S. Sørensen, and M. D. Lukin. Distributed quantum computation based on small quantum registers. *Physical Review A - Atomic, Molecular, and Optical Physics*, 76(6):062323, 2007.

W. Jiang, C. J. Sarabalis, Y. D. Dahmani, R. N. Patel, F. M. Mayor, T. P. McKenna, R. Van Laer, and A. H. Safavi-Naeini. Efficient bidirectional piezo-optomechanical transduction between microwave and optical frequency. *Nature Communications*, 11, 2020.

W. Jiang, F. M. Mayor, S. Malik, R. Van Laer, T. P. McKenna, R. N. Patel, J. D. Witmer, and A. H. Safavi-Naeini. Optically heralded microwave photon addition. *Nature Physics*, 19 (10):1423–1428, 2023.

X. Y. Jin, A. Kamal, A. P. Sears, T. Gudmundsen, D. Hover, J. Miloshi, R. Slattery, F. Yan, J. Yoder, T. P. Orlando, S. Gustavsson, and W. D. Oliver. Thermal and Residual Excited-State Population in a 3D Transmon Qubit. *Physical Review Letters*, 114(24):240501, 2015. ISSN 10797114.

J. J. D. Joannopoulos, S. Johnson, J. N. J. Winn, and R. R. D. Meade. *Photonic crystals: molding the flow of light*. Princeton University Press, Princeton, 2 edition, 2008. ISBN 9780691124568.

S. G. Johnson, M. Ibanescu, M. A. Skorobogatiy, O. Weisberg, J. D. Joannopoulos, and Y. Fink. Perturbation theory for Maxwell's equations with shifting material boundaries. *Physical Review E - Statistical Physics, Plasmas, Fluids, and Related Interdisciplinary Topics*, 65(6):1–7, 2002.

S. Joshi and S. Moazeni. Scaling up superconducting quantum computers with cryogenic rf-photonics, 2022.

M. Kalaee, M. Mirhosseini, P. B. Dieterle, M. Peruzzo, J. M. Fink, and O. Painter. Quantum electromechanics of a hypersonic crystal. *Nature nanotechnology*, 14(4):334–339, 2019.

M. Khezri, A. Opremcak, Z. Chen, K. C. Miao, M. McEwen, A. Bengtsson, T. White, O. Naaman, D. Sank, A. N. Korotkov, Y. Chen, and V. Smelyanskiy. Measurement-induced state transitions in a superconducting qubit: Within the rotating-wave approximation. *Physical Review Applied*, 20(5), 2023.

Y. Kim, A. Eddins, S. Anand, K. X. Wei, E. van den Berg, S. Rosenblatt, H. Nayfeh, Y. Wu, M. Zaletel, K. Temme, and A. Kandala. Evidence for the utility of quantum computing before fault tolerance. *Nature*, 618(7965):500–505, June 2023. ISSN 1476-4687.

H. J. Kimble. The quantum internet. *Nature*, 453(7198):1023–1030, June 2008. ISSN 1476-4687.

C. Knaut, A. Suleymanzade, Y.-C. Wei, D. Assumpcao, P.-J. Stas, Y. Huan, B. Machielse, E. Knall, M. Sutula, G. Baranes, et al. Entanglement of nanophotonic quantum memory nodes in a telecom network. *Nature*, 629(8012):573–578, 2024.

J. Koch, M. Y. Terri, J. Gambetta, A. A. Houck, D. I. Schuster, J. Majer, A. Blais, M. H. Devoret, S. M. Girvin, and R. J. Schoelkopf. Charge-insensitive qubit design derived from the cooper pair box. *Physical Review A*, 76(4):042319, 2007.

S. Krinner, S. Storz, P. Kurpiers, P. Magnard, J. Heinsoo, R. Keller, J. Lütolf, C. Eichler, and A. Wallraff. Engineering cryogenic setups for 100-qubit scale superconducting circuit systems. *EPJ Quantum Technology*, 6:2, 2019. ISSN 21960763.

V. Krutyanskiy, M. Galli, V. Krcmarsky, S. Baier, D. Fioretto, Y. Pu, A. Mazloom, P. Sekatski, M. Canteri, M. Teller, et al. Entanglement of trapped-ion qubits separated by 230 meters. *Physical Review Letters*, 130(5):050803, 2023.

A. Kumar, A. Suleymanzade, M. Stone, L. Taneja, A. Anferov, D. I. Schuster, and J. Simon. Quantum-enabled millimetre wave to optical transduction using neutral atoms. *Nature*, 615 (7953):614–619, 2023.

P. Kurpiers, P. Magnard, T. Walter, B. Royer, M. Pechal, J. Heinsoo, Y. Salathé, A. Akin, S. Storz, J.-C. Besse, S. Gasparinetti, A. Blais, and A. Wallraff. Deterministic quantum state transfer and remote entanglement using microwave photons. *Nature*, 558(7709):264–267, jun 2018.

P. Kurpiers, M. Pechal, B. Royer, P. Magnard, T. Walter, J. Heinsoo, Y. Salathé, A. Akin, S. Storz, J.-C. Besse, S. Gasparinetti, A. Blais, and A. Wallraff. Quantum Communication with Time-Bin Encoded Microwave Photons. *Physical Review Applied*, 12(4):044067, oct 2019. ISSN 2331-7019.

D. Lago-Rivera, S. Grandi, J. V. Rakonjac, A. Seri, and H. de Riedmatten. Telecom-heralded entanglement between multimode solid-state quantum memories. *Nature*, 594(7861):37–40, 2021a.

D. Lago-Rivera, S. Grandi, J. V. Rakonjac, A. Seri, and H. de Riedmatten. Telecom-heralded entanglement between multimode solid-state quantum memories. *Nature*, 594(7861):37–40, 2021b.

N. J. Lambert, A. Rueda, F. Sedlmeir, and H. G. L. Schwefel. Coherent Conversion Between Microwave and Optical Photons—An Overview of Physical Implementations. *Advanced Quantum Technologies*, 3(1):1900077, 2020. ISSN 2511-9044.

L. Landau and G. Rumer. On the absorption of sound in solids. *Physikalische Zeitschrift der Sowjetunion*, 11(18), 1937.

H.-K. Lau and A. A. Clerk. Ground-State Cooling and High-Fidelity Quantum Transduction via Parametrically Driven Bad-Cavity Optomechanics. *Physical Review Letters*, 124(10): 103602, mar 2020.

N. Lauk, N. Sinclair, S. Barzanjeh, J. P. Covey, M. Saffman, M. Spiropulu, and C. Simon. Perspectives on quantum transduction. *Quantum Science and Technology*, 5(2):020501, 2020.

F. Lecocq, J. B. Clark, R. W. Simmonds, J. Aumentado, and J. D. Teufel. Mechanically Mediated Microwave Frequency Conversion in the Quantum Regime. *Physical Review Letters*, 116(4):43601, jan 2016.

F. Lecocq, F. Quinlan, K. Cicak, J. Aumentado, S. A. Diddams, and J. D. Teufel. Control and readout of a superconducting qubit using a photonic link. *Nature*, 591(7851):575–579, Mar. 2021. ISSN 1476-4687.

C. U. Lei, S. Ganjam, L. Krayzman, A. Banerjee, K. Kisslinger, S. Hwang, L. Frunzio, and R. J. Schoelkopf. Characterization of Microwave Loss Using Multimode Superconducting Resonators. *Physical Review Applied*, 20(2):1, 2023. ISSN 23317019.

M. Leidinger, S. Fieberg, N. Waasem, F. Kühnemann, K. Buse, and I. Breunig. Comparative study on three highly sensitive absorption measurement techniques characterizing lithium niobate over its entire transparent spectral range. *Optics express*, 23(17):21690–21705, 2015.

R. Leijssen and E. Verhagen. Strong optomechanical interactions in a sliced photonic crystal nanobeam. *Scientific Reports*, 5:15974, 2015. ISSN 2045-2322.

N. Leung, Y. Lu, S. Chakram, R. Naik, N. Earnest, R. Ma, K. Jacobs, A. Cleland, and D. Schuster. Deterministic bidirectional communication and remote entanglement generation between superconducting qubits. *npj Quantum Information*, 5(1):18, 2019.

D. S. Levonian, R. Riedinger, B. Machielse, E. N. Knall, M. K. Bhaskar, C. M. Knaut, R. Bekenstein, H. Park, M. Lončar, and M. D. Lukin. Optical Entanglement of Distinguishable Quantum Emitters. *Physical Review Letters*, 128(21):213602, may 2022.

N. Li, Y.-H. Li, D.-J. Fan, L.-C. Han, Y. Xu, J. Lin, C. Guo, D.-D. Li, M. Gong, S.-K. Liao, X.-B. Zhu, and C.-Z. Peng. Optical transmission of microwave control signal towards large-scale superconducting quantum computing. *Optics Express*, 32(3):3989–3996, 2024.

R. Lifshitz and M. L. Roukes. Thermoelastic damping in micro-and nanomechanical systems. *Physical review B*, 61(8):5600, 2000.

C. Liu, A. Ballard, D. Olaya, D. Schmidt, J. Biesecker, T. Lucas, J. Ullom, S. Patel, O. Rafferty, A. Opremcak, K. Dodge, V. Iaia, T. McBroom, J. DuBois, P. Hopkins, S. Benz, B. Plourde, and R. McDermott. Single flux quantum-based digital control of superconducting qubits in a multichip module. *PRX Quantum*, 4:030310, Jul 2023.

X. Ma, J. J. Viennot, S. Kotler, J. D. Teufel, and K. W. Lehnert. Non-classical energy squeezing of a macroscopic mechanical oscillator. *Nature Physics*, 17(3):322–326, jan 2021.

G. S. MacCabe, H. Ren, J. Luo, J. D. Cohen, H. Zhou, A. Sipahigil, M. Mirhosseini, and O. Painter. Nano-acoustic resonator with ultralong phonon lifetime. *Science*, 370(6518): 840–843, nov 2020. ISSN 0036-8075.

P. Magnard, P. Kurpiers, B. Royer, T. Walter, J. C. Besse, S. Gasparinetti, M. Pechal, J. Heinsoo, S. Storz, A. Blais, and A. Wallraff. Fast and Unconditional All-Microwave Reset of a Superconducting Qubit. *Physical Review Letters*, 121(6), 2018. ISSN 10797114.

P. Magnard, S. Storz, P. Kurpiers, J. Schär, F. Marxer, J. Lütolf, T. Walter, J.-C. Besse, M. Gabureac, K. Reuer, A. Akin, B. Royer, A. Blais, and A. Wallraff. Microwave Quantum Link between Superconducting Circuits Housed in Spatially Separated Cryogenic Systems. *Physical Review Letters*, 125(26):260502, Dec. 2020.

F. Marquardt, J. P. Chen, A. A. Clerk, and S. Girvin. Quantum theory of cavity-assisted sideband cooling of mechanical motion. *Physical review letters*, 99(9):093902, 2007.

F. M. Mayor, S. Malik, A. G. Primo, S. Gyger, W. Jiang, T. P. Alegre, and A. H. Safavi-Naeini. A two-dimensional optomechanical crystal for quantum transduction. *arXiv preprint arXiv:2406.14484*, 2024.

S. M. Meenehan, J. D. Cohen, S. Gröblacher, J. T. Hill, A. H. Safavi-Naeini, M. Aspelmeyer, and O. Painter. Silicon optomechanical crystal resonator at millikelvin temperatures. *Physical Review A - Atomic, Molecular, and Optical Physics*, 90(1):1–7, 2014.

S. M. Meenehan, J. D. Cohen, G. S. MacCabe, F. Marsili, M. D. Shaw, and O. Painter. Pulsed excitation dynamics of an optomechanical crystal resonator near its quantum ground state of motion. *Physical Review X*, 5(4), 2015.

S. Meesala, D. Lake, S. Wood, P. Chiappina, C. Zhong, A. D. Beyer, M. D. Shaw, L. Jiang, and O. Painter. Quantum entanglement between optical and microwave photonic qubits. *arXiv preprint arXiv:2312.13559*, 2023.

S. Meesala, S. Wood, D. Lake, P. Chiappina, C. Zhong, A. D. Beyer, M. D. Shaw, L. Jiang, and O. Painter. Non-classical microwave–optical photon pair generation with a chip-scale transducer. *Nature Physics*, pages 1–7, 2024.

M. Mirhosseini, A. Sipahigil, M. Kalaee, and O. Painter. Superconducting qubit to optical photon transduction. *Nature*, 588(7839):599–603, Dec. 2020. ISSN 1476-4687.

S. Mittal, K. Adachi, N. E. Frattini, M. D. Urmey, S. X. Lin, A. L. Emser, C. Metzger, L. G. Talamo, S. Dickson, D. Carlson, S. B. Papp, C. A. Regal, and K. W. Lehnert. Annealing reduces Si3 N4 microwave-frequency dielectric loss in superconducting resonators. *Physical Review Applied*, 21(5), 2024. ISSN 23317019.

S. S. Mohan, M. del Mar Hershenson, S. P. Boyd, and T. H. Lee. Simple accurate expressions for planar spiral inductances. *IEEE Journal of solid-state circuits*, 34(10):1419–1424, 1999.

W. G. Nagourney. *Quantum electronics for atomic physics*. Oxford University Press, 2010.

J. Niu, L. Zhang, Y. Liu, J. Qiu, W. Huang, J. Huang, H. Jia, J. Liu, Z. Tao, W. Wei, et al. Low-loss interconnects for modular superconducting quantum processors. *Nature Electronics*, 6(3):235–241, 2023.

R. A. Norte, J. P. Moura, and S. Gröblacher. Mechanical resonators for quantum optomechanics experiments at room temperature. *Physical review letters*, 116(14):147202, 2016.

H. Paik, D. I. Schuster, L. S. Bishop, G. Kirchmair, G. Catelani, A. P. Sears, B. R. Johnson, M. J. Reagor, L. Frunzio, L. I. Glazman, S. M. Girvin, M. H. Devoret, and R. J. Schoelkopf. Observation of high coherence in josephson junction qubits measured in a three-dimensional circuit qed architecture. *Phys. Rev. Lett.*, 107:240501, Dec 2011.

T. A. Palomaki, J. W. Harlow, J. D. Teufel, R. W. Simmonds, and K. W. Lehnert. Coherent state transfer between itinerant microwave fields and a mechanical oscillator. *Nature*, 495 (7440):210–214, mar 2013.

S. J. Pauka, K. Das, R. Kalra, A. Moini, Y. Yang, M. Trainer, A. Bousquet, C. Cantaloube, N. Dick, G. C. Gardner, M. J. Manfra, and D. J. Reilly. A cryogenic CMOS chip for generating control signals for multiple qubits. *Nature Electronics*, 4(1):64–70, Jan. 2021. ISSN 2520-1131.

M. Pechal, L. Huthmacher, C. Eichler, S. Zeytinoğlu, A. A. Abdumalikov, S. Berger, A. Wallraff, and S. Filipp. Microwave-Controlled Generation of Shaped Single Photons in Circuit Quantum Electrodynamics. *Physical Review X*, 4(4):41010, oct 2014.

R. G. Povey, M.-H. Chou, G. Andersson, C. R. Conner, J. Grebel, Y. J. Joshi, J. M. Miller, H. Qiao, X. Wu, H. Yan, et al. Two-dimensional optomechanical crystal resonator in gallium arsenide. *Physical Review Applied*, 21(1):014015, 2024.

H. Qiao, E. Dumur, G. Andersson, H. Yan, M.-H. Chou, J. Grebel, C. R. Conner, Y. J. Joshi, J. M. Miller, R. G. Povey, et al. Splitting phonons: Building a platform for linear mechanical quantum computing. *Science*, 380(6649):1030–1033, 2023.

J. Qiu, Y. Liu, J. Niu, L. Hu, Y. Wu, L. Zhang, W. Huang, Y. Chen, J. Li, S. Liu, et al. Deterministic quantum teleportation between distant superconducting chips. *arXiv preprint arXiv:2302.08756*, 2023a.

L. Qiu, I. Shomroni, P. Seidler, and T. J. Kippenberg. Laser cooling of a nanomechanical oscillator to its zero-point energy. *Physical review letters*, 124(17):173601, 2020.

L. Qiu, R. Sahu, W. Hease, G. Arnold, and J. M. Fink. Coherent optical control of a superconducting microwave cavity via electro-optical dynamical back-action. *Nature Communications*, 14(1):3784, 2023b.

P. Rabl. Photon blockade effect in optomechanical systems. *Physical review letters*, 107(6): 063601, 2011.

M. Reagor, H. Paik, G. Catelani, L. Sun, C. Axline, E. Holland, I. M. Pop, N. A. Masluk, T. Brecht, L. Frunzio, M. H. Devoret, L. Glazman, and R. J. Schoelkopf. Reaching 10 ms single photon lifetimes for superconducting aluminum cavities. *Applied Physics Letters*, 102 (19):192604, 2013. ISSN 00036951.

E. Redchenko. *Controllable states of superconducting Qubit ensembles*. PhD thesis, Institute of Science and Technology Austria, 2022.

A. P. Reed, K. H. Mayer, J. D. Teufel, L. D. Burkhart, W. Pfaff, M. Reagor, L. Sletten, X. Ma, R. J. Schoelkopf, E. Knill, and K. W. Lehnert. Faithful conversion of propagating quantum information to mechanical motion. *Nature Physics*, 13:1163–1167, 2017.

M. D. Reed, L. DiCarlo, B. R. Johnson, L. Sun, D. I. Schuster, L. Frunzio, and R. J. Schoelkopf. High-Fidelity Readout in Circuit Quantum Electrodynamics Using the Jaynes-Cummings Nonlinearity. *Phys. Rev. Lett.*, 105(17):173601, oct 2010.

R. Riedinger, S. Hong, R. A. Norte, J. A. Slater, J. Shang, A. G. Krause, V. Anant, M. Aspelmeyer, and S. Gröblacher. Non-classical correlations between single photons and phonons from a mechanical oscillator. *Nature*, 530:313, jan 2016.

R. Riedinger, A. Wallucks, I. Marinković, C. Löschnauer, M. Aspelmeyer, S. Hong, and S. Gröblacher. Remote quantum entanglement between two micromechanical oscillators. *Nature*, 556(7702):473–477, 2018.

C. Rigetti, J. M. Gambetta, S. Poletto, B. L. Plourde, J. M. Chow, A. D. Córcoles, J. A. Smolin, S. T. Merkel, J. R. Rozen, G. A. Keefe, M. B. Rothwell, M. B. Ketchen, and M. Steffen. Superconducting qubit in a waveguide cavity with a coherence time approaching 0.1 ms. *Physical Review B - Condensed Matter and Materials Physics*, 86:100506, 2012.

D. Ristè, C. C. Bultink, M. J. Tiggelman, R. N. Schouten, K. W. Lehnert, and L. Dicarlo. Millisecond charge-parity fluctuations and induced decoherence in a superconducting transmon qubit. *Nature Communications*, 4(May):1–6, 2013. ISSN 20411723.

J. Rochman, T. Xie, J. G. Bartholomew, K. Schwab, and A. Faraon. Microwave-to-optical transduction with erbium ions coupled to planar photonic and superconducting resonators. *Nature Communications*, 14(1):1153, 2023.

J. Rodriguez, S. A. Chandorkar, C. A. Watson, G. M. Glaze, C. H. Ahn, E. J. Ng, Y. Yang, and T. W. Kenny. Direct Detection of Akhiezer Damping in a Silicon MEMS Resonator. *Scientific Reports*, 9(1):1–10, 2019. ISSN 20452322.

A. Rueda, F. Sedlmeir, M. C. Collodo, U. Vogl, B. Stiller, G. Schunk, D. V. Strekalov, C. Marquardt, J. M. Fink, O. Painter, G. Leuchs, and H. G. L. Schwefel. Efficient microwave to optical photon conversion: an electro-optical realization. *Optica*, 3(6):597–604, Jun 2016.

A. Rueda, F. Sedlmeir, M. Kumari, G. Leuchs, and H. G. Schwefel. Resonant electro-optic frequency comb. *Nature*, 568(7752):378–381, 2019.

A. R. Rueda Sanchez. *Resonant Electrooptics*. PhD thesis, Friedrich-Alexander-Universität Erlangen-Nürnberg (FAU), 2018.

A. Ruskuc, C.-J. Wu, E. Green, S. L. N. Hermans, J. Choi, and A. Faraon. Scalable Multipartite Entanglement of Remote Rare-earth Ion Qubits. 2024.

A. H. Safavi-Naeini, T. P. M. Alegre, J. Chan, M. Eichenfield, M. Winger, Q. Lin, J. T. Hill, D. E. Chang, and O. Painter. Electromagnetically induced transparency and slow light with optomechanics. *Nature*, 472(7341):69–73, 2011. ISSN 0028-0836.

A. H. Safavi-Naeini, S. Gröblacher, J. T. Hill, J. Chan, M. Aspelmeyer, and O. Painter. Squeezed light from a silicon micromechanical resonator. *Nature*, 500:185–189, 2013.

G. Sahasrabudhe and S. Lambade. Temperature dependence of the collective phonon relaxation time and acoustic damping in ge and si. *Journal of Physics and Chemistry of Solids*, 60(6): 773–785, 1999.

R. Sahu. *Cavity quantum electrooptics*. PhD thesis, Insititute of Science and Technology Austria (ISTA), 2023.

R. Sahu, W. Hease, A. Rueda, G. Arnold, L. Qiu, and J. M. Fink. Quantum-enabled operation of a microwave-optical interface. *Nature Communications*, 13(1):1276, Mar. 2022.

R. Sahu, L. Qiu, W. Hease, G. Arnold, Y. Minoguchi, P. Rabl, and J. M. Fink. Entangling microwaves with light. *Science*, 380(6646):718–721, may 2023. ISSN 0036-8075.

D. Sank, Z. Chen, M. Khezri, J. Kelly, R. Barends, B. Campbell, Y. Chen, B. Chiaro, A. Dunsworth, A. Fowler, E. Jeffrey, E. Lucero, A. Megrant, J. Mutus, M. Neeley, C. Neill, P. J. O'Malley, C. Quintana, P. Roushan, A. Vainsencher, T. White, J. Wenner, A. N. Korotkov, and J. M. Martinis. Measurement-Induced State Transitions in a Superconducting Qubit: Beyond the Rotating Wave Approximation. *Physical Review Letters*, 117(19):190503, nov 2016. ISSN 10797114.

S. Schmid, L. G. Villanueva, and M. L. Roukes. *Fundamentals of nanomechanical resonators*, volume 49. Springer, 2016.

J. A. Schreier, A. A. Houck, J. Koch, D. I. Schuster, B. R. Johnson, J. M. Chow, J. M. Gambetta, J. Majer, L. Frunzio, M. H. Devoret, et al. Suppressing charge noise decoherence in superconducting charge qubits. *Physical Review B*, 77(18):180502, 2008.

A. Sears, A. Petrenko, G. Catelani, L. Sun, H. Paik, G. Kirchmair, L. Frunzio, L. Glazman, S. Girvin, and R. Schoelkopf. Photon shot noise dephasing in the strong-dispersive limit of circuit qed. *Physical Review B—Condensed Matter and Materials Physics*, 86(18):180504, 2012.

H. Sekoguchi, Y. Takahashi, T. Asano, and S. Noda. Photonic crystal nanocavity with a q-factor of 9 million. *Optics Express*, 22:916, 2014. ISSN 1094-4087.

L. Sementilli, E. Romero, and W. P. Bowen. Nanomechanical Dissipation and Strain Engineering. *Advanced Functional Materials*, 32(3):1–22, 2022. ISSN 16163028.

K. Serniak, M. Hays, G. De Lange, S. Diamond, S. Shankar, L. D. Burkhart, L. Frunzio, M. Houzet, and M. H. Devoret. Hot Nonequilibrium Quasiparticles in Transmon Qubits. *Physical Review Letters*, 121(15):157701, 2018. ISSN 10797114.

R. Sett, F. Hassani, D. Phan, S. Barzanjeh, A. Vukics, and J. M. Fink. Emergent macroscopic bistability induced by a single superconducting qubit. *PRX Quantum*, 5:010327, Feb 2024.

M. Shen, J. Xie, Y. Xu, S. Wang, R. Cheng, W. Fu, Y. Zhou, and H. X. Tang. Photonic link from single-flux-quantum circuits to room temperature. *Nature Photonics*, 18(4):371–378, 2024.

S. Simbierowicz, M. Borrelli, V. Monarkha, V. Nuutinen, and R. E. Lake. Inherent thermal-noise problem in addressing qubits. *PRX Quantum*, 5(3):030302, 2024.

S. Sonar, U. Hatipoglu, S. Meesala, D. Lake, H. Ren, and O. Painter. High-efficiency low-noise optomechanical crystal photon-phonon transducers. *arXiv preprint arXiv:2406.15701*, 2024.

D. K. Sparacin, S. J. Spector, and L. C. Kimerling. Silicon waveguide sidewall smoothing by wet chemical oxidation. *Journal of lightwave technology*, 23(8):2455, 2005.

S. Storz, J. Schär, A. Kulikov, P. Magnard, P. Kurpiers, J. Lütolf, T. Walter, A. Copetudo, K. Reuer, A. Akin, et al. Loophole-free bell inequality violation with superconducting circuits. *Nature*, 617(7960):265–270, 2023.

C. Sun, M. T. Wade, Y. Lee, J. S. Orcutt, L. Alloatti, M. S. Georgas, A. S. Waterman, J. M. Shainline, R. R. Avizienis, S. Lin, B. R. Moss, R. Kumar, F. Pavanello, A. H. Atabaki, H. M. Cook, A. J. Ou, J. C. Leu, Y. H. Chen, K. Asanović, R. J. Ram, M. A. Popović, and V. M. Stojanović. Single-chip microprocessor that communicates directly using light. *Nature*, 528 (7583):534–538, dec 2015. ISSN 14764687.

B. M. Terhal. Quantum error correction for quantum memories. *Reviews of Modern Physics*, 87(2):307–346, 2015.

J. D. Teufel, T. Donner, D. Li, J. W. Harlow, M. S. Allman, K. Cicak, A. J. Sirois, J. D. Whittaker, K. W. Lehnert, and R. W. Simmonds. Sideband cooling of micromechanical motion to the quantum ground state. *Nature*, 475(7356):359–363, 2011a.

J. D. Teufel, D. Li, M. S. Allman, K. Cicak, A. Sirois, J. D. Whittaker, and R. Simmonds. Circuit cavity electromechanics in the strong-coupling regime. *Nature*, 471(7337):204–208, 2011b.

J. Thompson, B. Zwickl, A. Jayich, F. Marquardt, S. Girvin, and J. Harris. Strong dispersive coupling of a high-finesse cavity to a micromechanical membrane. *Nature*, 452(7183):72–75, 2008.

J. D. Thompson, T. G. Tiecke, N. P. De Leon, J. Feist, A. V. Akimov, M. Gullans, A. S. Zibrov, V. Vuletić, and M. D. Lukin. Coupling a single trapped atom to a nanoscale optical cavity. *Science*, 340(6137):1202–1205, 2013. ISSN 10959203.

T. G. Tiecke, K. P. Nayak, J. D. Thompson, T. Peyronel, N. P. de Leon, V. Vuletić, and M. D. Lukin. Efficient fiber-optical interface for nanophotonic devices. *Optica*, 2(2):70, feb 2015. ISSN 23342536.

S. Touzard, A. Kou, N. E. Frattini, V. V. Sivak, S. Puri, A. Grimm, L. Frunzio, S. Shankar, and M. H. Devoret. Gated conditional displacement readout of superconducting qubits. *Phys. Rev. Lett.*, 122:080502, Feb 2019.

M. Tsang. Cavity quantum electro-optics. *Phys. Rev. A*, 81:063837, 2010.

Y. Tsaturyan, A. Barg, A. Simonsen, L. G. Villanueva, S. Schmid, A. Schliesser, and E. S. Polzik. Demonstration of suppressed phonon tunneling losses in phononic bandgap shielded membrane resonators for high-q optomechanics. *Optics express*, 22(6):6810–6821, 2014.

Y. Tsaturyan, A. Barg, E. S. Polzik, and A. Schliesser. Ultracoherent nanomechanical resonators via soft clamping and dissipation dilution. *Nature Nanotechnology*, 12(8):776–783, 2017. ISSN 17483395.

A. Vainsencher, K. Satzinger, G. Peairs, and A. Cleland. Bi-directional conversion between microwave and optical frequencies in a piezoelectric optomechanical device. *Applied Physics Letters*, 109(3), 2016.

T. C. van Thiel, M. J. Weaver, F. Berto, P. Duivestein, M. Lemang, K. Schuurman, M. Žemlička, F. Hijazi, A. C. Bernasconi, E. Lachman, M. Field, Y. Mohan, F. de Vries, N. Bultink, J. van Oven, J. Y. Mutus, R. Stockill, and S. Gröblacher. High-fidelity optical readout of a superconducting qubit using a scalable piezo-optomechanical transducer. *arXiv*, (2310.06026), 2023.

E. Verhagen, S. Deléglise, S. Weis, A. Schliesser, and T. J. Kippenberg. Quantum-coherent coupling of a mechanical oscillator to an optical cavity mode. *Nature*, 482(7383):63–67, 2012.

A. Wallraff, D. I. Schuster, A. Blais, L. Frunzio, R.-S. Huang, J. Majer, S. Kumar, S. M. Girvin, and R. J. Schoelkopf. Strong coupling of a single photon to a superconducting qubit using circuit quantum electrodynamics. *Nature*, 431(7005):162–167, 2004.

A. Wallraff, D. I. Schuster, A. Blais, L. Frunzio, J. Majer, M. H. Devoret, S. M. Girvin, and R. J. Schoelkopf. Approaching unit visibility for control of a superconducting qubit with dispersive readout. *Phys. Rev. Lett.*, 95:060501, Aug 2005.

A. Wallraff, D. Schuster, A. Blais, J. Gambetta, J. Schreier, L. Frunzio, M. Devoret, S. Girvin, and R. Schoelkopf. Sideband Transitions and Two-Tone Spectroscopy of a Superconducting Qubit Strongly Coupled to an On-Chip Cavity. *Phys. Rev. Lett.*, 99:50501, 2007.

D. F. Walls and G. J. Milburn. *Quantum Optics*. Springer Verlag, 2008. ISBN 978-3-540-28573-1.

T. Walter, P. Kurpiers, S. Gasparinetti, P. Magnard, A. Potočnik, Y. Salathé, M. Pechal, M. Mondal, M. Oppliger, C. Eichler, and A. Wallraff. Rapid high-fidelity single-shot dispersive readout of superconducting qubits. *Phys. Rev. Appl.*, 7:054020, May 2017.

Y. Wan, D. Kienzler, S. D. Erickson, K. H. Mayer, T. R. Tan, J. J. Wu, H. M. Vasconcelos, S. Glancy, E. Knill, D. J. Wineland, A. C. Wilson, and D. Leibfried. Quantum gate teleportation between separated qubits in a trapped-ion processor. *Science*, 364(6443): 875–878, 2019. ISSN 10959203.

C. Wang, M. Zhang, B. Stern, M. Lipson, and M. Lončar. Nanophotonic lithium niobate electro-optic modulators. *Opt. Express*, 26(2):1547–1555, jan 2018.

C. Wang, Z. Li, J. Riemensberger, G. Lihachev, M. Churaev, W. Kao, X. Ji, J. Zhang, T. Blesin, A. Davydova, Y. Chen, K. Huang, X. Wang, X. Ou, and T. J. Kippenberg. Lithium tantalate photonic integrated circuits for volume manufacturing. *Nature*, 629(8013):784–790, may 2024. ISSN 14764687.

J. Wang, M. I. Ibrahim, I. B. Harris, N. M. Monroe, M. I. Wasiq Khan, X. Yi, D. R. Englund, and R. Han. 34.1 thz cryo-cmos backscatter transceiver: A contactless 4 kelvin-300 kelvin data interface. In *2023 IEEE International Solid- State Circuits Conference (ISSCC)*, pages 504–506, 2023.

K. H. Warner, J. Holzgrafe, B. Yankelevich, D. Barton, S. Poletto, C. J. Xin, N. Sinclair, D. Zhu, E. Sete, E. Langley, B. Batson, M. Colangelo, A. Shams-Ansari, G. Joe, K. K. Berggren, L. Jiang, M. Reagor, and M. Lončar. Coherent control of a superconducting qubit using light. *arXiv*, (2310.16155), 2023.

M. J. Weaver, B. Pepper, F. Luna, F. M. Buters, H. J. Eerkens, G. Welker, B. Perock, K. Heeck, S. de Man, and D. Bouwmeester. Nested trampoline resonators for optomechanics. *Applied Physics Letters*, 108(3), 2016.

M. J. Weaver, P. Duivestein, A. C. Bernasconi, S. Scharmer, M. Lemang, T. C. Thiel, F. Hijazi, B. Hensen, S. Gröblacher, and R. Stockill. An integrated microwave-to-optics interface for scalable quantum computing. *Nature Nanotechnology*, 19(2):166–172, 2024. ISSN 17483395.

S. Wehner, D. Elkouss, and R. Hanson. Quantum internet: A vision for the road ahead. *Science*, 362(6412), oct 2018. ISSN 10959203.

A. Weinstein, C. Lei, E. Wollman, J. Suh, A. Metelmann, A. Clerk, and K. Schwab. Observation and interpretation of motional sideband asymmetry in a quantum electromechanical device. *Physical Review X*, 4(4):041003, 2014.

S. Weis, R. Rivière, S. Deléglise, E. Gavartin, O. Arcizet, A. Schliesser, and T. J. Kippenberg. Optomechanically induced transparency. *Science*, 330(6010):1520–1523, 2010.

I. Wilson-Rae, N. Nooshi, W. Zwerger, and T. J. Kippenberg. Theory of ground state cooling of a mechanical oscillator using dynamical backaction. *Physical review letters*, 99(9):093901, 2007.

P. Winkel, I. Takmakov, D. Rieger, L. Planat, W. Hasch-Guichard, L. Grünhaupt, N. Maleeva, F. Foroughi, F. Henriques, K. Borisov, J. Ferrero, A. V. Ustinov, W. Wernsdorfer, N. Roch, and I. M. Pop. Nondegenerate Parametric Amplifiers Based on Dispersion-Engineered Josephson-Junction Arrays. *Physical Review Applied*, 13(2):24015, 2020. ISSN 23317019.

E. A. Wollack, A. Y. Cleland, R. G. Gruenke, Z. Wang, P. Arrangoiz-Arriola, and A. H. Safavi-Naeini. Quantum state preparation and tomography of entangled mechanical resonators. *Nature*, 604(7906):463–467, 2022.

E. E. Wollman, C. U. Lei, A. J. Weinstein, J. Suh, A. Kronwald, F. Marquardt, A. A. Clerk, and K. C. Schwab. Quantum squeezing of motion in a mechanical resonator. *Science*, 349 (6251):952–955, 2015.

Y. Wu, W.-S. Bao, S. Cao, F. Chen, M.-C. Chen, X. Chen, T.-H. Chung, H. Deng, Y. Du, D. Fan, et al. Strong quantum computational advantage using a superconducting quantum processor. *Physical review letters*, 127(18):180501, 2021.

Q. Xu, J. P. Bonilla Ataides, C. A. Pattison, N. Raveendran, D. Bluvstein, J. Wurtz, B. Vasić, M. D. Lukin, L. Jiang, and H. Zhou. Constant-overhead fault-tolerant quantum computation with reconfigurable atom arrays. *Nature Physics*, 20(7):1084–1090, 2024. ISSN 17452481.

J. Yin, Y. Cao, Y.-H. Li, S.-K. Liao, L. Zhang, J.-G. Ren, W.-Q. Cai, W.-Y. Liu, B. Li, H. Dai, et al. Satellite-based entanglement distribution over 1200 kilometers. *Science*, 356(6343): 1140–1144, 2017.

T. Yoshle, A. Scherer, J. Hendrickson, G. Khitrova, H. M. Gibbs, G. Rupper, C. Ell, O. B. Shchekin, and D. G. Deppe. Vacuum Rabi splitting with a single quantum dot in a photonic crystal nanocavity. *Nature*, 432(7014):200–203, nov 2004. ISSN 00280836.

A. Youssefi, I. Shomroni, Y. J. Joshi, N. R. Bernier, A. Lukashchuk, P. Uhrich, L. Qiu, and T. J. Kippenberg. A cryogenic electro-optic interconnect for superconducting devices. *Nature Electronics*, 4(5):326–332, May 2021. ISSN 2520-1131.

P.-L. Yu, K. Cicak, N. Kampel, Y. Tsaturyan, T. Purdy, R. Simmonds, and C. Regal. A phononic bandgap shield for high-q membrane microresonators. *Applied Physics Letters*, 104(2), 2014.

S. Zanker and M. Marthaler. Qubit dephasing due to quasiparticle tunneling. *Physical Review B*, 91(17):174504, May 2015.

M. Zemlicka, E. Redchenko, M. Peruzzo, F. Hassani, A. Trioni, S. Barzanjeh, and J. M. Fink. Compact vacuum-gap transmon qubits: Selective and sensitive probes for superconductor surface losses. *Physical Review Applied*, 20(4), 2023.

C. Zener. Non-adiabatic crossing of energy levels. *Proceedings of the Royal Society of London. Series A, Containing Papers of a Mathematical and Physical Character*, 137(833):696–702, 1932.

C. Zener. Internal friction in solids. i. theory of internal friction in reeds. *Physical review*, 52 (3):230, 1937.

C. Zener. Internal friction in solids ii. general theory of thermoelastic internal friction. *Physical review*, 53(1):90, 1938.

E. Zeuthen, A. Schliesser, A. S. Sørensen, and J. M. Taylor. Figures of merit for quantum transducers. *Quantum Science and Technology*, 5(3):034009, may 2020. ISSN 2058-9565.

M. Zhang, C. Wang, P. Kharel, D. Zhu, and M. Lončar. Integrated lithium niobate electro-optic modulators: when performance meets scalability. *Optica*, 8(5):652–667, 2021.

R. Zhang, C. Ti, M. I. Davanço, Y. Ren, V. Aksyuk, Y. Liu, and K. Srinivasan. Integrated tuning fork nanocavity optomechanical transducers with high fMQM product and stress-engineered frequency tuning. *Applied Physics Letters*, 107(13):131110, 2015.

H. Zhao, A. Bozkurt, and M. Mirhosseini. Electro-optic transduction in silicon via gigahertz-frequency nanomechanics. *Optica*, 10(6):790, 2023. ISSN 23342536.

H. Zhao, W. D. Chen, A. Kejriwal, and M. Mirhosseini. Quantum-enabled continuous microwave-to-optics frequency conversion. *arXiv preprint arXiv:2406.02704*, 2024.

T. M. Zhao, H. Zhang, J. Yang, Z. R. Sang, X. Jiang, X. H. Bao, and J. W. Pan. Entangling different-color photons via time-resolved measurement and active feed forward. *Physical Review Letters*, 112(10):103602, 2014. ISSN 10797114.

C. Zhong, Z. Wang, C. Zou, M. Zhang, X. Han, W. Fu, M. Xu, S. Shankar, M. H. Devoret, H. X. Tang, and L. Jiang. Proposal for Heralded Generation and Detection of Entangled Microwave–Optical-Photon Pairs. *Physical Review Letters*, 124(1):010511, Jan. 2020.

N. Zhu, X. Zhang, X. Han, C.-L. Zou, C. Zhong, C.-H. Wang, L. Jiang, and H. X. Tang. Waveguide cavity optomagnonics for microwave-to-optics conversion. *Optica*, 7(10):1291–1297, 2020.

A. Zivari, R. Stockill, N. Fiaschi, and S. Gröblacher. Non-classical mechanical states guided in a phononic waveguide. *Nature Physics*, 18(7):789–793, may 2022. ISSN 17452481.